CFD modelling of ocean wave interaction with thin perforated structures represented by their macro-scale effects

Submitted by *Anna Feichtner*, to the University of Exeter
as a thesis for the degree of
Doctor of Philosophy in Renewable Energy,
September 2021.

.....

To Rex and the rocks.

Abstract

Fluid interaction with thin perforated structures is of interest in a range of contexts. Applications in marine engineering include current and wave interaction with aquaculture containers, breakwaters and, as a new application, platforms for floating wind turbines with perforated outer shrouds. Another more general application is for tuned liquid dampers with baffles for motion attenuation. Thus, there is significant interest in the challenge of simulating the effect of these thin porous structures using Computational Fluid Dynamics (CFD).

This thesis proposes and assesses the use of a macro-scale approach to CFD modelling of wave interaction with thin perforated structures. The structures are not resolved explicitly but represented by their spatially averaged effects on the flow by means of a homogeneous porous pressure-drop applied to the Navier-Stokes momentum equation. Two options are explored where the pressure-drop is either applied as a volumetric porous zone or as a jump-condition across a porous surface.

The wave modelling capabilities and the basis of the macroscopic porosity implementations are readily available in the open-source code OpenFOAM®, which is used in this work. Minor code modifications were necessary to introduce orthotropic porosity for a cylindrically shaped structure. More significant code development was required to implement accurate motion of a floating porous structure as a new capability as part of a custom motion solver. The method is applied to fixed perforated sheets and cylinders as well as a floating tension leg platform (TLP), and the overall fluid flow behaviour and global forces and motions are assessed. The validation against experimental and potential-flow results demonstrates that a macro-scale porosity representation can accurately reproduce large-scale flow, force and motion effects of all conditions investigated. As the most representative case, the CFD results of the horizontal force on the perforated cylinder differ between 2 and 12 % from the experimental results. As part of this work, it is shown that, firstly, the Volume-Averaged Reynolds-Averaged Navier-Stokes (VARANS) equations can not only be used for large volumetric granular material, but also for thin perforated structures, and secondly, that the effects of applying a RANS turbulence model on the results are of minor significance and that the full Navier-Stokes equations give good results.

The presented macro-scale approach offers greater flexibility in the range of wave conditions that can be modelled compared to approaches based on linear potential-flow theory and requires a smaller computational effort compared to CFD approaches which resolve the micro-structural geometry of the openings and the fluid flow across it explicitly. This approach can therefore be an efficient alternative to assess large-scale effects for engineering problems.

Contents

List of Figures

List of Tables

List of Equations

Nomenclature

Acronyms

2D Two-dimensional

3D Three-dimensional

AWA Active Wave Absorption

BC Boundary Condition

BEM Boundary Element Method

BL Boundary Layer

CFD Computational Fluid Dynamics

COG Centre of Gravity

CPH Cells per wave Height

CPL Cells per wave Length

CPU Central Processing Unit

DNS Direct Numerical Simulation

DOF Degrees of Freedom

ER-AWA Extended Range - Active Wave Absorption

FDM Finite-Difference Method

FEM Finite-Element Method

FFT Fast Fourier Transform

FOWT Floating Offshore Wind Turbine

FSI Fluid-Structure Interaction

FV Finite-Volume

FVM Finite-Volume Method

GCI Grid Convergence Index

GFM Ghost Fluid Method

LES Large Eddy Simulation

LHS Left Hand Side

MULES Multidimensional Universal Limiter for Explicit Solution

NS Navier-Stokes

NWT Numerical Wave Tank

ODE Ordinary Differential Equation

OF OpenFOAM®

ORE Offshore Renewable Energy

PDE Partial Differential Equation

PISO Pressure Implicit with Splitting of Operator

RANS Reynolds-Averaged Navier-Stokes

RAO Response Amplitude Operator

RHS Right Hand Side

SIMPLE Semi-Implicit Method for Pressure-Linked Equations

SLERP Spherical Linear Interpolation

SPH Smoothed-Particle-Hydrodynamics (method)

SST Shear Stress Transport (κ-ω-SST turbulence model)

SW-AWA Shallow Waters - Active Wave Absorption

TLP Tension Leg Platform

VARANS Volume-Averaged Reynolds-Averaged Navier-Stokes

VIV Vortex Induced Vibrations

VOF Volume-of-Fluid (method)

WEC Wave Energy Converter

WG Wave Gauge

WSI Wave-Structure Interaction

Symbols

Bold symbols indicate vectors or tensors.

A	Mean wave amplitude	m
a	Linear porosity coefficient (Darcy coefficient)	
A_a	Water-plane area	m^2
$A(f)$	Amplitude spectrum	m
A_{input}	Input/target mean wave amplitude	m
α	Phase (water) fraction per unit volume	
$\boldsymbol{A_{ls}}$	(General) matrix coefficients	
β	Stokes-parameter	
$\boldsymbol{b_{ls}}$	(General) vector of boundary conditions and source terms	
B	Buoyancy	N
$\boldsymbol{C}$	Damping matrix	Ns/m
c	Transient porosity coefficient (Polubarinova-Kochina coefficient)	
C_f	Porosity/drag coefficient	
CFL	Courant-Friedrichs-Lewy number	
c_g	(Wave) group velocity	ms^{-1}
D	(Outer) cylinder diameter	m
d	Thickness of perforated barrier	m

δ	Discharge coefficient	
δ_{BL}	Boundary layer thickness	m
Δf	(Wave) frequency resolution	s^{-1}
Δp	Pressure-drop	Nm^{-2}
Δt	Time step	s
E	Error	
E_{κ_E}	Turbulent energy spectrum	
ϵ	Turbulence dissipation rate	$m^2 s^{-3}$
$\eta(t)$	Free surface / wave elevation	m
$\boldsymbol{F}$	Vector of the total force	N
F	Mean force amplitude	N
f	(Wave) frequency	s^{-1}
$\boldsymbol{s}_{f,i}$	Face area vector	m^2
F_s	Safety factor	
$f(t)$	Force time series	N
F_x	Linear spring restoring force	N
f_x	Normalised force amplitude	
$\boldsymbol{g}$	Gravitational acceleration	9.81 ms^{-2}
H	Wave height	m
h	Water depth	m
$\boldsymbol{I}$	Identity tensor	
I_t	Turbulence intensity	
$\boldsymbol{K}$	Stiffness matrix	N/m
k	Turbulent kinetic energy	$m^2 s^{-2}$
κ	Interface curvature	m^{-1}

κ_E	Eddy wave number	m^{-1}
KC	Keulegan-Carpenter number	
k_w	Wave number	$radm^{-1}$
L	Characteristic (turbulence) length scale	m
λ	Wave length	m
L_t	Tendon length	m
l_x, l_y, l_z	Mesh cell face lengths / dimensions	m
$\boldsymbol{M}$	Mass matrix	kg
M	Mass	kg
μ	Dynamic (molecular) viscosity	Nsm^{-2}
μ_{eff}	Effective dynamic viscosity	Nsm^{-2}
μ_t	Dynamic turbulent eddy viscosity	Nsm^{-2}
n	Porosity	
ν	Kinematic (molecular) viscosity	m^2s^{-1}
ν_t	Kinematic turbulent eddy viscosity	m^2s^{-1}
ω	Specific turbulence dissipation rate	s^{-1}
ω_w	Angular wave frequency	$rads^{-1}$
p	Pressure	Nm^{-2}
$p*$	Pseudo-dynamic pressure	Nm^{-2}
ϕ	Flux	m^3
$\boldsymbol{\phi_{ls}}$	(General) solution vector	
ψ_w	Wave phase shift	rad
$\boldsymbol{R}$	Reynolds-stresses	m^2s^{-2}
r	Perforation hole radius	m
$\boldsymbol{R_{dev}}$	Deviatoric component of Reynolds-stresses	m^2s^{-2}

Re	Reynolds number	
ρ	Density	kgm^{-3}
$\boldsymbol{r}_{A_M B_F}$	Moment vector	
R_{refl}	Reflection coefficient	
R_S	Ratio of solution change	
S	Solution of a specified parameter	
s	Perforation hole separation distance	m
$S(f)$	Variance density spectrum	$m^2 s$
S_h	Heave hydrostatic stiffness	$mkgs^{-2}$
σ	Standard deviation	
σ_{st}	Surface tension coefficient	
$\boldsymbol{TR}$	Transformation matrix	
T	Wave period	s
t	Time	s
θ	Wave phase	rad
T_p	Oscillation period	s
T_t	Total tendon stiffness	N
T_{t0}	Total tendon pretension	N
$\boldsymbol{U}$	Velocity vector (actual velocity inside porous medium)	ms^{-1}
$\boldsymbol{u}$	Darcy velocity (averaged velocity inside porous medium)	ms^{-1}
u_c	Characteristic velocity (amplitude)	ms^{-1}
$\boldsymbol{u_{ic}}$	Interface compression velocity	ms^{-1}
u_n	Velocity component normal to a surface	ms^{-1}
U_{unc}	Uncertainty	
V	Cell volume	m^3

V_m	Mean displaced water volume	m^3
$\boldsymbol{x} = (xyz)$	Position vector	m
X	Mean motion amplitude in x-direction (surge)	m
x	Position, displacement	m

Published Work

Many parts of this thesis originally appeared in the following journal articles or conference proceedings, published as first author:

A. Feichtner, E. Mackay, G. Tabor, P. R. Thies, and L. Johanning. Comparison of macro-scale porosity implementations for CFD modelling of wave interaction with thin porous structures. *Journal of Marine Science and Engineering*, vol. 9, no. 2, p. 150, 2021.

A. Feichtner, E. Mackay, G. Tabor, P. R. Thies, L. Johanning, and D. Ning. Using a porous-media approach for CFD modelling of wave interaction with thin perforated structures. *Journal of Ocean Engineering and Marine Energy*, vol. 7, no. 1, pp. 1–23, 2021.

A. Feichtner, G. Tabor, and E. Mackay, P. R. Thies, and L. Johanning. On the use of a porous-media approach for the modelling of wave interaction with thin perforated cylinders. In *Conference Proceedings of the 15th OpenFOAM Workshop (OFW15)*, Online, June 22-25 2020.

A. Feichtner, E. Mackay, G. Tabor, P. R. Thies, and L. Johanning. Modelling wave interaction with thin porous structures using OpenFOAM. In *Proceedings of the 13th European Wave and Tidal Energy Conference (EWTEC 2019)*, Naples, 2019.

Co-authored publications (where some are under review or in preparation) are:

L. Wang, B. Chen, E. Mackay, L. Johanning, and A. Feichtner. Numerical simulation of the wave load mitigation effect of a perforated wall mounted in front of a

floating structure. Unpublished manuscript, 2021

L. Huang, D. Benites, T. Smith, N. Charalambous, G. Tabor, P. Cardiff, E. Ransley, J. Davidson, C. Windt, Y. Li, R. Paredes, R. Song, M.. Li, M. Colombo, A. Feichtner, and S. Tavakoli. Wave-structural interactions using OpenFOAM – status and outlook". *OpenFOAM Journal*. Under Review, 2021

D. Qiao, E. Mackay, J. Yan, C. Feng, B. Li, A. Feichtner, D. Ning, and L. Johanning. Numerical simulation with a macroscopic CFD method and experimental analysis of wave interaction with fixed porous cylinder structures. *Marine Structures*, vol. 80, 2021

E. Mackay, A. Feichtner, R. Smith, P. R. Thies, and L. Johanning. Verification of a boundary element model for wave forces on structures with porous elements. In *Proceedings of the 3rd International Conference on Renewable Energies Offshore (RENEW 2018)*, 2018.

Further contributions are:

Tutorial: A. Feichtner. CFD modelling of wave interaction with thin porous structures (*Link to tutorial on YouTube*). At *The 3rd UCL OpenFoam Workshop*, University College London, Online, February 25, 2021.

Poster: A. Feichtner, E. Mackay, G. Tabor, P. R. Thies, and L. Johanning. Using porous-media for CFD modelling of wave interaction with thin perforated structures - Resilient Integrated-Coupled FOW platform design methodology (ResIn). At *The Final UK-China Virtual Conference*, Online, December 8-10, 2020.

Parts of this work were awarded as:

"One of the three best student presentations" at *The 16th OpenFOAM Workshop 2021 (OFW16)*, Online, June 8-11, 2021.

"The best presentation" at the *EMPS PGR Conference 2021*, College of Engineering, Mathematics and Physical Sciences, University of Exeter, Exeter, March 10-11, 2019.

Chapter 1

Introduction

1.1 Background and Motivation

Wave interaction with structures consisting of thin perforated or porous elements is of significant interest in various contexts. A general application is for tuned liquid dampers with baffles for motion attenuation in buildings [1–3]. Applications in ocean and marine engineering include current and wave interaction with aquaculture containers and net structures [4, 5] as well as breakwaters [6, 7].

A potentially new application in the marine renewable-energy domain is in motion damping of platforms for floating offshore wind turbines (FOWTs). Harnessing wind via FOWTs is gaining momentum as a promising renewable energy resource during the present era of acute climate crisis. The main advantage of floating platforms is the possibility to access sites with water depths larger than 60 m, which is about the limitation for bottom-fixed offshore wind turbines. The bathymetry data from the Global Wind Atlas (*https://globalwindatlas.info*) shows that most coastal regions quickly exceed that limit, see Fig. 1.1a. Further offshore, the wind resource is stronger and steadier [8–10]. For reference, Fig. 1.1b shows the wind power density which is an indicator for the wind resource.

(a) bathymetry in [m]: water depths over 60 m are coloured in dark blue (0 m are coloured in white)

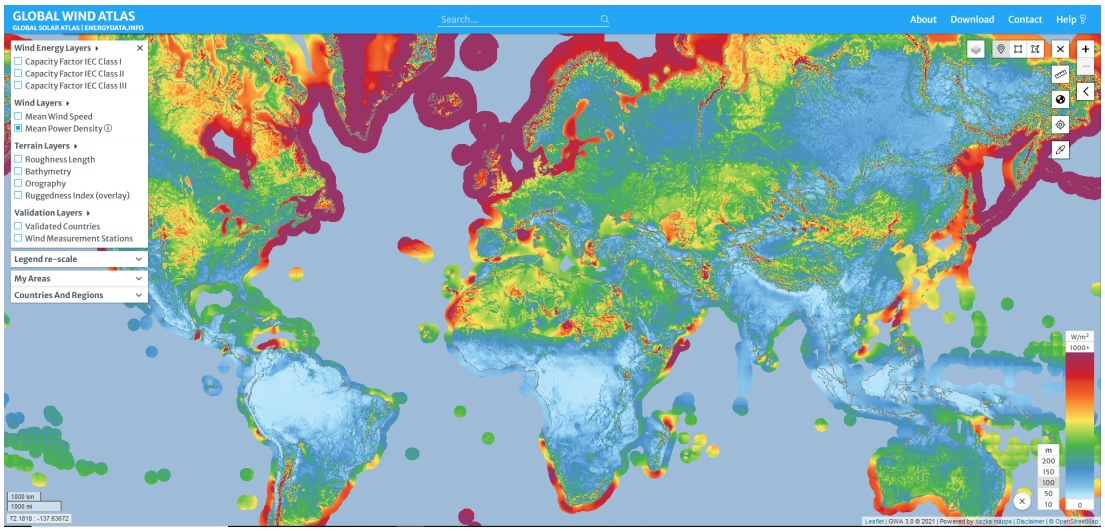

(b) mean wind power density in [W/m^2]: values over 1000 W/m^2 are coloured in purple (0 W/m^2 are coloured in white)

Figure 1.1: (a) Bathymetry and (b) mean wind power density across the globe. Taken from the Global Wind Atlas, *https://globalwindatlas.info*.

Other benefits of FOWTs are that they avoid any not-in-my-backyard (NIMBY) criticism, have environmental benefits due to reduced activity on the seabed during installation, that their installation is potentially cheaper due to their possible onshore assembly, and the avoidance of offshore heavy lift operations [9, 11]. However, as an emerging technology, FOWTs face multiple engineering challenges. Offshore they are exposed to harsh environmental conditions where wind, current and waves interact with the structure and its mooring lines. The interaction is complex and a stable platform is key to enable continuous energy capture as well as to provide structural resilience. Platform instability can lead to decreased lifetime due to fatigue failure of components [12],

snap failure of mooring lines [13, 14] as well as reduced turbine operation times due to excessive tower top motion [15].

Common approaches to reduce the FOWT's excitations, to avoid excessive nacelle accelerations and platform pitch motions are extended blade pitch control strategies [15–18] or direct vibration control strategies using vibration absorbers [19]. The latter include ball vibration absorbers [20], tuned mass dampers [21, 22] and tuned liquid dampers [19, 23]. A new concept may be the application of a perforated outer shroud by using it as an energy dissipation mechanism and thus, passive motion damping element. The findings of Molin [24] *"... suggest that perforating parts of marine or offshore structures can be an efficient means for reducing inertia and slamming loads, and for increasing the damping of resonant responses."*

Since experimental investigations are typically costly and time-consuming, only a small number of parameters is viable to be investigated experimentally. Numerical methods can overcome these limitations once they are validated. Various methods have been developed to investigate wave interaction with marine structures. These range from modelling using potential-flow theory, for instance applied to wave interaction with Jarlan-type breakwaters [25], to high-fidelity Large-Eddy-Simulations (LES), for instance applied to wave flow through vegetation [26]. The majority of past studies, using both potential-flow and Navier-Stokes based methods, deal with impermeable structures, e.g. [27–31]. A smaller number of investigations target fluid interaction with porous structures, e.g. [32–37]. Most Navier-Stokes models have focused on large volumetric granular material, e.g. [36–39], and fewer were targeted towards thin porous or perforated structures [4, 5, 40].

1.1.1 Knowledge Gap

The concept of using perforated outer shrouds to stabilize platforms of FOWTs is novel. Thus, this wave-structure interaction (WSI) problem has not yet been investigated comprehensively. Therefore, a suitable numerical method to study this problem is sought. The literature review highlights that related work on similar problems can be used as a basis for the present application, but further development and validation is required for the specific case of wave interaction with thin perforated structures.

1.2 Aim and Objectives

1.2.1 Aim

The aim of this thesis is to identify and establish a numerical method to simulate wave interaction with structures, both fixed and floating, that fully or partially consist of thin perforated elements. The idea is to use a numerical framework that meets the following requirements in terms of accuracy, flexibility and efficiency:

- The main interest lies in modelling the large-scale effects of WSI in terms of overall forces, motions and the mean fluid flow rather than the replication of the detailed flow behaviour on a small scale.
- Although the present work focuses on simplified structures and operational wave conditions, the underlying framework needs to provide options for extension to extreme wave conditions or to include current or wind effects.
- The intention is to keep the computational effort as small as possible whilst maintaining flexibility and without losing the targeted accuracy levels in terms of large-scale replication.

In order to derive a solution while meeting these criteria, a suitable numerical framework has been identified based on a literature review of available methods and existing work, see Chapter 2, in particular Sections 2.2 and 2.4. Numerical modelling of this WSI problem requires a reliable wave modelling method, an adequate mooring line representation, an appropriate mesh motion method, and a suitable representation of thin perforated structures. The latter is of primary importance, while all other aspects are of secondary relevance.

1.2.2 Method Proposal

The representation of the perforated structure has been identified as the key factor in achieving the targeted aim and requirements for CFD modelling of wave interaction with structures that fully or partially consist of thin perforated elements.

As a solution, this thesis proposes, establishes and validates a method within a Navier-Stokes (NS)-based CFD framework where thin porous structures are represented by their macro-scale effects by means of a volume-averaged pressure-drop, instead of an exact geometry resolution of the perforations. The general concept of using a macro-scale porosity representation is not new, but has scarcely been used in the context of CFD modelling of wave interaction with thin structures.

The main benefit of using macro-scale methods in combination with solving the NS equations is that this provides a trade-off between solution accuracy and computational demand. This is a valuable practical implication for the investigation of many engineering problems.

1.2.3 Research Questions

The key research questions this thesis seeks to address have been as follows:

- How can a macro-scale representation of thin perforated structures be implemented in a CFD framework in the context of large-scale WSI?
- How do various numerical implementations of macro-scale porosity compare and which are the best options for the specific conditions under consideration?
- What is the impact of various turbulence models and which one is best for the conditions under consideration?
- Can a macro-scale porosity representation be used for both fixed and dynamic structures, and what are the requirements?
- Can a macro-scale porosity representation be a valid and viable approach to model large-scale WSI, and what are its limitations?

1.2.4 Scope

It is desirable to find a comprehensive solution to the stated research questions for a wide range of marine engineering problems, covering operational and extreme environmental conditions, simple and complex geometries, or complex coupling effects. However, approaching this problem in a structured way, this thesis is the first step towards simulations of marine engineering problems that deal with thin perforated structures, such as aquaculture containers and fixed and floating breakwater structures.

The validation of the proposed method of porosity representation is of the main interest. Thus, this thesis focuses on operational regular wave conditions and geometrically simple structures, all in alignment with available experimental data. In other words, complexity of the WSI in terms of model setup has been kept limited throughout this thesis. The simplifications are introduced in the respective sections and discussed in detail in Chapter 8.

This thesis focuses solely on the CFD modelling but its results are compared against experimental data and data from a linear potential-flow model. The experimental campaign was planned and conducted by Mackay et al. [41, 42] and Mackay et al. [43],

and the potential-flow model was developed by Mackay et al. [41] and Mackay and Johanning [44]. Both data sets have been made available for the present work but any investigations on them are out of the scope of this thesis. Therefore, no details are given on either but relevant aspects are introduced in Chapter 4.

In theory, the present specific regular wave conditions could be investigated with reduced-order models such as models using potential-flow theory, see Section 2.2.1. The advantage of a NS-based CFD framework becomes relevant for more complex WSI investigations where the limitations of simpler models are exceeded, for instance in the context of extreme environmental conditions such as rogue or breaking waves. Modelling of extreme conditions is outside the scope of this thesis, but the assessment and validation of this work provides the basis for it.

1.2.5 Contributions

This work contributes to our knowledge in this area by providing validation of a novel method for the macro-scale representation of the microstructure of a thin perforated barrier under regular wave interaction. Instead of explicit geometry resolution of the perforations, a momentum source term that represents the effects of the perforated structure on the fluid in this region is added to the Navier-Stokes momentum equation.

The theoretical formulation used for the momentum source, which equates the pressure-drop across the thin perforated barrier, does not require any calibration procedures and is capable of replicating large-scale forces, global motions and the overall fluid flow behaviour of the WSI. The validity of the pressure drop model has been demonstrated for simulations of wave interaction with fixed structures for a range of regular wave conditions and porosity values. Various types of numerical macro-scale implementation have been assessed and compared for fixed perforated sheets and cylinders, the effects of various turbulence modelling settings has been assessed, and the best option for the investigated conditions has been identified. The latter has then been applied to wave interaction with a floating tension-leg platform (TLP) with an outer porous cylinder. Since existing motion solvers lack the required capabilities to account for the force on the porous structure parts, code development was required and thus, contributed as a custom motion solver. The custom motion solver is an extension of the existing dynamic mesh morphing solver for a single floating body. It has been used to validate the macro-scale porosity approach for moving structures for a small range of conditions.

The overall results indicate that the method proposed in this thesis can be an efficient and viable option for the application to similar problems in coastal and ocean engineering where a trade-off between modelling accuracy and computational cost is

desired in the context of large-scale forces and motions. Although this thesis focuses on operational regular wave conditions, a Navier-Stokes based CFD framework allows an extension to extreme wave conditions where simpler methods, for instance based on potential-flow theory, have limitations. The outcome of the method assessment in terms of required discretisation, scheme and solver settings can serve as a valuable starting point for the setup of similar CFD simulations. Furthermore, a first step has been taken towards modelling of floating platforms that include perforated elements in order to assess their feasibility and to enable engineering decisions.

To sum up, the macro-scale method proposed has been successfully validated for the present specific conditions in terms of regular wave conditions with moderate steepness, thin and circularly perforated rigid barriers, and simple geometrical structures. It is expected that it can confidently be applied to a wider range of marine engineering problems if those key conditions are similar to the ones validated. However, with increasing deviations, the method would require further evaluation. The parameters crucial in terms of method limitations are expected to be the wave steepness, particularly in regard to wave breaking effects, the thickness of the porous barrier, and the type of the porous barrier (i.e. the geometrical characteristics such as net-, foam-, or perforation-like shapes).

1.3 Methodology Overview

The conceptual and high-level methodology of this thesis is divided into chapters in the following manner. Chapter 2 covers the review of related literature and introduction of the numerical framework. Firstly, more general underlying numerical concepts are explained. Secondly, the more specific aspects concerning wave modelling, macro-scale porosity representation, mooring line representation, rigid body motion and dynamic meshing is described including their numerical implications.

The main work of this thesis is presented in Chapters 3-7. Chapter 3 describes the methodology that is adopted to answer the research objectives stated above. This includes the high-level decision-making processes and the overview of the step-by-step execution of the model simulations and method validation. Chapter 4 introduces general data analysis concepts for validation and verification procedures as well as the experimental and potential-flow data that is used for validation. Chapters 5-7 cover the results of all performed CFD simulations and the assessment and validation of the proposed macro-scale method for porosity representation. This includes the evaluation of requirements in the numerical setup to achieve reliable wave modelling, the method assessment for static porous structures and its extension to moving porous structures. The validation is followed by a discussion in Chapter 8, which covers the applicability

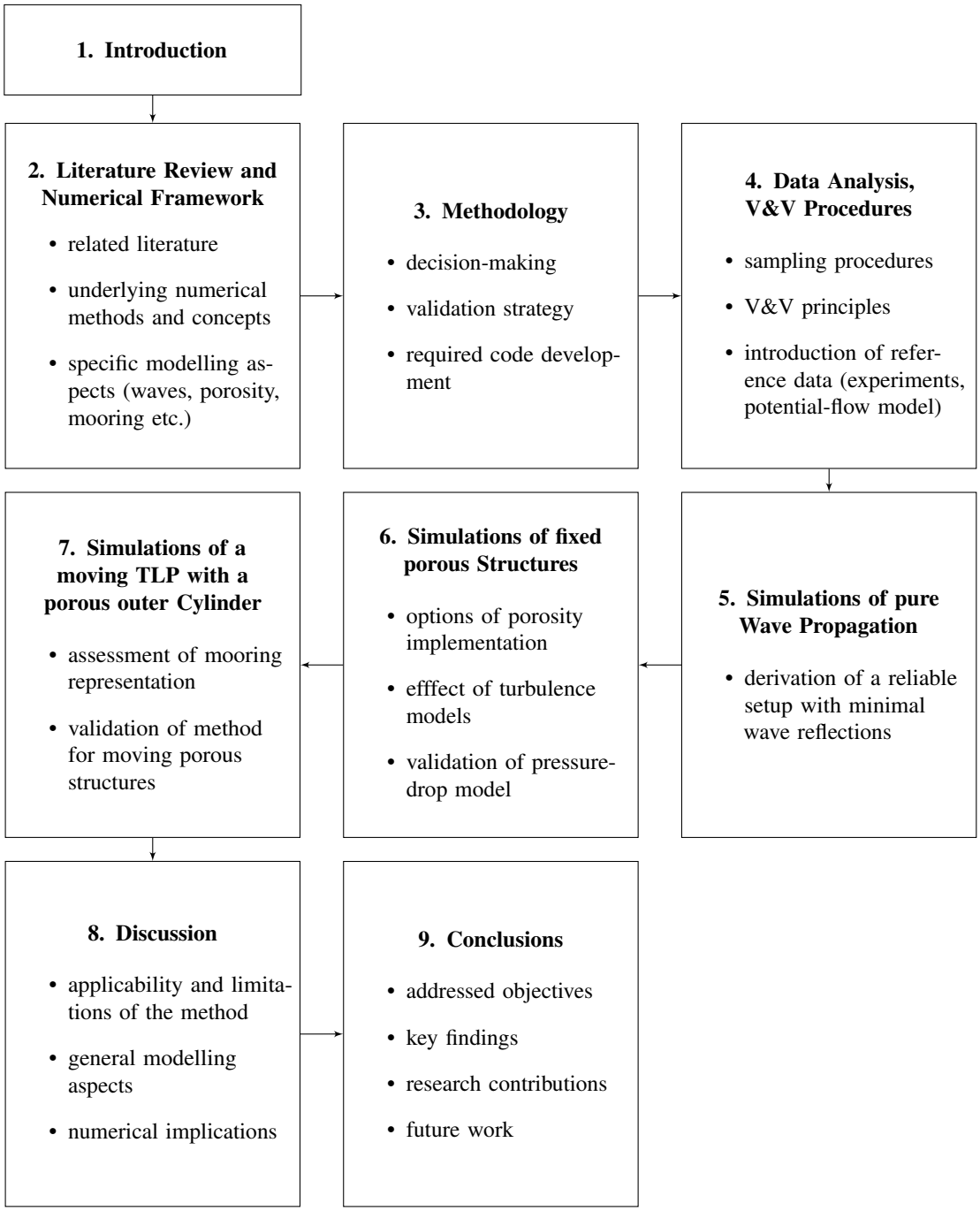

Figure 1.2: The conceptual methodology and structure of this thesis.

and limitations of the macro-scale porosity method, general modelling aspects and specific numerical implications. Chapter 9 summarizes the addressed objectives, the key findings and research contributions, as well as identified areas for future work. The conceptual methodology, which corresponds to the structure of this thesis, is illustrated in Fig. 1.2.

Chapter 2

Literature Review and Numerical Framework

2.1 Introduction

As stated in Chapter 1, the main objective of the present work has been to develop a numerical method to simulate hydrodynamics of FOWT platforms that are equipped with thin outer perforated shrouds. Due to the novel approach of using a perforated shroud as a passive motion damping system, this kind of structure does not exist yet and has therefore never been numerically studied before. However, related existing literature can be used as a base for this thesis. The detailed literature review on each key aspect is introduced in the corresponding section in the following, including:

- options of numerical methods,
- wave theory and modelling methods,
- the representation of thin perforated structures,
- dynamic mesh motion methods and
- methods of mooring line representation.

2.2 Numerical Method

Various approaches can be used to numerically model fluid dynamics. In general, the approaches differ in their governing equations which represent their underlying assumptions and simplifications. These relate to the level of accuracy and computational cost. Typically the accuracy increases with higher computational cost and vice versa [45].

2.2.1 Possible Approaches to model Fluid Dynamics

The main approaches from simple to more complex are methods based on potential-flow theory (Laplace Equation), methods that use the Euler equations and methods based on the Navier-Stokes (NS)-equations. The main options and their relative accuracy and computational demand are outlined in Fig. 2.1 and are discussed in more detail below.

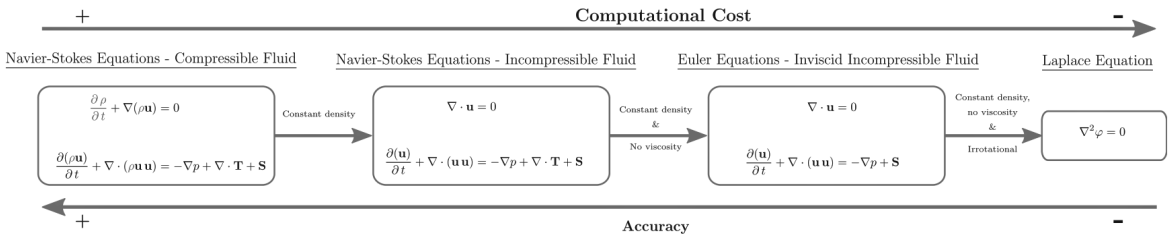

Figure 2.1: Methods for fluid dynamics modelling and their relative accuracy and computational cost. Taken from Windt et al. [45] who adapted from Guanche [46].

Potential-flow Theory

Potential-flow theory assumes the fluid to be inviscid and irrotational and the fluid can be either compressible or incompressible. Compressible potential-flow theory is complex and harder to solve compared to incompressible potential-flow theory. The assumption of incompressibility is typically used for WSI problems where the flow is represented by a velocity potential which satisfies Laplace's equation.

In the context of wave interaction with porous structures, two main types of linearisation can be employed to solve the boundary value problem, usually within the framework of a panel or boundary element method (BEM). One linearisation concerns the wave conditions, the other concerns the implementation of macro-scale porosity representation.

Regarding the wave conditions, there is a large volume of work on both linear and fully non-linear potential-flow models for wave interaction with impermeable structures. Potential-flow models for wave interaction with porous structures have mainly been

based on linear wave theory. This assumes that the wave steepness and body motions are small. Some examples of existing work are studies on a simplified representation of a Jarlan-type breakwater [25], work on a vertical porous barrier [32, 33, 47], or modelling of a series of vertical porous plates, done by Molin and Fourest [34]. Relatively little work has been done on higher-order or non-linear potential-flow models for porous structures. Interaction of cnoidal waves with an array of vertical concentric porous cylinders has been investigated by Weng et al. [48] and with a concentric cylindrical structure with an arc-shaped outer cylinder by Zhai et al. [49]. Solitary waves have been used to study interaction with a concentric porous cylinder system [50], or with vertical wall porous breakwaters [35]. Potential-flow models based on linear wave theory have the advantage of short computational times but their fundamental assumptions can limit them in their application, such as in the presence of steep or breaking waves. Non-linear potential-flow models can overcome the limitations in terms of wave conditions but require longer computation times and are still not able to capture viscous effects such as viscosity-induced drag forces. A brief introduction on wave theory is given in Section 2.3.1.

With regards to the representation of porosity, most potential-flow models apply the porous pressure-drop in a linearised approach and very few models use a non-linear formulation. Examples of work that use a linear relationship between pressure-drop and flow velocity include studies on a nearly vertical porous wall, undertaken by Chakrabarti and Sahoo [51], or for investigations on the effects of bottom topography, by Kaligatla and Sahoo [52] and Kaligatla et al. [53]. A quadratic pressure-drop formulation has for instance been used by Mei et al. [32] in combination with shallow water theory, by Bennett et al. [47] for thin vertical barriers and by Liu and Li [54] for an iterative BEM. The present CFD work is compared against a BEM model by Mackay et al. [41], Mackay and Johanning [44], introduced below in Section 4.5.

Euler Equations

The Euler assumptions define the fluid to be rotational, either compressible or incompressible, and inviscid. The Euler equations consist of a mass and a momentum conservation equation but no energy equation as the fluid is simplified as adiabatic (without heat or mass transfer to and from a system).

In the context of WSI, the Euler equations have been used for ship design [55], a bobbing wave energy converter (WEC) [56, 57], an overtopping discharge WEC [58], extreme wave interaction with bottom-fixed cylinders [59], and cnoidal wave loads on a coastal-bridge deck [60]. Furthermore, Palm et al. [61] compared Euler-simulation results against Reynolds-Averaged Navier-Stokes (RANS) results for a point-absorbing

WEC where they propose to use the comparison as a means to separate viscous drag from the induced drag on WECs. No application to thin perforated or porous structures could be found in literature. Overall, within the field of ocean engineering analysis, using potential-flow theory or the NS equations were found to be far more common.

Navier-Stokes Equations

The NS equations provide the representation of the fluid closest to reality, as rotational, viscid, either compressible or incompressible and consist of conservation equations for mass, momentum and energy.

Similar to the Euler equations, the NS equations can be written in convective (Lagrangian) and conservative (Eulerian) form [62, 63]. These formulations correspond to the discretisation methods to solve a problem. Lagrangian methods are mesh free and are based on observation of the motion of the fluid through space and time. Eulerian methods observe fixed locations in space through which the fluid traverses over time. The most common Lagrangian method is the Smoothed-Particle-Hydrodynamics (SPH) method [64] which tracks the motions of discrete fluid particles. The particles carry properties and are linked with their neighbouring particles. This method has the advantages to conserve mass, momentum and energy and perform advection perfectly, which is ideal for large fluid deformations and floating bodies [65]. However, despite its capability to be easily parallelized via Graphics Processing Units (GPUs) [66] it is generally considered to be computationally expensive due to the large number of particles required [67]. Other weaknesses at present are difficulties in turbulence modelling, low convergence rates and the implementation of solid boundaries [67, 68]. Eulerian methods are based on continuum representations of the fluid. In a multi-phase context, they can be divided into interface tracking methods and interface capturing methods. Details will be introduced later in Section 2.2.4.

In the context of WSI and marine renewable devices, the NS equations are used in a large volume of work covering a wide range of application. A small selection of examples are simple fixed and floating structures such as cylinders [28, 69, 70] boxes [71, 72], various types of WECs [29, 73], tidal turbines [74], FOWTs [75, 76], volumetric [37, 77] and thin [4, 5] porous structures.

2.2.2 Numerical Solution Methods

Three main numerical methods exist to solve the governing equations: the Finite-Element method (FEM), the Finite-Difference method (FDM) and the Finite-Volume method (FVM). All methods are means to transform the partial differential equations (PDEs) into a system of linear algebraic equations, which are then solved iteratively.

FDM is the most direct approach, relying on the differential form and Taylor-series expansion over grid points with infinitely small volume. It requires orthogonally structured grids, which poses challenges for complex structures [78]. FEM and FVM differ in their derivation, but both use the integral form and can deal better with irregular grids. FEM is generally more versatile regarding the interpolation inside the finite elements. For further information on the FDM and FEM methods, one is for instance referred to Peiró and Sherwin [79] and Zienkiewicz et al. [80], respectively.

The preferred and most commonly used method in fluid dynamics is the FVM [62]. Here, the fluid domain is divided into a mesh of finite cells or control volumes and the fluid fluxes are evaluated across the cell faces. The main advantages of the FVM method are its flexibility, its stability in the presence of discontinuities and its strict conservativeness [63]. The method consists of two main steps [63]. Firstly, the integral form of the PDEs is transformed into balance equations over each control volume to satisfy mass, momentum and energy conservation. Secondly, the relations between the cell value and the face values are defined and algebraic interpolation equations are obtained.

2.2.3 Using OpenFOAM®

For the present CFD modelling, the FV-based code OpenFOAM® (Open Field Operation And Manipulation) (OF) is used with The OpenFOAM® Foundation version v5 [81]. OF is an object-oriented C++ library with a modular structure and a wide range of functionalities that can be used for many engineering applications such as combustion, electro-magnetics, structural mechanics or fluid dynamics.

OF is an ideal tool for the present studies. Most required functionalities are readily available and all missing parts can be modified or extended. Some parts of this thesis use existing code and other parts require additions and alterations.

Used Libraries

This work uses OF in combination with two libraries, OlaFlow/IHFoam by Higuera et al. [36] and waves2Foam by Jacobsen et al. [82] (including contributions by Jensen et al. [37] for porous media). Both provide wave modelling capabilities and macro-scale porosity implementations. OlaFlow/IHFoam is denominated with two names since two slightly different versions exist. IHFoam is the name of the initial release and the subsequent releases from IH Cantabria, University of Cantabria, Spain, while OlaFlow is maintained by the original developer. Most functionalities and implementations are therefore identical but OlaFlow provides a few additional capabilities. Details of those

toolboxes are explained in the relevant sections such as Section 2.3 on wave modelling and Section 2.4 on porosity implementation.

Workflow

Field operation and manipulation in the context of fluid dynamics means that all fluid parameters such as pressure, velocity, phase-fractions, turbulence parameters, density etc. are represented as scalar or tensor fields in the geometrically specified fluid domain. Manipulations, calculations and operations are then executed on those fields, either in serial or in parallel mode.

The general procedure in OF and most other CFD software consists of pre-processing, solving and post-processing. During the pre-processing stage, a certain problem is defined by a domain, which is then split into small control volumes or cells that make up the computational grid. This is termed spatial discretisation. At all domain boundaries, boundary conditions (BCs) are specified that resemble the physical situation as closely as possible. All physical parameters such as fluid densities, viscosities, direction of body forces such as gravitation need to be specified. The governing equations, numerical schemes, physical models, solver algorithms and corresponding settings have to be defined. Also the output such as monitoring points, gauges or isosurfaces can be pre-defined. With all parameters specified, the solution process is performed iteratively until the desired accuracy level is met and a converged solution can be obtained. The results can then be analysed through post-processing.

Within this thesis, all numerical settings and key-words related to OF setup are indicated by this » `font` « from now on.

2.2.4 Governing Equations

Establishing the model based on the NS equations provides flexibility and enables expansion to more complex conditions in terms of waves, wind, current, or other aspects. Large-scale WSI problems are characterised by the following flow characteristics and valid assumptions and simplifications:

- The two phases water and air are present.
- Both phases are Newtonian fluids, i.e. their viscosities, μ_w and μ_a, respectively, are constant and display a linear relationship between shear stresses and shear rate.
- As for most fluids with subsonic speed, the fluids are assumed to be incompressible [83]. Thus, their densities, ρ_w for water and ρ_a for air, are assumed to be constant.

- The two phases are immiscible, i.e. a free surface is present at the air-water interface [83].
- Since heat transfer is negligibly small, the fluids are assumed to be isothermal. Thus, the energy conservation equation is no longer necessary.

These assumptions simplify the NS equations (see Fig. 2.1) and define the specific governing equations used in this thesis.

Levels of Fluid Flow Resolution

Various options exist to resolve the fluid flow in terms of accuracy and treatment of turbulence. Turbulence is characterized as a chaotic, irregular, non-linear and highly unsteady diffusive and dissipative process [84]. Energy is transferred from energetic and large-scale turbulence to small-scale turbulent motion with decreasing energy levels. The characteristics of this process were first defined by Kolmogorov [85] in his theories of the energy cascade and spectrum. Fig. 2.2 shows a sketch of the energy spectrum, $E(\kappa_E)$, which describes the relation between turbulent kinetic energy, k, and eddy wave number, κ_E.

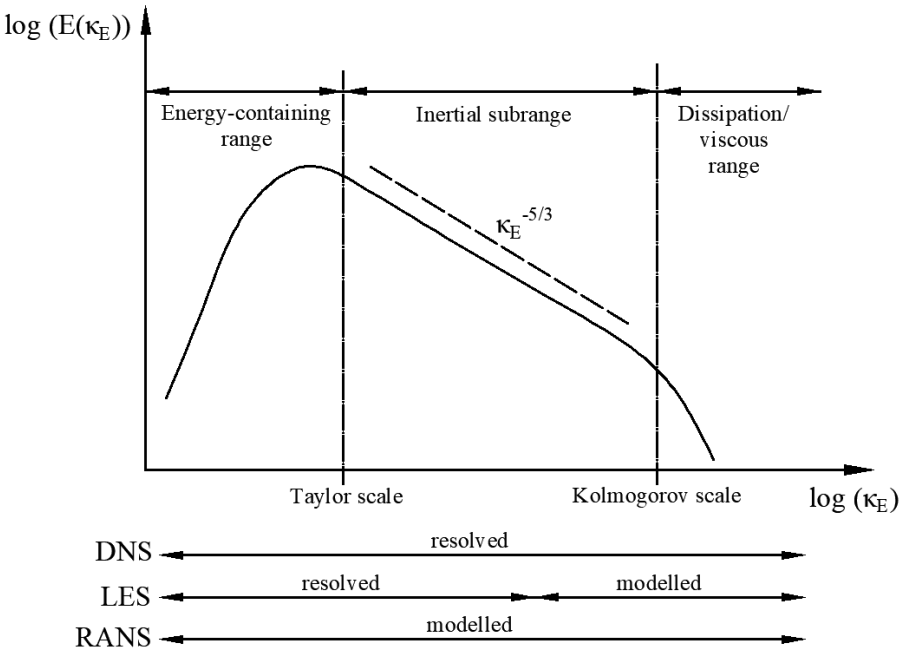

Figure 2.2: Schematic of the turbulent energy spectrum, $E(\kappa_E)$, containing the characteristics of the DNS, LES and RANS approach. Adapted from Tay-Wo-Chong [86].

Direct Numerical Simulation (DNS) uses the full NS equations and aims to resolve all scales of turbulence directly. To capture all sizes of turbulent eddies, a very fine mesh is required. This implies an excessive computational demand, which is prohibitive for

most applications. Thus, DNS is mainly used for academic purposes. For practical applications in engineering, simplifications by means of turbulence models are necessary. To avoid confusion, it is noted that simulations governed by the full NS equations but performed on relatively coarse spatial resolution are considered as under-resolved DNS and not as actual DNS - despite the fact that some other authors refer to it that way. Large Eddy Simulations (LES) resolve the main flow with its large-scale and anisotropic turbulence directly with instantaneous quantities. Implicit length-scale filtering is applied to filter out smaller turbulence which is then modelled by turbulence models that typically account for anisotropic characteristics. For further information on DNS and LES, the interested reader is referred to Moukalled et al. [63], Ferziger and Peric [84] or Versteeg and Malalasekera [62].

The most common approach, in particular for engineering purposes, is the Reynolds-Averaged-Navier-Stokes (RANS) method. This method uses models to represent all scales of turbulence, and only the time-mean values are directly simulated [63]. The computational demand of the RANS method is higher than simpler methods based on Euler or potential-flow assumptions, but significantly lower compared to LES or DNS.

Both the full NS equations (under-resolved DNS) as well as the Reynolds-Averaged variant are used in this thesis.

Reynolds-Decomposition and RANS Equations

The RANS equations are based on Reynolds decomposition [87], which is a mathematical technique to split an instantaneous quantity into a mean component and a fluctuating component. In general, the mean value can be obtained via ensemble, spatial or time averaging [63]. Ensemble averaging is the most general option since it is suitable for any kind of turbulent flows . Spatial averaging can be used for homogeneous turbulence only. Time-averaging can be used for inhomogeneous turbulence based on steady flow. This concept is illustrated for the velocity component u in Fig. 2.3. It can be written as:

$$\boldsymbol{u}(\boldsymbol{x},t) = \bar{\boldsymbol{u}}(\boldsymbol{x},t) + \boldsymbol{u}'(\boldsymbol{x},t), \tag{2.1}$$

where the mean fluctuating component $\bar{\boldsymbol{u}}'(\boldsymbol{x},t) = 0$. $\boldsymbol{u}(\boldsymbol{x},t)$ is the instantaneous velocity, $\bar{\boldsymbol{u}}(\boldsymbol{x},t)$ the mean part and $\boldsymbol{u}'(\boldsymbol{x},t)$ the fluctuations.

By taking the standard NS equations and substituting the instantaneous quantities by the mean and fluctuating parts, differential analysis with derivations and rearrangements result in the RANS equations. For a detailed derivation, see for instance Moukalled et al. [63] or Holzmann [88]. This set of equations appears similar to the NS equations but is formulated for the mean values instead of the instantaneous values and contains

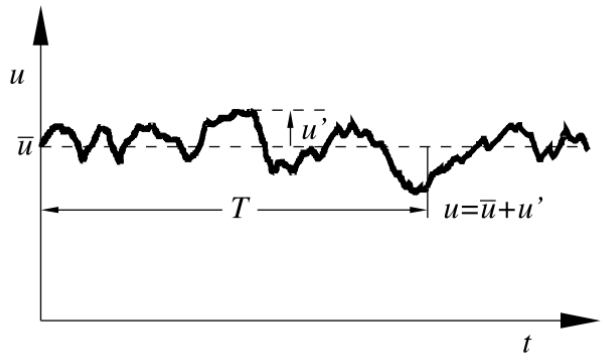

Figure 2.3: Schematic illustration of the RANS method. Taken from Oertel et al. [78].

an additional term that represents the turbulent part of the flow. This non-linear term is the result of the averaging procedure and is denoted as Reynolds-stress term, $\boldsymbol{R}$, in the momentum equation, and turbulent scalar fluxes for all other fluid quantities [88]. With the Reynolds-stresses and turbulent scalar fluxes, the number of unknowns has increased which requires closure.

Based on the fluid properties assumptions above, the RANS equations are defined as the mass conservation equation (see for instance Rusche [89]):

$$\nabla \cdot \bar{\boldsymbol{u}} = 0, \tag{2.2}$$

where ∇ is the Del- or Nabla-operator[1], and the momentum conservation equation as:

$$\frac{\partial \rho \bar{\boldsymbol{u}}}{\partial t} + \nabla \cdot (\rho \bar{\boldsymbol{u}} \bar{\boldsymbol{u}}) = \rho \boldsymbol{g} - \nabla \bar{p} + \mu \nabla^2 \bar{\boldsymbol{u}} - \nabla(\rho \boldsymbol{R}), \tag{2.3}$$

where ∇^2 is the Laplace-operator[2], $\mathbf{g}$ is the vector of gravitational acceleration, p is the pressure, μ the dynamic viscosity and $\boldsymbol{R}$ the Reynolds-stress tensor, $\overline{\boldsymbol{u}'\boldsymbol{u}'}$. Various options exist to describe $\boldsymbol{R}$ and to close the RANS equations, see for instance Ferziger and Peric [84] or Wilcox [90]. A very common approach is based on Boussinesq's hypothesis which assumes $\boldsymbol{R}$ to be linearly related to the mean velocity gradients [63]. $\boldsymbol{R}$ can be split into isotropic and deviatoric anisotropic components:

$$\boldsymbol{R} = \overline{\boldsymbol{u}'\boldsymbol{u}'} = \frac{2}{3} k \boldsymbol{I} + \boldsymbol{R}_{\boldsymbol{dev}} = \frac{2}{3} k \boldsymbol{I} + \overline{\boldsymbol{u}'\boldsymbol{u}'} - \frac{2}{3} k \boldsymbol{I}, \tag{2.4}$$

[1] used for the gradient/directional derivative (∇) of a scalar/vector field and the divergence ($\nabla\cdot$) of a vector field

[2] $\nabla \cdot \nabla = \nabla^2$

where $\boldsymbol{I}$ is the identity tensor and k is the turbulent kinetic energy. The latter is defined as:

$$k = \frac{1}{2}\overline{\boldsymbol{u}'\boldsymbol{u}'}. \tag{2.5}$$

The isotropic term of $\boldsymbol{R}$ can be added to the mean pressure induced stresses, $\bar{p}$, and the deviatoric component, $\boldsymbol{R_{dev}}$, needs to be represented by a turbulence model. Linearly relating $\boldsymbol{R_{dev}}$ to a turbulent eddy viscosity, ν_t, gives:

$$\boldsymbol{R_{dev}} = \overline{\boldsymbol{u}'\boldsymbol{u}'} - \frac{2}{3}k\boldsymbol{I} = -\nu_t \nabla \bar{\boldsymbol{u}} = 2\nu_t S_{ij}, \tag{2.6}$$

where

$$S_{ij} = \frac{1}{2}\left(\frac{\partial u_i}{\partial x_j} + \frac{\partial u_j}{\partial x_i}\right) \tag{2.7}$$

is the mean strain rate tensor. Adding ν_t to the molecular viscosity, μ, results in the effective dynamic viscosity, μ_{eff}:

$$\mu_{eff} = \mu + \rho\nu_t, \tag{2.8}$$

and the mean momentum equation can be written as:

$$\frac{\partial \rho\bar{\boldsymbol{u}}}{\partial t} + \nabla \cdot (\rho\bar{\boldsymbol{u}}\bar{\boldsymbol{u}}) = \rho\boldsymbol{g} - \nabla\bar{p}' + \mu_{eff}\nabla^2\bar{\boldsymbol{u}}, \tag{2.9}$$

with

$$\bar{p}' = \bar{p} + \frac{2}{3}\rho k \tag{2.10}$$

as the turbulent pressure. With this definition, μ_t is the only unknown. For simplicity, the mean velocity, $\bar{\boldsymbol{u}}'(\boldsymbol{x}, t)$, will be denoted as $\boldsymbol{u}(\boldsymbol{x}, t)$ or $\boldsymbol{u}$ from now on.

Turbulence Modelling

The lack of a universal description of turbulence makes turbulence modelling a complex task. The models following Boussinesq's approach are referred to as linear eddy-viscosity models where most of them assume turbulence to be of isotropic nature. In general, eddy-viscosity turbulence models are parametrizations of small-scale turbu-

lence relating the turbulent eddy viscosity, μ_t, to turbulence quantities such as turbulent kinetic energy, k, turbulent energy dissipation rate, ϵ, specific turbulent dissipation rate, ω, turbulence intensity, I_t, turbulence length scale, L, or eddy viscosity ratio, μ_t/μ. All these quantities are related to each other. All models represent additional equations to the system that are required to close the RANS equations, where at least one equation is necessary per unknown. Dependent on the number of equations added, the models are called zero-, one- or two-equation models. Many models and variations exist which have typically been developed for certain specific applications.

Two-equation turbulence models are most commonly use. The most well-known models are the k-ϵ- model by Jones and Launder [91], the k-ω- model by Wilcox [92] and their blended version, the k-ω-SST (Shear Stress Transport) model by Menter [93]. The k-ϵ- model assumes the flow to be fully turbulent and the molecular viscosity to have negligible effect. It is therefore only valid in fully turbulent free-shear flow regions with high Re-numbers and small pressure gradients, but cannot accurately model flow in near-wall regions such as predicting flow separation along boundaries. The k-ω-model replaces the equation for ϵ by an equation for ω which improves performance and robustness at near-wall regions where large pressure gradients are present. Its drawback is its sensitivity to the turbulence properties at the inlet in the free-stream region. The k-ω-SST (Shear Stress Transport) blends the k-ϵ-model with the k-ω- model with a blending function and therefore combines the benefits of both. It is widely used in many engineering fields and can be considered as an industry standard. Details on these models, various developments and modifications of those, as well as other models can for instance be found in Moukalled et al. [63]. Since this work uses the k-ω and k-ω-SST models, their key equations are introduced for reference in the following.

For the k-ω model, the turbulent eddy viscosity, ν_t is formulated as:

$$\nu_t = \frac{k}{\omega}. \tag{2.11}$$

The equation for the turbulent kinetic energy, k, is given as:

$$\frac{\partial k}{\partial t} + u_j \frac{\partial k}{\partial x_j} = \tau_{ij} \frac{\partial u_i}{\partial x_j} - \beta^* k\omega + \frac{\partial}{\partial x_j}\left[(\nu + \sigma^* \nu_t)\frac{\partial k}{\partial x_j}\right], \tag{2.12}$$

and the equation for the specific dissipation rate, ω, is given as:

$$\frac{\partial \omega}{\partial t} + u_j \frac{\partial \omega}{\partial x_j} = \alpha_m \frac{\omega}{k} \tau_{ij} \frac{\partial u_i}{\partial x_j} - \beta\omega^2 + \frac{\partial}{\partial x_j}\left[(\nu + \sigma \nu_t)\frac{\partial \omega}{\partial x_j}\right]. \tag{2.13}$$

The model constants and auxiliary relations are:

$$\begin{aligned}
\alpha_m &= \frac{5}{9} \\
\beta &= \frac{3}{40}, \\
\beta^* &= \frac{9}{100}, \\
\sigma &= 0.5, \\
\sigma^* &= 0.5, \\
\epsilon &= \beta^* \omega k.
\end{aligned} \tag{2.14}$$

For the k-ω-SST model, the turbulent eddy viscosity, ν_t is formulated as:

$$\nu_t = \frac{a_1 k}{\max(a_1 \omega, SF_2)}, \tag{2.15}$$

where S is the mean strain rate, (2.7), and

$$F_2 = \tanh\left[\left[\max\left(\frac{2\sqrt{k}}{\beta^* \omega y}, \frac{500\nu}{y^2 \omega}\right)\right]^2\right]. \tag{2.16}$$

The equation for the turbulent kinetic energy, k, is given as:

$$\frac{\partial k}{\partial t} + u_j \frac{\partial k}{\partial x_j} = P_k - \beta^* k\omega + \frac{\partial}{\partial x_j}\left[(\nu + \sigma_k \nu_t)\frac{\partial k}{\partial x_j}\right], \tag{2.17}$$

where

$$P_k = \min\left(\tau_{ij}\frac{\partial u_i}{\partial x_j}, 10\beta^* k\omega\right) \tag{2.18}$$

is a production limiter. The equation for the specific dissipation rate, ω, is given as:

$$\begin{aligned}
&\frac{\partial \omega}{\partial t} + u_j \frac{\partial \omega}{\partial x_j} = \alpha_t S^2 - \beta\omega^2 + \frac{\partial}{\partial x_j}\left[(\nu + \sigma_\omega \nu_t)\frac{\partial \omega}{\partial x_j}\right] \\
&+ 2(1 - F_1)\sigma_{\omega 2}\frac{1}{\omega}\frac{\partial k}{\partial x_i}\frac{\partial \omega}{\partial x_i},
\end{aligned} \tag{2.19}$$

where

$$F_1 = \tanh\left\{\left\{min\left[\max\left(\frac{\sqrt{k}}{\beta^*\omega y}, \frac{500\nu}{y^2\omega}\right), \frac{4\sigma_{\omega 2}k}{CD_{k\omega}y^2}\right]\right\}^4\right\}, \tag{2.20}$$

where

$$CD_{k\omega} = \max\left(2\rho\sigma_{\omega 2}\frac{1}{\omega}\frac{\partial k}{\partial x_i}\frac{\partial \omega}{\partial x_i}, 10^{-10}\right). \tag{2.21}$$

Then, any (k-ω-SST) model constant, ϕ_m, is a blended value of the k-ω value, ϕ_1, and the k-ϵ value, ϕ_2),

$$\phi_m = F_1\phi_1 + (1 - F_1)\phi_2, \tag{2.22}$$

where the model constants are:

$$\begin{aligned}
&\alpha_{m1} = \frac{5}{9}, \alpha_{m2} = 0.44,\\
&\beta_1 = \frac{3}{40}, \beta_2 = 0.0828,\\
&\beta^* = \frac{9}{100},\\
&\sigma_{k1} = 0.85, \sigma_{k2} = 1,\\
&\sigma_{\omega 1} = 0.5, \sigma_{\omega 2} = 0.856.
\end{aligned} \tag{2.23}$$

Turbulence is often induced by flow separation over a wall and a turbulent BL. Therefore, most models are coupled with certain boundary conditions (BCs). These will be introduced in Section 2.2.6.

Full NS Equations

In cases where turbulence is not of interest or not physically expected, it can be useful to omit a turbulence model and use a `laminar` setup, where no turbulent eddy viscosity is added to the system ($\nu_t = 0$). This can be sufficient in terms of targeted accuracy and speeds up the solution process since no turbulence parameters need to be solved. This approach equates to using the full NS equations on a coarse mesh and can be referred to as under-resolved DNS, as stated above.

Interface Capturing and the VOF Method

Since WSI is a transient process that involves an interface between water and air, a method is required to accurately replicate the transient behaviour of the interface.

Various options exist that either track or capture the immiscible interface over time. Interface-tracking methods consider the interface as a boundary that is tracked over time by an adaptive boundary-fitted mesh [84]. Tracking is very accurate since the interface is kept sharp by means of mesh adaptation. Downsides are its high computational demand and problems in the presence of complex flow conditions such as wave breaking [94]. These aspects make this method not suitable for the present work. Interface-capturing methods are less accurate but also significantly less computationally demanding. Capturing methods use fixed grids and capture the transient interface between phases via a phase-indicator function that obeys a transport equation [89]. One of the most commonly used interface-capturing methods is the Volume-of-Fluid (VOF) method, first introduced by Hirt and Nichols [95], which will be explained below. Other interface capturing methods include level-set methods [96, 97] or phase-field methods [98, 99]. Further information on those methods can be found in the respective references.

The VOF method is the standard implementation in the solvers of OF's `interFoam` family - introduced below in Section 2.2.7. Its benefits are complete conservativeness on phase unlike level-set methods [100] and that it provides a good trade-off between computational effort and accuracy. It is widely used and well validated for marine engineering applications [36, 82, 101–103], and furthermore, implemented in the OlaFlow/IHFoam and waves2Foam libraries, already introduced in Section 2.2.3. Consequently, it was considered to be the best choice for the present simulations.

The VOF phase-indicator function, α, is defined as:

$$\frac{\partial \alpha}{\partial t} + \left(\nabla \boldsymbol{u}\alpha + \nabla \boldsymbol{u_{ic}}(1-\alpha)\alpha\right) = 0, \tag{2.24}$$

where $\boldsymbol{u_{ic}}$ is an artificial compression velocity as part of an interface compression term [104]. ρ and μ represent the phase weighted averaged density and viscosity, calculated from the water and air densities (ρ_w, ρ_a) and viscosities (μ_w, μ_a) via

$$\rho = \alpha\rho_w + (1-\alpha)\rho_a \tag{2.25}$$

and

$$\mu = \alpha\mu_w + (1-\alpha)\mu_a, \tag{2.26}$$

respectively. α represents the volume fraction of each phase and is transported as a scalar field with values between 0 and 1 where $\alpha = 0$ corresponds to a cell full of air and

$\alpha = 1$ corresponds to a cell full of water. Consequently, cells with α-values between 0 and 1 contain the free water surface.

Due to the nature of this method, no sharp boundary exists and the interface can be smeared over multiple mesh cells. In order to address this deficit, noted by Ubbink and Issa [105] and Rusche [89], and retain sharpness and boundedness of the α volume-fraction between 0 and 1, OF uses an algebraic limiting scheme with an additional heuristic interface compression term. As for other scalar fields, OF's default method in the `interFoam` solver family is the application of an algebraic limiting scheme called Multidimensional Universal Limiter for Explicit Solution (MULES). To address the smeared character of the interface, an alternative approach has been taken by Roenby et al. [106, 107]. They developed the so-called `isoAdvector` method that uses geometric operations for the advection and reconstruction of the interface. Another crucial deficit of the standard VOF implementation is the appearance of unphysical high spurious air velocities at the phase interface. This has been reported for general cases by Deshpande et al. [108] and for the application to water waves by Tomaselli [69], Roenby et al. [107], Amini Afshar [109], Wroniszewski et al. [110], Larsen et al. [111]. Vukčević [112] and Vukčević et al. [94] explain this as a result of the solution algorithm where the dynamic pressure and density are not solved simultaneously but segregated. Vukčević et al. [94] proposed the use of the so-called Ghost-Fluid-Method (GFM) as an approach to address this deficit. In the GFM, the treatment of the interface jump-condition differs to the standard VOF implementation and the pressure-density coupling is relocated to the inside of the pressure equation. In general contexts, the GFM is an active area of research and not further explored here.

The improvement of the deficits of the VOF method are active areas of research. Therefore, any related problems that occur in the course of the present simulations are acknowledged but not actively addressed.

In order to account for surface tension effects along the interface, it is common to apply additional body forces to the momentum equation. The term $+\sigma_{st}\kappa\nabla\alpha$ is therefore added to the right-hand side (RHS) of (2.9) where σ_{st} is the surface tension coefficient and κ is the curvature of the interface. For many engineering applications in marine hydrodynamics where larger scales are of interest, surface tension plays a negligible role and might be omitted [94, 107].

2.2.5 Discretisation

As part of the FVM method, Gauss' Theorem, also known as divergence theorem, is used to transform the volume integrals including spatial derivatives of the NS equations into surface integrals. The theorem states that the divergence of a field enclosed in a

volume is equal to the flux of a vector field through a closed surface. After application of Gauss' Theorem (in space), the governing partial differential equations are discretised spatially and temporally in order to obtain an algebraic set of equations. This also involves interpolation between cell centres and cell faces.

Spatial Discretisation

Spatial discretisation is the subdivision of the computational domain into a mesh of finite control volumes or cells. The intention of the simulation and the targeted accuracy level define the cell size and distribution, possible cell refinement regions and the mesh generation approach. The mesh is crucial and the base for a successful and meaningful simulation. On one hand, it must capture the relevant physical effects in order to obtain correct results. Particularly, critical fluid regions in which significant change is happening and large gradients are present, require a sufficiently fine mesh resolution [62]. On the other hand, the mesh needs to fulfil certain quality criteria to support the stability of the numerical schemes and solution algorithms. Poor quality cells give numerical errors and cannot only lead to inaccurate results, but possibly divergence of the solution. Some quality issues can be corrected, for instance with applying non-orthogonal correction [63] (repetition of the pressure equation; `nNonOrthogonalCorrectors` in OF), but the focus should lie on careful mesh creation. The most important quality properties to consider are cell smoothness, uniformity, orthogonality, aspect ratio (ratio of longest to shortest edge length) and skewness [81]. Cell uniformity and orthogonality should be large whereas aspect ratio and skewness should be kept small. Regions around complex geometries, local refinement zones and BL regions tend to have a lower mesh quality and can be critical in the set-up. Based on these considerations, the current meshes were generated as highly orthogonal structured meshes with mostly hexahedral cells.

The target parameters of a simulation have to be pre-defined and their independence of the mesh should be proven by means of a convergence study. A minimum spatial discretisation is then obtained for a target accuracy. For highly transient simulations this can be challenging and formal convergence can not always be achieved for practical applications. This is further discussed in Section 4.3.

Temporal Discretisation

Transient processes also require temporal discretisation and the timeline has to be split into small time steps. The time step size is based on the present physical processes and needs to be small enough to replicate the relevant physics with a target accuracy level, but should be as large as possible to solve the simulation with a reasonable speed. The time step size is also crucial for numerical scheme and solver stability since too large

changes can likely initiate divergence or oscillations.

The time step size can either be predefined as a constant value or be set to being adjusted automatically based on the Courant-Friedrichs-Lewy (CFL)-number [113]. Automatic time stepping continuously adjusts the time step to give a maximum CFL-number which is calculated as:

$$CFL = \frac{\Delta t}{2V} \sum_{faces} |\phi| \,, \tag{2.27}$$

where Δt is the time step, V is the cell volume and ϕ the volume flux across the cell faces. It is interpreted as the number of cells that a scalar quantity traverses during one time step. For instance, for a maximum CFL-number of 0.5, the fluid crosses a maximum of half a mesh cell during one time step. In this case, the spatial and temporal convergence studies are directly linked since the time step decreases correspondingly with a decreasing cell size for a constant maximum CFL-number.

Automatic time stepping is a convenient way to support numerical stability and can therefore be considered preferential to fixed time stepping. It is implemented in various transient solvers in OF. It can be used with the `interFoam` solver family and is therefore used for all present simulations.

Discretisation and Interpolation Schemes

In OF, the discretisation method for each term of the governing equations, (2.2) and (2.3), and the interpolation between the cell and face centres can be specified by the user. The optimum choice and combination of numerical schemes such as the time discretisation scheme (`ddt`) or the convection scheme (`div(rhoPhi,U)`), requires comprehensive understanding and experience. In general, the schemes are usually either accurate but sensitive, or stable but diffusive. For the present simulations where complex transient interactions are dominating and a new method has been developed, stable schemes have been chosen over accurate ones. In the course of the present model development, sensitivity studies have been conducted to estimate the effect of various numerical schemes, presented in Section 6.3.

2.2.6 Boundary Conditions

Since FV CFD problems are boundary value problems, the specification of BCs at all domain boundaries is required. The BCs need to represent the physical conditions as accurately as possible.

In fluid dynamics, Dirichlet- and Neumann-type BCs are the most relevant [114] but

mixed types such as Robin- or Cauchy-type exist. A Dirichlet-type BC is a condition where a fixed value is specified and a Neumann-type condition is the specification of the gradient of a value. All other BCs are derived from these types, and all can be combined and applied to different parameters or fields. To replicate a wave tank numerically, the following sets of conditions are required:

- a wave generation condition (in combination with wave absorption);
- a wave absorption condition;
- an atmospheric condition; and
- wall conditions (free-slip, no-slip).

The first two conditions require a transient input for the phase-fraction field, α, and the velocity field, $\boldsymbol{u}$. Since wave modelling is one of the main topics of this thesis, further information is given in Section 2.3. The atmospheric and wall BCs are commonly used and therefore explained in the next paragraphs.

The Atmospheric Condition

The top section of the numerical wave tank (NWT) consists of air and requires an atmospheric BC. Typically, this is set to a mixed condition that combines an inlet with an outlet. With two phases, water and air, both water and air are allowed to flow out but only air can flow back into the domain [81]. In this regard, the top boundary needs to have sufficient distance to the water surface and any regions of WSI to keep the water mass conserved.

The Wall Condition and Boundary Layer Modelling

In a NWT, solid walls are present at the tank bottom and on structures inside the domain. At solid walls the fluid velocity is zero and a BL exists. The BL consists of two main sublayers, the inner and outer layer. The latter can be further divided into a viscous sublayer at the wall, a buffer layer or blending region and a fully turbulent layer near the free-shear flow. Figure 2.4 shows a sketch of the BL development for steady parallel flow over a flat plate. The progression of the BL thickness, δ_{BL}, and all sublayers is outlined.

When the velocity is set to zero at the wall and a no-slip condition is applied, two main approaches exist to account for the BL in a CFD model. It can either be resolved directly with a very fine boundary mesh or modelled via a wall function that is applied as a BC. Direct resolution requires a large number of mesh cells in order to capture the

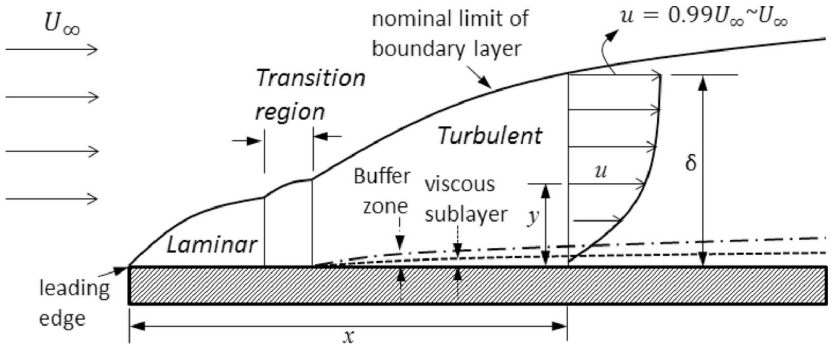

Figure 2.4: Schematic of the boundary-layer development over a flat plate. Taken from Shahmohamadi and Mehdi [115]. Note that δ in the sketch is the boundary-layer thickness, δ_{BL}.

velocity gradient in the near-wall region. This is not always necessary for engineering applications. A more efficient approach is the application of a theoretical BL profile and to use the universal logarithmic law of the wall [116] by means of a so-called wall function. This method is usually combined with the application of a turbulence model.

Free-slip Condition

For cases where the BL has no significant effect on the flow or where it is not of interest, the free-slip condition can be a valuable alternative since it reduces the computational effort significantly. Instead of setting all velocity components to zero at the wall, the velocity can be kept unrestricted. Therefore, the normal velocity component is set to zero and the tangential components are set as equal to the values inside the fluid region next to the wall (`zeroGradient`).

2.2.7 Solution Process

To solve a problem, all physical properties, discretisation, scheme and solver parameters and methods, BCs and all involved physical models have to be specified. Then the spatial and temporal discretisation of the governing equations result in a set of linear systems of algebraic equations. Here, one linear system is assembled for each transported quantity, ϕ_{ls}:

$$\boldsymbol{A_{ls}\phi_{ls} = b_{ls}}, \tag{2.28}$$

where $\boldsymbol{A_{ls}}$ are matrix coefficients, $\boldsymbol{b_{ls}}$ is the vector representing BCs and source terms, and $\boldsymbol{\phi_{ls}}$ is the solution vector.

In the context of solution process in OF, a distinction in terminology is made between linear solvers and application solvers [114]. Linear solvers, also known as

matrix solvers, are referred to the methods used to solve the linear systems of transport equations, (2.28). Application solvers refer to an entire set of algorithms to couple the equations and to solve specific physical problems such as heat transfer, interface capturing or moving mesh capabilities.

Linear Matrix Solvers

In general, the set of linear equations can be solved either directly or iteratively. Since matrices in the FVM method are generally segregated, decoupled and sparse (most coefficients are zero), linear solvers typically use an iterative solution process. Following a guess-and-correct procedure, the equation's error and residual levels are reduced successively until the target accuracy level is met.

Different algorithms to linear solvers for either symmetric or asymmetric matrices are available in OF. OF offers a wide range of linear solvers such as preconditioned-conjugate-gradient (Newton-Krylov) solvers, smooth solvers or geometric-algebraic multi-grid solvers. For the present simulations, various solvers are used with their default settings. Since all solvers are supposed to lead to a converged solution, no further examination of any performance parameters has been conducted in this work. The used solvers and corresponding settings are stated in the course of the present simulations in the Chapters 5-7 and in the Appendices.

Application Solvers

The NS equations are coupled and include non-linear terms. In the incompressible case where the density is assumed as constant, no link exists between the momentum and mass conservation equations, (2.2) and (2.3). This lack of direct connection is referred to as the pressure-velocity coupling problem [62] to which various solution strategies exist.

One of the first approaches for steady simulations is the Semi-Implicit-Method-Of-Pressure-Linked-Equations (SIMPLE) algorithm by Patankar and Spalding [117]. The linking between pressure and velocity is employed by an iterative procedure of guessing and correcting. In sequential manner, the pressure field is calculated firstly and the velocity field is obtained from the momentum equation secondly. Beyond SIMPLE, other application solvers in OF use this kind of segregated pressure-based approach. For transient single-phase problems, the Pressure-Implicit-Split-Operator (PISO) algorithm was developed by Issa [118]. The PISO algorithm uses automatic time-stepping as a stability preservation method already introduced in Section 2.2.5. It functions similarly to the SIMPLE algorithm but is applied to each time step and with additional correction steps.

A further development is the combination of SIMPLE and PISO to PIMPLE for transient problems, developed to enable the use of larger time steps and thus, the use of larger maximum CFL-numbers (CFL»1) [88]. Within PIMPLE, an outer and an inner loop exist where the former follows the SIMPLE and the latter the PISO procedure. In other words, the whole set of equations is calculated with `nOuterCorrectors`, i.e. SIMPLE-steps, and the inner loop performs the PISO pressure correction for `nCorrectors`-steps. The PIMPLE algorithm is implemented in many of OF's transient solvers. It can also be used in PISO-mode with only one outer (SIMPLE) loop for cases where small time steps are required anyway. For most present cases, the advantage of PIMPLE becomes irrelevant and small time steps are needed to resolve the transient flow patterns of wave propagation and WSI.

InterFoam

PIMPLE is also implemented in the `interFoam` application-solver family. `interFoam` is OF's standard solver for isothermal, incompressible and immiscible two-phase problems and therefore also used in this thesis. It solves the unsteady RANS equations and uses the algebraic VOF interface capturing method with MULES limiting - already introduced in Section 2.2.4.

Within the `interFoam` framework, the mass and momentum conservation equations, (2.2) and (2.3), are formulated as:

$$\nabla \cdot \boldsymbol{u} = 0 \tag{2.29}$$

and

$$\frac{\partial}{\partial t}\rho\boldsymbol{u} + \nabla \cdot (\rho\boldsymbol{u}\boldsymbol{u}) = -\nabla p^* - \boldsymbol{g} \cdot \boldsymbol{X}\nabla\rho + \nabla \cdot (\mu_{eff}\nabla\boldsymbol{u}) + \sigma\kappa\nabla\alpha, \tag{2.30}$$

where **X** is the position vector in Cartesian coordinates, **g** is the vector of gravitational acceleration and p^* is the pseudo-dynamic pressure (used for numerical convenience instead of the actual dynamic pressure [81]). The term with the surface tension coefficient, σ, and the curvature of the interface, κ, represents surface tension effects. ρ is the weighted averaged density and μ the weighted averaged viscosity, as in (2.25) and (2.26). μ_{eff} is the effective dynamic viscosity, defined in (2.8) as the sum of the molecular viscosity, μ, and the turbulent eddy viscosity, $\mu_t = \rho\nu_t$. The latter represents small-scale turbulence effects by means of a turbulence model.

Figure 2.5 shows a flow chart of the algorithm. The chart also includes the wave

modelling BCs (indicated as boxes with round-edges) which will be introduced in Section 2.3. The main steps of the algorithm are the VOF interface-capturing procedure, the solution process of all fields via the PIMPLE pressure-velocity coupling and the advancement of time based on the maximum CFL-number, all performed sequentially in this order. If mesh motion is required, further steps have to be introduced which will be pursued further in Section 2.5.

Within the VOF interface-capturing sub-routine, stability and accuracy can be supported by sub-division of the time step, Δt, into a number of sub-steps (`nAlpha-SubCycles`). Within each sub-cycle the phase-fraction matrix, α, is assembled and the α-equation is solved. This is performed at least once but can be corrected more often if `nAlphaCorrectors` is set to > 1. After the VOF procedure, the pressure-velocity coupling is performed. This consists mainly of the assembly of the momentum equation and an optional solution (predictor) step, before the inner PISO loop is entered to solve the pressure equation. The PISO routine consists of an initial calculation of velocity and flux, and the solution of the pressure equation. The pressure solution can be corrected with `nNonOrthogonalCorrectors` > 1 which is mainly used for meshes with lower orthogonality levels. After the pressure is obtained, the flux is corrected and the velocity reconstructed. The PISO loop can be performed for $1 \leqslant$ `nCorrectors` before the outer SIMPLE loop is resumed for $1 \leqslant$ `nOuterCorrectors` or until the solution has converged to the target residual levels. After the PIMPLE loop is finished and all fields are obtained, time is advanced and the main `interFoam`-loop continues until the end-time is reached. More detailed information on the algorithms can for instance be found in Versteeg and Malalasekera [62] or Moukalled et al. [63].

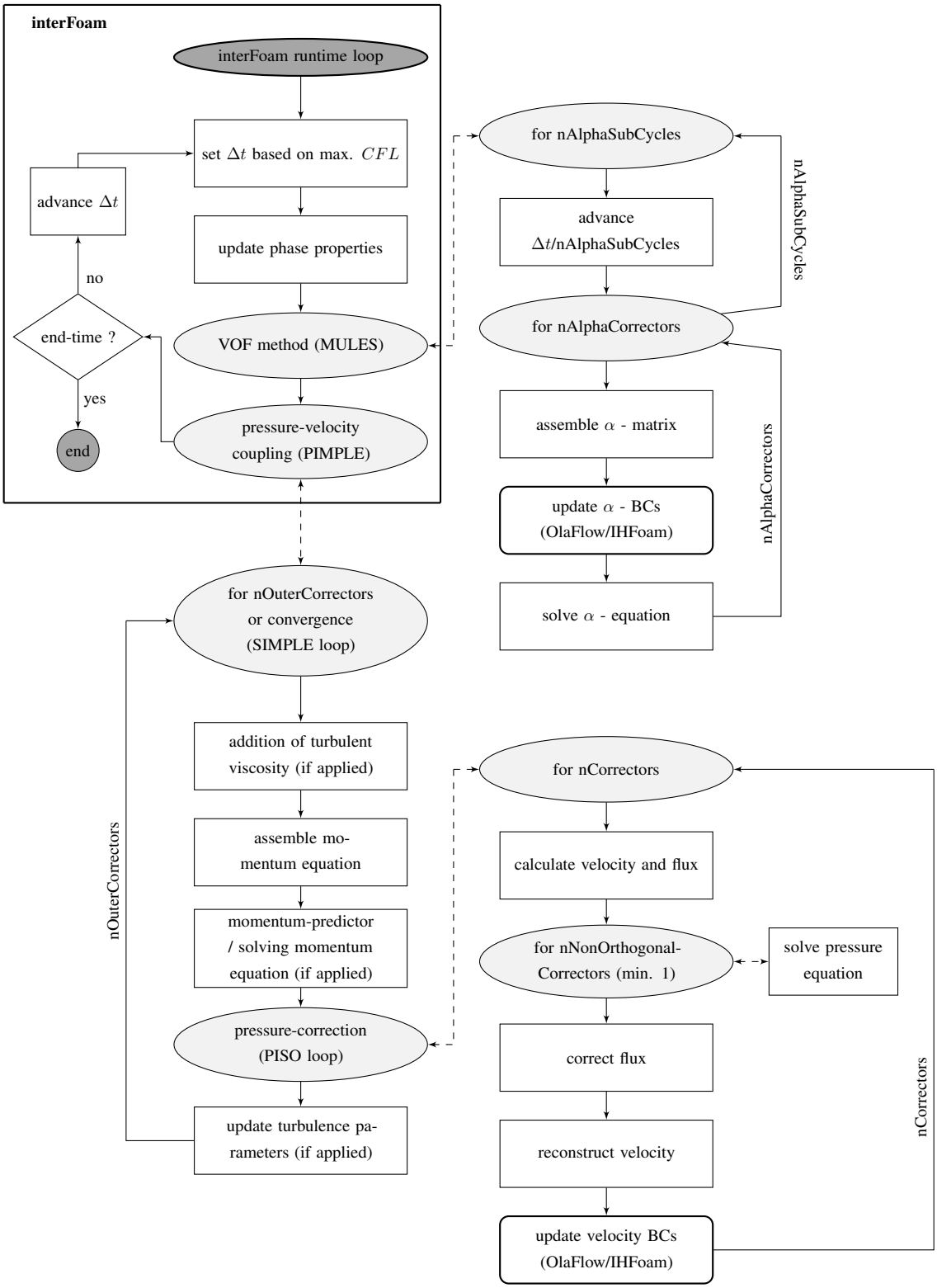

Figure 2.5: The `interFoam` algorithm flow chart, including wave modelling capabilities (boundary-condition corrections) of OlaFlow/IHFoam. Adapted from Higuera [119].

2.3 Wave Theory and Modelling

Ocean waves can be described by wave theories and their formulations for the wave elevation and velocity profiles across the water column. Wave theories are commonly known, so only key aspects are introduced next. This is then followed by a review of possible techniques to translate the theory into CFD model input, including their pros and cons. Furthermore, important modelling aspects in the context of WSI such as turbulence and BL modelling are reviewed.

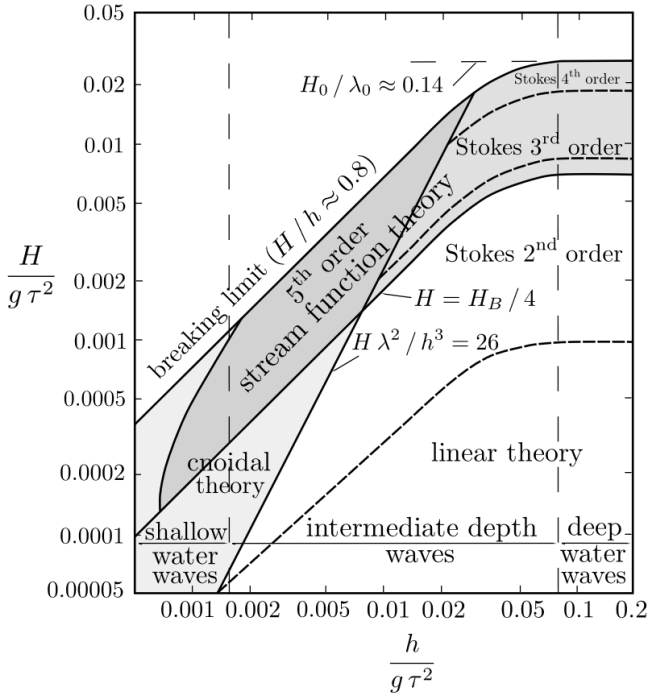

Figure 2.6: Applicability of wave theories - diagram by Le Méhauté [120]. Taken from $https://commons.wikimedia.org/wiki/File:Water\_wave\_theories.svg$. Note that τ in the diagram is the wave period, T.

2.3.1 Wave Theories

Most wave theories are based on potential-flow assumptions. Dependent on the targeted water depth, h, wave height, H, and wave period, $T = \tau$, the appropriate theory can be applied to represent the present wave regime. A diagram by Le Méhauté [120], shown in Fig. 2.6, can be used to determine the applicability of common theories to the present wave parameters. Dependent on the water depth and the way of transient particle motion, a distinction is made between shallow water waves (with linear particle orbits), intermediate water waves (with elliptical orbits) and deep water waves (with circular orbits). Figure 2.7 shows the water zone with the corresponding wave type in terms of particle motion and corresponding velocity profiles.

Each wave theory provides formulations for the free surface elevation, $\eta(t)$, and the velocity profiles of the water particles, u_x, u_y, u_z. Various techniques exist to translate the theories into wave modelling input to the numerical model.

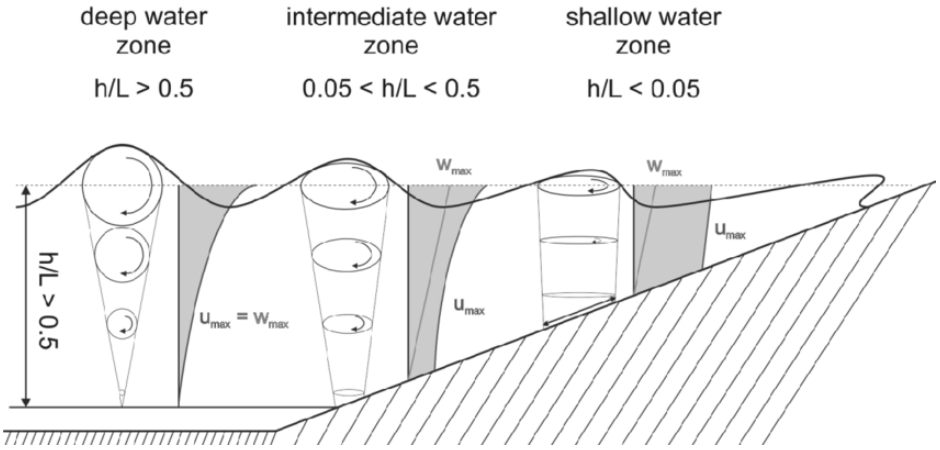

Figure 2.7: Schematic of ocean water zones and corresponding wave types where h is the water depth and $L = \lambda$ is the wave length. Taken from Karow et al. [121].

2.3.2 Wave Modelling Techniques

In general, wave generation and wave absorption can be seen as two separate mechanisms. However, often they are grouped together when they are based on the same concepts or when they require a certain combination. Wave generation is generally employed by either a BC at one end of the NWT or as an internal source inside the domain. All methods use a time-dependent input to prescribe the orbital motion of the water particles. The purpose of wave absorption methods is the minimization of wave reflections at the domain boundaries in order to avoid disturbance of the wave field in the test section of the NWT.

An overview of existing wave modelling techniques in a CFD framework is given by Windt et al. [122] and briefly introduced here. Corresponding sketches are shown in Fig. 2.8.

Wave Generation

The most common approaches to wave generation are the relaxation method (Fig. 2.8(a)), the static boundary method (Fig. 2.8(b)) and the dynamic boundary method (Fig. 2.8(c)). Those are all available in the most frequently used OF toolboxes for wave modelling, waves2Foam, developed by Jacobsen et al. [82] and OlaFlow/IHFoam, developed by Higuera [123]. Both provide coupled wave generation and absorption capabilities. The former uses the so-called relaxation approach and the latter uses both static and dynamic boundary methods.

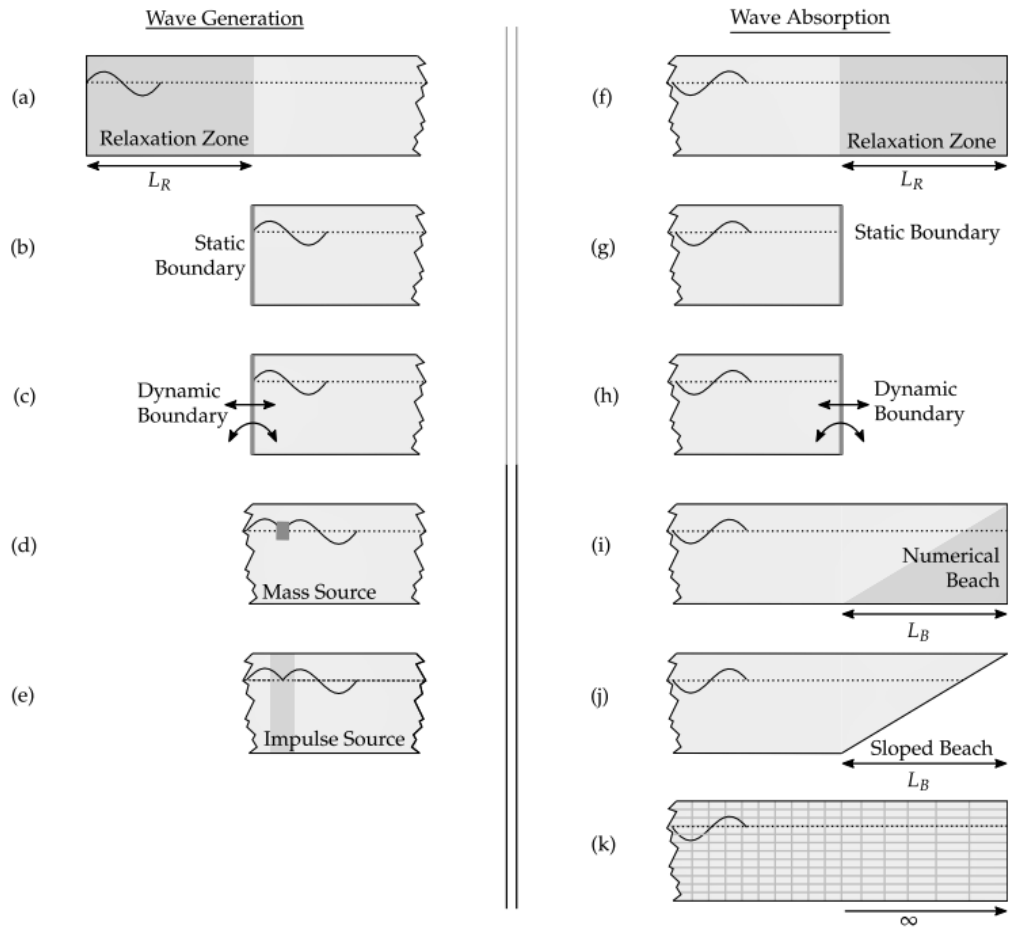

Figure 2.8: Schematics of available methods for wave generation (a–e) and wave absorption (f–k): (a, f) relaxation zone method, (b, g) static boundary method; (c, h) dynamic boundary method, (d) mass source method, (e) momentum source method, (i) numerical beach, (j) geometrically sloped beach, and (k) cell stretching. Taken from Windt et al. [122].

The relaxation method is based on using a blending function that is applied to the fluid fields at geometrically specified sections at both ends of the NWT. At the wave generation boundary, the blending function is applied to serve two purposes. The wave field is prescribed via time-dependent velocity profiles via the $\boldsymbol{u}$-field and the free surface elevation, $\eta(t)$, via the α-field. Simultaneously, both fields are relaxed towards the boundary in order to avoid wave reflections. At the tank end and pure absorption boundary, the blending function relaxes the fields across the relaxation zone until a still water level is reached at the boundary. As outlined in Fig. 2.8 (a, f), this method requires an extended domain at both ends of the NWT. This is not a problem for short waves but if long waves are modelled, this can lead to a significantly increased domain size. An extension of about one wavelength [82], better 2-4 wavelengths [124], per relaxation zone has been reported as a minimum requirement when a low level of reflections is

targeted.

The static boundary method applies wave generation and absorption directly at the domain boundaries at both ends of the domain, as outlined in Fig. 2.8 (b, g). The wave is directly generated at one boundary and prescribed by the $\boldsymbol{u}$- and α-fields where the wave elevation, $\eta(t)$, has been transferred to phase-fraction input. The wave generation BC can be coupled with absorption capabilities to reduce wave reflections, implemented so for instance in the OlaFlow/IHFoam toolbox.

Another wave generation method is the imitation of the motion of a physical wavemaker by means of a dynamic boundary, shown in Fig. 2.8 (c, h). Typically, the time-dependent displacement of either a piston- or paddle- type wavemaker is imposed in the model. A dynamic boundary can be applied for both wave generation and (active) absorption based on ad hoc measurements. The main downside of this method is the required mesh deformation which leads to a notably increased computational cost.

Less commonly used methods are mass source [72, 125] and momentum source [126, 127] wavemakers. As outlined in Fig. 2.8 (d, e), they can be imagined as pulsating sources and sinks at specified regions inside the domain. Applying a source term to the mass or momentum conservation equation requires a transfer function that translates from wave theory formulations to mass or momentum parameters. Since both methods only generate waves, absorption boundaries have to be applied at both tank ends. Similar to the relaxation method, an extended domain is required and entails an increased number of mesh cells and increased computational effort, respectively. Another inconvenience is the difficulty of achieving an accurate wave field which can involve an iterative trial-and-error procedure. Furthermore, sensitivities to source size and position have been reported by Schmitt and Elsaesser [124] in the context of shallow water regimes, unphysical vortex generation below mass source wavemakers has been reported by Peric and Abdel-Maksoud [128] and inaccuracies of momentum source wavemakers have been observed by Schmitt and Elsaesser [124] for simulations of extreme wave conditions.

Wave Absorption

As stated above, the relaxation method and the static and dynamic boundary method can be used for both wave generation and absorption. Alternative absorption techniques are numerical beaches, see Fig. 2.8 (i), sloped beaches, see Fig. 2.8 (j) or stretching of the mesh cells, see Fig. 2.8 (k). Those are typically used in combination with internal source wavemakers. Numerical beaches, also called sponge layers or dissipation zones function by application of vertical force terms to the momentum equation [129]. Here, the wave height is reduced along the beach or zone and forced to zero towards the tank

end. A sloped beach is simply a geometrically sloped domain where the waves break onto, similar to as in a physical wave tank. The energy dissipation, and hence reflection level, strongly depends on the wave parameters and can therefore not be regulated at all. Then there is the option to extend the domain at the end by increasingly stretching the mesh cells. This filters out any waves with lengths smaller than the cell length and therefore works particularly well for relatively short waves.

Wave absorption methods can be split into active and passive methods. Passive methods include relaxation zones, numerical beaches, sloped beaches and cell-stretching and typically require an extended domain to achieve high absorption levels. Active wave absorption (AWA) methods actively regulate the wave field based on real-time measurements at the (both static or dynamic) boundaries, similar to as in physical wave flumes. AWA methods have for instance be implemented in CFD models by Higuera [123], Troch and de Rouck [130], Spinneken et al. [131]. The active method is based on the fact that a perfectly reflected wave at a vertical wall is identical to the incident wave [132]. The wave heights, H, and periods, T, are the same but the direction of propagation is opposite. Consequently, the incident wave can be cancelled out at both the generation and pure absorption boundary by imposing the identical wave in the opposite direction [133] based on measurements of the $\boldsymbol{u}$- and α- fields. Since the action directly takes place at the boundary, no domain extension is required which can be advantageous in terms of cell count and computational cost.

Past work and reviews by Windt et al. [122], Schmitt and Elsaesser [124], Windt et al. [134], Miquel et al. [135] show that all absorption methods and their combinations have advantages and disadvantages. In general, passive methods tend to perform better for shorter waves [135] and active methods better for longer waves [136, 137].

2.3.3 Turbulence Modelling in the Presence of Waves

Dependent on the type of wave condition and flow problem, turbulence effects might be physically present and the modeller may take them into account.

For most operational wave conditions, turbulence plays a negligible role. In particular for pure non-breaking wave propagation, the water particle motion is laminar and potential-flow theory is applicable. Consequently, the use of a turbulence model in a CFD framework might be omitted. In extreme wave conditions where wave-breaking occurs, turbulence can play a significant role [82] and the amount of energy that is carried in the process usually has to be considered by means of a turbulence model. For instance, Kamath et al. [138] studied wave forces on and ringing of monopiles exposed to breaking focused waves by using a modified k-ω turbulence model.

WSI and Flow Scales

In the present context of wave interaction with thin perforated sheets and cylinders, two main flow scales are of interest, the flow around the perforated structure on a large scale, and the flow through the sheet openings on a small scale. Correspondingly, a distinction is made between large-scale and small-scale turbulence. The former concerns anisotropic effects such as horse-shoe or lee-wake vortex shedding around the cylinder which can be simulated directly to a large extent by a sufficiently fine temporal and spatial resolution. The latter refers to isotropic turbulence which in the RANS-approach is not simulated but modelled and represented by a turbulence model.

The characteristic non-dimensional numbers here are the Reynolds-number, Re, the Keulegan-Carpenter-number, KC, and the Stokes-parameter, β. Re represents the ratio of inertial forces to viscous forces and is defined as:

$$Re = \frac{u_m L}{\nu}, \tag{2.31}$$

where u_m is the amplitude of the oscillating flow velocity, L is a characteristic length and ν is the kinematic viscosity. Re can be expressed as $Re = \beta KC$ [139], where

$$KC = \frac{u_m T}{L}, \tag{2.32}$$

$$\beta = \frac{L^2}{\nu T}, \tag{2.33}$$

and T is the oscillation period (equal to the wave period). The KC-number represents the ratio of turbulent drag forces to inertia forces and predicts their relative importance. For an impermeable cylinder under wave loads, Fredsoe and Sumer [140] note that the KC-number has dominant influence on the flow regime, with β having a smaller effect. For linear waves in deep water, the amplitude of the horizontal fluid velocity at the free surface is $u_m = \omega_w H/2$, where H is the wave height and ω_w is the wave angular frequency. The wave period is $T = 2\pi/\omega_w$, substituting this into (2.32) gives:

$$KC = \frac{\pi H}{D}. \tag{2.34}$$

Re, KC and β are all calculated separately for the large and small scale flow. The relevance of the small-scale values comes in for the theoretical pressure-drop model,

further explained in Section 2.4.1. The estimation of those characteristic numbers helps to choose the turbulence modelling approach. When vortex-induced-vibrations (VIV) or wave run-up are of interest, wall treatment and turbulence modelling are critical requirements to capture BL effects and flow separation. In this context, a LES approach might be chosen over a RANS method. When wave-induced forces are of interest, the modelling approach usually depends on the dominating wave force regime. However, the modelling approach depends not only on the physical conditions, but also on practical implications of computing power.

Wave Force Regime and Vortex Generation

The overall force on a structure consists of viscous and inertial forces. Viscous forces are typically split into friction drag and form drag. Friction forces are a result of the roughness of a surface and can be considered to have negligible effects for most marine structures. Form drag forces result from flow separation at a surface's BL that can lead to vortex generation. Inertial forces comprise of mass and diffraction forces. The mass force, also referred to as Froude-Krylov-force [141], results from the pressure field induced by the undisturbed waves. The diffraction force results from scattering when waves bend around the edges of an obstacle.

In order to estimate the relative importance of viscous and inertial forces, the diagram by Chakrabarti [142], shown in Fig. 2.9, can be used. Its development is based on regular wave interaction with a bottom-fixed cylinder where the ratio of cylinder diameter, D, to the wavelength, λ, is used to classify the wave force regime.

If form drag and vortex effects are identified as important, further estimates can be made regarding the vortex regime. In the case of an impermeable bottom-fixed cylinder, the main possible vortex patterns are lee-wake and horse-shoe vortices [144].

Lee-wake vortices are caused by flow separation due to instabilities at the cylinder's BL. In the case of a steady current, the flow separates [141] and the vortex pattern is dependent on the cylinder geometry, the surface roughness and the Re-number [145]. A recommended practice by DNV [143] outlines two major categories for wave flow that depend on KC. For $KC > 40$, the vortex shedding appears to be very similar to as in steady currents. For $6 < KC < 40$, the vortex shedding frequency (usually defined by the Strouhal - number) is determined by the type of wave motion. For regular waves, the vortex shedding frequency will be a multiple of the wave frequency, $1/T$ [143]. For small KC-numbers ($KC \lesssim 5$), no flow separation and vortex shedding occurs [141] and a pair of symmetrically attached vortices is generated [144, 146, 147]. Sumer et al. [144] have identified more detailed KC ranges for lee-wake flow for wave interaction with a bottom-fixed cylinder. They have found that for $4 < KC < 6$, the symmetry of the

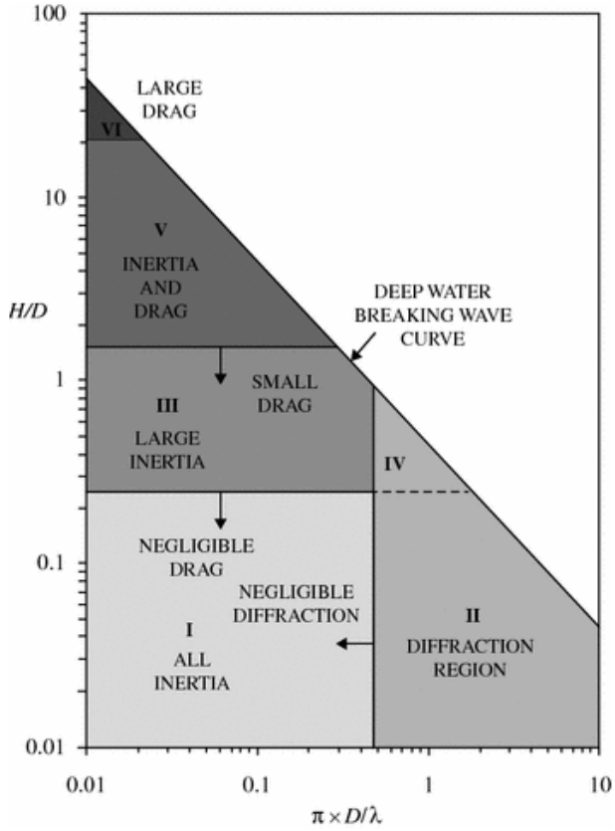

Figure 2.9: Diagram of wave force regimes by Chakrabarti [142]. Taken from DNV [143].

attached vortex pair breaks down; for $6 < KC < 17$ first shedding occurs and one vortex is shed in each half wave period; for $17 < KC < 23$, two vortices are shed in each half wave period and a Kármán-like vortex street is developed.

A horse-shoe vortex around a bottom of a fixed impermeable cylinder can be caused by rotation of the incident flow where the flow is separated at the bottom BL, rolls up, swirls around the cylinder and trails off downstream. Also here, the vortex development strongly depends on the KC-number. For $KC < 6$ no horse-shoe vortex occurred in the studies of Sumer et al. [144].

The turbulence modelling approach can be defined based on predictions of the wave-force regime, potential vortex patterns and the aim of the studies. In previous work, turbulence models have been used in the context of point-absorbing WECs [148], VIV of cylinders [70, 149–154], run-up on monopiles [27, 28, 153] and wave-induced forces on a monopile [155]. Other work that investigated similar WSI problems with fixed and floating cylinders, heaving buoys etc. have not used any turbulence models. Stated reasons for using the full NS equations are non-breaking and inertia-dominated wave-fore regimes [72, 156, 157], small Re-numbers [157, 158] and small KC-numbers [103, 157, 159, 160].

Spurious Turbulence Generation

When standard turbulence models are used for non-breaking wave propagation, unphysical turbulence generation at the air-water interface has been observed by Jacobsen et al. [82], Kamath et al. [155], Mayer and Madsen [161], Vanneste and Troch [162], Elhanafi et al. [163]. This can entail unrealistically large turbulence levels and wave damping effects. Two main reasons have been identified where both are coupled with each other. One source of spurious turbulence generation is the pressure-density coupling in the momentum equation of the segregated solution algorithm, as already stated in Section 2.2. Large density gradients at the air-water interface lead to large velocity gradients [28] which further lead to increased turbulence production. The second cause is the conditional instability of most turbulence models. This was first recognized by Mayer and Madsen [161] for the k-ω model by Wilcox [90], already introduced in Section 2.2.4.

Solutions have been presented as modified turbulence models that limit or stabilize turbulence generation. Durbin [164] have applied eddy-viscosity (ν_t) limiters to the k-ω model which has later also been used by Kamath et al. [138, 155, 165]. Devolder et al. [28] have developed a modified k-ω-SST model that suppresses turbulence generation at the interface (where a vertical density gradient is present) in applying additional buoyancy production in the turbulent kinetic energy equation. Larsen and Fuhrman [166] state that this approach does not fundamentally solve the conditional instability of the two-equation model and that the turbulence levels may still be overproduced. Consequently, they have developed a modified k-ω model that formally stabilizes the turbulence production in nearly potential-flow regions by additional stress limiters. However, the standard k-ω model is known to be sensitive to the turbulence BCs at the inlet, see Section 2.2.4. Thus, the enhanced model by Devolder et al. [28] might be advantageous since it is based on the blended k-ω-SST model.

Accurate modelling of turbulence generation is particularly important for long-term wave propagation and the prediction of wave breaking [166]. It is considered to be less relevant for non-breaking wave propagation in shorter domains of NWTs. In this context, other modelling aspects such as mesh resolution or discretisation schemes are considered to be more important.

Wave Boundary Layer

As stated in Section 2.2.4, turbulence modelling is typically coupled with BL modelling. The BL can be laminar or turbulent and correspondingly, appropriate BC settings (free-slip vs. no-slip, direct resolution vs. wall-functions) need to be applied.

In the context of wave propagation and WSI, BLs can occur at the ocean or flume

bottom and on structures. The BL development in oscillatory flow is based on the same principles as in steady flow but the BL thickness, δ_{BL}, is limited to the turnaround cycle of the flow, i.e. half of the wave period, T [167]. In wave flow, δ_{BL} is generally small and of rather turbulent nature. The KC-number can be an indicator to estimate whether a BL develops in oscillating flow.

In reality, the bottom of the ocean is rough and the BL is in the turbulent regime. In testing facilities, the bottom and walls of wave flumes are usually smooth enough to be in the laminar regime. In all cases, the wave bottom BL can be important for the development of horse-shoe vortices [144].

2.4 Macro-scale Porosity Representation

In general, two main approaches exist to CFD modelling of fluid interaction with a perforated or porous structure: a microscopic approach or a macroscopic, also called macro-scale, approach.

Microscopic Representation The intuitive approach to CFD modelling of fluid interaction with a perforated structure is to resolve the microstructural geometry explicitly. This approach is necessary when the detailed fluid flow behaviour needs to be analysed. It is often used for simulating smaller domains or 2D models. For example, Filho et al. [168] simulated water flow through perforated sheets as part of a pressurized water reactor and Guo et al. [169] analysed gas flow through perforated plates in a general context. This approach can also be used to derive porosity parameters or hydrodynamic coefficients from the numerical model. This was done by Chen et al. [170] for a 2D vertical perforated sheet, by George and Cho [171] to investigate sloshing effects in 2D tanks with porous baffles or by Mentzoni and Kristiansen [172] who developed a 2D NS solver to study the sensitivities of geometrical porosity and motion parameters for perforated plates in oscillating flow. It is also used when the perforations are large and the flow behaviour is highly anisotropic. For example, Lee et al. [6] studied the interaction of irregular waves with a caisson breakwater with circular perforations and Tsai et al. [173] the performance of a breakwater-integrated oscillating-water-column device. Poguluri and Cho [174] used results from a RANS model of a vertically slotted barrier to validate an analytical model in addition to experiments.

In all these cases, a fine mesh with a large number of mesh cells is required for both a sufficient geometry resolution as well as to achieve high mesh-quality levels in order to support solver and scheme stability. Also determining the geometry itself can be challenging for irregular structures such as foams. Generally, this can lead to a very high computational demand and can make the microscopic approach prohibitive for

larger domains and when the perforations are small and numerous. Valizadeh et al. [7] stated this approach to be impractical for their investigations of solitary wave interaction with a vertical perforated-sheet breakwater.

Macro-scale Representation A macroscopic approach can offer a more efficient alternative for engineering problems where large-scale force effects and the overall flow behaviour are of interest rather than details of the flow near the structure. Here, the micro-scale geometry of the perforated structure is not resolved explicitly but represented by a spatially averaged macro-scale model in a geometrically defined porous region. The porous structure can either be represented as a volumetric porous region or as a surface with a pressure-jump condition [175]. In both options, source terms are added to the momentum equation.

The properties of the porous structure are averaged in space and their bulk effect on the fluid are parameterized by a model by means of a theoretical pressure-drop source. The pressure-drop model and its parameters are of paramount importance since the quality of the model is dependent on the underlying assumptions and simplifications.

A macroscopic porous-media approach within a CFD framework addresses the limitations of both linear potential-flow models and microscopic CFD models. This approach does not require the restrictive assumptions of linear wave theory. It also simplifies mesh generation and reduces the number of cells required compared to microscopic CFD approaches. However, the characteristics and advantages of this approach also imply its limitations. The averaged representation as continuous and homogenous zone leads to a smoothing effect and the real flow field inside and close to the porous structure cannot be replicated. Furthermore, the BL on the structure cannot be represented since no actual boundary exists in the model. Thus, a macroscopic approach is inadequate when flow separation processes need to be captured with greater accuracy.

Previous work that is similar to the present WSI problem was done by Shim et al. [5], Zhao et al. [40, 176] and Chen and Christensen [4] who used various macro-scale CFD approaches to study fluid interaction with rigid fish net and cage structures. Shim et al. [5] studied steady single-phase current flow through and around a cylindrical net cage with finite length. Zhao et al. [40] investigated various angles of attack of plane net sheets under steady single-phase flow and Zhao et al. [176] looked at wave interaction with vertical bottom-fixed, vertical truncated and inclined truncated surface-piercing plane sheets. Chen and Christensen [4] simulated steady current and wave interaction with plane net sheets under various angles of attack and truncated cylinders in steady current single-phase flow. Their studies have only looked at static structures and the majority investigated steady single-phase flow conditions. Only Zhao et al.

[176] investigated 2D wave interaction with rigid plane nets.

The present work adds the investigation of wave interaction with a bottom-fixed cylinder with a 3D model and provides an extension to modelling of floating structures. Furthermore, this thesis uses a different pressure-drop formulation as a key distinction, introduced next.

2.4.1 Theoretical Pressure-Drop Model

The pressure-drop or gradient, Δp, across any porous structure can be written as a function of the Darcy-velocity, $\boldsymbol{u}$, (the fluid velocity averaged over the cell area) as:

$$\frac{\Delta p}{\rho} = a\boldsymbol{u} + \frac{C_f}{2}\boldsymbol{u}\left|\boldsymbol{u}\right| + c\frac{\partial \boldsymbol{u}}{\partial t}, \tag{2.35}$$

where a, C_f and c are porosity or pressure-drop coefficients. The Darcy-velocity, $\boldsymbol{u}$, is related to the actual velocity in the porous media, $\boldsymbol{U}$, by $\boldsymbol{u} = \boldsymbol{U} \times n$, where n is the porosity. The first linear term at the RHS of (2.35) represents dissipation losses due to viscous friction, typically dominant for low Re-numbers. The second quadratic term represents dissipation losses due to turbulence within regions with high Re-numbers. The third transient term accounts for the acceleration of the fluid through the voids. The relative importance of the three components depend on the structure type and corresponding flow regime.

In the context of granular material, these terms are typically referred to as Darcy-term [177] for the linear term, as Forchheimer-term [178] for the non-linear drag component and as Polubarinova-Kochina-term [179] for the transient term.

In the context of gravity wave interaction, first efforts on pressure-drop formulation in combination with linear wave theory were made by Ward [180] and Sollitt and Cross [181] for generic porous structures and by Mei et al. [32] and Bennett et al. [47] for slotted breakwaters. Their formulation and others are all based on the generic equation (2.35). Differences arise from the porosity coefficients and their derivations. The coefficients a, C_f and c in (2.35) are input parameters to the CFD model and therefore determine its quality. They can either be obtained empirically, from theoretical models or a combination of both. The coefficients are highly problem specific and are an active field of research. Examples of studies on derivations of coefficients for specific problems are the studies by Madsen [182] and Chwang and Chan [183] for generic porous structures, by Gan and Riffat [184] and McIver [185] for single orifices and by Mei et al. [32], Li et al. [186] and Mentzoni et al. [187] for thin permeable barriers in oscillatory flow.

Thin Perforated Barriers and Porosity Coefficients In general, wave interaction with thin perforated barriers is characterized by eddy generation and dissipation due to flow separation across the barrier [24]. Hence, the Re-numbers are large and turbulent losses dominate over viscous losses for the small-scale flow across the barrier. Viscous losses are considered to have negligible effects [181]. Transient losses have a minor effect and tend to zero when the size of the perforations is small in relation to the wavelength since the wakes close to the perforated sheet are quickly homogenised [24]. Consequently, the focus lies on the nonlinear pressure term in (2.35), which equals a drag force with the drag coefficient, C_f. This is further argued in Chapter 3.

In the context of fluid interaction with fish net cages, Shim et al. [5] have used a drag force with a porosity coefficient obtained from experiments. Zhao et al. [40, 176] have used both a viscous force and drag force with coefficients based on empirical formulations within a porous-media RANS-implementation. With a porous-media VARANS-approach, Chen and Christensen [4] have applied both a drag and a transient resistance term. The drag coefficient was obtained from a Morison-type load-model that assumes a fish net being composed of cylindrical twines without knots. The transient coefficient was set to 0.43 without further investigations and declared to be an inherited parameter from work on large volumetric dams by Jensen et al. [37]. To their disadvantage, the approaches by Shim et al. [5] and Chen and Christensen [4] require calibration procedures for the coefficients in the model.

Thus, a different approach without the requirement of calibration is desirable. Based on reviews of models for C_f by Huang et al. [188] and Molin [24], Mackay and Johanning [44] have identified the models by Mei et al. [32] and Molin and Fourest [34] as commonly used ones. Mei et al. [32] formulated C_f as:

$$C_f = \left(\frac{1}{nC_c} - 1 \right)^2, \tag{2.36}$$

where n is the porosity of the surface and C_c a coefficient for contraction which is estimated as $C_c = 0.6 + 0.4n^2$. Molin and Fourest [34] and Molin [24] defined C_f as:

$$C_f = \frac{1-n}{\delta n^2}, \tag{2.37}$$

where δ is an empirically defined discharge coefficient, usually in the range of 0.3-0.5 [24, 44]. Mackay and Johanning [44] have compared the models of Mei et al. [32] and Molin and Fourest [34]. It was shown that the formulation by Mei et al. [32] gives higher values for $n < 0.4$ but lower values for $n > 0.41$ than the formulation by Molin

and Fourest [34]. Overall, Mackay et al. [41] and Mackay and Johanning [44] have achieved good results using the model by Molin and Fourest [34] with $\delta = 0.5$ for their linear potential-flow model.

For wave and oscillatory flow, the discharge coefficient, δ, and hence C_f vary with the KC-number. Tait et al. [2] and Hamelin et al. [3] investigated the variation of the drag coefficient, C_f, with KC for slatted screens, where the characteristic length scale, L, for the KC calculation, equation (2.32), was defined as the slat width. They estimated a relationship of $C_f = C_f^{steady}(8.9\mathrm{KC}^{-0.9} + 1)$, where C_f^{steady} is the drag coefficient in steady flow. For larger KC-numbers ($KC > 15$), corresponding to closely spaced openings or large flow velocities, the influence of the KC-number decreases and the drag coefficient tends to the value for steady flow. Since the experiments considered in the present work used perforated rather than slatted sheets it is not clear how the findings of Tait et al. [2] and Hamelin et al. [3] would translate to this case.

However, the KC-numbers have been estimated for the local pressure-drop across a perforated barrier where the sheet thickness, d, is used as the characteristic length, L, the horizontal velocity at the free surface as u_m, and T as the wave period. For the present range of investigated wave conditions (Table 4.1) and thicknesses $3\,\mathrm{mm} \leqslant d \leqslant 10\,\mathrm{mm}$, the KC-numbers range between approximately $10 \leqslant KC \leqslant 3980$. Consequently, the KC-numbers are considered to be large enough to assume a constant value for δ and C_f, respectively. In other words, C_f is set as independent of any wave conditions in this work and only depends on the porosity, n, of the structure.

To note, the large-scale fluid flow effects around the whole structure are seen as a separate scale, as outlined in Section 2.3.3.

2.4.2 Implementation Options

Macro-scale porosity representation by means of a pressure-drop can either be implemented as a 3D region (2D in 2D modelling) as so-called porous media, or as a 2D surface (1D in 2D models) with a pressure-jump condition, also referred to as porous jump or porous baffle. The formulation of the momentum conservation equations differs depending on the type of porosity implementation. The pressure-drop application varies for the isotropic and orthotropic porous media and the porous baffle implementation, as outlined in Fig. 2.10 where the main options of macro-scale implementations, as in Fig. 2.11, are shown. In the schematics, the arrows outline velocity vectors close to the porous barrier and the bold lines along the cell faces indicate the components of the velocity that are subject to a pressure-drop. Details will be explained in the following sections.

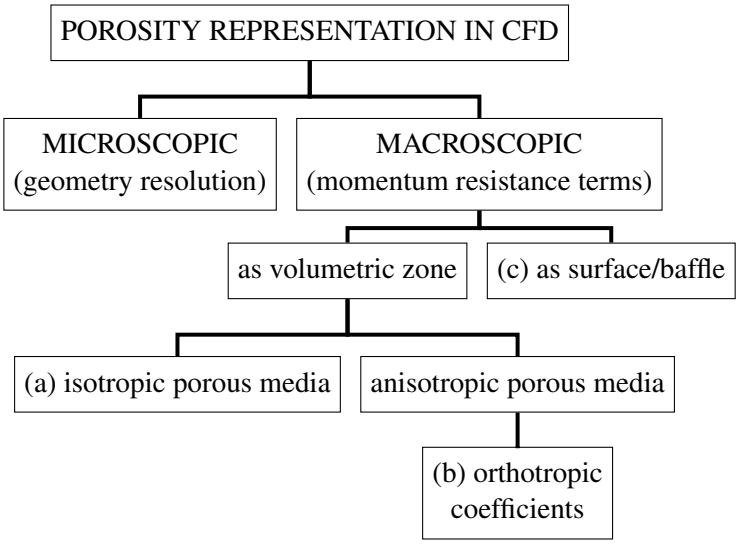

Figure 2.10: Options for porosity representation in CFD modelling for thin porous structures.

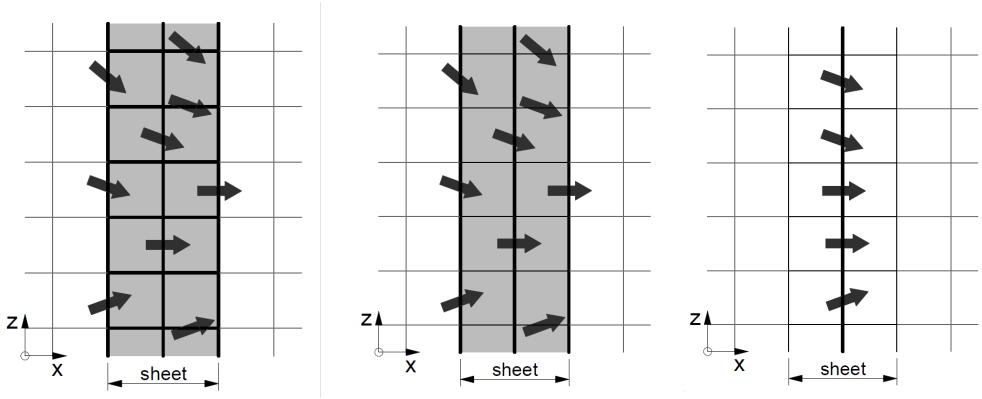

(a) isotropic volumetric (same resistance in x-, y- and z-direction)

(b) orthotropic volumetric (resistance only in x-direction)

(c) baffle (resistance in normal direction to a surface)

Figure 2.11: Schematics of the investigated porosity implementations, showing mesh cells and arrows that represent the velocity vectors close to a porous sheet; shades represent porous-media zones; bold lines along the cell faces indicate the components of the velocity that are subject to a pressure-drop (note that in (a) the pressure-drop is applied in all directions and that in (b) it is only applied in x-direction).

Porous Baffle

If the thickness, d, of a porous structure is significantly smaller than its other dimensions, d may be assumed as infinitesimally small. Thus, the volumetric dimension of a thin structure can be represented by a porous surface with zero thickness.

In this case, the pressure-drop, Δp, is applied as a jump condition at the mesh cell faces of a geometrically specified surface. Here, the porous resistance terms of the

theoretical formulation are applied to the momentum equation formulated (within the `interFoam`-framework) as:

$$\frac{\partial}{\partial t}\rho\boldsymbol{u} + \nabla\rho\boldsymbol{u}\boldsymbol{u} = -\nabla p^* - \boldsymbol{g}\boldsymbol{X}\nabla\rho + \nabla\cdot(\mu_{eff}\nabla\boldsymbol{u}) + \sigma\kappa\nabla\alpha - \Delta p, \tag{2.38}$$

and where the (drag term of the) pressure-drop defined in (2.35) reduces to:

$$\Delta p = \frac{\rho C_f}{2} u_n \left|u_n\right|, \tag{2.39}$$

where u_n is the volumetric flow rate per unit area in direction normal to the porous surface.

This approach is commonly used for structures where the thickness can be assumed to be negligibly small such as membranes, fans, actuator disks, perforated baffles or fish nets. For example, this approach has been used to represent membranes including studies on separation processes by Li and Cheng [189] or examinations of the flow field through perforated tiles in data centres by Arghode and Joshi [190]. For fans, the baffle-implementation has been used by Chacko et al. [191] to improve radiator efficiency by air flow optimization, by van der Spuy and von Backström [192] and Sumara and Šochman [193] to represent fans in air-cooled condensers. In the form of a perforated baffle it has been used to simulate contact tanks for water treatment by Kizilaslan et al. [194] or in refrigeration cabinets by Wang et al. [195]. The same pressure-jump principle has also been used in the form of actuator disks for wind turbine rotors [196], tidal turbines [197], ship propellers [198] and helicopter rotors [199, 200]. As a marine engineering application similar to the present case, Shim et al. [5] have used a porous baffle to model current flow through and around a cylindrical fish net cage. Most of the existing research described here has been performed for steady-state conditions and in single phase flow. Bakica et al. [198] investigated ship resistance with two phases, but the actuator-disk that represents the ship propeller was fully submerged in the water. Apart from applications to actuator disks [196, 199, 200] and for water treatment [194], steady-state solutions have been calculated in most previous examples.

Though applied to a wide range of applications as described above, the porous baffle implementation has to date only been used for single-phase current flow. In this thesis, however, it is explored and applied for transient two-phase wave flow.

Volumetric Porous-Media

Representing the porosity as a volumetric porous zone, often referred to as porous media, is implemented as momentum resistance applied to the cell centres (in a cell-centred FV framework) of a volumetrically defined geometric region.

This approach can be used with or without consideration of the reduced amount of fluid inside the volume as a result of the geometric blockage of the porous structure. Typically, for large volumetric structures such as dams or breakwaters, the reduced amount of fluid needs to be taken into account and the volume-averaged NS equations or Volume-Averaged Reynolds-Averaged Navier-Stokes (VARANS) equations are used. Higuera et al. [36], del Jesus et al. [39], Lara et al. [201] have used porous-media VARANS-formulations with isotropic material characteristics for studies on fluid interaction with dams and cubical porous barriers. Beyond that, Brito et al. [202] and Hadadpour et al. [203] have used it for fluid interaction with vegetation. Chen and Christensen [4] used a volume-averaged NS-formulation with anisotropic material characteristics for plane and circular fish nets. Using 2D models, they investigated current flow across a truncated plane with various angles of attack, wave interaction with bottom-fixed vertical sheets, whilst in a 3D model they looked at current flow across a truncated fully-submerged cylinder. For other cases of thin porous structures, the NS or RANS equations have previously been used inside and outside the porous structure neglecting the effects of a reduced fluid amount in the openings. This was carried out with anisotropic material assumptions by Kyte [204] for the representation of a filter as part of a domestic ventilation waste heat recovery system and by Zhao et al. [40, 176] for rigid plane fish nets. The anisotropic approach can also be used to direct the fluid flow in a certain way, as demonstrated for instance by Hafsteinsson [205] to model flow through a conical diffuser.

The first mathematical fundamentals of spatial averaging for porous media equations were developed by Whitaker [206] and Slattery [207]. The first proposals for application to gravity wave interaction can be found in papers by Ward [180] and Sollitt and Cross [181] which further evolved to first VARANS modelling by Liu et al. [208]. OlaFlow/IHFoam, utilizes formulations of the VARANS equations that are based on averaging procedures by Whitaker [206], Slattery [207] and Gray [209]. The detailed derivation of the VARANS equations from the RANS equations, (2.2) and (2.3), can be found in Higuera et al. [36] or Jensen et al. [37]; the final set of equations is stated in the following.

The VARANS equations for incompressible, immiscible two-phase flow are equivalent to (2.29) and (2.38), but formulated for the intrinsic velocity, $\boldsymbol{u}/n$ (the mean velocity of the fluid inside the porous medium where $\boldsymbol{u}$ is the Darcy-velocity), instead

of $\boldsymbol{U}$ (the actual velocity of the fluid inside the perforations). The mass conservation equation is thus written as:

$$\nabla \cdot \frac{\boldsymbol{u}}{n} = 0, \tag{2.40}$$

where n is the porosity and the momentum equation as:

$$\frac{\partial}{\partial t}\frac{\rho \boldsymbol{u}}{n} + \nabla \frac{\rho \boldsymbol{u}\boldsymbol{u}}{n^2} = -\nabla p^* - \boldsymbol{g}\boldsymbol{X}\nabla\rho + \nabla(\mu_{eff}\nabla\frac{\boldsymbol{u}}{n}) + \sigma\kappa\nabla\alpha - \Delta p, \tag{2.41}$$

with the drag term of the pressure-drop as defined in (2.35):

$$\Delta p = \frac{\rho C_f}{2}\frac{\boldsymbol{u}}{n}\left|\frac{\boldsymbol{u}}{n}\right|, \tag{2.42}$$

where Δp represents both the macro-scale effects of the perforated structure on the fluid and the closure terms that arise from the volume-averaging procedures.

Since the present work uses the MULES VOF-method, the advection equation for the α phase-fraction field, (2.24) is also volume-averaged and written as:

$$\frac{\partial \alpha}{\partial t} + \frac{1}{n}\left(\nabla \boldsymbol{u}\alpha + \nabla \boldsymbol{u_{ic}}(1-\alpha)\alpha\right) = 0. \tag{2.43}$$

In the present cell-centred FV method, the pressure-drop term is applied to the cell centres within the geometrically specified porous zone and interpolated to the cell faces. The source accounts for the limited amount of fluid inside the structure and the effects of the porous structure on the fluid such as friction forces, pressure forces and added mass effects [102]. Outside the porous zone, the VARANS equations are equivalent to the standard RANS equations and OlaFlow's porosity application-solver `olaFlow` reduces to `interFoam`.

Depending on the properties of the porous material, the porous media can be implemented with either isotropic or anisotropic characteristics and the resistance-source terms can be formulated by means of either scalar or tensor values, respectively.

Isotropic Porous Media In the isotropic case, the pressure-drop is applied as a single scalar quantity, identical in all directions, outlined in Fig. 2.11a. An isotropic implementation can be realized either by using the same value for C_f in all three main directions of a tensor field, $\boldsymbol{C_f}$, or by directly using a scalar field for C_f. The latter is the standard implementation in OlaFlow/IHFoam which has been used without

modifications.

The isotropic implementation is applicable to two types of structures; either for thin structures as in the present case, where the pressure-drop component in tangential direction of the structure can be neglected, or for large-volumetric structures that can be assumed to have isotropic material properties. In the literature, it has mainly been used for the latter case and in the context of vegetation [202, 203], dams and cubical porous barriers [37, 39, 77, 201].

Anisotropic Porous Media An anisotropic implementation is required for structures and materials with distinctive directionality. Here, the pressure-drop is implemented by a tensor field, where the porosity coefficients can vary in location and direction. It is often implemented in terms of orthotropic characteristics with three main directions (as a sub-type of anisotropic properties). For the case of a thin perforated sheet this corresponds to a normal direction across the sheet and two in-plane directions, as outlined in Fig. 2.11b, and this ideally reflects the reality of a sheet with holes cut in it (i.e. small resistance to flow in one direction, infinite in the perpendicular directions). The orthotropic porosity implementation is realized with the porosity coefficient, C_f, implemented as a tensor field, $\boldsymbol{C_f}$. For the specific case of a thin perforated barrier, the pressure-drop is only applied in normal direction across the sheet and therefore dependent on the flow velocity normal to it. This means, the drag-related porosity coefficient is implemented as:

$$\boldsymbol{C_f} = \begin{pmatrix} C_f & 0 & 0 \\ 0 & 0 & 0 \\ 0 & 0 & 0 \end{pmatrix}, \tag{2.44}$$

where C_f is the scalar value of the coefficient as in (2.42). The implementation of $\boldsymbol{C_f}$ as a tensor field is the standard implementation in waves2Foam. By default and as implemented in waves2Foam, the tensor $\boldsymbol{C_f}$ is constant across the entire domain and the directions of the pressure-drop is aligned with the x-, y- and z-direction of the global Cartesian coordinate system, also denoted as e_x, e_y, e_z.

A directed pressure drop with orthotropic characteristics has been used in previous work on filters for heat recovery systems [204], for conical diffusers [205] or rigid aquaculture structures such as plane nets [4, 40, 176] and circular nets [4].

2.4.3 Turbulence Modelling in the Presence of thin porous Structures

If turbulence effects are of interest, some considerations need to be addressed when a turbulence model has to be applied in combination with the porous-media method. If a porous baffle is used, nothing changes since the pressure-drop is only applied at the cell faces. Inside volumetric porous media however, the turbulence generation needs to be adapted to take the altered velocity field into account since the standard turbulence models generate turbulence as if the porous structure has no effect on the fluid [102]. So in a coherent VARANS context, also the turbulence model would need to be modified.

One key question is whether macro-scale turbulence can occur inside porous media at all and whether a turbulence model is required or not. In the context of WSI, Higuera et al. [36], del Jesus et al. [39] and Losada et al. [102] argue that the large shear stresses at the interface between clear fluid region and porous media caused by the spatial porosity gradient require the use of a model to capture the increase in turbulence production. Alternatively and disputably, Srineash et al. [210] have applied the standard k-ω model outside the porous zone, but have not applied any model inside the porous zone for studies on wave interaction with dams. So mostly, the standard models such as the k-ϵ, k-ω or k-ω-SST models have been applied. A few authors proposed volume-averaged models to align with the VARANS approach, where Nakayama and Kuwahara [211] and Hsu et al. [212] adapted the k-ϵ model and del Jesus et al. [39] the k-ω-SST model. Their volume-averaging procedure introduces new additional terms in the model equations which need to be specified. Nakayama and Kuwahara [211] have provided closure terms for their volume-averaged k-ϵ model. However, no closure formulation has been presented for the averaged k-ω-SST model in the literature, yet [36]. This might be rooted in the complexity of turbulence in porous media where many fundamental questions are unanswered [213].

Jensen et al. [37], Vanneste and Troch [162] and Jacobsen et al. [214] have not applied turbulence models for their studies on wave interaction with dams and rubble-mound breakwaters based on the argument that turbulent losses within the porous structure are already incorporated by the pressure-drop model. They argue that the application of a turbulence model would represent an extra contribution to the applied momentum resistance. This is particularly relevant when the porosity coefficients have been obtained from experimental studies. The former arguments concern volumetric structures, but Chen and Christensen [4] put the same opinion forward for their investigations on thin net structures where no turbulence model was used. Also Zhao et al. [40] and Zhao and Wan [215] have used the full NS equations without a turbulence model, but without explaining their choice. Morgan [216] did not use a model due to the

uncertainties associated with the initial parameters and the lack of practical guidance on their estimation. The initial turbulence-related BCs are rarely stated in literature. Only Devolder [217] and Larsen and Fuhrman [166] state their initial BCs for turbulence parameters in the course of the validation of their own modified models.

Overall, the literature suggests that the results with and without a turbulence model do not differ significantly and that good agreement could be achieved between experimental results and CFD results where no turbulence models were applied [4, 37, 40, 162, 214–216]. Furthermore, the application of a turbulence model depends on the aim of the study. The authors that were explicitly interested in turbulence effects postulate the importance of a model [36, 39, 77, 133], and those who were not interested in turbulence levels argue that the application of turbulence models is superfluous [4, 37, 162, 214]. The effect of applying common turbulence models for the present context of large-scale WSI is assessed below in Section 6.5.

2.5 Body Motion and Dynamic Meshing

CFD modelling of a floating structure requires a meshing approach that dynamically adapts the mesh in accordance with the motion of the body. In the present case, the structure is assumed as a rigid body and its motion is solution dependent. In other words, the body does not deform and it moves interdependently due to the fluid flow forces. Various dynamic meshing methods with varied capability and fidelity exist, and are introduced in the following sections.

2.5.1 Rigid Body Motion

The equation of motion of a rigid body follows Newton's second law and is defined as (see e.g. Horoub [218]):

$$\boldsymbol{M}\ddot{\boldsymbol{x}} + \boldsymbol{C}\dot{\boldsymbol{x}} + \boldsymbol{K}\boldsymbol{x} = \boldsymbol{F}, \tag{2.45}$$

where $\boldsymbol{x}$ is the position vector, $\boldsymbol{M}$, $\boldsymbol{C}$ and $\boldsymbol{K}$ are the mass, damping and stiffness matrices of the body and $\boldsymbol{F} = [\, F_x\, F_y\, F_z\, M_x\, M_y\, M_z\,]^T$ is the vector of the total forces and moments acting on the body. The mass matrix, $\boldsymbol{M}$, consists of the structural mass and the added or hydrodynamic mass, $\boldsymbol{M} = \boldsymbol{M_s} + \boldsymbol{M_a}$. The latter is added inertia that accounts for the water mass that surrounds a de-/ accelerating body and has to be moved with it. The damping matrix, $\boldsymbol{C}$, accounts for mooring line effects and hydrodynamic damping such as viscous friction and related energy dissipation. The stiffness matrix, $\boldsymbol{K}$, consists of the mooring system stiffness and the hydrostatic stiffness, $\boldsymbol{K} = \boldsymbol{K_m} + \boldsymbol{K_h}$. The latter results from the fluid around the structure. The

total force vector, $\boldsymbol{F}$, includes all external forces such as the fluid's pressure and viscous forces and moments on the structure. These result for instance from wind, current or wave excitation.

Within a NS- based CFD approach, the force contributions due to added mass, $\boldsymbol{M_a}$, hydrostatic stiffness, $\boldsymbol{K_h}$, and fluid forces in $\boldsymbol{F}$ are automatically considered. Other acting forces such as gravity, buoyancy or mooring restoring forces can be further introduced by means of contributions in the damping and mooring stiffness matrices, $\boldsymbol{C}$ and $\boldsymbol{K_m}$, or as external force in $\boldsymbol{F}$.

2.5.2 Mesh Motion Methods

The standard approach for the formulation of moving bodies within a fluid domain is the Arbitrary-Lagrangian-Eulerian (ALE) approach where the formulation of the governing equation combines Lagrangian and Eulerian characteristics [219]. It was first introduced by Hirt et al. [220] and other early developments were initiated by Starius [221, 222], Steger et al. [223] and Benek et al. [224]. The hybrid formulation allows both an arbitrary motion of the grid points with the fluid in a Lagrangian fashion and tracking of the solid-fluid interface from an Eulerian perspective.

The ALE formulation can be applied to two main types of dynamic mesh methods, overlapping or non-overlapping methods. The latter are commonly denoted as domain conforming methods which can further be divided into re-meshing, sliding and morphing approaches. All methods vary in their range of applicability and their computational cost, which are directly related as outlined in Fig. 2.12. The methods are introduced in the following sections.

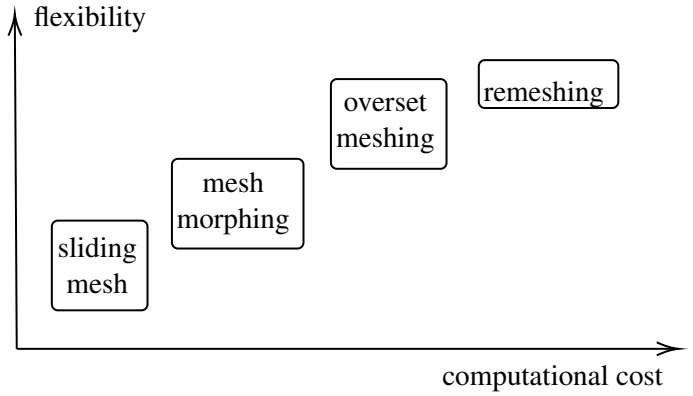

Figure 2.12: Methods for dynamic mesh motion and their relative flexibility (in terms of range of applicability, i.e. gaps, overturning etc.) and computational cost.

Overset Meshing The overset mesh method, also called chimera or the overlap method, is based on the concept of using a number of body-fitted grids that overlap and

can move relatively to each other on top of a background mesh.

The key advantage of this method is that the mesh quality can be maintained while multiple bodies can move arbitrarily. This allows for large motions and geometries with narrow gaps and exceeds limitations of various other methods. In the ocean engineering domain, the overset mesh approach has for instance been applied to wave interaction of floating WECs [225–227], ship hydrodynamics [228, 229] and FOWTs [75, 230, 231]. Those examples involve large motions, multiple independently moving structure parts and/or gaps where other dynamic mesh approaches might fail. However, the method exhibits two downsides. It is not strictly conservative due to interpolation procedures between the body-fitted mesh and the background mesh [84]. This could also lead to convergence issues. Furthermore, the flexibility of the approach demands a relatively large computational effort.

Re-meshing Another method that maintains mesh quality levels while allowing for arbitrary body motion is the re-meshing method. With this method, the mesh is regenerated for each time step or, if combined with a mesh deformation method, every time when the mesh quality exceeds a certain limit. Re-meshing has for instance been used in the context of gear pumps [232], nozzle injections [233] or external weapon ejection [234].

Similar to the overset method, re-meshing provides flexibility which implies a high computational demand. Typically, a large number of mesh cells requires interpolation of the flow fields between the sequentially newly generated meshes of each time step. This method can rarely provide a convincing trade-off between capability and computational cost.

Mesh Morphing A computationally less expensive method is the morphing or deforming mesh method. Here, the mesh deforms in accordance with the transient motion of a moving body while the number of mesh cells is maintained. Therefore, this method is fully conservative.

Various methods can be used to define the transient distribution of the mesh points from a moving boundary to the inner parts of the fluid domain. All methods aim to preserve mesh quality in terms of vertex spacing and discretisation error. Popular options are the utilization of physical analogies or interpolation methods. Physical analogies treat the mesh as a physical process [235] such as deformation of a linear elastic solid, done so for instance by Johnson and Tezduyar [236], Tezduyar [237], Jasak and Tuković [238] assuming small deformation, or inter-cell connectivity by linear or modified springs, used for instance by Batina [239], or as a diffusion process using Laplace's equation, as used by Jasak and Tuković [238]. Alternatively, it can be useful

to apply interpolation methods such as transfinite interpolation [240], algebraic damping interpolation [241], Radial Basis Functions [242] or spherical linear interpolation (SLERP) [243]. For further information and other mesh morphing methods, the interested reader is referred to a survey by Selim and Koomullil [235] where many methods are listed and described.

Although some morphing methods such as Radial Basis Function interpolation provide increased capabilities, mesh morphing is generally limited to smaller motion ranges, and geometrical gaps and overturning can not be dealt with.

Sliding Meshes Another non-overlapping mesh motion method is the sliding method, where the body-fitted grid slides along the stationary part of the mesh. The interface between the moving and stationary part can either be of plan, cylindrical or spherical shape while both the moving and stationary mesh parts retain constant in shape, cell number and distribution.

This method is computationally relatively cheap but also very limited in its application and way of motion. It is often used for problems with one DOF such as 1-DOF rotation or translation. In the former case, it has been used for tidal turbines [244], stirring tanks [245, 246], vertical axis turbines [247, 248] or WECs [29, 217]. With appropriate combination of moving mesh parts an extension to multiple DOF is possible. This was for instance applied to FOWTs by Liu et al. [249] and Ren et al. [250].

2.5.3 Mesh Morphing in OpenFOAM

As elaborated below in Chapter 3, the mesh morphing method is deemed to be the most suitable method for the present specific cases. Its implementation in OF is introduced in this section.

The motion of a rigid body within immiscible two-phase fluid flow consists of three main aspects: the body motion, the dynamic mesh adaptation and the fluid flow. In OF, coupling of these is provided by the `interDyMFoam`-framework. Here, the `rigidBodyMotion`-library allows for multiple body motion, while the `sixDoFRigidBodyMotion`-library is specifically provided for single body motion. The latter is explored for the present targeted case of a floating TLP. The rigid body motion solver allows 6-DOF motion evaluated as Ordinary Differential Equation (ODE) as force balance based on the equation of motion, (2.45). The total forces exerted on the body's centre of gravity (COG) encompass fluid, buoyancy, and gravity forces, as well as mooring restraints and other possible external forces. The three default options to solve the body motion are an explicit symplectic solver, an implicit Newmark solver [251] and a Crank-Nicolson motion solver [252]. The mesh deformation is calculated

through a displacement field; the boundary patches of which specify the motion, and from which the interior values are calculated to determine the mesh point displacements. The standard mesh morphing method in OF is based on the SLERP interpolation algorithm. Alternatives are mesh motion routines using Laplacian diffusion or Radial Basis Function interpolation [253]. The boundary patches also determine the BCs for the PDEs being solved for the fluid field.

The `interDyMFoam` application solver has been used for various marine engineering applications such as ship hydrodynamics [196, 254], WECs and simplifications of them [255–257], and FOWTs [76, 258].

InterDyMFoam

In `interDyMFoam`, the motion routine is located inside the outer PIMPLE (SIMPLE) loop. This allows for stronger coupling between the body motion and the fluid flow [259], which increases solution accuracy and solver stability. Strong coupling addresses the so-called artificial added-mass effect, which is an inherent instability caused by the lag between fluid and body motion solution of the sequential solution process of weakly coupled partitioned routines [260]. Further information on the artificial added-mass effect of partitioned schemes and enhanced coupling methods can be found in Chow and Ng [259], Förster et al. [260], Matthies and Steindorf [261], Causin et al. [262], Gatin et al. [263], Dunbar et al. [264] and Devolder et al. [265], which are examples of an active area of research.

The `interDyMFoam` flow chart is outlined in Fig. 2.13. The algorithm works as follows. The main runtime-loop is entered with an initial time step and further looped through with time steps, Δt, that automatically adjust to give the specified maximum CFL-number. First, the motion solver is entered and the body position is updated. Then, the fluid forces on the body are calculated via integration of the pressure field at the solid boundary. The (pressure and viscous) fluid forces and all other forces, such as gravity and mooring restraints, and their moments exerted on the COG, are applied to the 6-DOF body motion equation. From this ODE, the body acceleration and the new position are obtained. The body is moved and the mesh is being deformed. Next, the motion solver passes the moving-wall information as BC on to the fluid solver. The fluid solver corrects the flux field to account for the mesh motion. The phase properties are being updated and the free-surface VOF equation is solved following the steps outlined in Fig. 2.5 in Section 2.2.7. Then, the PIMPLE pressure-velocity coupling is initiated to solve for fluid velocity and pressure, including the pressure-correction procedure of the PISO algorithm.

The subsequent step depends on whether weak or strong coupling between the struc-

ture motion and fluid flow is employed, and whether the switch `moveMeshOuterCorrectors` is specified to be on or off, respectively. For weak coupling and `moveMeshOuterCorrectors = no`, the outer PIMPLE (SIMPLE) routine is continued and looped through for the number of `nOuterCorrectors` specified. Thus, the motion solver is entered only once before the fluid flow solution has converged and time is advanced. For strong coupling and `moveMeshOuterCorrectors = yes`, the motion solver is entered again after the PISO correction. Here, the whole system consisting of the motion solver, the VOF routine, and the pressure-velocity coupling is executed for the number of `nOuterCorrectors` employed, before time is advanced. Increasing the number of outer PIMPLE iterations can increase stability. However, the larger the number of iterations, the longer the computational times.

The following specifications need to be provided for the three coupled sub-solvers: the mesh morphing routine, the 6-DOF body motion solver and the fluid solver.

Mesh Morphing Controls The SLERP interpolation morphing provides a smooth mesh displacement based on the distance between the mesh cells and the moving object. Therefore, the boundary patches of the solid body need to be specified. By default, these are identical to the patches used to obtain the fluid forces to calculate the body motion. Furthermore, an inner and outer distance to the object's boundaries between which the mesh gets morphed need to be predefined. Mesh cells inside the inner distance experience rigid motion in accordance with the body. Mesh cells outside the outer distance remain unchanged without any displacement. All mesh cells between the inner and outer distance get morphed utilizing SLERP interpolation.

Body Motion Specification Apart from selecting solvers for the mesh and body motion, the body properties and additional external forces need to be specified. Body properties include the mass, the COG, moments of inertia and possible initial velocity conditions. Also, the boundary patches on which the fluid forces are obtained by pressure integration need to be indicated. Optionally, restraints and constraints can be specified. Restraints are external forces such as constant, spring or damper forces that are added to the equation of motion. Constraints are imposed limitations of the way of motion and can thus be used to reduce the DOFs.

Furthermore, OF provides control to support numerical stability of transient simulations via relaxation of the moving body's acceleration. An under-relaxation factor (`accelerationRelaxation`) can be employed to counteract the destabilising artificial added mass effect, stated above. While some have worked on various tightly coupled fluid and solid solvers [259, 264, 266, 267], others have achieved sufficiently stable solution processes with the utilization of under-relaxation. The required relax-

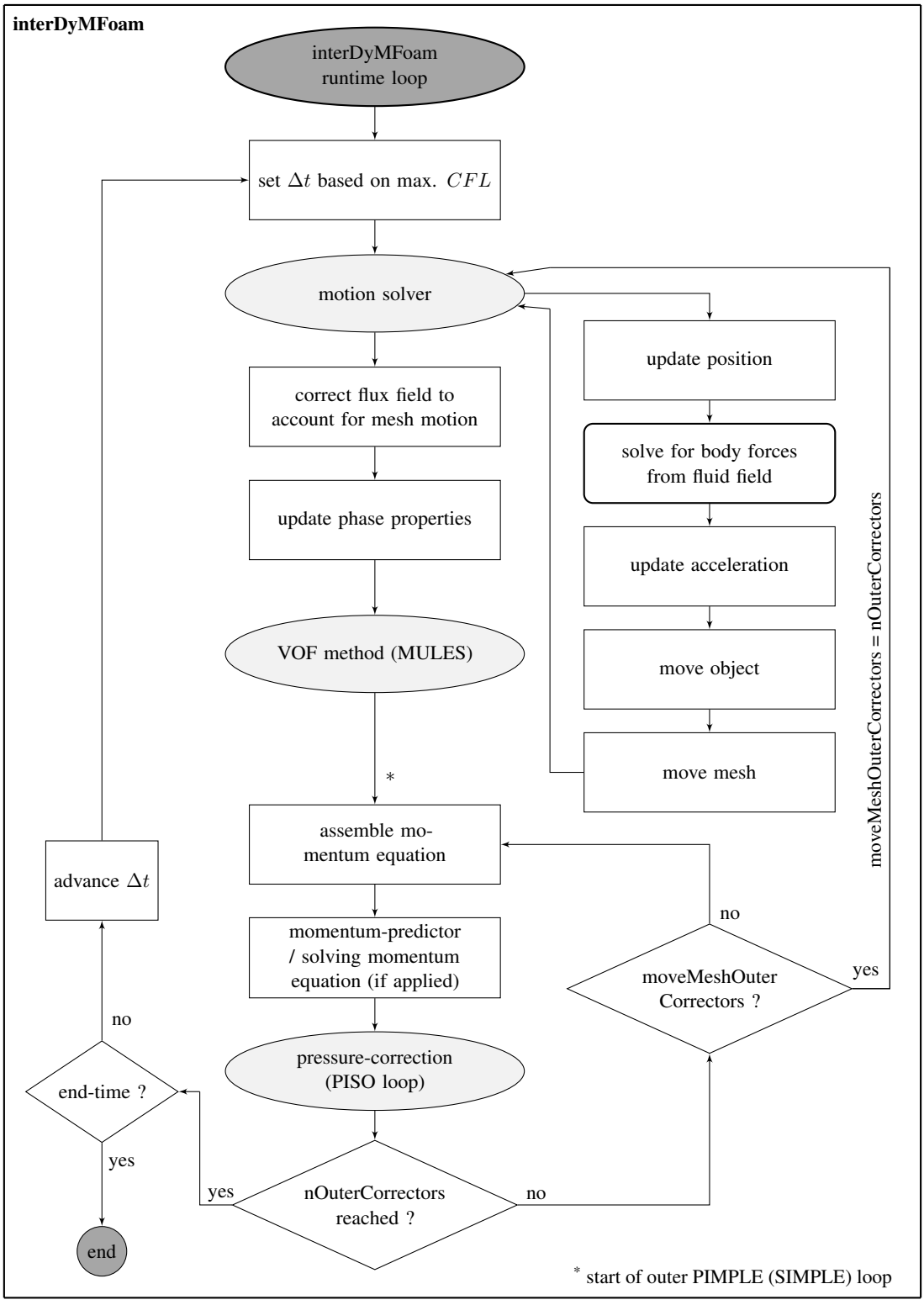

Figure 2.13: The `interDyMFoam` (and also `olaDyMFlow`) algorithm flow chart. Details of the VOF and PISO sub-routines are shown in the algorithm flow chart of `interFoam` in Fig. 2.5.

ation factor is problem-dependent. Brown et al. [257] have achieved stability of a floating WEC in focused waves with a relaxation factor of 0.9; Ransley et al. [256] successfully used a factor of 0.7 for wave interaction with a point-absorber WEC; and Bruinsma et al. [258] used 0.5 for wave interaction with a semi-submersible FOWT platform.

Moving Boundary Condition As part of the coupled solution process, the fluid solver needs the updated velocity BC of the moving structure. Therefore, a specific velocity condition is applied at the solid boundary of the body by means of a moving wall with a no-slip condition. All other BCs are identical to the models with static structures.

2.6 Mooring Line Modelling

Moorings of marine renewable devices and structures can be categorized into two main types, catenary and taut lines. Both exist in variations, where the former can be combined with buoys and clump weights and the latter can be taut spread or vertical. The effects and forces on the mooring lines include compliance, inertia, resistance and possible seabed interaction and snap loads [268]. Mooring line compliance includes structural elasticity and geometrical flexibility [268]. Taut lines work mainly by elastic stretching, whereas slack lines by their geometric straightening. Mooring line inertia includes the lines' structural mass and hydrodynamic added mass. Mooring line resistance includes hydrodynamic drag, VIV and structural damping due to internal friction.

Mathematical and numerical representation of moorings can vary in terms of model

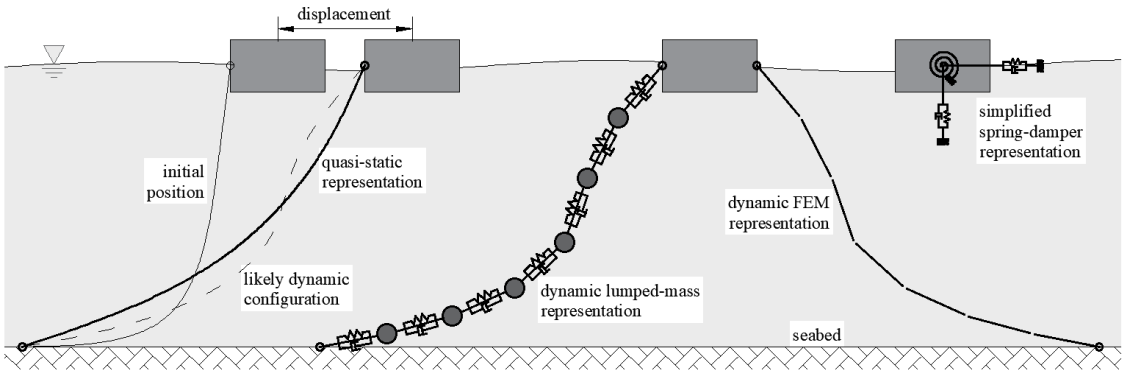

Figure 2.14: Options of mooring line representation and their relative fidelity. Combined and modified from Davidson and Ringwood [268], Paredes et al. [269] and Hall and Goupee [270].

fidelity and complexity. For transient modelling of fluid-structure interaction (FSI) processes, the possible options are a dynamic, a quasi-static or a spring-damper mooring representation. These are depicted in Fig. 2.14 and described in the sections below.

2.6.1 Dynamic Representation

Dynamic methods capture all or most of the above stated effects. With dynamic methods, the mooring lines are discretised and their dynamic response is evaluated. The two main discretisation methods are the lumped-mass and the FEM method. The former approximates the mooring lines with a number of lumped masses that are internally connected with a spring and damper each. The dynamic interaction among all acting forces is evaluated transiently. This method is implemented in the open-source application MoorDyn by Hall and Goupee [270]. A FEM approach is used in the open-source code Moody by Palm et al. [31, 271, 272] where a discontinuous Galerkin method with high-order Legendre polynomial expansion bases is utilized. Both MoorDyn and Moody are external stand-alone solvers that can be coupled to a fluid or hydrodynamics solver such as OF. The coupling can be strong or weak [268], which relates to the number of iterations between the solid and fluid solver.

Due to their high fidelity, these methods are computationally the most expensive. They are mainly needed for carrying out stochastic dynamic analysis and reliability design of mooring cables. Hoeg and Zhang [273] have used the lumped-mass method to investigate the former for FOWT interactions. The FEM method has been used for catenary moored structures such as general floating objects, done by Aliabadi et al. [274], for spar-type FOWTs, done by Jeon et al. [275], and for WECs, done by Palm et al. [31]. The latter used their Moody code for the analysis.

2.6.2 Quasi-static Representation

Contrary to dynamic methods, quasi-static approaches assume that hydrodynamic and inertia effects can be neglected [268] and that the line profile can be reasonably well described by a catenary equation at all times [276]. The catenary equation, for instance by Huse [277], Liu and Bergdahl [278] or Bauduin and Naciri [279], determines the shape, tension and restoring force of the mooring lines dependent on the relative position of the attachment points. For each time step, the force is applied to the structure as a spring or spring-damper force.

This method is computationally cheap and is suitable fo preliminary design studies or when nonlinear effects are insignificant. In the context of FOWTs this method has been used for spar-type platforms [230, 280] and semi-submersible platforms [75, 249, 281–283].

For conditions that exceed the underlying assumptions of a quasi-static approach, such as in extreme load situations or where the size of the structure is small in relation to the wave size (e.g. WECs), a dynamic representation may be needed to sufficiently capture the WSI.

2.6.3 Simplified Spring and Damper Analogies

The simplest option is to use one or multiple restoring forces by means of springs and dampers. Dependent on the specific wave-mooring-structure interaction, linear and nonlinear spring and/or damping forces can be used to represent the mooring line effects. This method requires the smallest computational demand and is suitable for initial designs or for body motions with reduced number of DOFs.

Previous works that have used linear springs are for instance CFD simulations of WECs by Ransley et al. [73], Coe et al. [226] and of a FOWT by Hoeg and Zhang [273]. Nonlinear springs have been used by Li et al. [284] to simulate a hydro-elastic fish cage. Leble and Barakos [65] have used sets of springs and dampers to simulate the dynamics of a semi-submersible FOWT with the SPH method.

2.7 Summary

Literature that covers all required aspects to model the present WSI problem has been reviewed. This has covered

- possible options of numerical approaches in terms of governing equations,
- numerical solution methods and corresponding numerical aspects such as discretisation principles,
- specifically required boundary conditions (BCs) to represent a numerical wave tank (NWT) such as wave modelling techniques,
- the representation of thin perforated structure with a focus on a macro-scale representation,
- the concept of rigid body motion and possible dynamic meshing methods, and
- options of mooring line representation.

The representation of thin perforated structures has been identified to be the key aspect of this thesis. A suitable macro-scale representation employing a pressure-drop within a NS-based CFD framework overcomes the limitations of both models with both lower

and higher fidelity. It allows a wider range of wave conditions compared to potential-flow models and is less computationally demanding compared to a micro-scale CFD approach with an explicit geometry resolution. Thus, the research need lies in the identification of a suitable macro-scale representation, the establishment of an optimal setup with it, the implementation of missing functionalities into OpenFOAM (OF), and the thorough validation of the proposed method.

All other aspects are required to generate a reliable and accurate NWT but are not directly addressed by this work. Key capabilities such as wave modelling methods or mooring line models are readily available. Here, the importance lies in their appropriate usage rather than development.

Chapter 3

Methodology

3.1 Introduction

Based on the literature review, this chapter explains the decision-making process and the validation strategy taken to address this work's aim. This covers the recall of the requirements that the present work builds on, the sequential decisions made in terms of governing equations, wave modelling, mooring representation, dynamic meshing and the overall strategy taken to validate the method and modelling. All points are explained in the following sections, an overview of this methodology is given in Fig. 3.1.

Since not all required functionalities are readily available, code development has been necessary. The requirements and modifications are explained in Section 3.4, and the newly developed capabilities have then been used in Chapters 6 -7 for the validation of the macro-scale method.

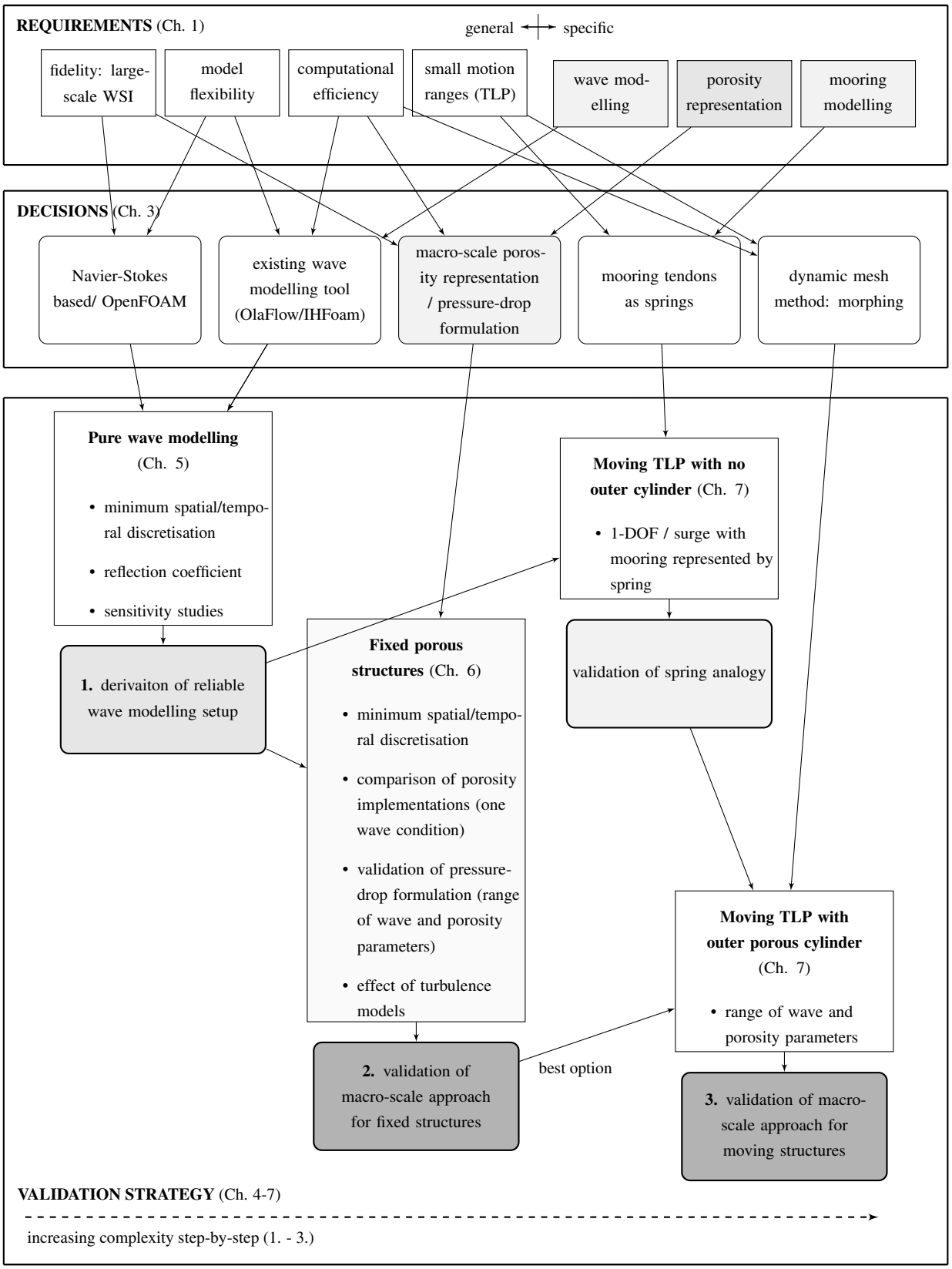

Figure 3.1: Chart of the methodology of this thesis, including decision procedures and the validation strategy.

3.2 Decision Process

Based on the determined requirements in terms of accuracy, flexibility and efficiency as stated in Chapter 1 and the specific experimental data that was available for model validation, the following decisions have been made. The experimental conditions will be introduced in Chapter 4.

3.2.1 Using CFD with OpenFOAM

In consideration of the high-level goal to simulate wave interaction processes of FOWTs, it has been clear that a CFD approach using the Navier-Stokes equations can provide the greatest level of fidelity and flexibility. It can overcome the limitations of simpler models based on potential-flow theory, see Section 2.2.1. Among possible NS-based CFD codes, OpenFOAM (OF) appeared to be the best option for the present case due to a number of reasons. From a general point of view,

- it is open source and its code can therefore be adapted and extended,
- most functionalities are already available and extensively validated,

and regarding specific requirements,

- toolboxes for wave modelling are openly available,
- macro-scale porosity implementations for volumetric granular materials are implemented in those tools, and
- turbulence models tuned for wave propagation are freely available.

Thus, a valuable basis exists that can be used and modified in order to implement the presently required functionalities.

3.2.2 Wave Modelling Method

Considering the relevant literature it has been concluded that all existing wave modelling techniques are applicable in general and could be used in this work. In particular, the toolboxes OlaFlow/IHFoam and waves2Foam are readily available and have been used and validated extensively. Considering the present conditions, OlaFlow/IHFoam with its implemented static boundary technique and active wave absorption (AWA) method has been considered as most promising due to the following considerations.

- The computational cost is deemed to be the smallest among all methods, mainly because the boundaries are static and do not require moving mesh support which would increase the computational effort significantly. Furthermore and compared to passive methods which require an extended domain, the domain can be kept small leading to a smaller number of mesh cells.
- The AWA method can optionally be combined with cell-stretching to accommodate for irregular wave input or to improve the absorption levels for breaking waves if required.

Based on the `interFoam`-framework, OlaFlow/IHFoam's wave modelling capabilities are executed at the wave generation and absorption boundaries. Its adaptive BC correction is applied to the phase-fraction (α)- and velocity ($\boldsymbol{u}$)- fields based on ad hoc measurements at the boundary. The algorithm flow chart in Fig. 2.5 shows the correction steps for α in the VOF sub-cycle and for $\boldsymbol{u}$ in the PISO loop. It is noted that in the initial version of OlaFlow/IHFoam, the correction velocity profile was implemented based on shallow water theory ($h < \lambda/20$ where h is the water depth and λ is the wavelength). In this so-called SW-AWA, a constant velocity profile is applied as outlined in Fig. 2.7. As this does not account for the variable velocity profiles for intermediate ($\lambda/20 < h < \lambda/2$) and deep water ($h > \lambda/2$) wave ranges, which are also shown in Fig. 2.7, the performance of the SW-AWA decreases with increasing water depth. An improved version that enables the use of a more general formulation for any water depth, referred to as extended range AWA (ER-AWA) was released by Higuera [137] in 2019. This enhanced formulation is only applied at the pure absorption boundary. Still, at the generation boundary a constant velocity profile is assumed for absorption.

3.2.3 Porosity Representation

In regard to the required accuracy levels and the main interest on large-scale WSI effects such as forces and motions, a macro-scale porosity representation has been used instead. Both OlaFlow/IHFoam and waves2Foam provide a porous media implementation in combination with the VOF interface capturing method as part of their application solvers. The former uses isotropic porous media (implemented as a scalar field) and the latter uses anisotropic porous media (implemented as a tensor field). Both are suitable starting points for the present work.

Pressure-drop Formulation

Apart from the numerical implementation, the formulation of the pressure-drop source-term is of key importance. The objective here is to use a suitable theoretical formulation to avoid calibration procedures or experiments to derive coefficients, which were required in the approaches by Shim et al. [5] and Chen and Christensen [4] for simulations of fluid interaction with fish nets. As stated in Section 2.4.1, the pressure-drop across a thin perforated barrier, Δp, equals a drag force. Viscous and inertial losses can be neglected and therefore, viscous and transient losses are assumed to be zero in this work. The coefficients of the linear and transient term, a and c, in (2.35) are both set to zero and the pressure-drop is formulated as:

$$\Delta p = \frac{\rho C_f}{2} \boldsymbol{u} \left| \boldsymbol{u} \right|, \tag{3.1}$$

where C_f is the porosity drag coefficient. Following the excellent results that Mackay et al. [41] have achieved for their linear potential-flow model with the use of C_f as formulated by Molin and Fourest [34], (2.37), and with a discharge coefficient of $\delta = 0.5$, the same approach is adopted in this work.

Force on the porous Structure

In the general case of a solid structure, the total force on it is the sum of the pressure drag force and the viscous drag force. The former is evaluated by integrating the normal stresses in each point over the whole boundary. The latter, also called skin-friction drag, is calculated by integrating the tangential shear stresses over the boundary. To note, skin-friction is only included in a CFD model when the boundary is set to a no-slip condition. This has previously been introduced in the context of BCs in Section 2.2.6.

In the specific case of a perforated structure represented by its macro-scale effects, additional momentum resistance is applied at the porous region or baffle, but no actual boundary exists in the model. Consequently, it is not possible to calculate the viscous forces on the porous structure at all. The viscous friction force is neglected and only the pressure drag force can be assessed by default. The latter can be calculated for the thin porous structure as with an impermeable structure with a solid boundary. Here, the force on the porous structure equals the pressure-drop across it. It can be evaluated with pressure integration on two internal cyclic patches that represent the front and the back of the porous zone or baffle.

For the present conditions where large-scale effects are of the main interest, viscous drag has insignificant effect on the overall force. Thus, it is sufficiently accurate to

neglect its contribution in this work. The validity of this assumption for the present simulations is demonstrated in Chapter 6. It has to be highlighted that this assumption does not hold for cases with significant viscous drag. If viscous drag is important and has to be taken into account, a macro-scale approach is potentially not accurate enough and a different approach may need to be adopted.

3.2.4 Body Motion and Mooring

The present work focuses on simulating wave interaction with a TLP. Since TLPs have vertical tethers that provide a relatively large stability, the motion of a TLP is arc-shaped with small motion ranges [285, 286]. Surge dominates over little pitch and negligible other ways of motion [8]. The experimental tests by Mackay et al. [42] have confirmed that surge is clearly the dominant mode of the TLP motion for the present specific platform geometry. Consequently, it has been decided to reduce the complexity of the CFD model to 1-DOF body motion in the horizontal x-direction. In this context, it is considered to be sufficient to neglect all inertia, drag, dynamic and VIV effects and to represent the mooring line effects simplistically with a horizontal restoring force by means of a linear spring. This is one kind of specific simplification as introduced in Section 2.6 which is solely applicable to the present conditions and characteristics of the wave-TLP interaction. It cannot be generalized and for other cases a different approach might need to be taken.

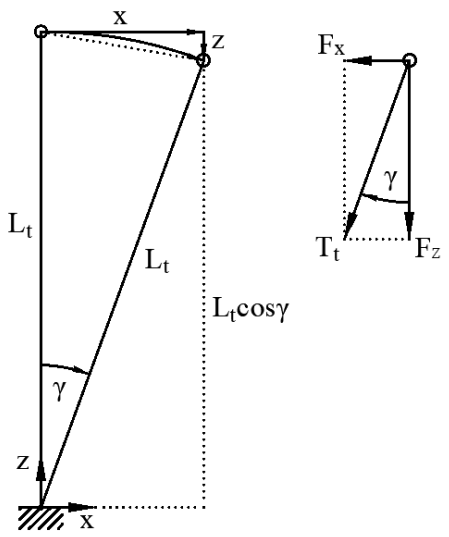

Figure 3.2: The applied simplified mooring configuration where the three mooring tendons are represented by one quasi-tendon.

The present approach is similar to the approach taken by Mackay et al. [42] who used a numerical BEM model [287] to investigate the hydrodynamic response of TLP FOWT

with and without a porous outer column. With this approach, all three tendons are represented by one quasi-tendon with central attachment points, both at the structure and the flume bottom. As outlined in the sketch of the configuration in Fig. 3.2, L_t is the mooring tendon length, T_t the tendon tension, x the horizontal (surge) displacement and $z = L_t(1 - cos\gamma)$ is the vertical (heave) displacement of the structure. Given the large axial tendon stiffness the tendons (and the quasi-tendon) are assumed as inextensible. With γ as the angle of the quasi-tendon to the vertical, the horizontal component of the restoring force due to all three tendons is:

$$F_x = T_t sin\gamma = T_t \frac{x}{L_t}, \tag{3.2}$$

and the vertical component is:

$$F_z = T_t cos\gamma = B - Mg, \tag{3.3}$$

where B is the buoyancy and M is the mass of the structure. The buoyancy of the structure is defined as:

$$B = \rho_w V_m g + S_h z, \tag{3.4}$$

where ρ_w is the water density, V_m is the mean displaced volume and S_h is the heave hydrostatic stiffness. The latter is given as:

$$S_h = \rho_w g A_a, \tag{3.5}$$

where A_a is the water-plane area. Substitution of (3.4) into (3.3) results in a function for the total tendon stiffness, given as:

$$T_t = \frac{(\rho_w V_m g - Mg) + S_h z}{\cos\gamma}, \tag{3.6}$$

where

$$T_{t0} = \rho_w V_m g - Mg \tag{3.7}$$

is the total tendon pretension that accounts for all mooring tendons. Substitution of

(3.6) into (3.2) and rearrangement gives:

$$F_x = (T_{t0} + S_h L_t(1 - \cos\gamma))\tan\gamma, \tag{3.8}$$

and with expression of z and $\tan\gamma$ via x and L_t and the application of a Maclaurin series expansion further gives:

$$F_x = T_{t0}\frac{x}{L_t} + (T_{t0} + S_h L_t)\left(\frac{1}{2}\left(\frac{x}{L_t}\right)^3 + \frac{3}{8}\left(\frac{x}{L_t}\right)^5 + ...\right). \tag{3.9}$$

This nonlinear expression resembles the nonlinear arc-shaped motion of the TLP model. Since this nonlinearity is relatively small, this work uses the linearised form of the horizontal restoring force and

$$F_{x,lin} = T_{t0}\frac{x}{L_t}, \tag{3.10}$$

respectively. Mackay et al. [42] concluded that the linear assumption by means of a linear spring can be a good approximation for surge amplitudes less than 100 mm for the present model scale of 1:50. However, the adequacy of this simplification for the present investigations has been reviewed in Chapter 7.

3.2.5 Dynamic Mesh Method

For the present specific case of small motion ranges of a TLP, the mesh morphing method is considered to be the most suitable method. It requires a reasonable computational demand and is deemed to be capable of dealing with the required motion ranges. The latter statement is supported by conclusions by Windt et al. [225] who have compared mesh morphing and overset meshing for large motions of a moored point-absorbing WEC. They found that both methods lead to the same results, with the overset method being significantly more costly.

In theory, the sliding mesh method could be used for most of the present dynamic models, too, where the motion has been constrained to 1-DOF. However, to have the option of a straight-forward extension to multiple DOF modelling, mesh morphing is chosen over the sliding method.

3.3 Validation Strategy

Based on the decisions made, the strategy to assess and validate the proposed approach of macro-scale representation of thin fixed and floating structures, is to increase the model complexity step-by-step. This is reflected in the sequence of the Chapters 5-7 on the CFD simulations and method validation, respectively. Each chapter informs the following chapter, beginning with pure wave modelling.

3.3.1 Wave Modelling

The basis for setting up a reliable CFD model to investigate WSI processes in a wave flume, is a sufficiently accurate wave modelling technique. Therefore, pure wave propagation in an empty flume is studied in Chapter 5. To obtain a reliable setup, the metrics for accurate wave replication and propagation have been identified and assessed in terms of spatial and temporal discretisation, wave reflection coefficients and sensitivity studies on crucial numerical settings. The best setup has been derived which has been used in the subsequent section on wave interaction with fixed thin perforated structures in Chapter 6.

3.3.2 Macro-scale Porosity

The pressure-drop formulation has been determined to be a drag force formulated by means of Molin's theoretical formulation, (2.37). Its applicability to the present context of thin perforated barriers is assessed extensively for fixed sheets and cylinders. The key points that are investigated are:

- the minimum temporal and spatial discretisation required to obtain converged results,
- the comparison of different types of macro-scale porosity implementation (with the same pressure-drop formulation) ,
- the validation of the pressure-drop formulation for a range of wave conditions and porosity values and
- the effect of the application of turbulence models.

Before the orthotropic porous-media implementation as introduced in Section 2.4.2 could be assessed for the bottom-fixed cylinder model, a cylindrical coordinate transformation was required as a new capability. The principles are introduced below in Section 3.4.1.

The different types of porosity implementation (the baffle, isotropic and orthotropic porous media) are compared in terms of the force, wave elevation and velocity profile results. The effect of the application of the k-ω-SST and Larsen and Fuhrman [166]'s stabilized k-ω turbulence model is assessed in combination with the various porosity implementations. The former model is selected since it is a widely implemented model with a long validation history. The latter is regarded to be the most suitable model for wave propagation since its enhancement is based on the resolution of the fundamental problem of spurious turbulence generation of two-equation models in potential-flow wave propagation, see Section 2.3.3. Also the computational runtimes and numerical stability of all models are assessed to identify the best method for the present conditions. The outcome of the assessment for static porous structure then informs the extension to the moving TLP with outer perforated cylinder in Chapter 7.

3.3.3 Moving porous Structures

In the subsequent work, the method is extended to simulate wave interaction with a TLP with and without an outer porous cylinder that is restricted to surge motion only (Chapter 7). First of all, the adequacy of the simplified mooring representation by means of a spring has been assessed for the TLP model with no outer porous cylinder. Then, the mesh morphing capabilities have been analysed as follows.

OlaFlow has built its application solver for moving bodies, `olaDyMFlow`, on top of `interDyMFoam`. Therefore, the algorithm is identical but the governing momentum equations differ. As introduced in Section 2.4.2 for the static porosity solver, the moving solver utilizes a macro-scale porosity implementation by means of using the intrinsic velocity and momentum source terms.

However, the mesh morphing inside `olaDyMFlow` only works for impermeable moving structures in combination with static porous structures only. In the case of wave interaction with a solid TLP with outer porous shroud, the body motion solver would lack the contribution of the force on the porous shroud. This would lead to an incorrect motion response although the rest of the algorithm would work as implemented. Consequently, code development has been necessary to include the force on the porous part of the structure as a new capability. The principles are introduced below in Section 3.4.

3.4 Code Development

The code modifications and extensions that are required to use the orthotropic porosity implementation for a cylindrical shape and to use the macro-scale porosity representa-

tion for moving (thin perforated) structures are explained in this section. The detailed code can be found in Appendix C.

3.4.1 Orthotropic Porosity for Cylinder Model

The functionality to represent the thin perforated cylinder by orthotropic porous media was not readily available and had to be addressed.

Status quo

Waves2Foam's porosity implementation incorporates an orthotropic porous media implementation where the porous media is represented by a tensor field that aligns with the global coordinate system in x-, y- and z direction in all cell points. In other words, the pressure-drop is specified to be constant and with the same direction within a region of porous media. Within the application solver, this is coupled with the passive relaxation wave modelling method, as introduced in Section 2.3.

Required Functionality

In order to apply the pressure-drop in normal direction to the cylinder surface, the orthotropic porosity implementation needs to be directed cylindrically. The input to the model should remain to be a single porosity tensor, $\boldsymbol{C_f}$, that is then applied in cylindrical direction dependent of the cell location. Furthermore, the capability of using the static boundary wave modelling method of the OlaFlow/IHFoam libraries has to be maintained.

Code Modifications

Therefore, the porosity solver of waves2Foam and OlaFlow/IHFoam's wave libraries have been combined into a custom application solver, named `poroWavesFoam` into which a transformation between the local cylindrical coordinate system (radial, tangential, vertical) and the global Cartesian coordinate system has been implemented so that $\boldsymbol{C_f}$ is applied correctly. Therefore, transformations from the local polar coordinates (e_θ, e_r, e_z) to local Cartesian coordinates (e_1, e_2, e_z) and further to global Cartesian coordinates (e_x, e_y, e_z) have been introduced to adjust $\boldsymbol{C_{flocal}}$ to $\boldsymbol{C_{fglobal}}$. Figure 3.3 outlines the relation between the respective coordinate systems. The transformation

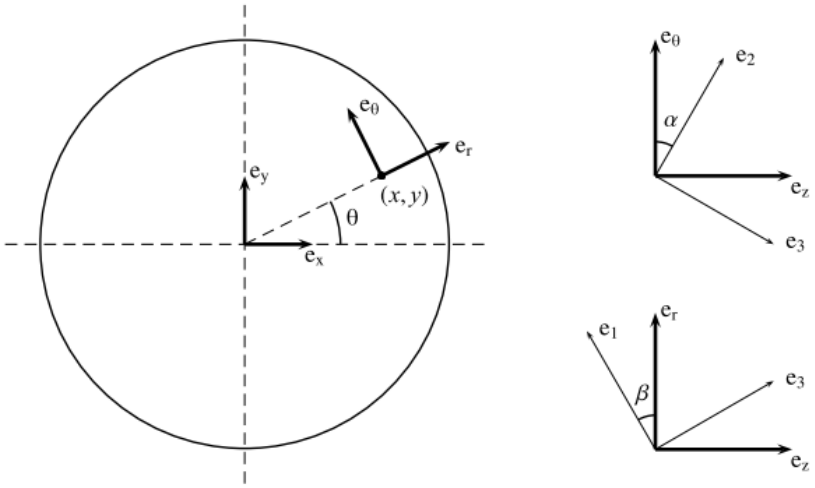

Figure 3.3: Schematic of the relation between the local polar (e_θ, e_r, e_z), the local Cartesian (e_1, e_2, e_z) and the global Cartesian (e_x, e_y, e_z) coordinate system. Taken from Hafsteinsson [205].

matrix for rotation around two axes is specified as

$$\boldsymbol{TR} = \begin{pmatrix} \cos\theta & -\sin\theta & 0 \\ \sin\theta & \cos\theta & 0 \\ 0 & 0 & 1 \end{pmatrix}. \tag{3.11}$$

The transformation from cylindrical to local Cartesian coordinates gives an intermediate result of

$$\boldsymbol{C_{finterm}} = \boldsymbol{TR}\boldsymbol{C_{flocal}}\boldsymbol{TR}^T, \tag{3.12}$$

and the transformation from local to global Cartesian coordinates gives the required result of

$$\boldsymbol{C_{fglobal}} = \boldsymbol{TR}\boldsymbol{C_{finterm}}\boldsymbol{TR}^T, \tag{3.13}$$

The equations (3.11) - (3.13) are implemented so that the tensor field of the porosity coefficient, $\boldsymbol{C_f}$, is set based on the coordinates that define the cylinder axis. Details of the implemented code are presented in Appendix B.2.

3.4.2 Correct Body Motion including Porosity

For the moving TLP model, code extension has been required to include the force on the porous part of the structure and to guarantee correct body and mesh motion.

Status quo

As introduced in Section 2.5.3, the coupled rigid body motion and mesh morphing motion consists of three main aspects: the body motion, the mesh adaptation and the fluid flow. Here, the default 6-DOF solver calculates the fluid forces by means of pressure integration at the boundary of a moving solid structure. The used boundary patches have to be specified in the `dynamicMeshDict` under the keyword `patches`. Moreover, these specified boundary `patches` are not only used as input for the body motion solver but also for the two following steps in the course of the mesh motion algorithm. The interior mesh point displacement follows from the displacement of the boundary patches and are determined by a displacement field. Furthermore, the same boundary patches determine the BCs for the actual PDEs being solved by the fluid solver routine. In other words, all three aspects (body motion, mesh motion and fluid solution) are coupled with the same patch specification. Their sequential execution is shown in the `interDyMFoam` algorithm flow chart in Fig. 2.13.

Required Functionality

Since the default solver does not consider the forces on the porous elements of the structure, this needs to be included to correctly model wave interaction with a TLP with an outer porous shroud. Therefore, the calculation of the forces on the porous structure parts needs to be added and linked to the 6-DOF body motion solver. Only pressure forces (and no skin-friction forces) can be accounted for (Section 3.2.3), however, due to the nature of the porous media implementation.

The required adaptations do not concern the definition of the patches for the mesh morphing routine and the BC for the fluid solver. These can remain specified with solely the solid boundary. Furthermore, the porous part of the structure automatically imposes its porosity momentum resistance during the transient FSI process. The main thing to consider in the setup, is that the inner distance of the mesh motion routine needs to be specified outside the whole structure (outside the porous part) to ensure that the mesh does not get morphed in regions where porosity is applied.

Code Modifications

To include the required functionalities, the existing `libsixDoFRigidBodyMotion.so` library is duplicated and extended to `libsixDoFRigidBodyMotionPor.so`.

The calculation of the force on the porous part of the structure is implemented without interfering with the `patches` specifications for the mesh morphing procedure and fluid solver. Therefore, separate patch specifications for both the solid and the porous part have been introduced with the keywords `patchesSolid` and

`patchesPorous`. The request for its specification in the simulation is introduced in the `dynamicMeshDict` and the force calculation on both the solid and the porous patches is included in the existing force calculation routine.

The total force on a boundary, $\boldsymbol{F} = \boldsymbol{F_p} + \boldsymbol{F_v}$, comprises of normal pressure, $\boldsymbol{F_p}$, and tangential viscous contributions, $\boldsymbol{F_v}$, calculated by integration over the cell faces i with

$$\boldsymbol{F_p} = \sum_i \rho_i \, \boldsymbol{s}_{f,i} \, p_i \tag{3.14}$$

and

$$\boldsymbol{F_v} = \sum_i \boldsymbol{s}_{f,i} \cdot \mu \, \boldsymbol{R_{dev}}, \tag{3.15}$$

respectively, where $\boldsymbol{s}_{f,i}$ is the face area vector. Then the total moment can be calculated about a specified moment centre, A_M:

$$\boldsymbol{M_{A_M}} = \boldsymbol{r}_{A_M B_F} \times \boldsymbol{F}, \tag{3.16}$$

where B_F is the force origin and $\boldsymbol{r}_{A_M B_F}$ is the moment vector. Equations (3.14) - (3.16) were already implemented for the calculation over cell faces of solid boundary patches (`patchesSolid`), i_{solid}, and have additionally been implemented for the calculation over cell faces of porous boundary patches (`patchesPorous`), i_{porous}, so that

$$\boldsymbol{F_{tot}} = \boldsymbol{F_{solid}} + \boldsymbol{F_{porous}} \tag{3.17}$$

and

$$\boldsymbol{M_{tot}} = \boldsymbol{M_{A_M\,solid}} + \boldsymbol{M_{A_M\,porous}}. \tag{3.18}$$

$\boldsymbol{F_{tot}}$ and $\boldsymbol{M_{tot}}$ are then added to the vector of external forces and moments, $\boldsymbol{F}$, in the equation of motion, (2.45), see Section 2.5. This means that the force on the porous part is added to the 6-DOF force balance and linked to the 6-DOF body motion solver. Thus, for the calculation of the body acceleration and the subsequentially new body position, the contribution of the porous structure parts are taken into account, and correct WSI is provided. Looking at the `interDyMFoam/olaDyMFlow` algorithm flow chart in Fig. 2.13, the modifications refer to the motion solver sub-step "solve for body forces from fluid", which is indicated by a rectangular box with round edges. The corresponding code modifications are presented in Appendix C.

3.5 Summary

This chapter has presented the methodology for this thesis. It lays out the decisions made in all key modelling aspects, the strategy taken to assess the proposed method of macro-scale porosity modelling and the contributions made in terms of code development. The decisions and the strategy are the basis for the Chapters 5-7 where the detailed assessment and method validation will be presented.

Chapter 4

Data Analysis Concepts and Reference Data

4.1 Introduction

Before the detailed assessment is presented in the following Chapters 5-7, all reference data and data analysis concepts used in this thesis, such as sampling, verification and validation principles, are introduced in this chapter. The reference data includes experimental results and results from a linear potential-flow model, introduced below.

4.2 Sampling and Analysis

The critical validation parameters in this thesis, which mostly correspond to the available experimental data, are velocity profiles along the water column, isosurfaces and gauges of the free water surface, forces on structures and body motions. Those parameters are sampled over time and both the transient behaviour and the mean values are analysed. The transient behaviour is directly assessed by means of the comparison of the time series of the CFD and experimental results.The mean values are mainly used to compare the CFD results against the results from the potential flow model (which operates in the frequency domain instead of the time domain).

To obtain a reliable mean value, a periodically steady state of the sampled signal is required. Inspired by Vukčević [112]'s approach to assess the uncertainty associated with simulating a fixed number of wave periods, this work uses two indicators to estimate the beginning of the periodically steady state of a signal: the moving mean with a sliding window length of at least one wave period, and the mean of the peaks as the average of the top and bottom envelopes of the signal.

The initial time series section has been cut off at a point in time after the running and peak means have achieved a quasi-steady state. If possible, the time series have also been cut-off at the point in time when the waves have travelled across the NWT, been reflected at the opposite tank end and then travelled back to the tank centre or position of any object. This is only applicable to short waves where the section of time series without reflected waves is long enough. Since most waves are longer and travel faster, their time series do include reflected waves in order to achieve a representative mean value (of at least 10 periods). The actual effect of reflected waves on the results will be assessed in detail in Chapter 5. After cutting off the initial transient period and (if possible) the section that includes wave reflections, the remaining quasi-steady signal section was cropped into a whole number of periods. To conform with the mean calculation used for the processing of the experimental data, the mean amplitudes have been calculated using the standard deviation, σ, of the signal, which is valid for sinusoidal signals. For instance, the mean wave amplitude, A, can be obtained by:

$$A = \sqrt{2}\sigma(\eta(t)), \tag{4.1}$$

where $\eta(t)$ denotes the transient free surface or wave elevation at a certain location in the NWT. This procedure is illustrated by an example of a time series of the wave elevation, $\eta(t)$, of wave condition A02 (see Table 4.1) at WG B2 at the tank centre of a 2D NWT (see Fig 5.1). Figure 4.1 shows the signal $\eta(t)$, the envelopes of the signal's peaks (both the wave crests and troughs), the input amplitude $A_{input}^{StokesII}$, the mean of the signal's peaks and the signal's moving mean. The vertical dashed red line indicates the point in time, $t = 36.27$ s, when the reflected wave reaches the tank centre for the second time. The dark-grey area defines the section of the time series that is used to calculate the mean amplitude, A. This section begins after the initial transient period, characterised by a nearly steady behaviour of both peak and running mean, does not contain wave reflections and consists of 10 periods. However, for most other wave conditions, the processed signal section contains wave reflections since the wave length is very long in relation to the tank length. The section contaminated with reflections is indicated by the light-grey shaded area.

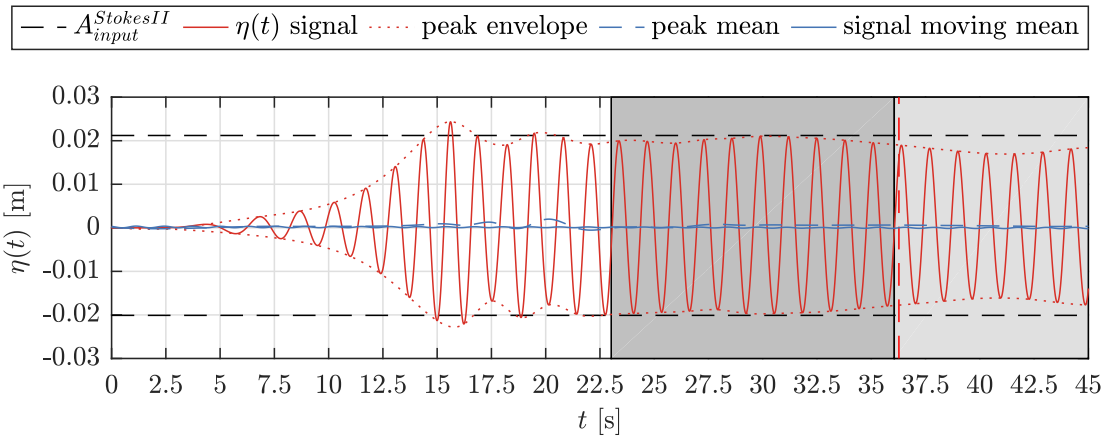

Figure 4.1: Wave elevation of wave condition A02 over time, $\eta(t)$, at the tank centre at WG B2. All relevant aspects that outline the analysis procedures are indicated in the figure.

4.3 Verification and Validation

The verification and validation in this thesis follow definitions and concepts as in Roache [288], Stern et al. [289] and Eça and Hoekstra [290]. Accordingly, the sources of errors and uncertainties of results from CFD simulations are divided into two distinct parts: numerical and modelling sources.

The estimation of numerical errors and uncertainties is referred to as verification. It is defined as a purely mathematical procedure to check whether the model is correctly implemented in the code and that the "equations are solved right" [288]. This includes the errors and uncertainties due to numerical schemes, iterative solution methods and parameter specifications such as discretisation settings [289]. The estimation of modelling errors and uncertainties is referred to as validation. It is defined as an assessment of the used modelling concepts and whether "the right equations are solved" [288]. Principally, validation is performed as comparison of CFD results against experimental data to assess how well the model represents reality.

Within this work, quantitative verification and validation focuses on the mean values of the CFD results by means of discrete data points. This mainly concerns mean wave amplitudes, A, and mean force amplitudes, F, from the parameters of interest stated above. Time-series results are compared qualitatively.

4.3.1 Error and Uncertainty

Error is defined as the difference between the CFD (or experimental) solution and the exact solution. It has a sign and can be absolute or relative. As absolute value it can be

written as:

$$E_{abs} = S_2 - S_1 \tag{4.2}$$

and as relative value as:

$$E_{rel} = \frac{S_2 - S_1}{S_1} \times 100, \tag{4.3}$$

where S_1 and S_2 are the two solutions being compared. Since the exact solution is rarely known, errors are estimated by means of uncertainties. Uncertainty can be considered to be an error estimate [289], has a plus-minus sign and describes an interval that contains the exact solution with a certain level of confidence.

4.3.2 Verification

Numerical errors can be divided into round-off errors, iterative errors and discretisation errors. The former two concern a computer's finite precision and the non-linearity of the equations to be solved iteratively and have a relatively small effect. The most crucial error is the discretisation error as a result of the sub-division of space and time into finite parts.

The estimation of the discretisation error and its uncertainty calculation, respectively, is principally conducted by means of spatial and temporal convergence studies. Roache [288] introduced the most common approach to mesh convergence studies for steady-state simulations. Based on calculation of the ratio of solution change, R_S, of a specified parameter, S, the convergence behaviour is assessed and the numerical error and uncertainty can be estimated. R_S is defined as:

$$R_S = \frac{S_{fine} - S_{medium}}{S_{medium} - S_{coarse}}, \tag{4.4}$$

where S is the solution of any target value due to different meshes with a fine, medium and coarse resolution. The convergence behaviour can then be categorized (see e.g. Eça and Hoekstra [291]) into

1. monotonic convergence: $0 < R_S < 1$,
2. oscillatory convergence: $R_S < 0$ and $|R_S| < 1$,
3. monotonic divergence: $R_S > 1$ and
4. oscillatory divergence: $R_S < 0$ and $|R_S| > 1$.

Monotonic convergence is a prerequisite for the most common error and uncertainty estimation procedure developed by Roache [288]. The procedure is based on generalized Richardson-Extrapolation and safety factors are applied to obtain numerical uncertainties and the so called Grid Convergence Index (GCI), which is a uniform measure of grid convergence. However, the requirements for this method are the use of geometrically similar grids and that the meshes must be in the asymptotic convergence-range. For practical applications these are difficult to meet [289, 290], since oscillatory scatter is common.

Oscillatory behaviour also commonly occurs in most of the present convergence studies. Therefore, this thesis follows an approach for uncertainty estimation by Stern et al. [289], where the largest deviation among multiple solutions is used. Here, for oscillatory convergence, the uncertainty, U_{unc-i}, is defined as:

$$U_{unc-i} = F_s \cdot 0.5 \left| S_i^{max} - S_i^{min} \right|, \tag{4.5}$$

where the index i denotes the source of uncertainty such as wave reflection, numerical schemes or the time series window used for further processing. S_i^{max} is the maximum value and $S_i^{\min}$ is the minimum value of the target parameter which are obtained from a minimum of four meshes as advised by Stern et al. [289] and Eça and Hoekstra [290]. F_s is a safety factor which is often set to 1.25 [92, 288, 290, 291]. In the present work, F_s = 1.25 is used when a single uncertainty source is assessed. When multiple sources of uncertainty, U_{unc-i}, are added together to obtain an overall uncertainty, U_{unc}, F_s is reduced to 1.1.

In the case of multiple uncertainty sources, the overall uncertainty, U_{unc}, is obtained by:

$$U_{unc} = \sqrt{\sum_i \left(\frac{U_{unc-i}}{v_i} \right)^2}, \tag{4.6}$$

where v_i is the mean of the value range of each uncertainty source, defined as:

$$v_i = 0.5 \left(S_i^{max} + S_i^{min} \right). \tag{4.7}$$

4.3.3 Validation

The validation concerns the comparison of the CFD results against experimental results. The difference between a CFD solution, S_{CFD}, and an experimental solution, S_{exp}, can

be described by the comparison error [289]:

$$E_{comp} = S_{exp} - S_{CFD}. \tag{4.8}$$

To accurately estimate the uncertainty of E_{comp}, both the errors of the CFD and the experimental results have to be considered and estimated. For the error estimation of the CFD results, the concepts above have been applied as stated. Since the experimental campaign was not within the scope of this PhD, the error estimation for the experimental results could not be performed with the same level of detail due to the limited number of data sets. Instead, and as a simplified approach, the mean uncertainty of the experimental results has been calculated based on the mean value of a limited number of repeat tests where repeatability of the experiments was proven.

The uncertainties, calculated using (4.5) - (4.7), of both the CFD and experimental results have been incorporated in the results diagrams by means of error bars, later introduced in Chapters 5-7.

4.4 Experimental Data for Model Validation

The validation of the numerical model is focused on the comparison against experimental results. Mackay et al. [41, 42, 43] conducted experiments at Dalian University of Technology, China to study wave interaction with thin perforated structures. The wave flume used is 60 m long and 4 m wide, has a single piston wavemaker at one side and a sloped beach at the other end. The perforated structures investigated are bottom fixed vertical sheets and thin hollow cylinders, and a model of a TLP with and without an outer perforated cylinder. The aim was to assess the influence of a range of geometrical parameters and regular and irregular wave conditions on the forces on the fixed structures as well as the motion response of the TLP. Detailed information can be found in the stated papers. Only aspects that are relevant for the present numerical work are introduced in the following sections.

4.4.1 Wave interaction with perforated Sheets and Cylinders

For the experiments with the bottom-fixed structures, a vertical wall with a length of 13.20 m was positioned along the central tank section to split the tank into two separate test sections. One contained a vertical sheet mounted onto a rigid frame and the other one a cylinder model. The section with the sheet had a width of 1 m and the section with the cylinder a width of 3 m. Load cells were mounted at the bottom and top ends

of both structures. The flat sheets occupied the full width of the channel and full height of the water column. A water depth of $h = 1$ m was used. Figure 4.2 shows photos of the experiments for both the sheet and cylinder. An example of wave interaction with the porous sheet during the experiments in the flume is shown in Fig. 4.2a where one can see how the sheet is mounted onto the brown rigid frame. The configuration of the cylinder model in the empty tank is shown in Fig. 4.2b and during wave tests in Fig. 4.2c.

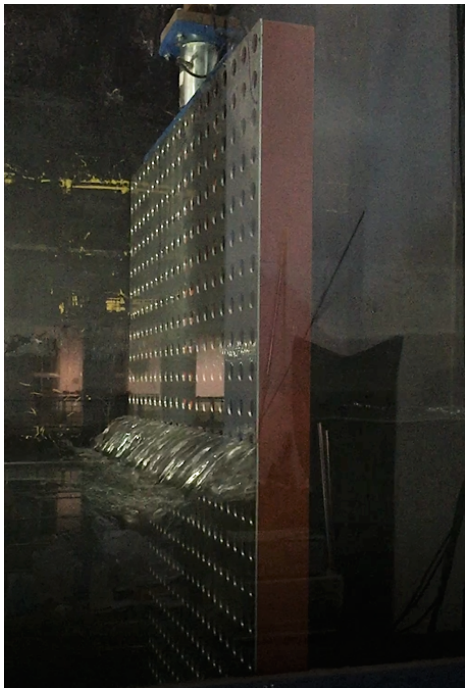

(a) Wave interaction with the sheet ($s = 5\,0$mm, $n = 0.2$).

(b) Cylinder model ($D = 0.5$ m, $n = 0.1$).

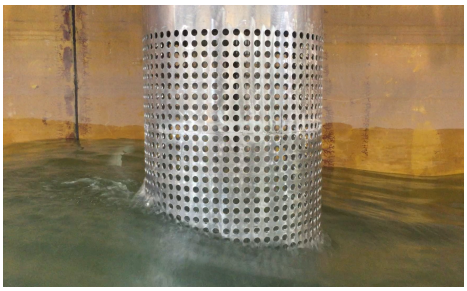

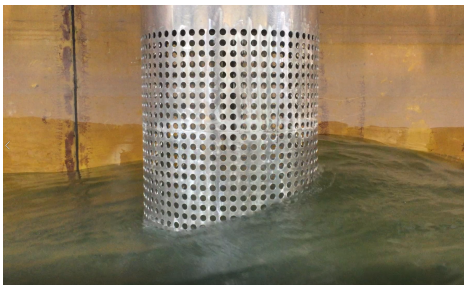

(c) Wave interaction with the cylinder model ($D = 0.375$ m, $n = 0.3$) for two points in time.

Figure 4.2: Photos of the experiments: (a) wave interaction with the perforated sheet, which is mounted onto a rigid steel frame (brown color) facing towards the wavemaker, (b) the cylinder model in the empty wave flume with the separation wall on the right (yellow) and (c) under wave interaction. The direction of wave propagation is from the left to the right in the case of the sheet and from the right to the left in the case of the cylinders.

The perforated sheets and cylinders had circular holes arranged in a regular square grid of side, s, and hole radius, r, such that the porosity, n, is defined by $n = \pi r^2/s^2$. In the experiments, a number of geometrical parameters such as sheet thicknesses (3 mm$\leqslant d \leqslant$ 10 mm), hole separation distances (25 mm $\leqslant s \leqslant$ 100 mm), outer cylinder diameters (0.375 m $\leqslant D \leqslant$ 0.750 m) and porosities ($0.1 \leqslant n \leqslant 0.4$) have been tested under a range of regular and irregular wave conditions.

For the CFD investigations, the number of investigated parameters has been reduced to a representative selection. This has been considered to be sufficient to validate the proposed macro-scale porosity approach. For extensive design studies, methods based on potential-flow theory with shorter execution times are more suitable. The geometrical parameters have been limited to the cases with the sheet and cylinder thickness of d = 3 mm, a cylinder diameter of D = 0.5 m and porosities of n = 0.1, 0.2 and 0.3, further described in Chapter 6 as part of the model setup. The wave conditions used in the CFD simulations are listed in Table 4.1. The input waves cover non-dimensional wave numbers of $0.61 < k_w h < 3.34$ and wave steepnesses of $0.05 \leqslant k_w A \leqslant 0.20$, where $k_w = 2\pi/\lambda$ is the wave number and A is the wave amplitude. All conditions listed in Table 4.1 were used for the 2D model with the porous sheet. For the 3D model with the porous cylinder, only a subset with $k_w A$ = 0.1 (B03-B06) was used.

Table 4.1: Regular wave conditions used for models with the sheet and cylinder (CFD model input / target parameters).

Index	T [s]	λ [m]	H [m]	$k_w h$ [-]	$k_w A$ [-]	c_g [a] [m/s]
A01	1.1	1.88	0.0300	3.34	0.05	0.86
A02	1.3	2.60	0.0413	2.42	0.05	1.08
A03	1.5	3.35	0.0533	1.88	0.05	1.31
A04	1.7	4.11	0.0654	1.53	0.05	1.56
A05	1.9	4.85	0.0772	1.30	0.05	1.77
A06	2.1	5.58	0.0887	1.13	0.05	1.96
A07	2.3	6.29	0.1001	1.00	0.05	2.12
A08	2.5	6.99	0.1112	0.90	0.05	2.25
A09	2.7	7.67	0.1221	0.82	0.05	2.36
A10	2.9	8.35	0.1330	0.75	0.05	2.45
A11	3.1	9.03	0.1437	0.70	0.05	2.53
A12	3.3	9.69	0.1543	0.65	0.05	2.60
A13	3.5	10.36	0.1548	0.61	0.05	2.65
B03[*]	1.5	3.35	0.1066	1.88	0.10	1.31
B04[*]	1.7	4.11	0.1307	1.53	0.10	1.56
B06[*]	2.1	5.58	0.1775	1.13	0.10	1.96
C03	1.5	3.35	0.2133	1.88	0.20	1.31
C04	1.7	4.11	0.2614	1.53	0.20	1.56

[a] group velocity [*] subset used for the 3D cylinder cases

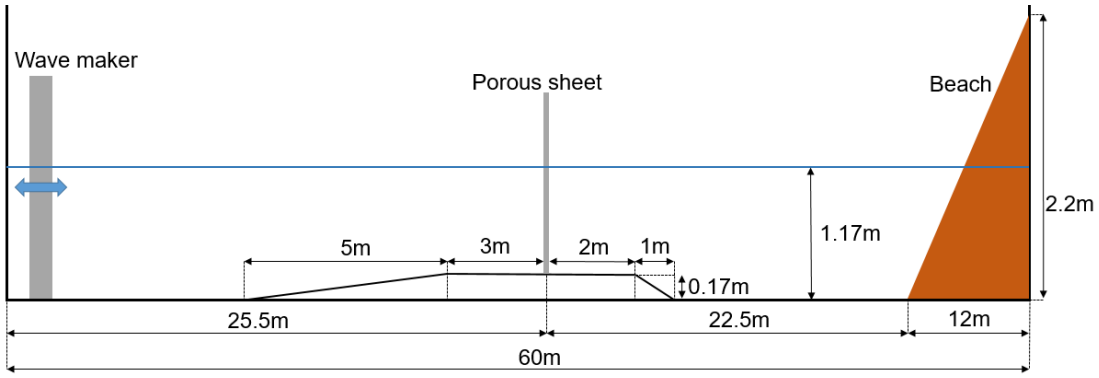

Figure 4.3: Sketch of the experimental tank including the sheet and the raised section of the floor. Not to scale.

The experimental data is suspected to be unreliable for the wave conditions A09, A10, A12 and A13 for both the sheet and cylinder tests for all configurations. For the sheet with a porosity of $n = 0.1$ the wave condition A05 is also suspected. For these conditions there is a large deviation between experimental results and numerical results from both the CFD and potential-flow model (see Fig. 6.34a). Possible reasons for the discrepancies are considered to be a raised section of the floor in the physical flume, potential resonance effects between the fluid and the structures, experimental errors or other unexpected physical phenomena.

A raised section of the floor was required to submerge load cells beneath the structures. The raised section had a total length of 11 m and the side facing the wave maker had a gentle slope, the height increasing over the first 5 m to 0.17 m above the tank floor, as shown in Fig. 4.3. The rear sloped section was 2 m in length and the central flat section was 5 m long. Below the structure, a water depth of $h = 1$ m was maintained (next to the raised floor the water was 1.17 m deep). In order to assess potential interaction effects of the raised floor, simulations with the potential-flow (BEM) model by Mackay et al. [41] and the present CFD model were performed with and without the raised floor. Particularly, the CFD model was expected to be capable of picking up related physical phenomena. However, both the BEM and and CFD simulations resulted in indistinguishable results of the WG and force signals between the models using the two different floor geometries. Since the numerical result did not support the hypothesis on the floor causing interactions, a flat bottom was used for all following CFD models.

Resonance effects can be dismissed as a possible reason for the outliers since the natural frequencies of the sheets (with various porosities, attached to a rigid frame) are far away from the wave frequencies. Qualitatively described, the natural frequencies of the sheet structures are due to their large stiffness, which is significantly higher than the relatively low wave frequencies.

It is possible that experimental and mechanical errors have caused the discrepancies for certain wave conditions, although this is unlikely in consideration of the reasonable results for the majority of conditions. Since none of these hypothesised reasons can explain the unreliable results satisfactorily, the real cause for these outlying data points for certain wave conditions is still unknown.

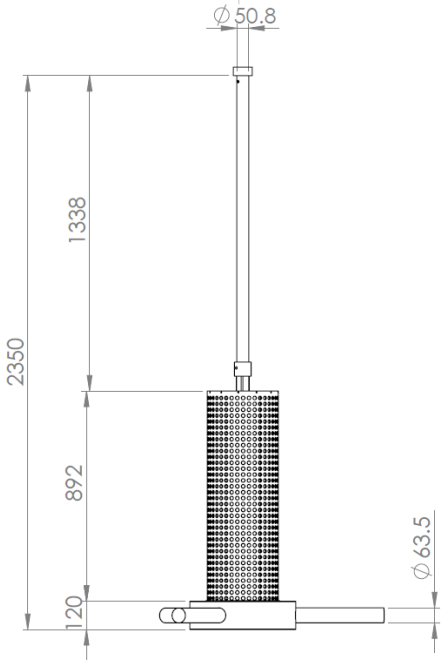

(a) side view of the model, dimensions in [mm]

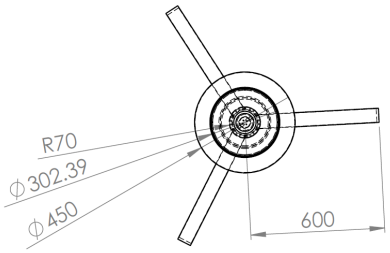

(b) plan view of the model, dimensions in [mm]

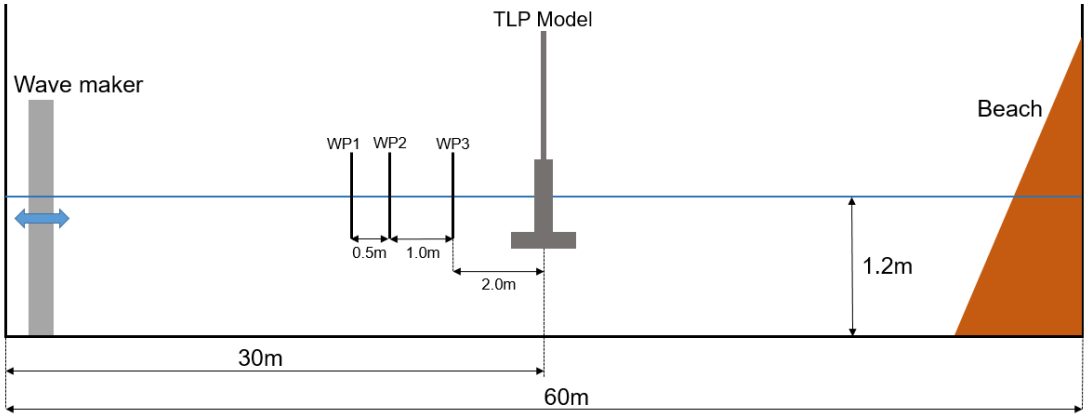

(c) side view of the configuration in the flume (not to scale)

Figure 4.4: Sketch of the flume including the TLP model (with diameters of the inner solid and outer perforated cylinders of $D = 0.140$ m and $D = 0.3024$ m, respectively): (a) side view and (b) plan view of the model, and (c) the experimental configuration in the flume.

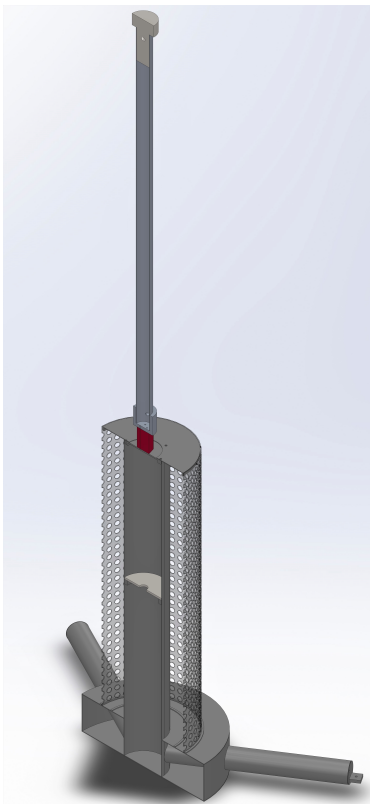

(a) cross-section of the CAD model

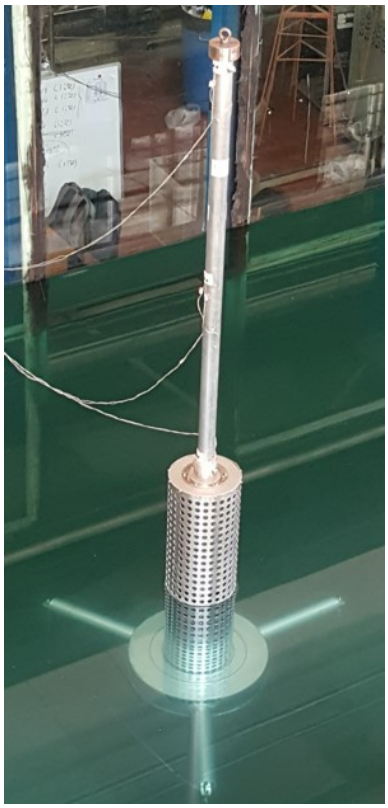

(b) photo of the TLP model in the flume

Figure 4.5: Illustrations of the experimental TLP model: (a) CAD model of the TLP, (b) photo of the WSI during the experiments where the waves were propagating from the right to the left.

4.4.2 Wave interaction with a TLP with a perforated outer Cylinder

For the experiments with the TLP model, the full flume width of 4 m was used. The water depth was set to $h = 1.2$ m. The TLP model is based on NREL design [292, 293] with the 5 MW turbine design [294] with a scale of 1:50. Since only hydrodynamic effects were investigated, the model consisted of the platform and tower only. The rotor and nacelle were represented by an equivalent mass at the top of the tower. The diameter of the inner platform cylinder was 0.140 m. The dimensions of the simplified model are shown in Fig. 4.4 and the key model parameters are listed in Table 4.2. The mooring of the model consisted of three vertical tendons attached to the ends of the legs and fixated at the flume bottom. The attachment point radius was 0.567 m, the attachment point depth 0.647 m and the tendon's axial stiffness was 14.4 kN. Various thin perforated cylinders could be attached to the baseline model. The outer cylinders had various diameters and porosities and were tested under a range of wave conditions.

As for the static models, the circular perforations were arranged in a square grid. The hole centre spacing was set to $s = 25$ mm for all TLP models. The physical model including a perforated outer cylinder and a photo of it during the tests are shown in Fig. 4.5. The model was designed containing an internal adjustable mass to keep the total mass of $M = 16.18$ kg, the mean displaced water volume of $V_m = 29.6$ l and the position of the COG of 0.222 m above still water level constant. The moments of inertia did vary. The draft was 0.6 m. The model was stiff enough to be treated as a rigid body. Its 6-DOF body motion was recorded using an infrared motion capturing system and the tension of the mooring lines was measured using submersible inline load cells. The large stiffness of the tendons resulted in negligible heave and small pitch and roll motion ranges. Surge was the dominant motion. For a more detailed description of the experimental campaign, the reader is referred to Mackay et al. [42].

Table 4.2: Key parameters of the TLP model used in the experiments.

Parameter	**Value**
Model geometry	
Scale	1:50
Diameter, D, of inner solid cylinder [m]	0.14
Diameter, D, of outer perforated cylinder [m]	0.22, 0.30
Porosities, n, of perforated cylinder [-]	0.15, 0.30
Mass, M [kg]	16.18
Water depth, h [m]	1.20
Draft [m]	0.60
COG, vertical distance above still water level [m]	0.22
Displaced volume, V_m [l]	29.60
Mooring tendons	
Attachment point radius [m]	0.57
Top attachment point depth [m]	0.65
Bottom attachment point above floor [m]	0.04
Tendon length, L_t [m]	0.51
Tendon axial stiffness [kN]	14.40

For the present CFD studies, the geometrical and wave parameters have been limited. An outer cylinder diameter of $D = 0.2228$ m is used throughout and a porosity value of $n = 0.15$ is applied. The wave conditions used in the CFD simulations with the TLP are listed in Table 4.3. The input waves cover wave numbers of $0.55 < k_w < 1.39$ and wave steepnesses of $0.014 \leqslant k_w A \leqslant 0.045$. Key aspects are further described in Chapter 7 as part of the model setup.

Table 4.3: Regular wave conditions used for models with the TLP (CFD model input / target parameters).

Index	T [s]	λ [m]	H [m]	k_w [1/m]	$k_w A$ [-]	c_g [a] [m/s]
D01	2.8	7.27	0.04	0.72	0.014	2.52
D02	1.8	3.78	0.04	1.39	0.028	1.59
E01	3.54	9.47	0.08	0.55	0.022	2.82
E02	2.00	3.35	0.08	1.13	0.045	1.88

[a] group velocity

4.4.3 Corresponding Wave Theory

Using the diagram by Le Méhauté [120] as introduced by Fig. 2.6 in Section 2.3.1, the applicable wave theories were identified for all present wave conditions as listed in Table 4.1 for the static structures and in Table 4.3 for the TLP models. In Fig. 4.6, the conditions used for the simulations with the TLP are indicated with yellow circles; the ones used for the static cylinder models are marked with red crosses; and the ones used for the sheet are indicated with blue asterisks. The ones used for the cylinder models have also been used for the simulations with the sheet. It is shown that the majority of conditions is within the validity of Stokes 2[nd]- order wave theory.

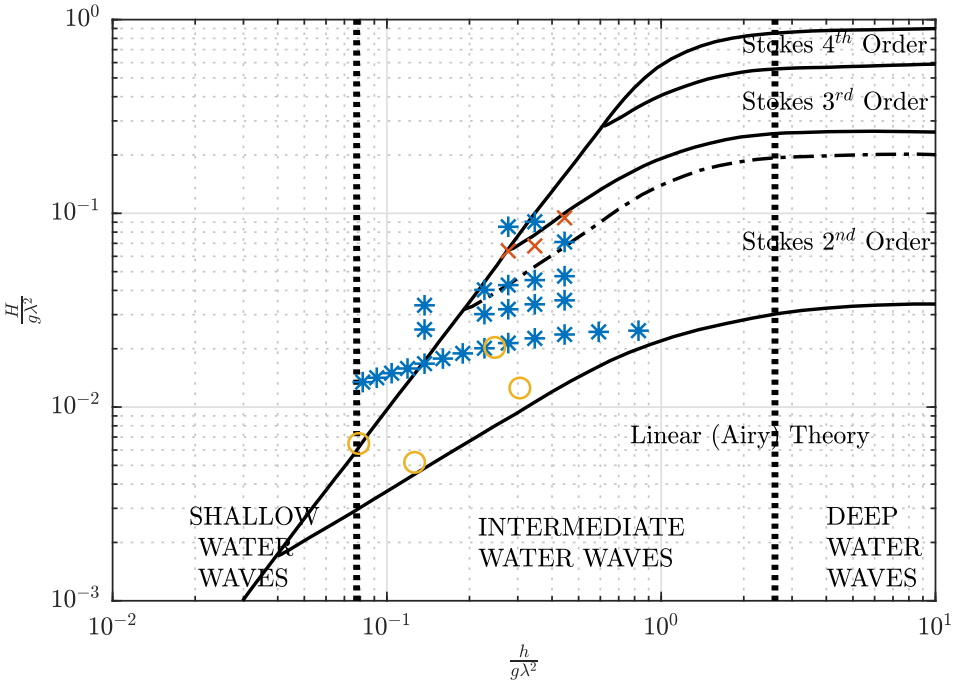

Figure 4.6: All wave conditions used in this thesis in the diagram by Le Méhauté [120]: blue asterisks/2D sheet, red crosses/2D sheet and cylinder, yellow circles/TLP) .

The free surface elevation, $\eta(t)$, of Stokes 2nd- order theory is defined as:

$$\eta(t) = \frac{H}{2}\cos(\theta) + k_w \frac{H^2}{4} \frac{3 - \tanh^2(k_w h)}{4\tanh^3(k_w h)} \cos(2\theta), \tag{4.9}$$

where $\theta = k_w x - \omega_w t + \psi$ is the wave phase, k_w is the wave number, ω_w is the angular frequency, ψ is the wave phase shift, x is the horizontal coordinate and t is the time. The horizontal and vertical velocity profiles, u_x and u_z, are given as:

$$u_x(x,z,t) = \frac{H}{2}\omega_w \frac{\cosh(k_w z)}{\sinh(k_w h)} \cos(\theta) + \frac{3}{4} \frac{H^2 \omega_w k_w \cosh(2k_w z)}{4\sinh^4(k_w h)} \cos(2\theta) \tag{4.10}$$

and

$$u_z(x,z,t) = \frac{H}{2}\omega_w \frac{\sinh(k_w z)}{\sinh(k_w h)} \sin(\theta) + \frac{3}{4} \frac{H^2 \omega_w k_w \sinh(2k_w z)}{4\sinh^4(k_w h)} \sin(2\theta), \tag{4.11}$$

where z is the vertical coordinate of the water column.

4.5 Potential-flow Data for Comparison

In addition to validation against experiments, the CFD results are compared to results from a potential-flow (BEM) model by Mackay et al. [41], Mackay and Johanning [44] and Mackay et al. [43].

The BEM model uses the same quadratic pressure-drop formulation as the CFD models, (3.1), but the time dependence in the velocity-squared term is linearised using Lorenz's principle of equivalent work. In other words, the time-dependence of the force on the porous barrier is sinusoidal and not reproduced with its more realistic non-sinusoidal shape. The model is based on linear (Airy) wave theory, see Fig. 2.6. Since all wave conditions used in the experiments (and CFD simulations) are in the nonlinear range and mainly within the applicability of Stokes 2nd- order theory, as shown in Fig. 4.6, the accuracy of the linear potential-flow model is expected to decrease as the wave non-linearity increases. The non-linearity of the wave conditions increases with decreasing relative water depth, $k_w h$, and increasing wave steepness, $k_w A$.

4.6 Summary

This chapter covered the introduction of all data analysis, verification and validation procedures and reference data used in this thesis. The analysis approaches are general concepts and methods used in CFD modelling. The reference data includes the results obtained from experiments and a linear potential-flow (BEM) model. The experimental campaign and the BEM model were introduced.

The following three chapters cover a detailed method assessment where the CFD results are compared against the experimental and potential-flow results by using the stated data and analysis concepts.

Chapter 5

Simulations of pure Wave Propagation

5.1 Introduction

Models of empty numerical wave tanks (NWT) are generated based on the experimental setup as introduced in Section 4.4. OlaFlow/IHFoam, with its implemented static boundary technique and active wave absorption (AWA) method, has been considered to be the most promising option. Its performance and accuracy levels have been assessed in terms of model setup and numerical settings to derive reliable wave modelling.

5.2 General Model Setup

All experimental and present numerical investigations have been conducted in a unidirectional wave flume. Thus, the assessment of the wave modelling capabilities has been carried out with a 2D model of an empty tank (Fig. 5.1).

5.2.1 Dimensions, Mesh and BCs

The length of the NWT was set to 26 m in order to contain a minimum of approximately 2.5 wavelengths based on the longest wavelength of $\lambda = 10.36$ m (A13 in Table 4.1). The domain height is set to 1.3 m and the water depth to $h = 1.0$ m. WGs have been

placed in the NWT corresponding to the positions of the WGs in the experiments, all in distance relative to the tank centre.

The baseline mesh was generated using a uniformly structured mesh with regular hexahedral cells with a size of $l_x = l_z = 20$ mm, where l_x is the cell length in horizontal x-direction and l_z is the cell height in vertical z-direction. A refinement region has been applied along the free water surface. It covers the maximum target wave height of $H = 0.26$ m of the range of wave conditions (C04 in Table 4.1). The required spatial resolution of the refinement region has been evaluated in the mesh independence study below.

For consistency, Stokes 2$^{\text{nd}}$- order wave input, via (4.9), (4.10) and (4.11), as introduced in Section 2.3, has been used for all present models without distinguishing between wave steepnesses. The top boundary was set to an atmospheric condition. At the tank bottom a free-slip wall condition was applied in accordance with the smooth surface of the physical flume. At both ends of the NWT, the AWA method has been activated. A sketch of the 2D model configuration including all dimensions, BCs and WG positions is shown in Fig. 5.1. The waves were imposed at the generation boundary at the left-hand side (LHS) of the NWT and are propagating towards the pure absorption boundary on the right-hand side (RHS).

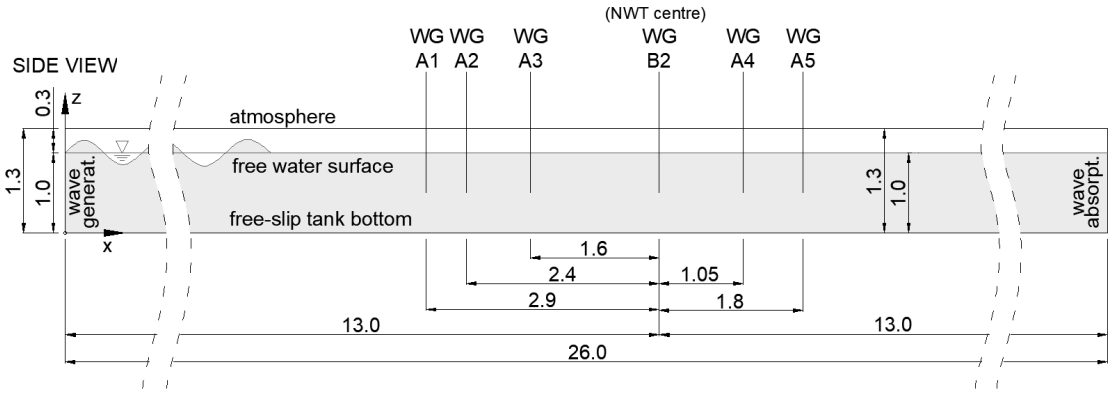

Figure 5.1: Sketch of the 2D numerical wave tank, including all boundary conditions and wave gauge (WG) positions relative to the tank centre at WG B2; dimensions in [m].

5.2.2 Numerical Settings

The solver and scheme settings listed in Table A.1 in Appendix A were selected as the baseline setup. From those settings, the ones that have been identified as critical by Larsen et al. [111], have been assessed by means of a sensitivity study on their impact on the results.

As common for CFD modelling of wave flumes, this work uses automatic time step control, controlled by the specification of the maximum CFL-number, already introduced in Section 2.2. Based on similar modelling of waves and WSI processes [28, 37, 295–297] where maximum CFL-numbers ranged between 0.1 and 0.75, an initial maximum CFL of 0.5 was employed in the present model. The PIMPLE solution algorithm was used in PISO-mode (`nOuterCorrectors` = 1) with three inner pressure-corrector loops (`nCorrectors` = 3) and with a momentum predictor step which solves the momentum equation once before entering the inner loop. The MULES VOF method, as standard implementation in OF, was used with two sub-cycles (`nAlphaSubCycles` = 2), which means that the adjusted initial time step was split in half for the calculation of the α-equation. Due to the high-quality hexahedral mesh, the non-orthogonality correction was set to 1 which means that the pressure equation was solved only once per PISO loop without any further corrections. The settings related to the solver algorithm-control are shown in the flow chart in Fig. 2.5 and indicated by grey shades.

Since the present wave conditions are in the potential-flow regime, no turbulence generation is expected for pure wave propagation. Also, for the present case of wave propagation over a smooth, flat bottom, no significant bottom BL is expected to develop, and a free-slip condition is applied at the bottom boundary. Therefore, no turbulence model was applied and the full NS equations have been solved for the cases of pure wave propagation.

5.3 Assessment of the Method and Setup

5.3.1 Criteria for Accurate Wave Modelling

The key aspects of reliable wave modelling are accurate wave generation, stable wave propagation and minimal wave reflection at the boundaries. These criteria are addressed in the following assessment of the performance of OlaFlow/IHFoam's wave modelling capabilities for the present wave conditions. Further considerations such as turbulence and BL modelling were made subsequently.

Accurate wave generation is directly controlled by the input BC and is achieved by imposing the appropriate wave theory or wavemaker type. Hence, no explicit assessment was conducted here.

Stable wave propagation is mainly achieved by appropriate spatial and temporal discretisation and numerical scheme and solver settings. Larsen et al. [111] have assessed the performance of OF's `interFoam` solver for pure wave propagation and identified a range of important settings. Apart from cell and time-step size or maximum

CFL- number, they identified the time discretisation scheme (`ddt`), the convection scheme (`div(rhoPhi,U)`), the surface normal gradient scheme (`snGrad`, e.g. used in the discretisation of the Laplacian in (2.3) and the interphase-capturing method as most critical. The following assessment estimates the impact of these settings on the wave propagation by means of the wave elevation over time, $\eta(t)$, at certain wave gauges (WGs) and by means of the mean wave amplitude, $A(x)$, along the NWT.

Wave reflections can occur at both domain ends and over time a standing wave is generated, similar to in a physical wave flume. In that context the ratio of wave length to domain length and relative position of a structure can become important since it is impossible to avoid reflections in the NWT completely (just as in a physical flume). However, appropriate treatment can keep reflections to a minimum.

The reflection levels and performance of an absorption method, respectively, are usually assessed with the reflection coefficient, R_{refl}. The most common methods to estimate R_{refl} are a two-gauge method by Goda and Suzuki [298] and a three-gauge method by Mansard and Funke [299]. The latter one is used in this thesis.

The wave modelling assessment has been performed for two wave conditions, a shorter wave (A02) and a longer wave (A09) from the range of wave conditions with a wave steepness of $k_w A = 0.05$ as listed in Table 4.1.

5.3.2 Spatial Discretisation

Beginning with the baseline mesh with the uniform cell dimensions stated above, the free-surface region was successively refined locally. The refinement region along the free-surface covers the maximum wave height of the range of wave conditions, H = 0.26 m (see Table 4.1).

The main mesh convergence metric was specified as the mean wave amplitude, A, at WG B2 at the tank centre at an x-position of 13 m. The mean was obtained by the standard-deviation, σ, of the WG signal $\eta(t)$. All wave elevation signals used in this work have the initial transient section removed for further processing, following the procedures introduced in Chapter 4. Since the performance of the absorption method is part of the assessment, presented in the following section, wave reflections have been kept included.

Table 5.1 shows a summary of the mesh independence study for the free-surface region at WG B2 by means of cells per wave height (CPH) and cells per wavelength (CPL). The measured mean wave amplitudes, A, are presented including the successive percentage change between the meshes. The values are compared to the target wave amplitudes based on Stokes 2$^{\text{nd}}$- order input, A_{input}. It can be observed in Table 5.1 that no monotonic convergence could be achieved for the mean wave amplitude, A. The

Table 5.1: Mesh independence study for the free-surface region for the wave amplitude, A, at WG B2 in terms of cells per wave height (CPH) and cells per wavelength (CPL).

		l_x	l_z	Wave A02			Wave A09		
Mesh	No. Cells	[mm]	[mm]	CPH	CPL	A [mm]	CPH	CPL	A [mm]
1	97500	20.0	10.0	4.1	130	19.3	12.2	383	61.8
2	123500	10.0	10.0	4.1	260	19.4 (+0.5%)	12.2	767	61.8 ($\pm$0.0%)
3	175500	10.0	5.0	8.2	260	20.8 (+7.2%)	24.4	757	61.7 (-0.2%)
4	487500	5.0	2.5	16.5	520	18.8 (-9.6%)	48.8	1534	61.7 ($\pm$0.0%)
A_{input}						20.7			61.1

differences between A_{input} and A are 4-9 % for wave A02 and around 1 % for wave A09. As the absolute wave height of A02 is relatively small compared to the cell heights, the accuracy was deemed to be acceptable since the mesh aims to cover the whole range of wave conditions. Mesh 3 with $l_x = 10$ mm and $l_z = 5$ mm was selected for all following studies. This corresponds to a minimum number of 6 CPH for the smallest wave height (A01) and 52 CPH for the largest wave height (C04) and 188 CPL for the shortest wave (A01) and 1036 CPL for the longest wave (A13), see Table 4.1.

The reasons for differences between the measured and target conditions are identified as a combination of numerical scheme settings and the performance of the wave absorption method. The former can for instance lead to high-frequency ripples at the air-water interface and the latter determines the level of wave reflections and the corresponding relevance of the ratio of wavelength to domain length as well as relative sheet position.

5.3.3 Wave Reflections

To assess the influence of the wave absorption method, the reflection coefficients, R_{refl}, have been estimated using WG B2, WG A2 and WG A5 as shown in Fig. 5.1. R_{refl} have been compared between results obtained from models with the SW-AWA and ER-AWA methods. The assessment was performed on a limited number of wave conditions with a wave steepness of $k_w A = 0.05$. All frequencies (A01-A13) have been used with the SW-AWA. For results from models with the ER-AWA, only a subset of wave conditions (A02, A03, A04, A09) was used.

The results of R_{refl} are presented in Fig. 5.2 where it is shown that the ER-AWA method performs significantly better than the SW-AWA for all conditions investigated. While the SW-AWA method yields coefficients up to about 28.0 %, in particular for the shorter waves with larger $k_w h$, the ER-AWA achieves R_{refl} = 1-2 %. This highlights the importance of the absorption method.

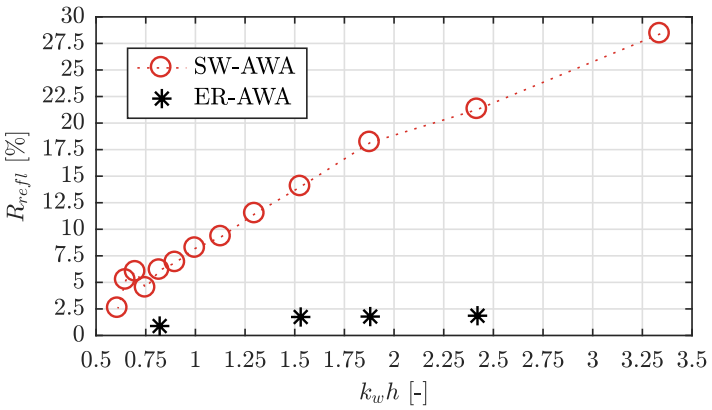

Figure 5.2: Reflection coefficients, R_{refl}, for all wave conditions with $k_w A = 0.05$, using the shallow-water active wave-absorption (SW-AWA) method for the whole range of frequencies and the extended-range active wave-absorption (ER-AWA) for a subset.

5.3.4 Sensitivity of Numerical Settings

To estimate the impact of the numerical scheme and solver settings, a sensitivity study has been conducted. Based on the findings of Larsen et al. [111], a small set of settings was selected from the baseline settings in Table A.1 and varied for comparison. The initial setting for the maximum CFL-number was 0.5, which was compared to a value of 0.1, inspired by the recommendation of Larsen et al. [111] and Roenby et al. [107] to use very small maximum CFL-numbers in the context of similar work. The initial setting for the time discretisation scheme (`ddt`) is the `Euler` scheme, selected due to its robustness. It is only first-order accurate but in combination with a small time step (maximum $CFL < 1$) numerical diffusion is considered to be insignificant. One comparison was performed with a scheme that blends between the Euler and the Crank-Nicolson scheme, where a blending factor of 0.6 was employed. The `CrankNicolson ddt` scheme is second-order accurate but oscillatory and a blending factor can help stabilizing it, where a factor of 0 corresponds to a pure Euler setting and a factor of 1 to a pure Crank-Nicolson scheme. The baseline setting for the advection discretisation scheme (`div(rhoPhi,U)`), a `linearUpwind` scheme was used. It is second-order accurate and bounded since it applies upwind discretisation at regions of rapidly changing gradients. It was compared to the more diffusive and first-order accurate pure `upwind` scheme. The default VOF implementation with MULES interface-capturing has been compared to the `isoAdvector` method to explore possible advantages. No turbulence model has been used in the baseline model since turbulence is physically not expected. However, to explore possible unphysical wave height damping, the effect of applying the k-ϵ model has been assessed. This model was selected for the empty tank since it performs well in free-shear fluid flow, as

stated in Section 2.2.4.

A matrix of all assessed parameters and their combinations (cases C1-C6) are listed in Table 5.2. The table includes the results of the normalised mean wave amplitude, A/A_{input}, at WG B2 at the tank centre for the wave conditions A02 and A09.

Table 5.2: Matrix of combinations of numerical settings (cases C1-C6) and comparison of the normalised averaged wave amplitude A/A_{input} at WG B2.

Numerical setup	Case:	C1	C2	C3	C4	C5	C6
max. CFL	0.5	x		x	x		x
	0.1		x			x	
`ddt`	`Euler`	x	x	x	x	x	
	`CrankNicolson 0.6`						x
`div(rhoPhi,U)`	`limitedLinearV 1`	x	x	x	x	x	
	`upwind`						x
VOF method	MULES	x	x	x			
	`isoAdvector`				x	x	x
Turb. model	none	x	x		x	x	x
	k-ϵ			x			
A/A_{input} at	Wave A02	1.00	1.01	0.94	1.00	1.01	1.19
WG B2 ($x = 13$ m)	Wave A09	1.01	1.01	0.80	1.02	1.02	1.01

The normalised mean amplitude, A/A_{input}, was not only analysed at the tank centre at WG B2 but along the whole length of the NWT. This data was obtained by sampling of the whole free water surface along the wave flume over time. Here, the isosurface of the phase-field (α-field) was processed with an iso-value of $\alpha = 0.5$, which represents the free water surface, and the mean value of the wave elevation was obtained at every 50 mm of the tank.

Figure 5.3 shows $A(x)/A_{input}$ for the waves A02 and A09 obtained from the isosurface data. For clarity, each figure shows only a subset of the cases C1-C6. The vertical black lines indicate the tank centre and position of WG B2 at $x = 13$ m. Reflected waves are included in Fig. 5.3b for wave A02 and in Fig. 5.3c for wave A09. For comparison and to highlight the effect of reflected waves, Fig. 5.3a does not include any reflections. The time series here is cut off at $x = 17.7$ m, where less than one wave period would have been left to calculate the mean. In all cases, the amplitude of the oscillations increases along the NWT since a decreasing number of wave periods are available to calculate the average. However, the more significant increase in amplitude along the tank results from wave reflections.

The results for A/A_{input} presented at the bottom of Table 5.2 were obtained including wave reflections. Comparison with the graphs in Fig. 5.3b and 5.3c shows that $A(x = 13\,\mathrm{m})/A_{input}$ agree qualitatively. However, there is a quantitative discrepancy which originates from the different processing methods and the nature of the algebraic

VOF method where no exact interface is present. Consequently, the post-processing method is considered to be an additional source of uncertainty and was taken into account in the uncertainty estimation in the next section.

Despite quantitative discrepancies, the results show two main findings. Firstly, the setup that uses a turbulence model (case C3) leads to a decrease in amplitude along the NWT, in particular for the long wave A09. This behaviour confirms previous observations in the context of spurious turbulence generation at the air-water interface, already stated in Section 2.3.3. Secondly, the mean amplitude significantly increases along the NWT when the Crank-Nicolson scheme was used (in combination with the `isoAdvector` VOF method). This confirms the importance of the `ddt` scheme for wave propagation as already stated by Larsen et al. [111]. All other combinations of settings (cases C1, C2, C4 and C5) exhibit minor impact on the wave propagation. In particular, a maximum CFL of 0.5 leads to sufficiently small temporal discretisation giving the same results as a maximum CFL of 0.1 for the cases investigated.

5.3.5 Final Setup and its Uncertainty

The outcome of the assessment above results in the following settings for all further models. The mesh along the refinement region was set to a cell size of $l_x = 10\,\text{mm}$ and $l_z = 5\,\text{mm}$, respectively. Although it was shown that the ER-AWA outperforms the SW-AWA, both methods have been used for the simulations with the vertical sheet. This is due to the relatively late official release of the ER-AWA toolbox. Hence, most of the present simulations have already been performed with the SW-AWA. As a result of the sensitivity study on numerical settings, it has been concluded that the baseline setup (C1) shown in Table A.1 gives reliable wave modelling results. Hence, these settings have been used for all following simulations. The standard VOF method MULES is selected over the alternative `isoAdvector` method for two reasons. No accuracy gains could be identified for the present cases by using the latter. In particular for case C6, the combination of the Crank-Nicolson `ddt` scheme with the `isoAdvector` leads to significant deviations of the wave elevation for wave A02. It is likely that a more detailed assessment on the specific requirements of the latter may lead to reliable results since Roenby et al. [107] stated that the performance of `isoAdvector` is strongly dependent on the solver setup. However, this is considered to introduce unnecessary challenges for the present work.

The selected combination of setup corresponds to case C1 in Table 5.3 where a normalised mean amplitude, A/A_{input}, of 1.00 for wave A02 and of 1.01 for wave A09 was achieved at the tank centre. To estimate the level of confidence of these results, an uncertainty study was performed. The absorption method, the numerical settings and

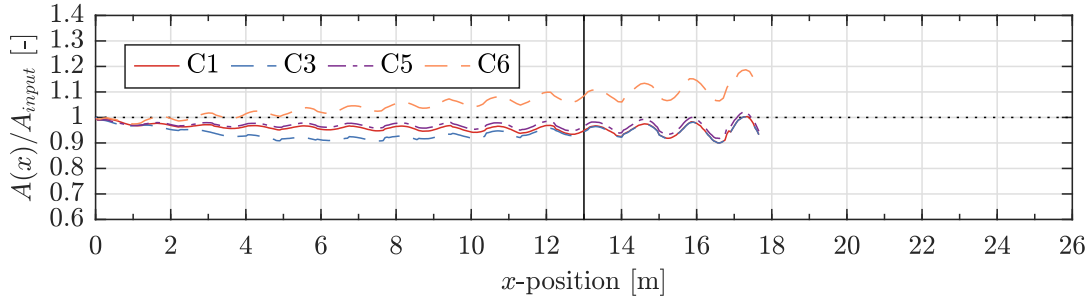

(a) Wave A02, no reflected waves included.

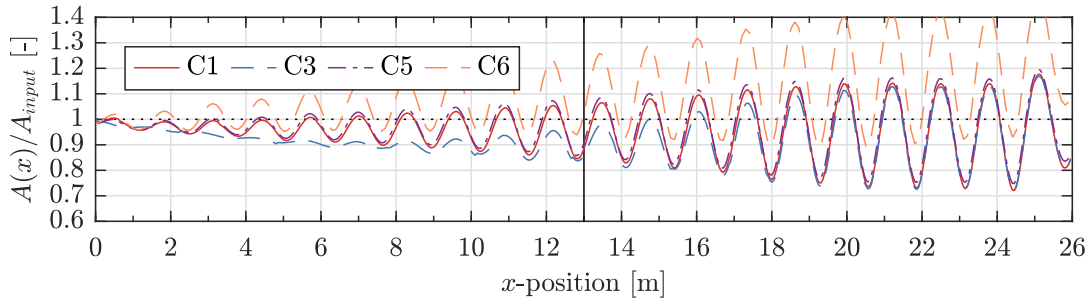

(b) Wave A02, reflected waves included.

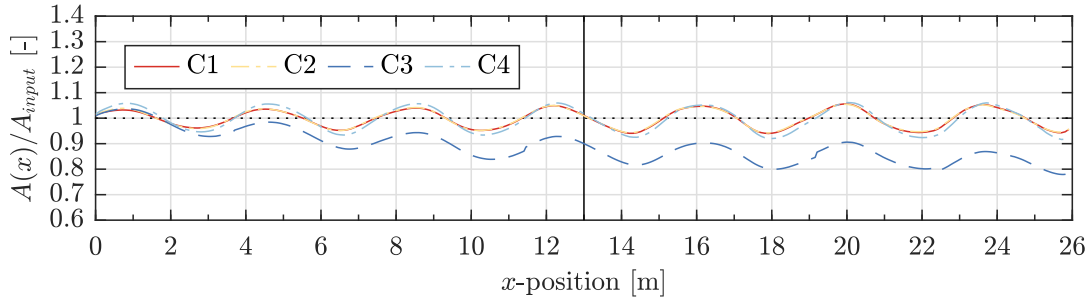

(c) Wave A09, reflected waves included.

Figure 5.3: Normalised mean wave amplitude, $A(x)/A_{input}$, along the numerical wave tank in respect to the x-position with comparisons for (a) wave A02 (excluding reflected waves), (b) wave A02 (including reflected waves) and (c) wave A09 (including reflected waves) from Table 4.1. Note the differences in selected cases (C1-C6) for A02 and A09. The vertical line indicates the tank centre and where a structure would be placed.

the post-processing procedures have been identified as the main sources of uncertainty. The uncertainty of the post-processing method concerns the unsteady nature of the solution and the appropriate selection of the time series window, over which the mean is calculated. Therefore, the mean wave amplitude, A, was calculated for various windows of length 10 wave periods for wave A02. For wave A09, which has a longer period and consequently fewer periods in the record, the uncertainty was estimated by comparing results averaged over 5 or 10 periods. The sensitivities of numerical settings have been incorporated as a source of uncertainty, and been analysed in two ways. Firstly, all scheme variations and results from the cases in Table 5.2 (C1-C6) have been included

in the uncertainty estimation. Secondly, the results obtained from the models with the `isoAdvector` VOF method have been excluded since the standard MULES VOF method was selected instead.

The uncertainty analysis was performed using the procedures introduced in Section 4.3. The uncertainty for source i, U_i, is calculated via (4.5); the mean value of each uncertainty source, v_i, via (4.7); and the overall uncertainty, U, via (4.6). The summary of the analysis and its final results are shown in Table 5.3. The values in bold represent the uncertainty results for the most relevant case where model results using the `isoAdvector` method have been excluded.

Table 5.3: Uncertainty estimation by means of the mean wave amplitude, A, (where $S = A$) for the waves A02 and A09.

	A02			A09		
Source i	S_i^{max}	S_i^{min}	U_i/v_i [%]	S_i^{max}	S_i^{min}	U_i/v_i [%]
1 - wave absorption method	0.021	0.020	3.5	0.062	0.061	0.9
2 - numerical settings	0.025	0.020	12.7	0.062	0.049	13.3
*	**0.021**	**0.021**	**0.3**	**0.062**	**0.062**	**0.2**
3 - post-processing	0.020	0.017	7.0	0.062	0.061	0.2
Overall uncertainty U			$\pm$ 15.0			$\pm$ 13.3
*			$\pm$ **7.9**			$\pm$ **0.9**

* the values in bold denote uncertainties that exclude results obtained using the `isoAdvector` VOF method

Table 5.3 indicates that the numerical scheme and solver settings can introduce the largest uncertainties with an average of $U_2^{mean} = 13.0\,\%$ when all variations of settings are included. However, when the results from models with the `isoAdvector` VOF method are removed, the numerical uncertainties decrease significantly to an average of $U_2^{mean} = 0.25\,\%$. The wave absorption and post-processing methods seem to have a minor effect on the results on the simulations with the longer wave A09, while they have considerable impact on the wave elevation results for the shorter wave A02. Here, the uncertainties are $U_1^{A02} = 3.5\,\%$ and $U_3^{A02} = 7.0\,\%$, respectively.

When the results from models with the `isoAdvector` VOF method are excluded, which is the most relevant case, the overall uncertainty was estimated to be $\pm U = 7.9\,\%$ for wave A02 and $U = 0.9\,\%$ for wave A09. This gives a mean overall uncertainty, $\pm U$ of 4.4 % for the wave modelling settings for pure wave propagation.

5.4 Summary

The wave modelling assessment for the waves A02 and A09 shows that a reasonably accurate and stable wave propagation can be achieved with the settings as listed in

Table A.1. The target amplitudes, A_{input}, of those two wave conditions could be reproduced with a maximum deviation of 1 % at the tank centre where the perforated structures will be positioned.

The level of uncertainty due to the model setup and numerical settings in particular, is on average $\pm U = 4.4\,\%$ (when the MULES VOF method is used), which is considered to be a sufficiently accurate level of confidence. Therefore, no alternative wave modelling methods have been investigated and OlaFlow/IHFoam's AWA method with static boundaries is used for all cases.

As stated above, the level of wave reflections that has been obtained with the ER-AWA is very low with values of up to $R_{refl} = 2.0\,\%$. Due to the late release of this enhanced method, some of the present simulations have already been performed with the SW-AWA where R_{refl} is up to 28.0 %. However, the effect of the absorption method is incorporated in the numerical uncertainty, U.

The performance of the AWA can be further enhanced by combining it with cell-stretching towards the tank end. This is later adopted for 3D models including a fixed porous cylinder, see Chapter 6, and a moving TLP platform, see Chapter 7. For the latter case, it is moreover a useful means to reduce the number of mesh cells.

The limitation of the assessment above is the small sample number in terms of the number of wave conditions and settings tested. However, a detailed assessment is considered to be an extensive task that does not directly support the aim of this thesis and was partly done in previous work by Windt et al. [122], Schmitt and Elsaesser [124], Windt et al. [134] and Miquel et al. [135].

The work presented here has demonstrated the accuracy and efficiency of the ER-AWA method with static boundaries as implemented in OlaFlow/IHFoam in wave conditions relevant for the simulation of floating offshore wind platforms. With this method and the selected model setup and the numerical settings as in Table A.1, sufficiently accurate wave modelling could be achieved. This is considered to be a reliable model setup on which the main work of this thesis is based.

Chapter 6

Simulations of fixed thin perforated Structures

6.1 Introduction

This thesis explores the use of a macro-scale porosity representation for wave interaction with thin perforated structures. In contrast to similar work by Shim et al. [5], Zhao et al. [40, 176] and Chen and Christensen [4], already discussed in Section 2.4, this thesis aims to provide a comprehensive methodology for both fixed and floating structures and furthermore one which avoids calibration procedures.

The main objective of this section is the assessment of the selected pressure-drop formulation for wave interaction with fixed structures and the comparison of different options of porosity implementation (as outlined and illustrated in Figs.2.10 and 2.11). To evaluate the validity of the proposed macro-scale approach, its accuracy and limitations, the following research questions are addressed:

- Is a macroscopic porosity representation a valid approach to model large-scale WSI effects?
- Which type of porosity implementation is the most suitable in terms of accuracy and computational efficiency?

- What effect do common turbulence models have on the large-scale results?
- Is the applied theoretical pressure-drop model valid for the present context of thin perforated structures?

The outcome of the investigations on static porous structures in the current section has informed the application to moving structures in the subsequent chapter.

6.2 General Model Setup

A 2D model with a vertical perforated sheet and a 3D model with a circular vertical perforated cylinder have been simulated. The former has been used to evaluate the minimum mesh requirements and to identify the most influential settings more extensively. The outcome of the model development for the 2D model has then been used for the setup of the 3D model including the cylinder.

6.2.1 Domain and Boundary Conditions

As for the simulations of pure wave propagation in the empty NWT, the domain height and the water depth of the 2D NWT containing the vertical sheet were set to 1.30 m and $h = 1.0$ m, respectively. The 2D NWT with the sheet was generated twice, once with a length of 26 m (for earlier models and as for the empty NWT), and once with a length of 16 m. The 3D model including the cylinder had a width of 3 m. Both structures were placed at the tank centres at an x-position of 8 m and 13 m, respectively, in order to achieve the same amount of time for reflected waves travelling back from both ends of the domain. The top boundary was set to an atmospheric condition and the tank bottom to a free-slip wall BC. Stokes 2$^{\text{nd}}$- order waves were imposed at the generation boundary, defined by the free-surface elevation, $\eta(t)$, and the horizontal and vertical velocity profiles, u_x and u_z, (via (4.9), (4.10) and (4.11), as introduced in Section 2.3). The wave input parameters cover the whole range of regular wave conditions listed in Table 4.1.

A sketch of the model configuration including all BCs and WG positions is shown in Fig. 6.1a. The WGs with index A (WG A1-A5) in the NWT correspond to the WGs in the experimental setup. These are the closest ones available for a direct comparison between CFD and experimental results. In order to study differences between the various types of porosity implementations closer to the structures, the WGs B1-B3 and C1-C2 have been added to the CFD models. The WGs B1-B3 have been used for the 3D model with the cylinder and the WGs C1 and C2 have been used for the 2D model with the sheet. The coloured rectangles in the sketch of Fig. 6.1a refer to related sections of

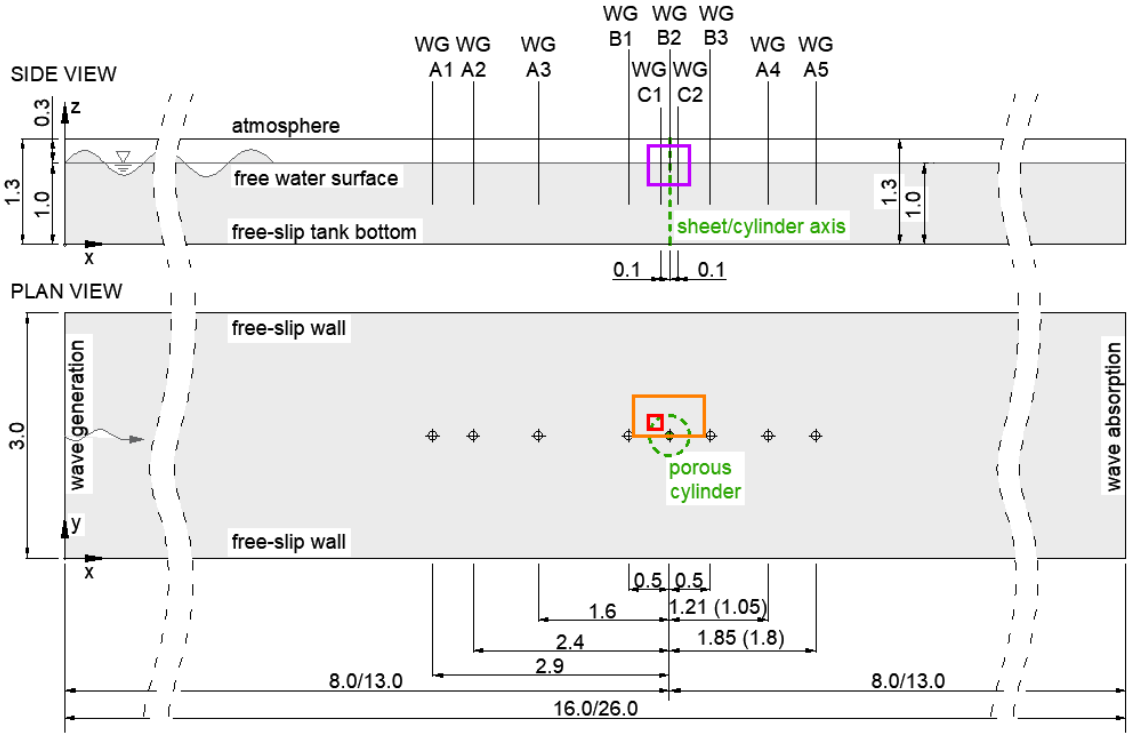

(a) Sketch of the model configuration for both the 2D (side view only) and 3D (plan- and side view) numerical flume, all dimensions in [m]. The positions for the WGs A4 and A5 vary between the 2D sheet model and cylinder - the dimensions for the 2D model are stated in brackets

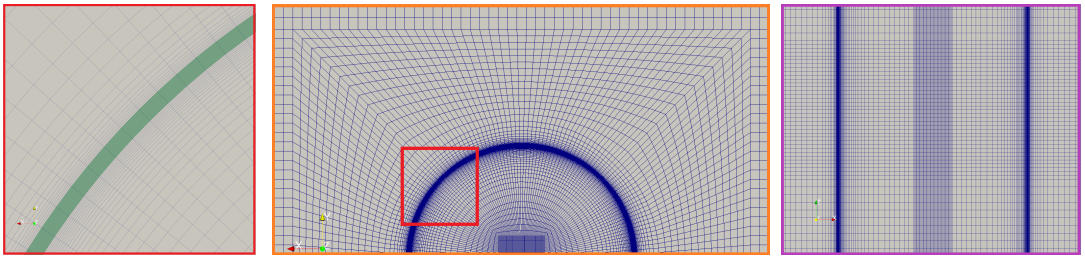

(b) Mesh close-up in plan view

(c) Mesh section in plan view

(d) Clipped mesh section in side view

Figure 6.1: CFD model setup: (a) sketch of the model configuration for both the 2D and 3D numerical flume, (b-d) sections of the mesh of the 3D model with the cylinder represented by porous media where (b-c) show sections in plan view and (d) in side view of a clip across the vertical x - z symmetry plane; the colours of the rectangles in (a) correspond to the colours of the figure frames of (b-d).

the mesh close to the porous cylinder shown in the Figs. 6.1b-6.1d. Figures. 6.1b-6.1c show mesh sections in plan view and Fig. 6.1d shows a section of the mesh in side view along the vertical symmetry (x - z) plane across the cylinder axis. It is important to note that the porous cylinder is not resolved explicitly in the mesh, but is part of the fluid domain instead, with the effect of the porous structure on the flow represented by

the momentum source terms. A snapshot of the simulation of wave interaction with a thin perforated cylinder represented by porous media is exhibited in Fig. 6.2 to better illustrate the setup.

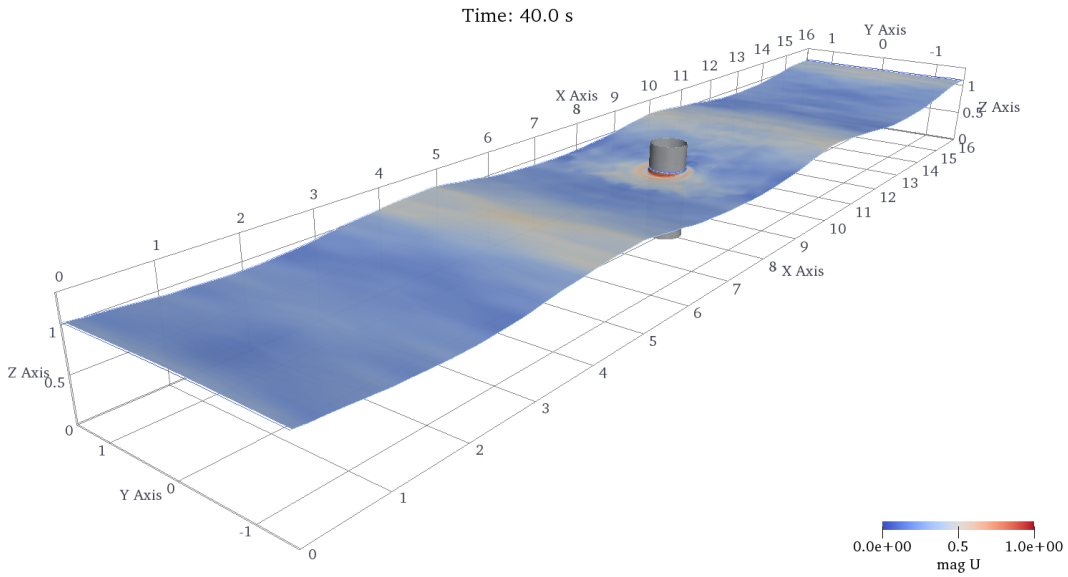

Figure 6.2: Perspective view of the 3D domain showing wave interaction with a porous cylinder represented by porous media; the waves are travelling along the x-axis from the LHS to the RHS; the water surface is represented by the isosurface of the phase field ($\alpha = 0.5$), coloured in the magnitude of velocity within the limits of 0 and 1 m/s.

6.2.2 Porous Structures

As stated in Section 4.4, only a limited set of geometrical parameters has been investigated in the present CFD work:

- sheets and cylinders with porosities of $n = 0.1$, 0.2 and 0.3;
- one cylinder diameter of $D = 0.5$ m;
- a physical sheet thickness of $d = 3$ mm; and
- a physical cylinder thickness of $d = 3$ mm.

The applied porosity coefficient, C_f, and pressure-drop values, Δp, in the CFD models have been calculated using (2.37) and (2.35) in correspondence to the stated porosities and thicknesses. For the models with the porous baffle implementation, the pressure-drop is directly applied at the porous surface. For the models with volumetric porous-media implementations, constant thicknesses, d, have been used for the 2D and 3D models. The thickness of the vertical sheet was set to $d = 10$ mm (which allows a direct comparison with experimental data) and to $d = 5$ mm for the cylinder. This simplifies

the mesh generation process by avoiding complex refinement procedures in order to meet the exact physical thickness, and is valid since the porosity coefficient is calculated per unit length and thus, in accordance with the applied thickness. The validity of this simplification has also been verified for the 2D sheet model and for a thickness range of $5\,\text{mm} \leqslant d \leqslant 20\,\text{mm}$. The crucial factor in that context is the use of at least 16 cells per thickness (N_x/d) to provide a converged pressure-drop across the porous barrier. This value has been derived from the mesh convergence study below in Section 6.3.1, see Fig. 6.4. To note, with a constant number of cells per thickness, the cell size across the sheet changes with changing thickness.

Based on the mesh settings that are required for accurate wave modelling as assessed in Section 5, the baseline mesh consists of a block-structured mesh with hexahedral cells with a size of $l_x = l_y = l_z = 20\,\text{mm}$ in the free-shear flow region and of a refinement region along the free surface with $l_x = 10\,\text{mm}$ and $l_z = 5\,\text{mm}$. The assessment of the minimum spatial resolution across the porous barrier has been part of this study and is presented in Section 6.3.1. In addition to the Figs. 6.1b-6.1d, Fig. 6.3 shows further illustrations of the meshes for both the 2D and 3D model.

6.2.3 Flow Regime and Turbulence Modelling

The fluid flow regime is estimated via the KC-number as introduced in Section 2.3.3 where the characteristic length scale, L, is set to the cylinder diameter, D, in (2.34).

For the present setup, with $D = 0.5\,\text{m}$ and the wave conditions listed in Table 4.1, we have $46946 \leqslant \beta \leqslant 149374$, $0.19 \leqslant KC \leqslant 1.6$ and $0.048 \leqslant D/\lambda \leqslant 0.27$. For these conditions, wave forces on an impermeable cylinder are inertia-dominated, with small or negligible viscous drag. In particular, Sumer et al. [144] found that there was no significant lee-wake vortex generation for $KC < 4$ and no horse-shoe vortex generation for $KC < 6$. For the case of a perforated cylinder, vortex generation is expected to be lower than for an impermeable cylinder. Therefore, neither large-scale nor small-scale turbulence are expected to have significant effects for the present conditions. However, since turbulence modelling is the core of the RANS method, the effect of the application of common turbulence models is assessed to prove this hypothesis. The evaluation is presented below in Section 6.5.

6.3 Spatial and Temporal Discretisation

Mesh convergence and sensitivity studies have been carried out with the 2D model with the perforated sheet for a porosity of $n = 0.2$ and wave B06 as listed in Table 4.1.

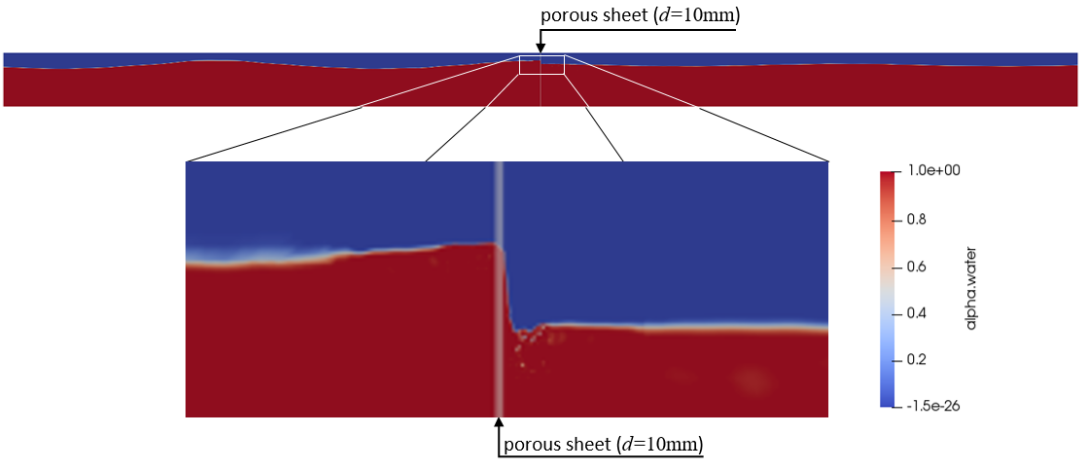

(a) Side view with a close-up of the 2D model, showing wave interaction with the porous sheet; the waves are travelling from the LHS to the RHS; "alpha.water" represents the phase fraction, α, where $\alpha = 1$ corresponds to a cell full of water and $\alpha = 0$ to a cell full of air.

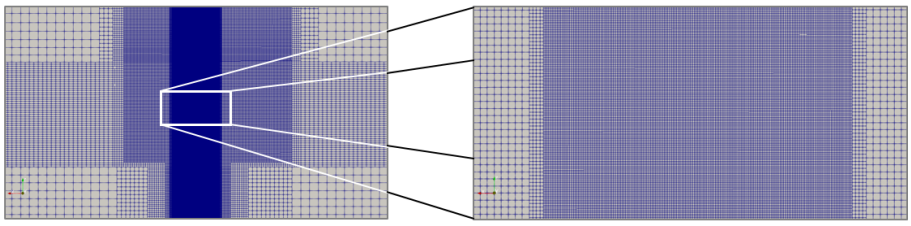

(b) Close-up of the mesh at the free-surface region at the sheet at the centre of the 2D NWT.

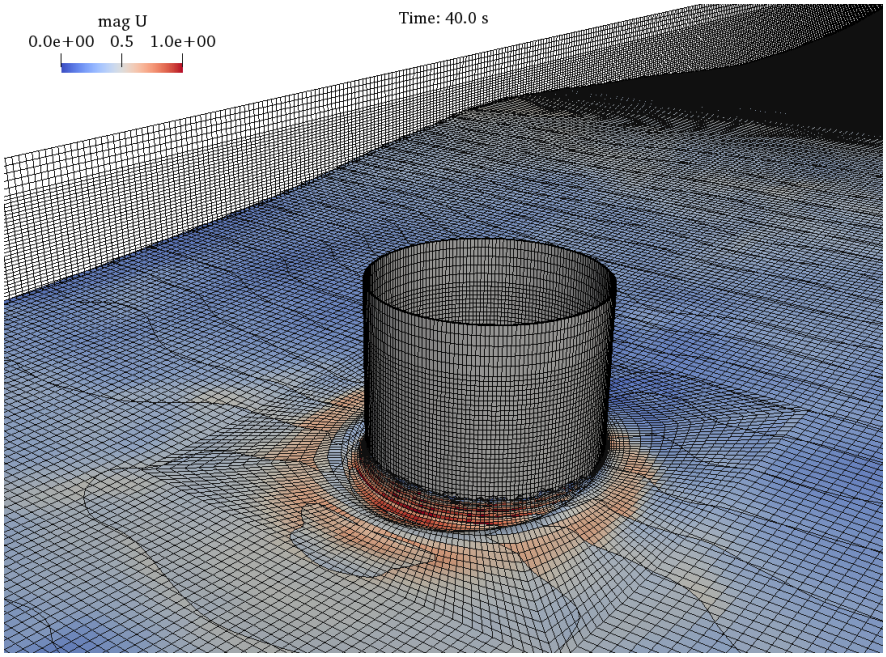

(c) Close-up of the 3D model with a porous cylinder showing the mesh and contours of the water (iso-)surface ($\alpha = 0.5$) which is coloured in the magnitude of velocity within the limits of 0 and 1 m/s.

Figure 6.3: Illustrations of the (a) wave interaction with the porous sheet, (b) the mesh around the sheet and along the free-surface of the 2D tank, and (c) the mesh of the 3D model including the porous cylinder.

6.3.1 Mesh Convergence Study

A mesh convergence study was performed separately for each type of porosity implementation. The mean amplitude of the horizontal force on the 2D sheet, F, was compared for a number of meshes. The meshes were generated with a successively increasing number of cells separately for the horizontal x- and vertical z-direction, starting off from the cell size in the clear flow region ($l_x = l_z = 20$ mm). Firstly, the horizontal cell length, l_x, was decreased successively until a quasi-converged state was reached. Secondly, the vertical cell length, l_z, was reduced while l_x was kept constant. The mean force amplitudes obtained from the CFD results, F, have been scaled to correspond to the experimental sheet width of 1 m. F has then been normalised over the mean force amplitudes obtained from the experiments, $F_{exp} = 382.63$ N. Figure 6.4 shows the normalised force amplitude, F/F_{exp}, over the mesh refinement levels in terms of number of cells per sheet thickness in x-direction, N_x/d, and number of cells per wave height in z-direction, N_z/H. For the baffle implementation, the refinement level was only investigated in vertical z-direction as it has zero thickness. No result was obtained for 284 N_z/H since the skewness of the cells would have been excessive. For all other models, highly skewed cells have been avoided and mesh quality has been maintained.

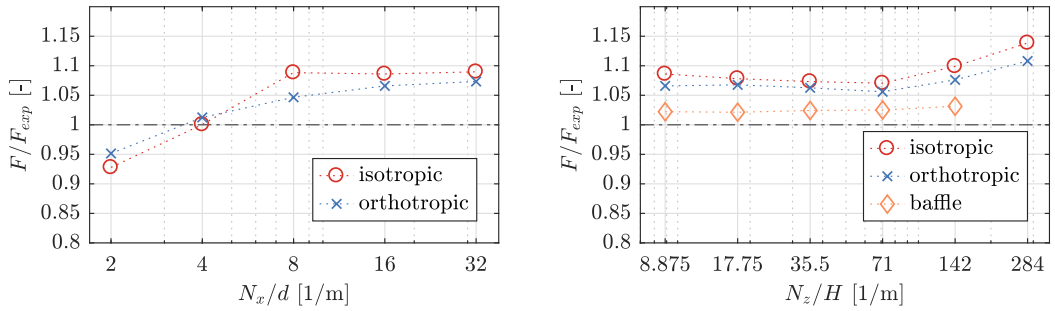

(a) refinement in horizontal x-direction

(b) refinement in vertical z-direction

Figure 6.4: Mesh independence study for the normalised horizontal force on the 2D sheet, F/F_{exp}, separate in terms of number of (a) cells per sheet thickness (where $d = 10$ mm) in horizontal x-direction (N_x/d) and (b) cells per wave height (where $H = 177.5$ mm) in vertical z-direction (N_z/H), containing the force results from models with all porosity implementations investigated.

Figure 6.4a indicates that 8 cells per sheet thickness, N_x/d, give a converged force amplitude, F, for the isotropic implementation. Further horizontal refinement has an insignificant effect. For the orthotropic implementation, convergence can be observed towards 32 N_x/d. The difference between 16 and 32 N_x/d is 3 % relative to the smaller value. No clear convergence behaviour can be determined from Fig. 6.4b for the number of cells per wave height in z-direction, N_z/H, for neither of the implementations. It

is not clear why the value of F in both porous-media implementations (isotropic and orthotropic) is seen to increase significantly for an increasing number of cells in vertical direction. A comparison of water velocity profiles along the water column for the gauges WG C1 and WG C2, 0.1 m before ($x = 7.90$ m) and 0.1 m after ($x = 8.10$ m) the sheet, inferred that smearing of the air-water interface due to the VOF interface-capturing method causes the observed increase in F for increasing cells. Based on the number of cells per sheet thickness, N_x/d, the profiles of the horizontal velocity component, u_x, and the profiles of the vertical component, u_z, require a minimum of 8 N_x/d for the isotropic and 16 N_x/d for the orthotropic implementation to achieve a reasonable converged profile in front of the sheet at WG C1. The vertical mesh size, N_z/H, has barely any influence on the velocity profiles, u_x and u_z, before and after the sheet for either the volumetric (isotropic and orthotropic) implementation and the baffle implementation. There are no significant differences after the sheet and only small deviations in front of it, where the largest deviations of u_z are located along the free-surface. Overall, these differences are considered to be insignificant and mostly related to the smeared nature of the phase interface.

For the following models, a mesh resolution corresponding to 16 N_x/d and 8.88 N_z/H was used for all volumetric models (both isotropic and orthotropic) and 8.88 N_z/H has been used for the models with the porous baffle. These values can serve as a guide for similar structures and wave conditions but the dependence is likely to change for different conditions, in particular for significantly deviating wave parameters.

6.3.2 Automatic Time-Stepping

For the models with porous-media implementations, the maximum CFL-number was set to 0.3, which provides accurate wave propagation, solver and scheme stability. This value results in $CFL \approx 0.1$ at the free-water surface away from the structure since this maximum CFL is strongly influenced by the fine mesh region around the sheet. This magnitude is in agreement with similar work on propagating waves, for example work by Roenby et al. [107] or Larsen et al. [111]. For the models with the porous-baffle implementation, a stable solution process could only be achieved with a maximum CFL of 0.05. This is suspected to be a direct result of the deficits in `interFoam`'s segregated pressure-velocity coupling algorithm [94, 112] in combination with the VOF method as implemented. In this context it is known that due to the large dynamic pressure and density gradients at the air-water interface, spurious velocities can be generated [69, 107, 109, 111]. Since the pressure-drop is a function of velocity, this can lead to unphysical spikes and even to a solver crash if the time step is not kept small enough.

6.3.3 Factors of Influence

Other factors that affect the results of the models including porous structures are the wave generation and absorption methods and numerical scheme and solver settings. If the level of wave reflections is large, the test section in the flume is disturbed and the ratio of wavelength to domain length and the relative position of the structure becomes important. Thus, the better the absorption method is, the less significant the lengths and positions are, and the smaller the domain can be. Those aspects have already been assessed for pure wave propagation in Section 5.3.

The solver and scheme settings applied for the simulations of pure wave propagation (as listed in Table A.1 in Appendix A) have also been used for the simulations with the static structures.

6.4 Assessment of the Options for Porosity Implementation

In the present work, the following porosity representations (shown in Fig. 2.11), have been assessed:

a) a simplified representation as isotropic material, where the coefficient is implemented as scalar (C_f);

b) an anisotropic implementation with the pressure-drop applied in direction normal to the sheet plane, where the coefficient is implemented as tensor with orthotropic characteristics ($\boldsymbol{C_f}$);

c) a porous baffle/surface.

The options b) and c) are in accordance with the assumptions of the porous resistance formulation being physically more accurate. Option a) is considered as a viable simplification. Potential differences between these three types of macro-scale porosity implementations are assessed in terms of qualitative flow visualizations, velocity profiles along the water column, the wave elevation near the structures and the horizontal force on the structures. For this assessment, only one combination of wave and geometrical parameters per structure have been investigated. Both structures had a porosity of $n = 0.2$ and the wave condition used was B06 from Table 4.1. The CFD results obtained from models with the different porosity implementations are compared against the experimental results, but mainly focus on the differences between the CFD results.

Differences between the experimental and CFD results are expected for two reasons. Firstly, the lengths of the physical flume and the NWT are different, which entails

differences in the interaction between the incident and reflected waves. All following figures of time series contain a vertical line that indicates the point in time when the wave has travelled across the NWT, been reflected at the tank end and reached the tank centre (or WG location) again. Secondly, the distance from the wave generation boundary to the sheet/cylinder in the CFD model is different to that in the physical tank. Thus, the experimental time series have been cropped to correspond with the CFD time series. Moreover, the ramping-up of the waves differs between the CFD and experiments, which leads to differences in the initial transient part of the records. Here, differences in the free-surface elevation, $\eta(t)$, directly result in deviations of the force response, $f(t)$. However, both the CFD and experimental results reach an approximately periodically-steady state.

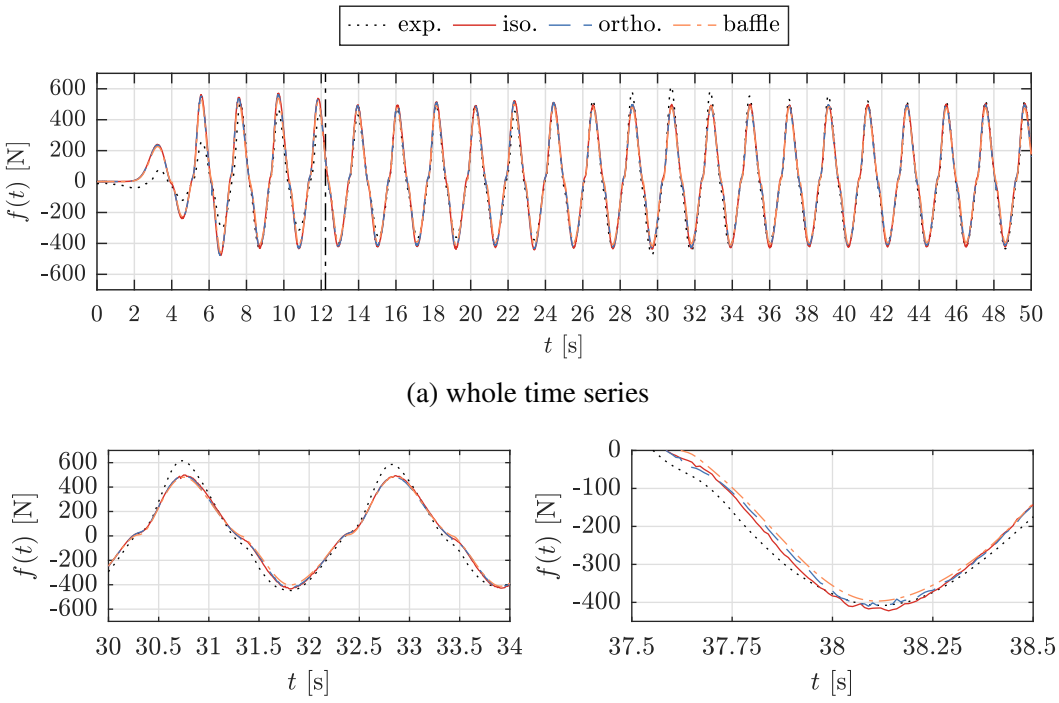

(a) whole time series

(b) section of the time series

(c) close-up of the time series

Figure 6.5: Comparison of the horizontal force on the porous 2D **sheet**, $f(t)$, for the investigated types of porosity implementation (isotropic and orthotropic porous media and porous baffle).

6.4.1 Force on the Sheet

The horizontal force on the structures is specified as the main parameter of interest. The results of the force on the sheet of the 2D model, which had a width of 0.01 m, have been scaled to match the width of 1 m of the physical flume.

A comparison between the time series of the horizontal force, $f(t)$, due to the

different types of porosity implementation is shown in Fig. 6.5.

All types of porosity implementation are capable of reproducing the shape of the time series, which exhibits a non-sinusoidal shape due to the quadratic pressure-drop. The notable deviations between the CFD and experimental results for the initial transient section of the time series in Fig. 6.5a are due the differences in the wave ramp-up between the numerical model and the physical wavemaker, discussed above. The experimental results are slightly contaminated with wave reflections, shown for a section of the time series in Fig. 6.5b. The numerical results exhibit a clean periodically steady-state after about $t = 24$ s. The numerical results agree well among each other. Only minor deviations can be observed at small local sections of the signal which are outlined for an example in Fig. 6.5c. The mean force amplitudes, F, of the CFD results are 391 N for the baffle implementation ($F/F_{exp} = 1.024$ where $F_{exp} = 382$ N), 408 N for the orthotropic implementation ($F/F_{exp} = 1.066$) and 416 N for the isotropic implementation ($F/F_{exp} = 1.086$).

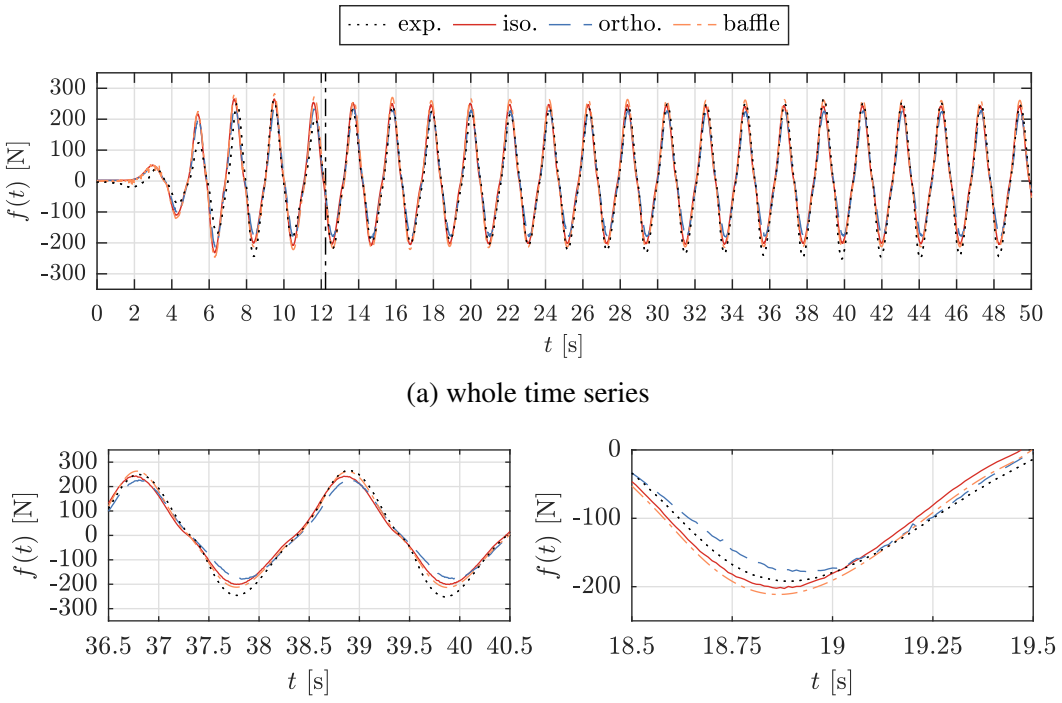

(a) whole time series

(b) section of the time series

(c) close-up of the time series

Figure 6.6: Comparison of the horizontal force on the **cylinder**, $f(t)$, for the investigated types of porosity implementation.

6.4.2 Force on the Cylinder

Next, the results of the horizontal force on the cylinder are assessed and the time series, $f(t)$, are shown in Fig. 6.6.

Also for the cylinder model, the initial transient period differs between the numerical and experimental results due to differences in the wave ramp-up. After the initial period, the CFD results exhibit a nearly periodically steady state due to negligible reflections in the NWT. The reflections are more noticeable for the experimental results. The non-linearity of the force on the cylinder is replicated by all CFD models and all types of porosity implementations. The overall force response is reproduced with reasonably good agreement between the numerical and experimental results, as shown in Fig. 6.6a. However, the deviations among the numerical results are larger for the cylinder than for the 2D sheet. The baffle implementation and the isotropic porous-media implementation agree well but the orthotropic porous-media implementation deviates more notably. This can be observed for a section and close-up of the time series in the Figs. 6.6b and 6.6c. The mean force amplitudes, F, of the CFD results are 219 N for the baffle implementation ($F/F_{exp} = 1.108$ where $F_{exp} = 197$ N), 189 N for the orthotropic implementation ($F/F_{exp} = 0.957$) and 205 N for the isotropic implementation ($F/F_{exp} = 1.039$).

6.4.3 Wave Gauges near the 2D Sheet

Next, the wave elevation, $\eta(t)$, at the WGs close to the structures is assessed. The whole time series for a physical runtime of 50 s and close-ups of selected sections of the signals are presented. Again, the vertical lines indicate the point in time when the wave has travelled across the NWT and back to the WGs.

The analysis of the WG results for the 2D model with the sheet focuses on the comparison between the CFD results. The comparison against the experimental results is omitted since the latter are suspected to be unreliable due to a raised section of the floor in the physical tank, previously discussed in Section 4.4. Figure 6.7 shows the water surface elevation, $\eta(t)$, for all types of porosity representation and for the WGs C1 and C2, which are placed 0.1 m before and 0.1 m after the sheet, respectively.

The time series match very well among all CFD results and for all types of porosity implementation. In particular, the close-ups exhibit that the results are nearly identical both before and after the sheet. At WG C1, 0.1 m before the sheet, the mean wave amplitudes, A, are 0.119 m for the baffle implementation ($A/A_{input} = 1.340$ where $A_{input} = 0.089$ m), 0.120 m for the orthotropic implementation ($A/A_{input} = 1.352$) and 0.120 m for the isotropic implementation ($A/A_{input} = 1.348$). At WG C2, 0.1 m after the sheet, A is 0.060 m for the baffle implementation ($A/A_{input} = 0.670$), 0.058 m for the orthotropic implementation ($A/A_{input} = 0.654$) and 0.058 m for the isotropic implementation ($A/A_{input} = 0.657$).

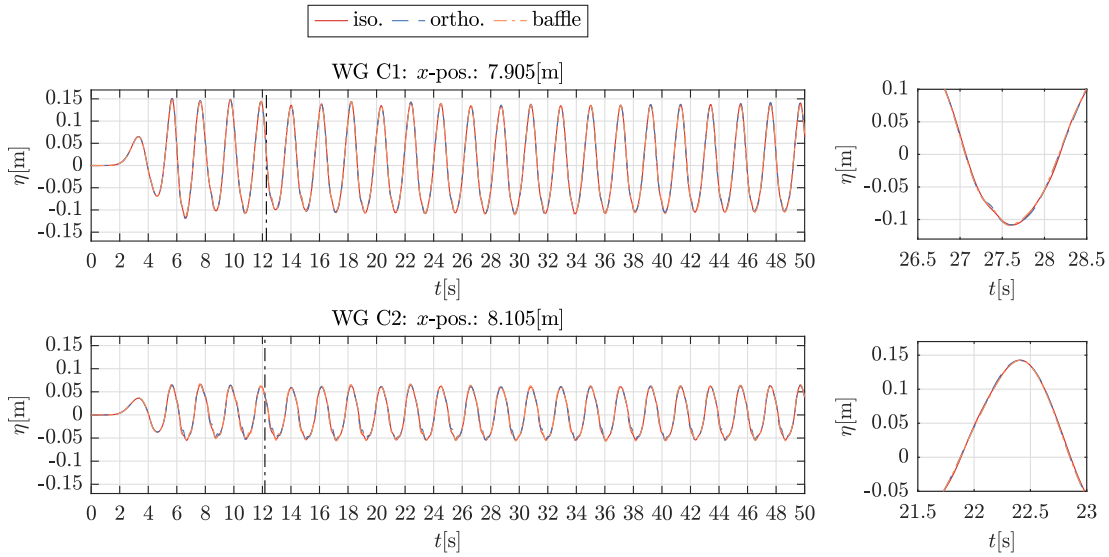

Figure 6.7: CFD results of the wave elevation, $\eta(t)$, at selected wave gauges close to the porous **sheet** for the investigated types of porosity implementations, including the whole time series and selected close-ups.

6.4.4 Wave Gauges near the Cylinder

For validation of the 3D model with the cylinder, the analysis includes experimental data. Figure 6.8 presents the wave elevation, $\eta(t)$, for the WGs shown in the sketch of Fig. 6.1a. Figure 6.8a shows the WG signals from the numerical results due to all types of porosity implementation and the experimental results further away from the cylinder. Figure 6.8b shows the WG results closer to the cylinder where WG B1 is positioned 0.5 m before the cylinder axis, WG B3 0.5 m behind the cylinder axis and WG B2 at the cylinder axis and centre.

Similarly to the time series of the force results, the figures exhibit differences at the initial transient section and wave reflections in the experimental results. Again, the overall agreement between CFD and experimental results is relatively good. The most noticeable differences can be observed between the CFD results for WG A3, positioned 1.6 m before the cylinder (Fig. 6.8a). This is suspected to be rooted in the different wave ramp-up between the numerical and physical flume. The isotropic implementation produces larger amplitudes after the wave has travelled across the tank and back to the centre. For the WG A4, 1.21 m after the cylinder, the results match very well. The time series for the WG B2 in the centre of the cylinder exhibits small ripples for all types of porosity implementation. The ripples are suspected to be a result of instabilities in the VOF phase-fraction (α)-field and to be related to the very fine mesh in the cylinder centre due to mesh generation procedures.

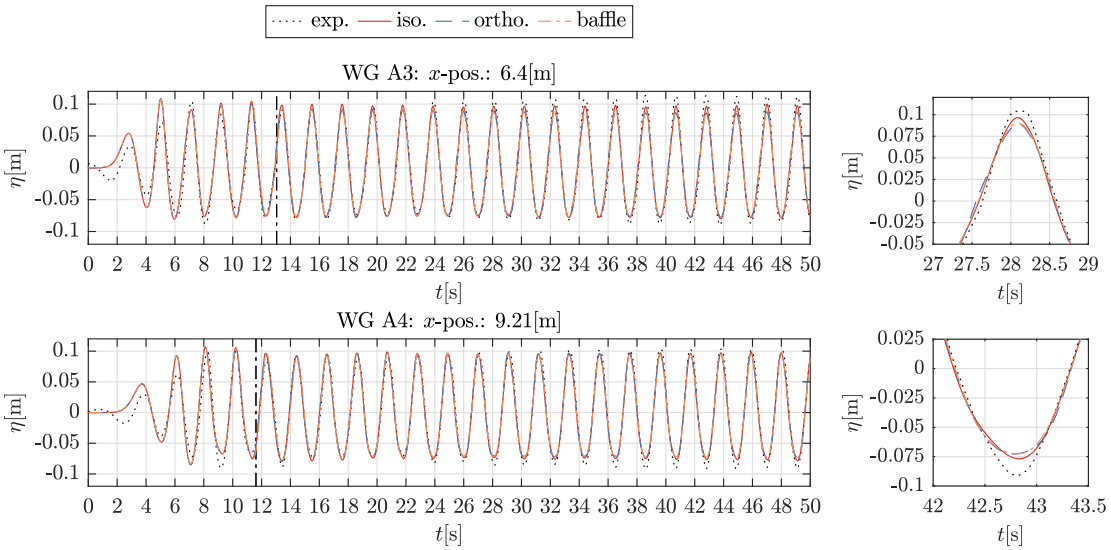

(a) comparison of the CFD and experimental results further away from the cylinder

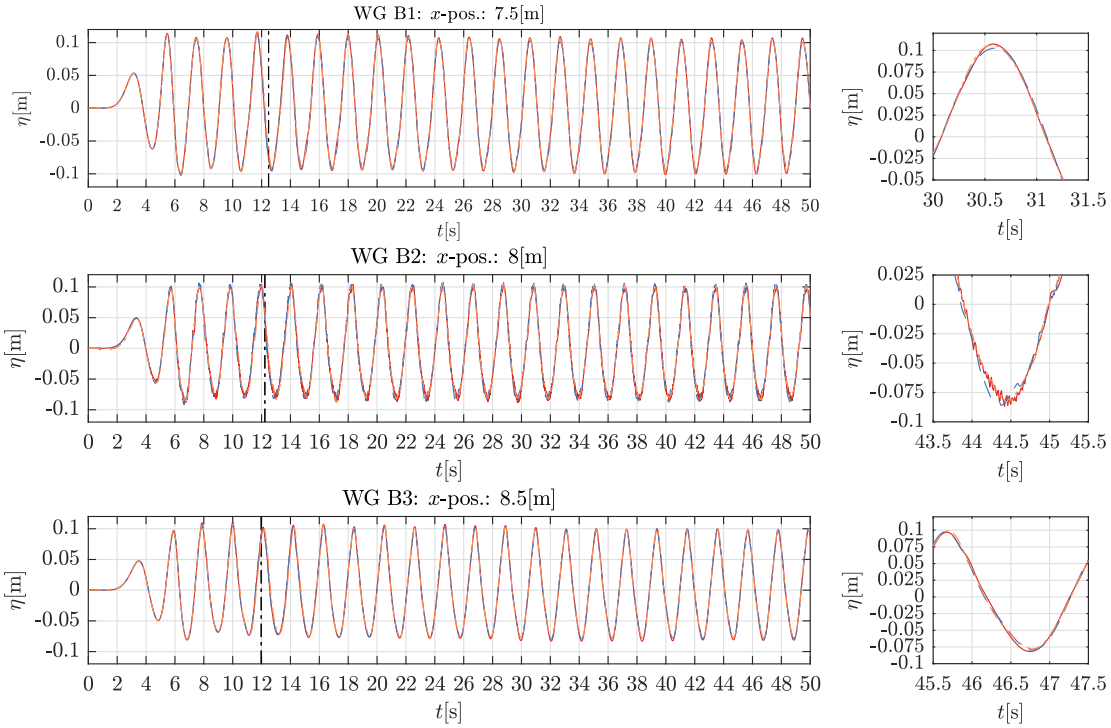

(b) comparison of the CFD results close to the cylinder (no experimental wave gauge results available)

Figure 6.8: Experimental and CFD results of the wave elevation, $\eta(t)$, at selected wave gauges close to the porous **cylinder** for all types of porosity implementation, including the whole time series and selected close-ups.

Normalised mean wave amplitudes Next, the normalised mean wave amplitudes, A/A_{input}, where $A_{input} = 0.089$ m is the CFD wave amplitude input, are analysed for all WG positions and all types of porosity implementation. The comparison between the mean amplitude results is shown in Fig. 6.9. For the WGs A1-A5, experimental results are included, for the WGs B1-B3 only CFD results are available.

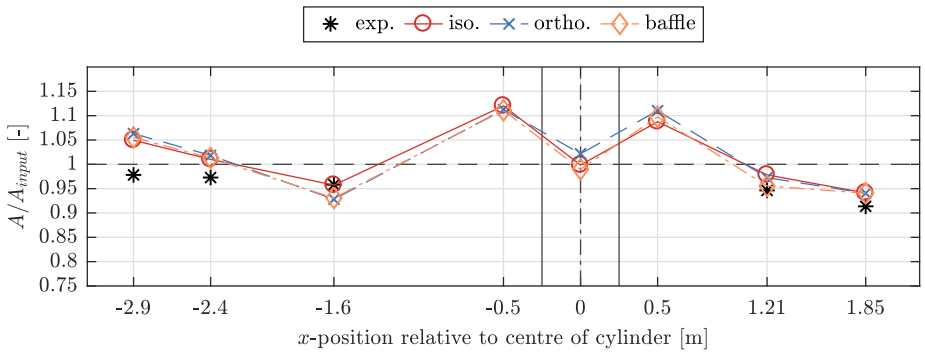

Figure 6.9: CFD and experimental results of the normalised mean wave amplitudes, A/A_{input}, for all wave gauges before and after the **cylinder**. The position of the centre of the cylinder is indicated with a dashed vertical line and the cylinder front and back are indicated with solid vertical lines.

The qualitative agreement between the experimental and all CFD results is relatively good at all WG positions. The deviations among the CFD results are small and do not exhibit clear patterns. The largest deviation of the mean amplitudes, A, among the CFD results is given at WG B2 at the tank centre at an x-position of 8.0 m. There, the largest value of $A = 0.0907$ m was obtained for the model with the orthotropic porous-media implementation. This results in a 3.23 % larger value than the smallest value of $A = 0.088$ m from the model with the porous baffle implementation. The smallest deviation has been obtained for the WG A5, 1.85 m after the cylinder centre at an x-position of 9.85 m. where all values result in a mean amplitude of $A = 0.084$ m ($A/A_{input} = 0.941$).

Overall, Fig. 6.9 shows that the porous cylinder represents a barrier to the flow that reduces the wave amplitude and free-surface level inside the cylinder and causes an increase and retention both before and after the cylinder. The waves are propagating from the LHS to the RHS, so the results of A/A_{input} are larger in front of the cylinder compared to the values after the cylinder. Since the used porosity of $n = 0.2$ is relatively small, these patterns are exhibited clearly. With increasing porosity values the imposed momentum resistance decreases, the water can pass through the cylinder easier, and the values of A/A_{input} are expected to be more balanced between the inner and outer region around the cylinder.

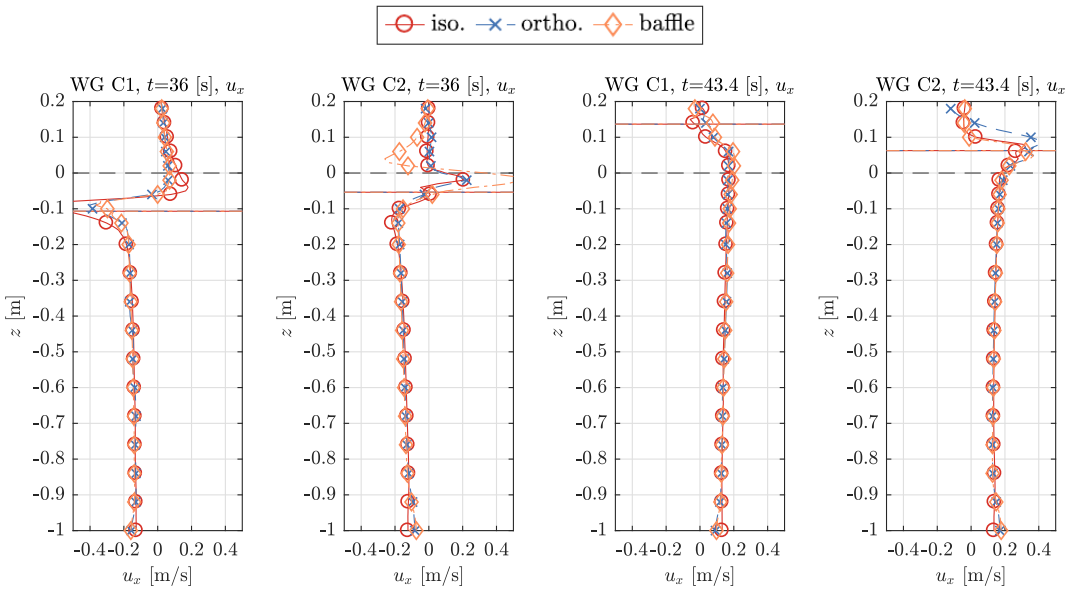

(a) u_x at WG C1 for a wave trough

(b) u_x at WG C2 for a wave trough

(c) u_x at WG C1 for a wave crest

(d) u_x at WG C2 for a wave crest

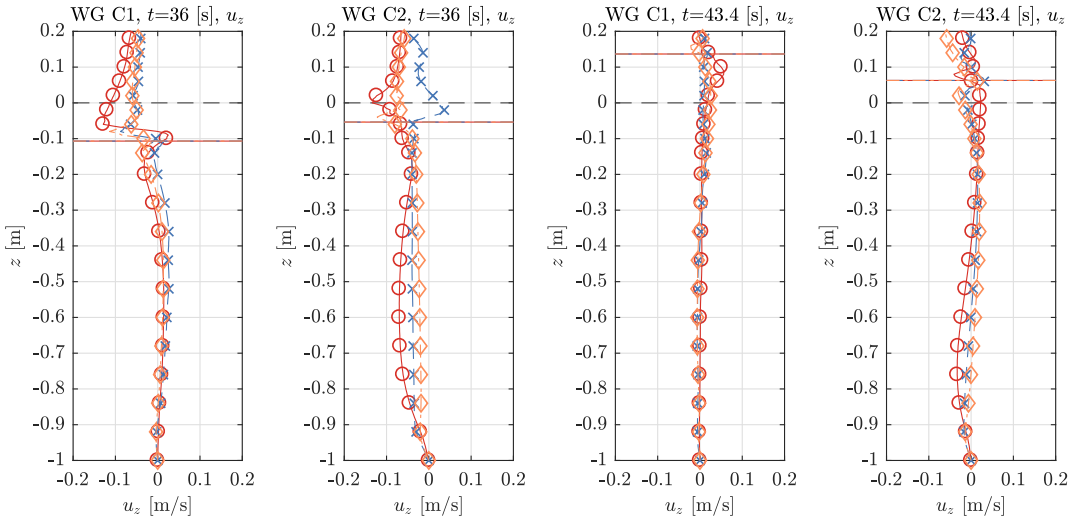

(e) u_z at WG C1 for a wave trough

(f) u_z at WG C2 for a wave trough

(g) u_z at WG C1 for a wave crest

(h) u_z at WG C2 for a wave crest

Figure 6.10: Velocity profiles in horizontal, u_x (a-d), and vertical, u_z (e-h) direction 0.1 m before (WG C1) and 0.1 m after (WG C2) the **sheet** for a wave **trough** ($t = 36$ s - a,b,e,f) **and crest** ($t = 43.4$ s - c,d,g,h,) at the sheet. Note that the x-axis scales range between -0.5 and 0.5 for the horizontal profile, u_x (a-d), and between -0.2 and 0.2 for the vertical profiles, u_z. Since local spurious velocities can be very high (»1 m/s) in the air just above the free-surface, it is not viable to include the whole profile in all figures. So for clarity, the x-scales have been kept the same and those very local data points are outside the axis bounds.

6.4.5 Velocity Profiles near the 2D Sheet

The velocity profiles are assessed by means of a comparison between the CFD results from models with different types of porosity implementations. The positions of the velocity profiles correspond to the WG positions around both the sheet and cylinder, see Fig. 6.1a. A limited number of selected profiles and points in time are presented for one wave trough and one wave crest each. These indicate the overall trend of results.

Figure 6.10 shows examples of the velocity profiles of the horizontal component, u_x, and the vertical component, u_z, with a distance of 0.1 m before (WG C1) and after (WG C2) the sheet. The dashed black horizontal lines indicate the mean water surface level with a water depth of $h = 1.0$ m. The continuous coloured horizontal lines represent the instantaneous water level at a specific time step. Both the horizontal and vertical velocity profiles, u_x and u_z, cover the whole water column and a section of the air phase above the water level. Note that the x-axis scales range between -0.5 and 0.5 m/s for all horizontal profiles, u_x, and between -0.2 and 0.2 m/s for all vertical profiles, u_z. Since velocities in horizontal x-direction can be locally very high (»1 m/s) in the air just above the free-surface, it is not viable to include these data points in all figures, see for instance Fig. 6.10a. Instead and for clarity, the x-scales have been kept within the stated range and it was accepted that those very local data points are outside the axis bounds.

It can be observed that the largest differences are present for the horizontal velocities, u_x, along the air-water interface with the largest values in the air just above the water surface. Some local high velocities are unphysical and a direct result of the large pressure and density gradients at the phase interface due to the segregated solution algorithm for the pressure-velocity coupling, already introduced in Section 2.2.

Excluding the profile section in the air from the analysis, the agreement of the profiles in the water column match with insignificant differences for both the horizontal and vertical component, u_x and u_z. The largest deviations have been obtained for the vertical velocity profile, u_z, 0.1 m after the sheet.

6.4.6 Velocity Profiles near the Cylinder

Figure 6.11 exhibits the velocity profiles, u_x and u_z, for $t = 36.0$ s, where a wave trough passes the cylinder centre. Figure 6.12 shows the same for $t = 43.4$ s at a wave crest. Again, the dashed black and coloured horizontal lines indicate the initial flat and instantaneous water levels, respectively.

Both Figs. 6.11 and 6.12 indicate similar patterns of locally large velocity values close to the air-water interface. For clarity, not all data points and profile sections are shown in the selected sub-figures, since some values are »1 m/s locally. This is for instance indicated in Fig. 6.11e.

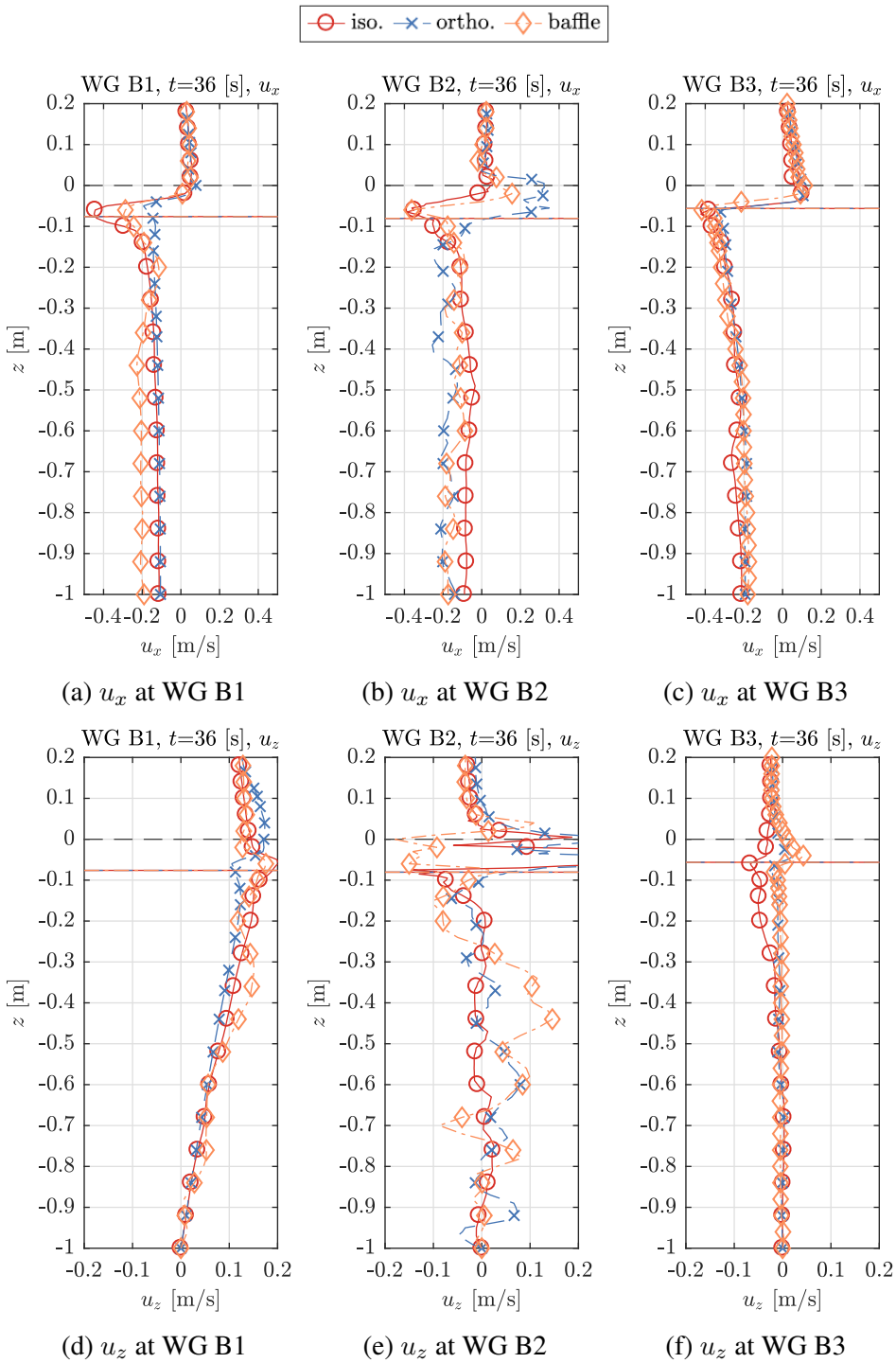

(a) u_x at WG B1 (b) u_x at WG B2 (c) u_x at WG B3

(d) u_z at WG B1 (e) u_z at WG B2 (f) u_z at WG B3

Figure 6.11: Velocity profiles in horizontal, u_x (a-c), and vertical, u_z (d-f), direction at the **cylinder** centre (WG B2 - b,e), 0.5 m before (WG B1 - a,d) and 0.5 m after (WG B3 - c,f) the axis for a wave **trough** ($t = 36$ s) at the cylinder centre. Note that the x-axis scales range between -0.5 and 0.5 for the horizontal profile, u_x (a-d), and between -0.2 and 0.2 for the vertical profiles, u_z. Since local spurious velocities can be very high (»1 m/s) in the air just above the free-surface, it is not viable to include the whole profile in all figures. So for clarity, the x-scales have been kept the same and those very local data points are outside the axis bounds.

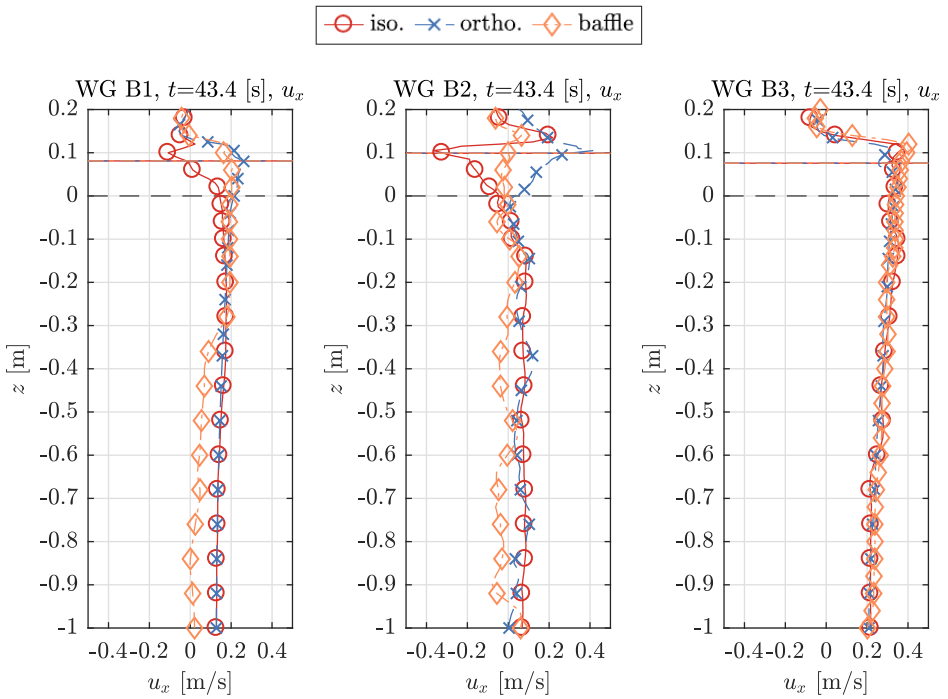

(a) u_x at WG B1 (b) u_x at WG B2 (c) u_x at WG B3

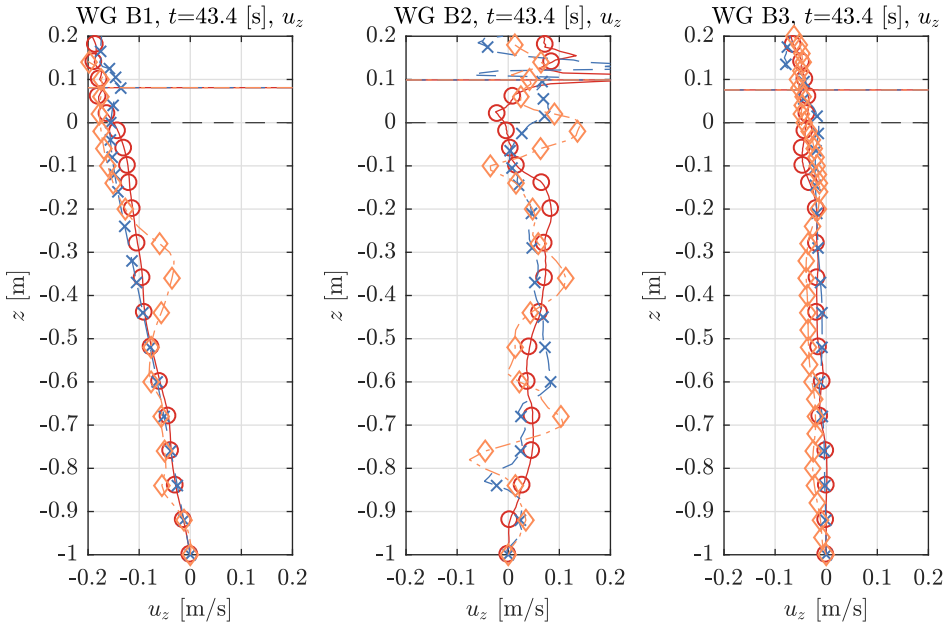

(d) u_z at WG B1 (e) u_z at WG B2 (f) u_z at WG B3

Figure 6.12: Velocity profiles in horizontal, u_x (a-c), and vertical, u_z (d-f), direction at the **cylinder** centre (WG B2 - b,e), 0.5 m before (WG B1 - a,d) and 0.5 m after (WG B3 - c,f) the axis for a wave **crest** ($t = 43.4$ s) at the cylinder centre. Note that the x-axis scales range between -0.5 and 0.5 for the horizontal profile, u_x (a-d), and between -0.2 and 0.2 for the vertical profiles, u_z. Since local spurious velocities can be very high (»1 m/s) in the air just above the free-surface, it is not viable to include the whole profile in all figures. So for clarity, the x-scales have been kept the same and those very local data points are outside the axis bounds.

The overall differences between the results due to the different porosity implementations are relatively small, both before (WG B1) and after (WG B3) the cylinder. At the cylinder centre at WG B2, the profiles exhibit significant scatter for both the horizontal and vertical component, u_x and u_z, so no clear trend can be identified from these results. The chaotic behaviour of the velocity field at WG B2, see Figs. 6.11b, 6.11e, 6.12b and 6.12e, corresponds to the spiky appearance of the wave elevation signals, shown in Fig. 6.8. This correspondence indicates that the chaotic flow field inside the cylinder is due to sloshing effects.

The differences between the results are the smallest for WG B3 after the cylinder and 0.5 m after the cylinder axis, respectively. At WG B1, 0.5 m in front of the cylinder axis, the profiles obtained from the porous-media models, both isotropic and orthotropic, match with insignificant deviations. The profiles due to the baffle-implementation deviate more notably from both porous-media implementations.

6.4.7 Flow Visualization near the Cylinder

To assess potential differences between the flow field due to different types of porosity implementations, the velocity vectors have been inspected qualitatively on a horizontal cross section across half of the cylinder. The cross section is represented by a 0.05 m thick horizontal slice of the domain that ranges from $z = 0.75$-0.80 m. The initial flat water level was at $z = h = 1.0$ m. In Fig. 6.13 the velocity vectors are shown for all types of investigated porosity implementations for two points in time. On the left, the flow field is presented for $t = 36.0$ s which corresponds to a wave trough at the cylinder centre and on the right for $t = 43.4$ s which corresponds to a wave crest.

Despite the very good agreement between all numerical results in terms of the force response and the flow field further away from the structures, differences are present for the flow field very close to the structure. From a qualitative point of view, the isotropic porosity implementation seems to produce flow patterns that are smoother compared to the orthotropic porous media and porous-baffle methods. In particular the orthotropic implementation creates a more chaotic flow field and higher local velocities (for identical meshes), see Fig. 6.13b. This could explain the reason for the requirement of smaller time steps in order to meet the target maximum CFL-number during the automatic time stepping process, which increases the computational time for the orthotropic implementation. The flow patterns agree better between the isotropic porous-media and the baffle implementation, see Figs. 6.13a and 6.13c. This corresponds to a better match of the force results between the isotropic and baffle implementations, see Fig. 6.6. The orthotropic implementation results in larger deviations for both the force results and the qualitative flow field (Fig. 6.13b).

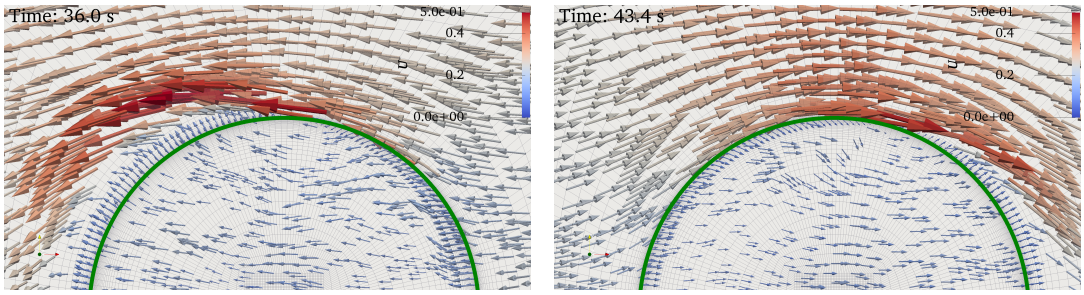

(a) isotropic porous-media implementation

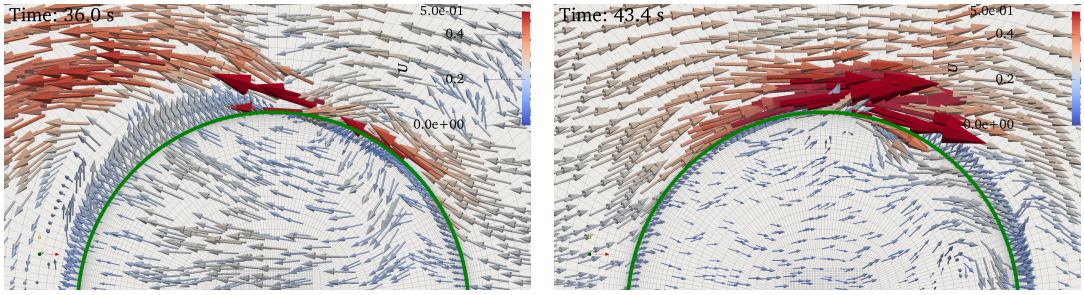

(b) orthotropic porous-media implementation

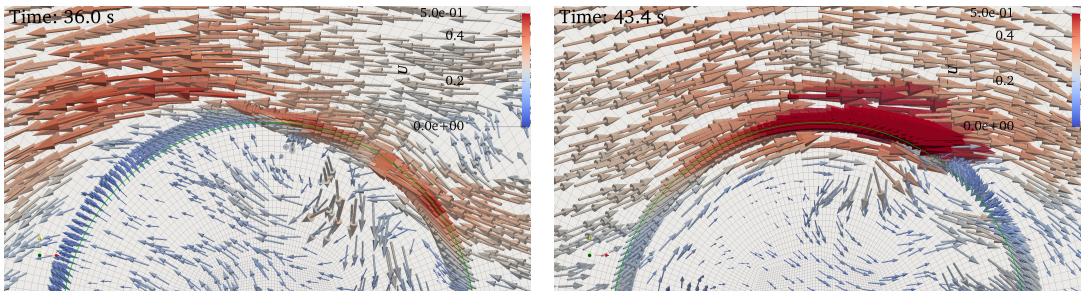

(c) baffle implementation

Figure 6.13: Velocity vectors for two points in time, $t = 36.0$ s at a wave trough (on the left) and $t = 43.4$ s at a wave crest (on the right) at the cylinder centre. The waves propagate from the left to the right. The velocity magnitude, indicated by the size and colour of the velocity vectors, ranges between 0.0-0.5 m/s.

6.4.8 Tabular Summary

A summary of the main results is given in Table 6.1. It shows the results of the mean force amplitudes, F, and the mean wave amplitudes, A, at the WGs for both the 2D and 3D model, and includes the mesh cell number and approximate execution times for each model due to the different porosity implementations.

All models were simulated for 50 s of physical runtime on 14-core dual Intel(R) Xeon(R) Gold 5120 CPU @ 2.20GHz processors. The 2D models with the sheets were run on a single core. For the 3D models with the cylinder 28 CPUs were used.

Table 6.1: Summary of the normalised mean force amplitude results, F/F_{exp}, and the normalised mean wave amplitude results, A/A_{input} at the WGs, including mesh cell number and execution times for all static models. The execution time is stated for a physical runtime of 50s.

Model	**2D sheet**			**3D cylinder**		
Porosity Impl.	**iso.**	**ortho.**	**baffle**	**iso.**	**ortho.**	**baffle**
Number of Cells	68,890	68,890	68,060	9.84 MIO	9.84 MIO	7.19 MIO
Max. CFL	0.3	0.3	0.05	0.3	0.3	0.05
Used CPUs	1	1	1	28	28	28
Execution Time	6.6 h	7.8 h	1 d 9.9 h	8 d 14.1 h	13 d 2.7 h	72 d 17 h
F/F_{exp}	1.086	1.066	1.024	1.039	0.957	1.108
A/A_{input}						
WG A1	1.307	1.312	1.305	1.049	1.063	1.055
WG A2	1.207	1.203	1.207	1.020	1.018	1.013
WG A3	0.654	0.656	0.687	0.957	0.928	0.931
WG A4	0.640	0.641	0.660	0.978	0.941	0.941
WG A5	0.633	0.637	0.657	0.941	0.941	0.941
WG B1	-	-	-	1.120	1.113	1.111
WG B2	-	-	-	0.999	1.022	0.990
WG B3	-	-	-	1.088	1.110	1.098
WG C1	1.348	1.352	1.340	-	-	-
WG C2	0.657	0.654	0.670	-	-	-

6.5 Assessment of the Effect of Turbulence Models

The effects of local turbulence generation and related losses caused by flow separation across the porous barrier are taken into account by the theoretical pressure-drop model and the structure's representation as continuous medium.

No large-scale turbulence effects are expected for the present physical conditions and the effects of applying a turbulence model are presumed to be insignificant. However, since turbulence modelling is the core of the RANS method, the hypothesis of the validity of omitting a model is still assessed.

In the following, the effect of turbulence models in combination with the investigated porosity implementations (isotropic and orthotropic porous media, and the baffle implementation) has been assessed in three variations:

- with a laminar setup without a turbulence model (as used so far);
- with the k-ω-SST turbulence model by Menter [93]; and
- with the stabilized k-ω model by Larsen and Fuhrman [166] (in the following

denoted as k-ω-stable and abbreviated as k-ω-st.).

The k-ω-SST turbulence model can be considered as an industry standard for a wide range of applications and is therefore a standard implementation in OF. The k-ω-stable model is not included in OF since it is a specific model tuned for potential-flow wave propagation. Therefore, it had to be linked to the present modelling. Both models have already been introduced in Section 2.2.4 and Section 2.3.3, respectively. For the 2D model with the sheet all combinations have been simulated and compared against each other. For the 3D model with the cylinder, the investigation in combination with the baffle implementation has been cancelled because of the requirement of a very small time step size. For the laminar setup, the baffle implementation entailed by far the longest execution times (see Table 6.1). With the application of a turbulence model, the execution times would further have significantly increased making this setup an unviable option.

Due to the longer execution times with turbulence models, the physical runtimes have been reduced from 50 s to 30 s. As before, only one combination of wave and geometrical parameters has been investigated. Both structures had a porosity of $n = 0.2$ and the wave condition used was B06 from Table 4.1. The forces on the structures, the wave elevation at WGs and velocity profiles near the structures are compared between the CFD results and against the experimental data (where available).

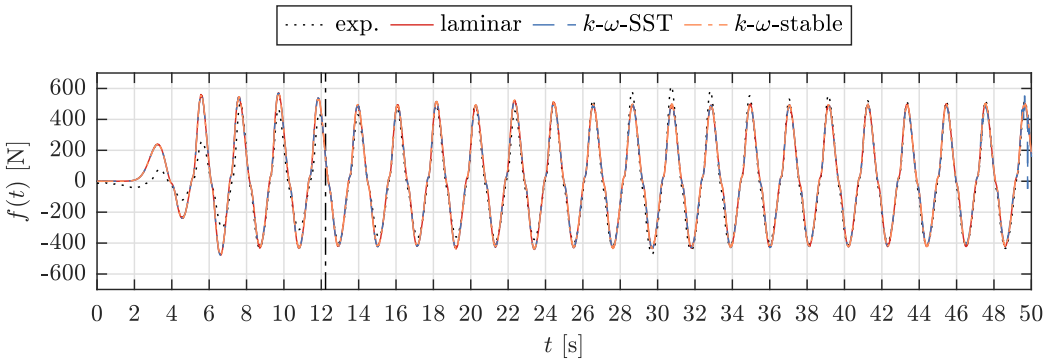

(a) whole time series

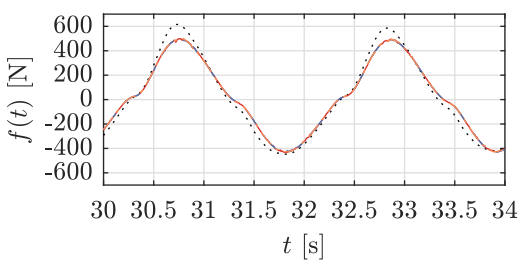

(b) section of the time series

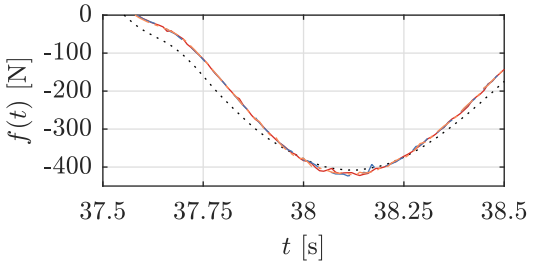

(c) close-up of the time series

Figure 6.14: Comparison of the horizontal force on the porous 2D **sheet**, $f(t)$, for the **isotropic** porosity implementation with the investigated turbulence settings.

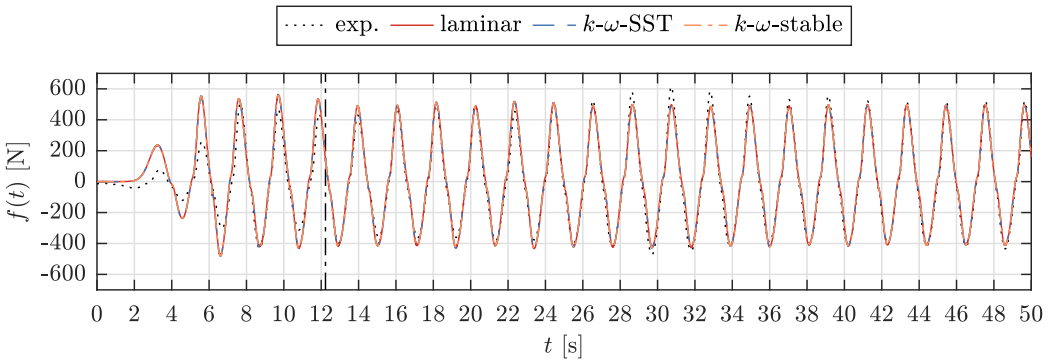

(a) whole time series

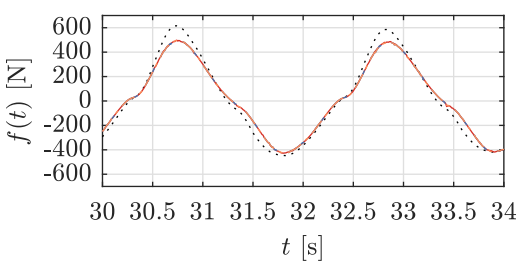

(b) section of the time series

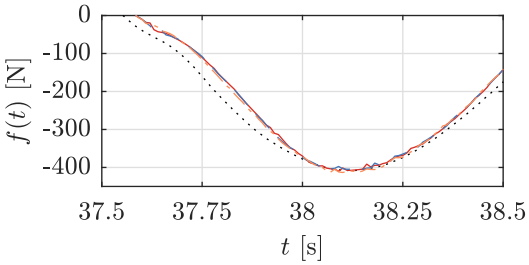

(c) close-up of the time series

Figure 6.15: Comparison of the horizontal force on the porous 2D **sheet**, $f(t)$, for the **orthotropic** porosity implementation with the investigated turbulence settings.

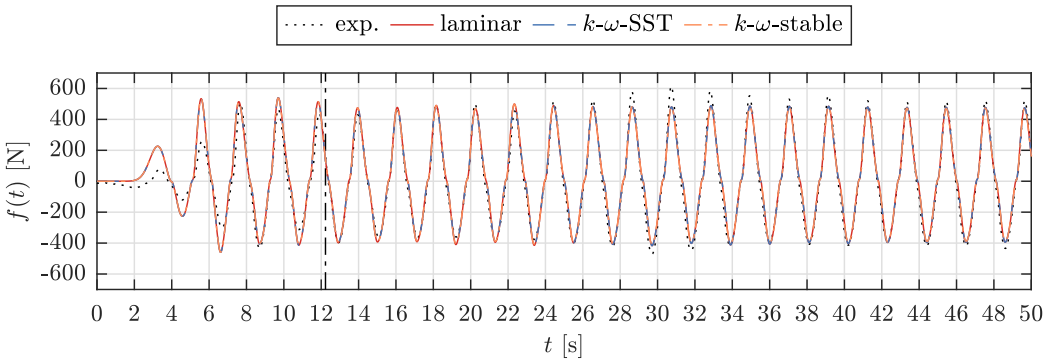

(a) whole time series

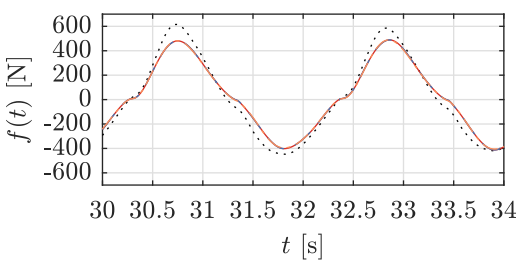

(b) section of the time series

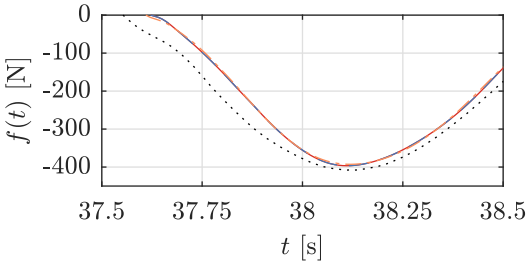

(c) close-up of the time series

Figure 6.16: Comparison of the horizontal force on the porous 2D **sheet**, $f(t)$, for the **baffle implementation** with the investigated turbulence settings.

6.5.1 Force on the Sheet

A comparison between the time series of the horizontal force on the sheet, $f(t)$, for models with the investigated turbulence settings are shown in the following figures. Figure 6.14 shows the results for the isotropic, Fig. 6.15 for the orthotropic and Fig. 6.16 for the baffle implementation. The vertical lines indicate the point in time when the wave has travelled across the tank and back to the centre.

Figures 6.14-6.16 show that the application of neither the k-ω-SST nor the k-ω-stable turbulence model has significant effect on the horizontal force on the vertical sheet. The deviations from the experimental results root in the differences between the numerical and physical wave ramp-up and the different amount of wave reflections, as previously discussed in Section 6.4.

The CFD time series are almost identical, but the mean force amplitudes, F, vary slightly. For the isotropic implementation, the application of both turbulence models leads to smaller force amplitudes. No clear pattern can be observed for the orthotropic porous-media and the baffle implementations. Without the use of a filter, the mean force amplitudes, F, of the CFD results for the models with isotropic porosity are 416 N for the laminar setup ($F/F_{exp} = 1.086$ where $F_{exp} = 383$ N), 409 N for the model with the k-ω-SST model ($F/F_{exp} = 1.069$) and 415 N for the model with the k-ω-stable turbulence model ($F/F_{exp} = 1.030$). The force results for the models with orthotropic porosity are 408 N for the laminar setup ($F/F_{exp} = 1.066$), 407 N for the model with the k-ω-SST model ($F/F_{exp} = 1.064$) and 412 N for the model with the k-ω-stable turbulence model ($F/F_{exp} = 1.076$). The force results for the models with the baffle implementation are 392 N for the laminar setup ($F/F_{exp} = 1.024$), 394 N for the model with the k-ω-SST model ($F/F_{exp} = 1.029$) and 391 N for the model with the k-ω-stable turbulence model ($F/F_{exp} = 1.022$). A summary of the results is presented below in Table 6.2. A signal filter is omitted on purpose to highlight the effect of applying turbulence models. The deviations of F for the CFD models with turbulence models are caused by the spiky characteristics of the signals (shown in Fig. 6.14c-6.16c) which root in the additional turbulent eddy viscosity applied in local regions of larger velocity gradients (according to Boussinesq's hypothesis as introduced in Section 2.2.4). The generation of turbulence equals additional resistance that affects the calculation of the force on the porous structure by means of a pressure-drop across the structure, as explained in Section 3.2.3. Thus, local turbulence spikes can lead to local pressure spikes that cause slight spikes on the overall force time series.

6.5.2 Force on the Cylinder

Next, the results of the horizontal force on the cylinder are assessed and the time series, $f(t)$, are shown in Fig. 6.17 for the isotropic and in Fig. 6.18 for the orthotropic implementation.

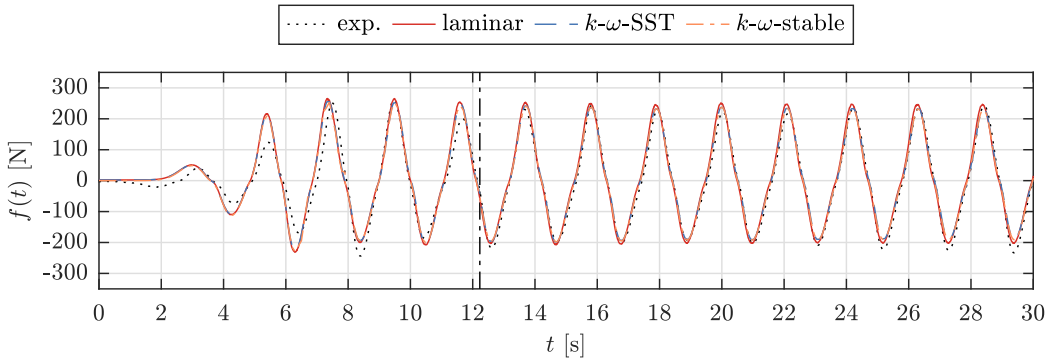

(a) whole time series

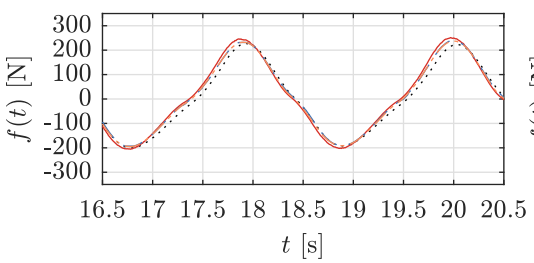

(b) section of the time series

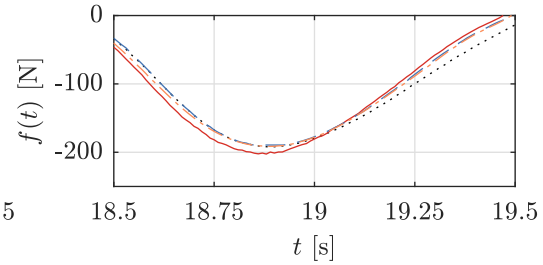

(c) close-up of the time series

Figure 6.17: Comparison of the horizontal force on the porous **cylinder**, $f(t)$, for the **isotropic** porosity implementation with the investigated turbulence settings.

The deviations among the numerical results are larger for the cylinder than for the 2D sheet. The results for the isotropic porous-media implementation agree better with the experimental results than those with the orthotropic implementation. For both types of porosity implementation, the application of turbulence models leads to smaller force amplitudes. Without the use of a filter, the mean force amplitudes, F, of the CFD results for the models with isotropic porosity are 205 N for the laminar setup ($F/F_{exp} = 1.039$), 196 N for the model with the k-ω-SST model ($F/F_{exp} = 0.995$) and 194 N for the model with the k-ω-stable turbulence model ($F/F_{exp} = 1.982$). The force results for the models with orthotropic porosity are 189 N for the laminar setup ($F/F_{exp} = 0.957$), 161 N for the model with the k-ω-SST model ($F/F_{exp} = 0.814$) and 162 N for the model with the k-ω-stable turbulence model ($F/F_{exp} = 0.822$).

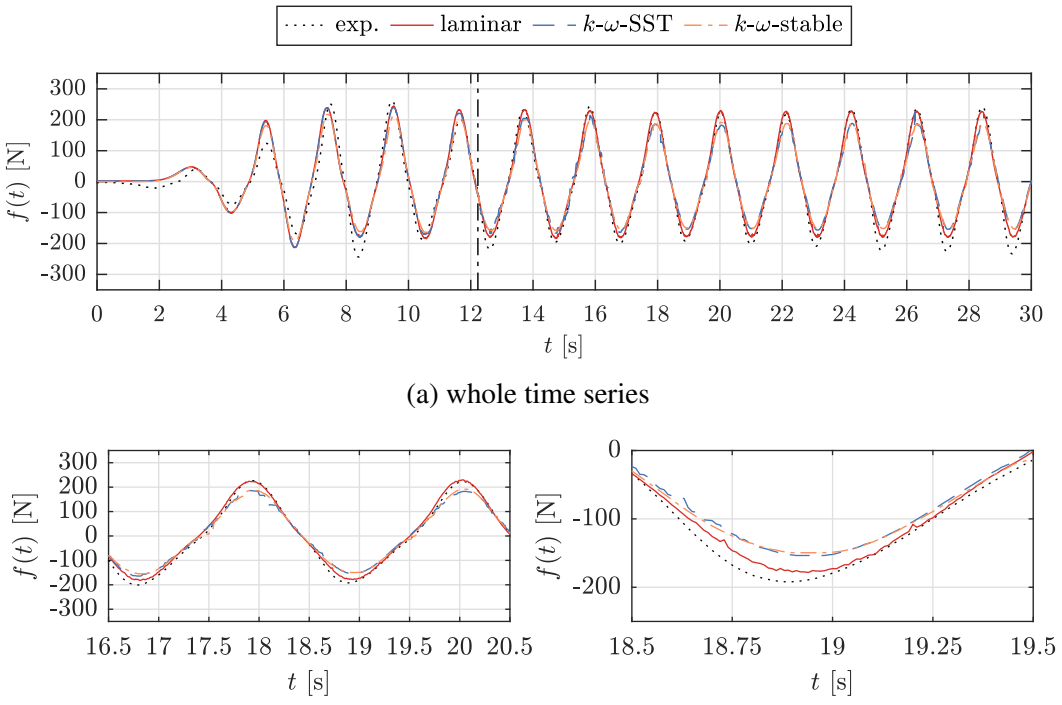

(a) whole time series

(b) section of the time series

(c) close-up of the time series

Figure 6.18: Comparison of the horizontal force on the porous **cylinder**, $f(t)$, for the **orthotropic** porosity implementation with the investigated turbulence settings.

6.5.3 Wave Gauges near the 2D Sheet

As before, the wave elevation, $\eta(t)$, at the WGs close to the structures is assessed for the 2D models with different turbulence settings and with a focus on the comparison between the CFD results.

Figures 6.19-6.21 show the wave elevation, $\eta(t)$, for the WGs C1 and C2 which are placed 0.1 m before and 0.1 m after the sheet, respectively. Figure 6.19 shows the results of the models with the isotropic, Fig. 6.20 for the orthotropic porous-media implementation and Fig. 6.21 for the baffle implementation.

Similar to the force results, the application of any of the investigated turbulence models has negligible effect on the WG results and large-scale free surface behaviour. In particular, the close-ups exhibit that the results are nearly identical both before and after the sheet. The results of the normalised mean wave amplitudes, A/A_{input}, for all WGs around the 2D sheet are presented in Table 6.2.

6.5.4 Wave Gauges near the Cylinder

For the 3D model with the cylinder, the analysis of the results due to different turbulence settings covers the comparison among the CFD results and against the experimental

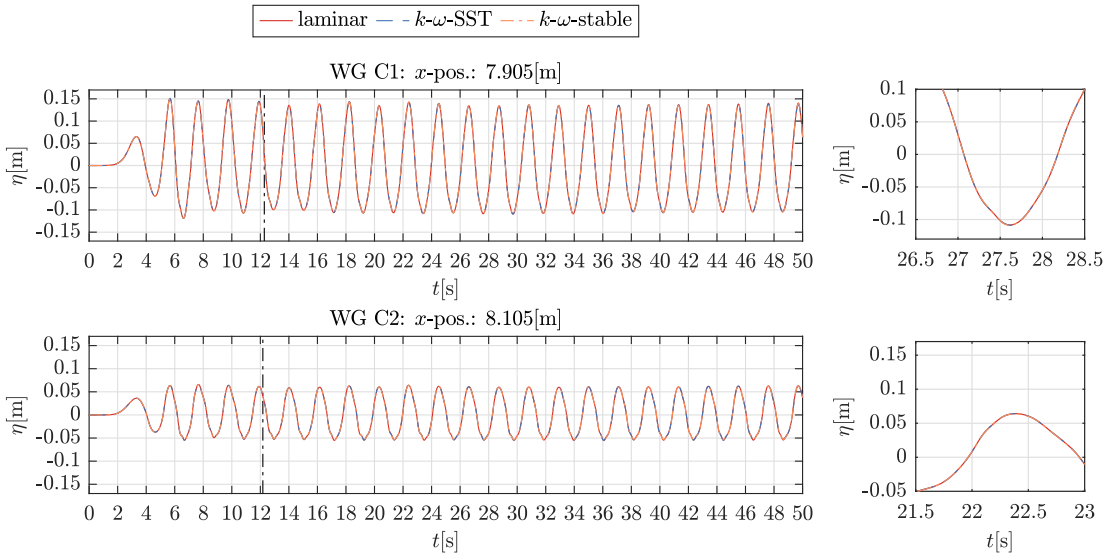

Figure 6.19: CFD results of the wave elevation, $\eta(t)$, at selected wave gauges close to the porous **sheet** for the models with **isotropic** porosity implementation and the investigated turbulence settings, including the whole time series and selected close-ups.

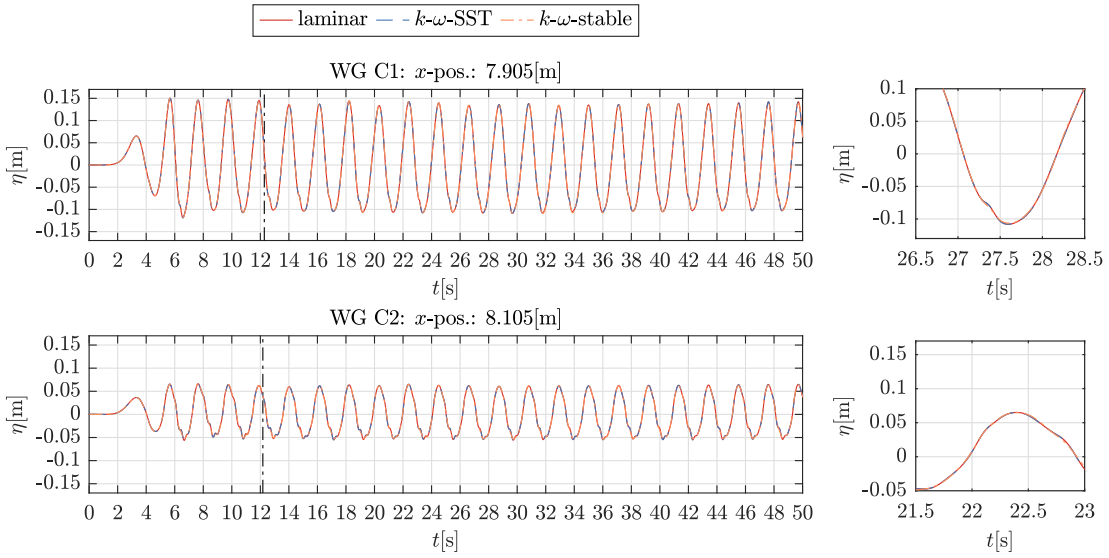

Figure 6.20: CFD results of the wave elevation, $\eta(t)$, at selected wave gauges close to the porous **sheet** for the models with **orthotropic** porosity implementation and the investigated turbulence settings, including the whole time series and selected close-ups.

data. Figure 6.22a presents the time series of the wave elevation, $\eta(t)$, for the models with isotropic porosity implementation. Figure 6.23 shows the same WG signals for the models with the orthotropic porosity implementation. As shown in Fig. 6.1a, WG B1 is positioned 0.5 m before the cylinder axis, WG B3 0.5 m behind the cylinder axis and WG B2 at the cylinder axis and centre. The WGs with index A have experimental measurements. WG A3 is located 1.6 m before the cylinder axis and WG A4 is located

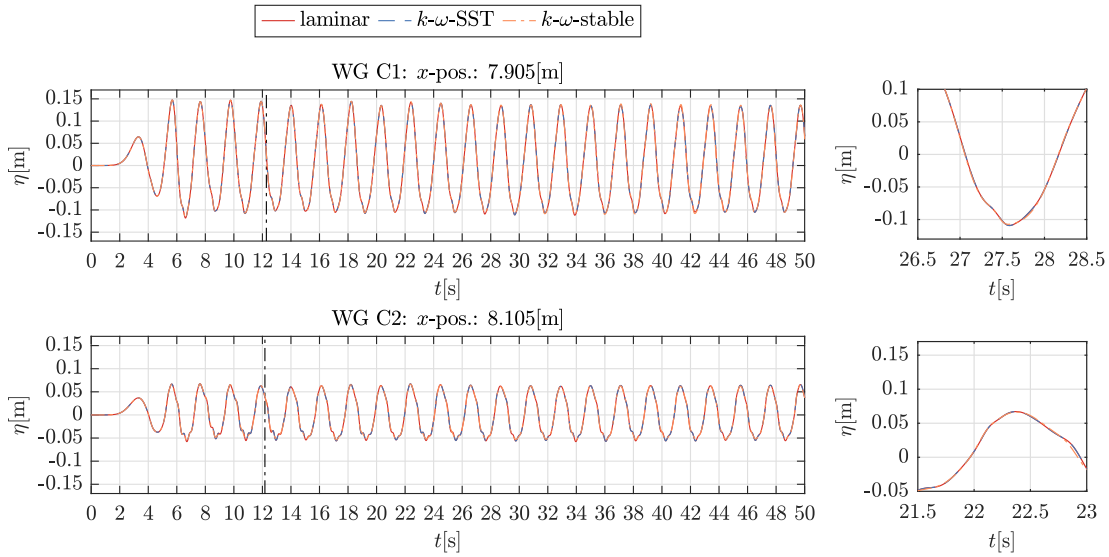

Figure 6.21: CFD results of the wave elevation, $\eta(t)$, at selected wave gauges close to the porous **sheet** for the models with **baffle implementation** and the investigated turbulence settings, including the whole time series and selected close-ups.

1.85 m after the axis.

Time series for the isotropic porous media implementation The overall agreement between the CFD and the experimental results for the models with isotropic porosity implementation is relatively good. However, the signals of the CFD models with both turbulence models exhibit unsteady spikes. Particularly, the time series for WG B2 in the centre of the cylinder exhibits significant spikes. This is suspected to be related to the instabilities caused by the VOF method which was already observed for the models without a turbulence model applied. Here, the instabilities have occurred in combination with the very fine mesh resolution in the cylinder centre as a consequence of mesh generation procedures. It is suspected that this effect is amplified with the application of a turbulence model. A very smeared air-water interface is generated that does not allow for a reliable WG trace. It can be observed that the spikes are the most significant for the model with the k-ω-stable turbulence model. It is unclear why this is affects the model with the k-ω-stable turbulence model significantly more than the model with the k-ω-SST turbulence model. A more detailed investigation is considered to be outside the scope of this thesis, but may be an interesting topic to explore in the future.

Time series for the orthotropic porous media implementation The overall agreement between the CFD and the experimental results for the models with orthotropic porosity implementation is as good as with the isotropic porosity implementation. In contrast to the results with isotropic porosity, the orthotropic results are not affected by

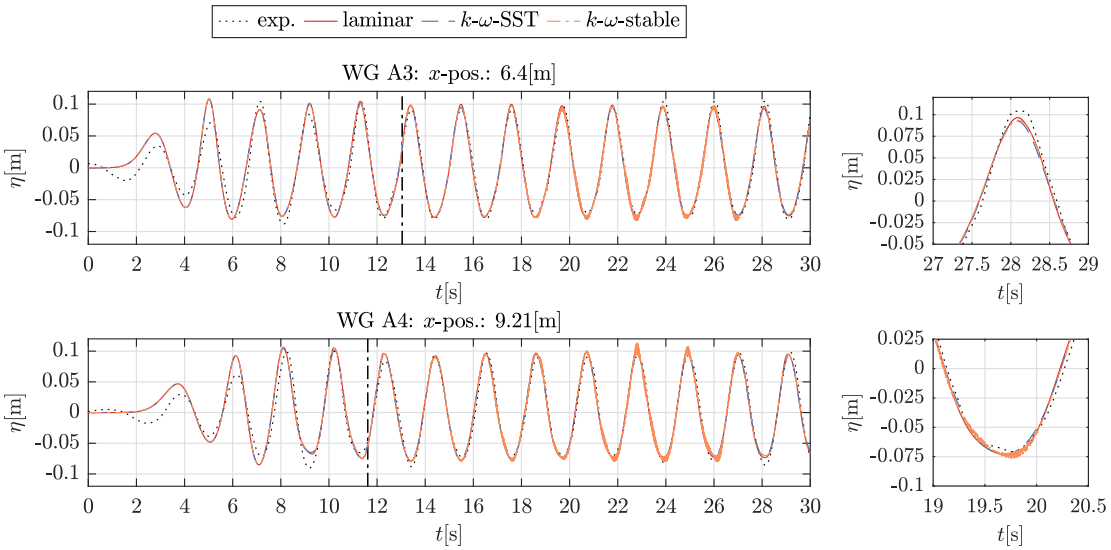

(a) comparison of the CFD and experimental results further away from the cylinder

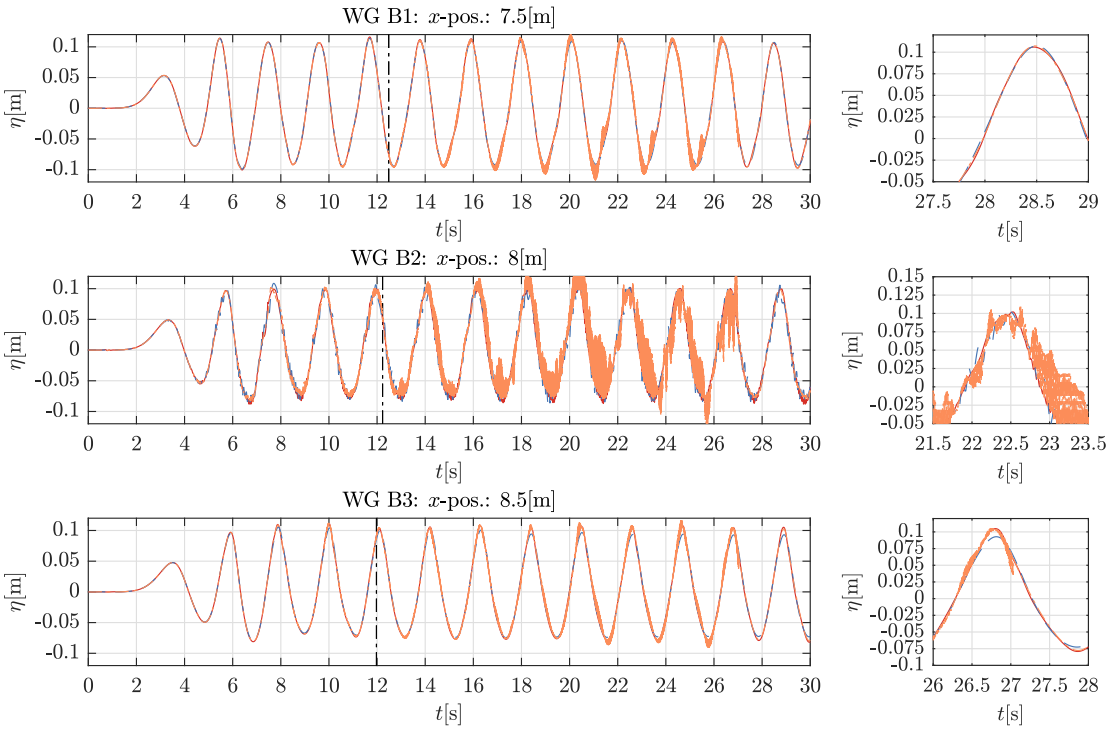

(b) comparison of the CFD results close to the cylinder (no experimental WG results available)

Figure 6.22: Experimental and CFD results of the wave elevation, $\eta(t)$, at selected wave gauges close to the porous **cylinder** for the **isotropic** porosity implementation and all investigated turbulence settings, including the whole time series and selected close-ups.

signal spikes. The reason for that is unclear since the mesh is identical. Apart from the differences in the quality of the signal, the results with the orthotropic implementations

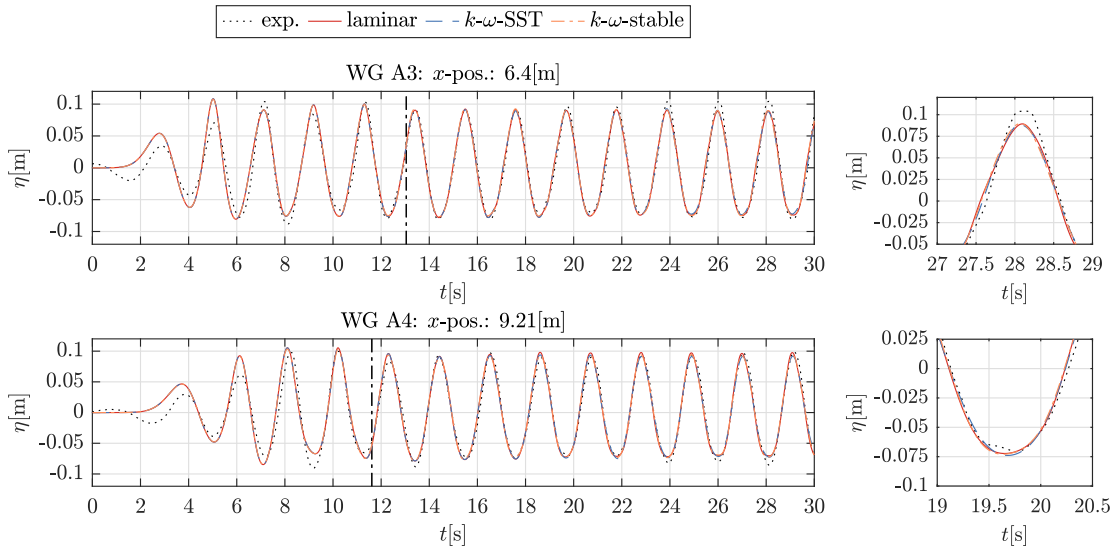

(a) comparison of the CFD and experimental results further away from the cylinder

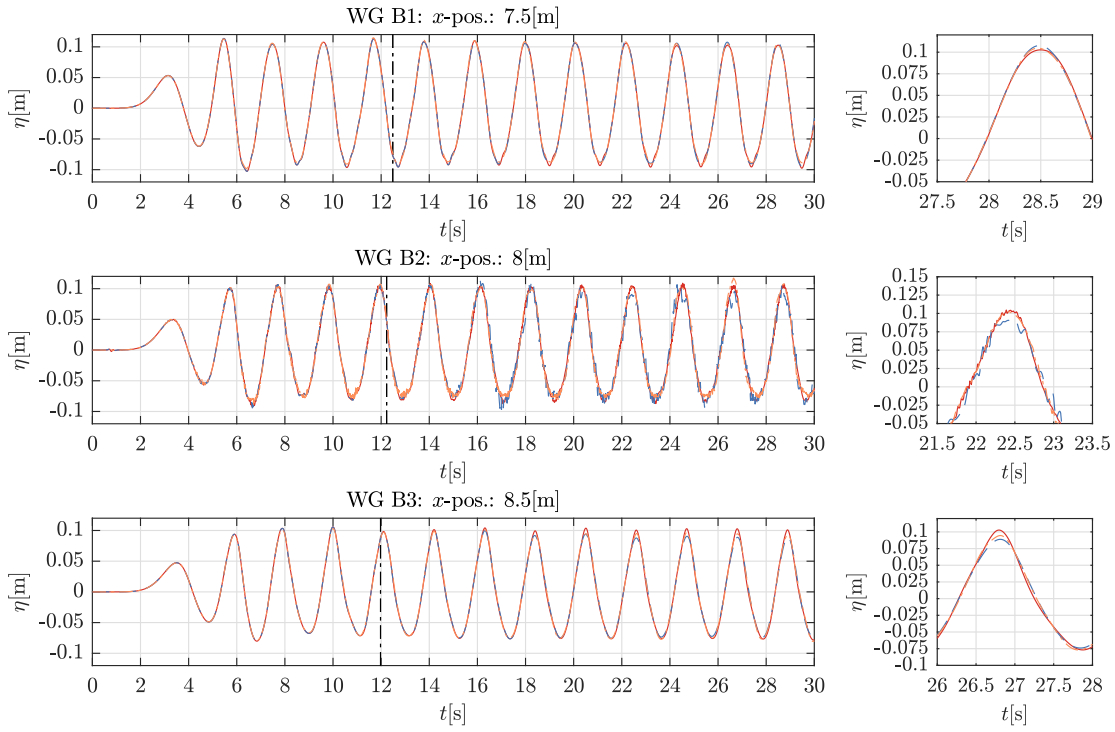

(b) comparison of the CFD results close to the cylinder (no experimental WG results available)

Figure 6.23: Experimental and CFD results of the wave elevation, $\eta(t)$, at selected wave gauges close to the porous **cylinder** for the **orthotropic** porosity implementation and all investigated turbulence settings, including the whole time series and selected close-ups.

lead to slightly reduced wave amplitudes for the WGs A3 and A4 further away from the cylinder. This can be best observed by comparing Fig. 6.22a and Fig. 6.23a. The results close to the cylinder at the WGs B1-B3 are quasi identical. The summary of all wave amplitude results for the cylinder models is given in Table 6.3.

Normalised mean wave amplitudes Next, the normalised mean wave amplitudes, A/A_{input}, where $A_{input} = 0.089$ m is the CFD wave amplitude input, are analysed for all WG positions for the models with isotropic and orthotropic porous-media and the investigated turbulence settings. The results for the models with isotropic porosity are shown in Fig. 6.24a and the ones for the orthotropic implementation are shown in Fig. 6.24b. For the WGs A1-A5, experimental results are included, for the WGs B1-B3 only CFD results are available.

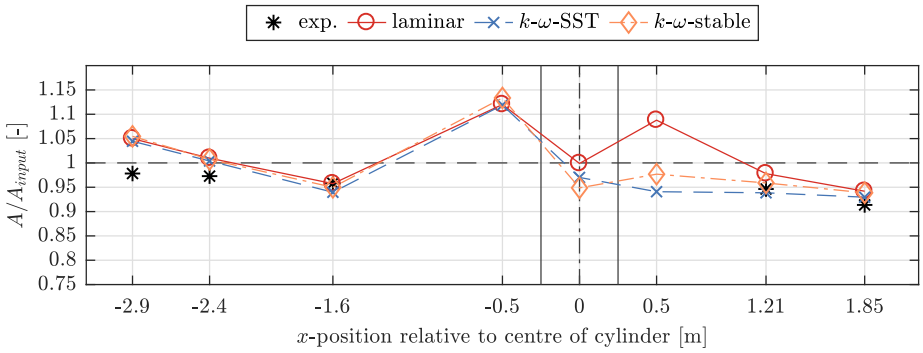

(a) isotropic porous media implementation

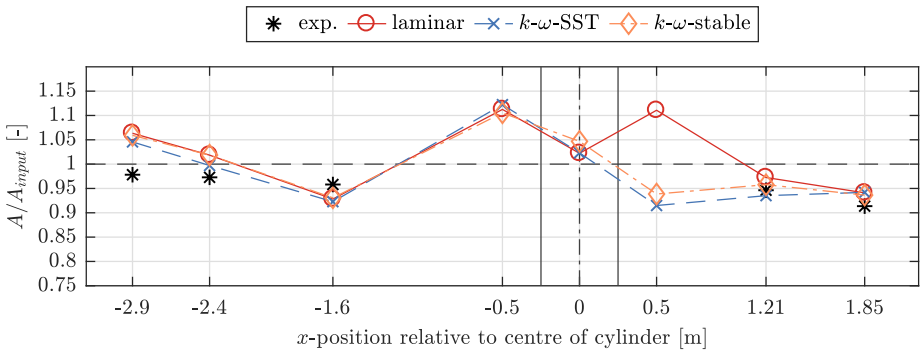

(b) orthotropic porous media implementation

Figure 6.24: CFD and experimental results of the normalised mean wave amplitudes, A/A_{input}, for the models with (a) isotropic and (b) orthotropic porosity implementation in combination with the investigated turbulence settings for all wave gauges before and after the **cylinder**. The position of the cylinder centre is indicated with a dashed vertical line and the cylinder front and back are indicated with solid vertical lines.

Both figures exhibit significant differences of the mean wave amplitude results of the CFD models with the turbulence models both inside and after the cylinder. The most significant deviations can be observed at WG B3 0.5 m after the cylinder axis. For the models with isotropic porosity implementation, the results of the model with the k-ω-SST model ($A/A_{input} = 0.941$) deviate by 13.5 % from the model with the laminar setup and those with the k-ω-stable model ($A/A_{input} = 0.9767$) deviate by 10.2 %. For the models with orthotropic porosity implementation, the results of the model with the k-ω-SST model ($A/A_{input} = 0.915$) deviate by 17.6 % from the model with the laminar setup and those with the k-ω-stable model ($A/A_{input} = 0.938$) deviate by 15.5 %. It is suspected that the turbulence generation causes increased wave height damping in the centre and the lee-wake of the cylinder. The results for the models with the isotropic porous media implementation exhibit smaller mean wave amplitudes, $A4$, at the cylinder centre. This is suspected to be a direct result of the isotropic resistance application which entails that less water enters the interior of the porous cylinder. In the models with orthotropic porosity implementation, more water can enter the interior of the cylinder and the lee-wake forms more significantly. Therefore, the difference of the wave amplitude values between the cylinder centre and after the cylinder differ more noticeable.

The smaller wave heights after the cylinder at WG B3 in Fig. 6.24 for the results obtained from simulations using turbulence models correspond to the force time series results, see Figs. 6.17 and 6.18, which exhibit smaller force amplitudes, particularly for the orthotropic implementation, see Fig. 6.18c. It is not fully clear, why the application of the turbulence models causes a significant difference in wave height without affecting the force results in a similarly significant amount. Unfortunately, the lack of experimental WG results close to the cylinder prohibits further investigations and studies on the real behaviour.

6.5.5 Velocity Profiles near the 2D Sheet

Similar to Section 6.4.5, the velocity profiles are assessed by means of a comparison between the CFD results from models with various turbulence settings. As a representation of the overall trend of the results, a limited number of selected profiles and points in time are presented for one wave trough and one wave crest each.

Figures 6.25-6.27 show examples of the velocity profiles of the horizontal component, u_x, and the vertical component, u_z, with a distance of 0.1 m before (WG C1) and after (WG C2) the sheet. Figure 6.25 shows the results for the models with the isotropic, Fig. 6.26 the orthotropic porous media implementation and Fig. 6.27 of the model with the baffle implementation.

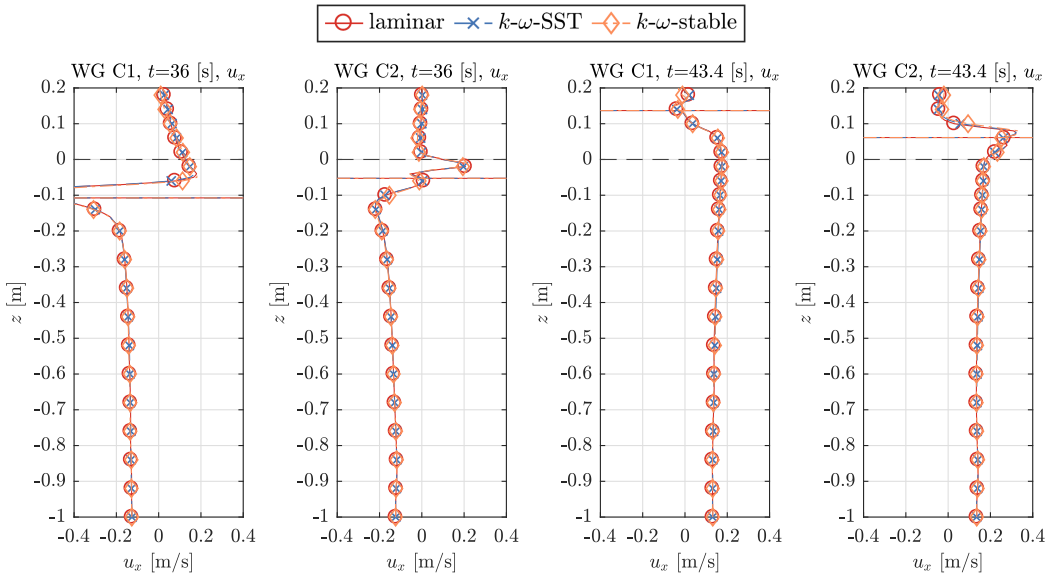

(a) u_x at WG C1 for a wave trough

(b) u_x at WG C2 for a wave trough

(c) u_x at WG C1 for a wave crest

(d) u_x at WG C2 for a wave crest

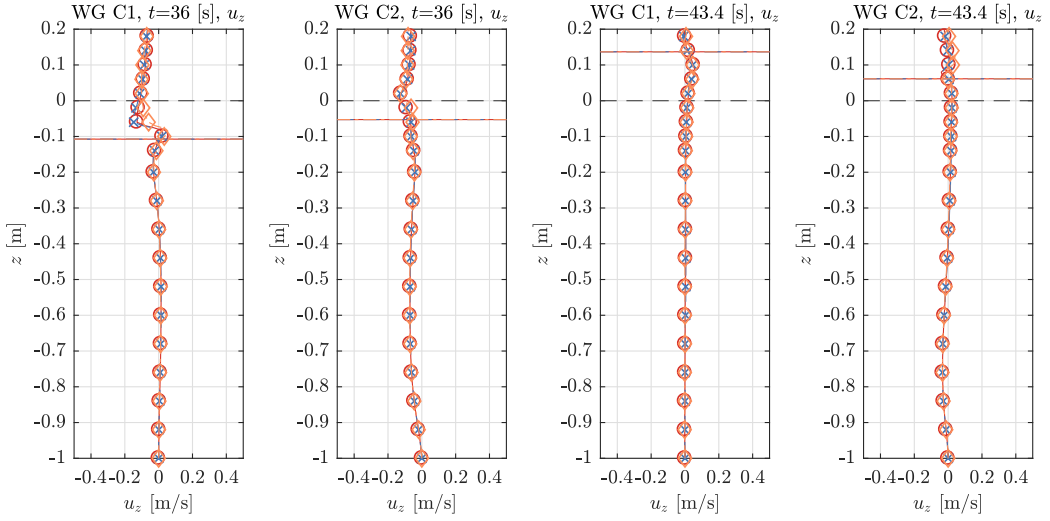

(e) u_z at WG C1 for a wave trough

(f) u_z at WG C2 for a wave trough

(g) u_z at WG C1 for a wave crest

(h) u_z at WG C2 for a wave crest

Figure 6.25: Velocity profiles in horizontal, u_x (a-d), and vertical, u_z (e-h) direction 0.1 m before (WG C1 - a,c,e,g) and 0.1 m after (WG C2 - b,d,f,h) the **sheet** for a wave **trough** ($t = 36$ s - a,b,e,f) **and crest** ($t = 43.3$ s - c,d,g,h)at the sheet for the models with the **isotropic** porosity implementation and the investigated turbulence settings. Since local spurious velocities can be very high (»1 m/s) in the air just above the free-surface, it is not viable to include the whole profile in all figures. So for clarity, the x-scales have been kept the same and those very local data points are outside the axis bounds.

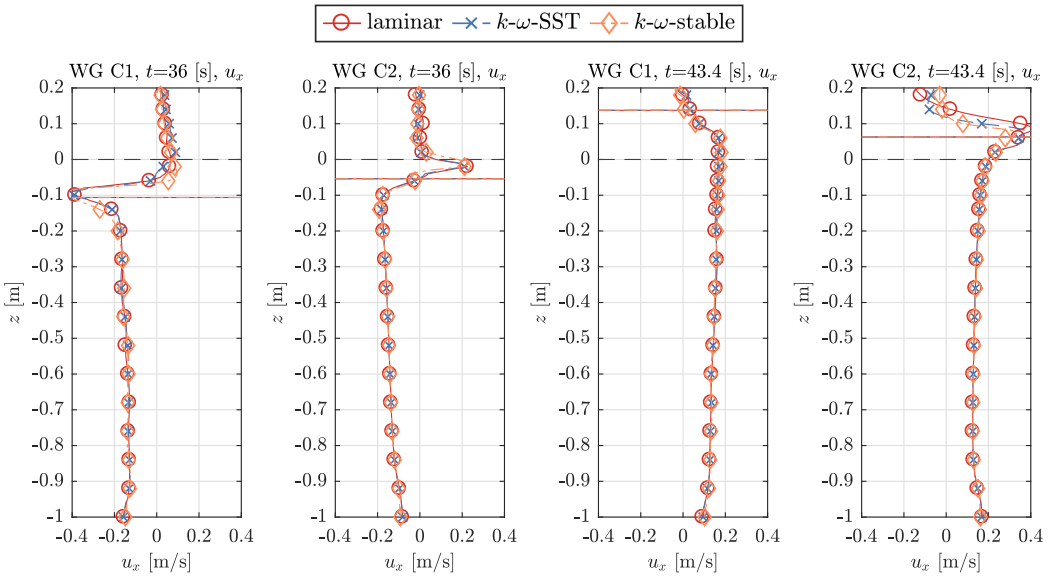

(a) u_x at WG C1 for a wave trough

(b) u_x at WG C2 for a wave trough

(c) u_x at WG C1 for a wave crest

(d) u_x at WG C2 for a wave crest

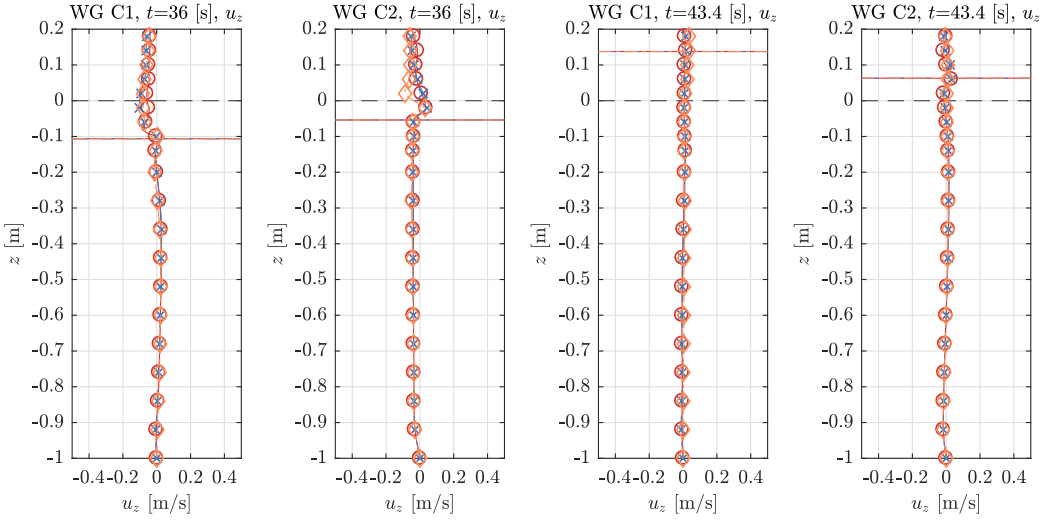

(e) u_z at WG C1 for a wave trough

(f) u_z at WG C2 for a wave trough

(g) u_z at WG C1 for a wave crest

(h) u_z at WG C2 for a wave crest

Figure 6.26: Velocity profiles in horizontal, u_x (a-d), and vertical, u_z (e-h) direction 0.1 m before (WG C1 - a,c,e,g) and 0.1 m after (WG C2 - b,d,f,h) the **sheet** for a wave **trough** ($t = 36$ s - a,b,e,f) **and crest** ($t = 43.3$ s - c,d,g,h)at the sheet for the models with the **orthotropic** porosity implementation and the investigated turbulence settings. Since local spurious velocities can be very high (»1 m/s) in the air just above the free-surface, it is not viable to include the whole profile in all figures. So for clarity, the x-scales have been kept the same and those very local data points are outside the axis bounds.

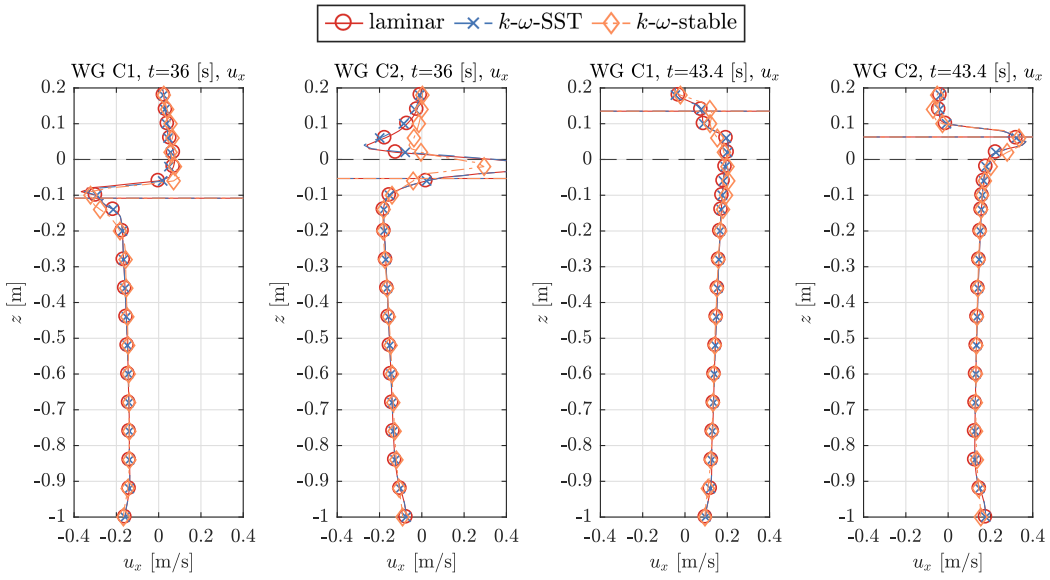

(a) u_x at WG C1 for a wave trough

(b) u_x at WG C2 for a wave trough

(c) u_x at WG C1 for a wave crest

(d) u_x at WG C2 for a wave crest

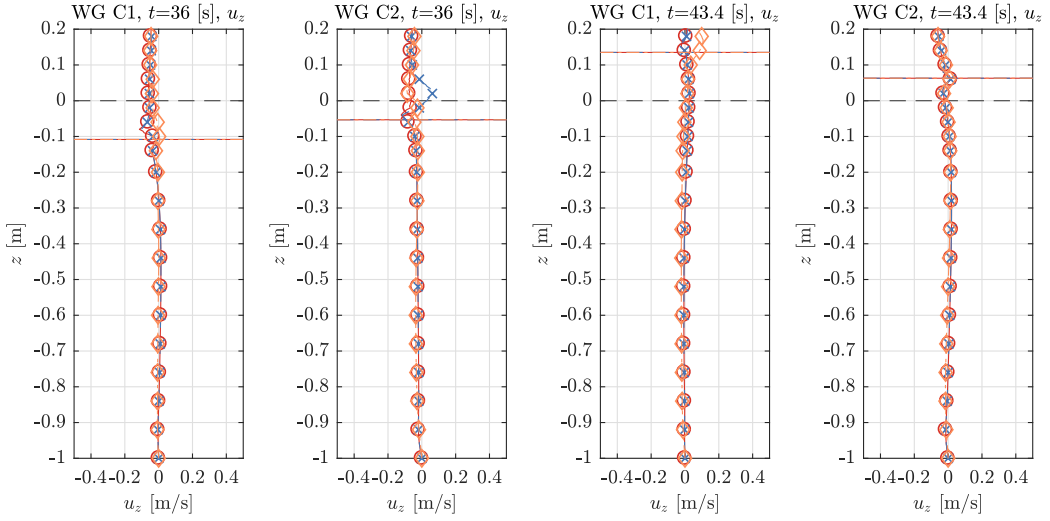

(e) u_z at WG C1 for a wave trough

(f) u_z at WG C2 for a wave trough

(g) u_z at WG C1 for a wave crest

(h) u_z at WG C2 for a wave crest

Figure 6.27: Velocity profiles in horizontal, u_x (a-d), and vertical, u_z (e-h) direction 0.1 m before (WG C1 - a,c,e,g) and 0.1 m after (WG C2 - b,d,f,h) the **sheet** for a wave **trough** ($t = 36$ s - a,b,e,f) **and crest** ($t = 43.3$ s - c,d,g,h)at the sheet for the models with the **baffle implementation** and the investigated turbulence settings. Since local spurious velocities can be very high (»1 m/s) in the air just above the free-surface, it is not viable to include the whole profile in all figures. So for clarity, the x-scales have been kept the same and those very local data points are outside the axis bounds.

The differences between the velocity profiles in vicinity to the porous sheet due to different turbulence settings are insignificant. In particular for the isotropic porosity implementation, shown in Fig. 6.25, no differences are exhibited at all. The results of both the orthotropic porous media (Fig. 6.26) and porous baffle (Fig. 6.27) implementations exhibit minimal deviations in the air just above the free surface level. The spurious air velocities that are the cause for that have been discussed previously.

6.5.6 Velocity Profiles near the Cylinder

As before, the velocity profiles in the vicinity of the cylinder are assessed for isotropic and orthotropic porosity implementation in combination with the investigated turbulence settings.

Figure 6.28 shows the velocity profiles, u_x and u_z, for $t = 17.1$ s, where a wave trough passes the cylinder centre. Figure 6.29 shows the same for $t = 20.3$ s at a wave crest. Again, the dashed black and coloured horizontal lines indicate the initial flat and instantaneous water level, respectively. Figure 6.30 shows the velocity profiles, u_x and u_z, for $t = 17.1$ s, where a wave trough passes the cylinder centre. Figure 6.31 shows the same for $t = 20.3$ s at a wave crest.

As before, all figures indicate similar patterns of locally large velocity values close to the air-water interface. For clarity and to see the differences of the values in the water column rather than the air above, some local air velocities are outside the x-axis bounds, see for instance Fig. 6.31e. The overall differences between the results due to the different turbulence settings are relatively small. The differences between the results are the smallest both 0.5 m before (WG B1) and after (WG B3) the cylinder axis. At the cylinder centre at WG B2, the profiles exhibit scatter for both the horizontal and vertical component, u_x and u_z, so no clear trend can be identified from the results. The effect of the turbulence models in the cylinder interior at WG B2, see the sub-figures (b) and (e) of Figs. 6.28 - 6.31, are less significant than the effect of the different porosity implementations, see Figs. 6.11b, 6.11e, 6.12b and 6.12e. This indicates that the chaotic flow field inside the cylinder is due to sloshing effects in the cylinder interior rather than turbulence generation. Turbulence generation, though, affects the wave elevation signal significantly, shown for WG B2 in Figs. 6.22b and 6.23b.

6.5.7 Tabular Summary

A summary of the main results of the models with the investigated turbulence settings is given in Tables 6.2-6.3. They show the results of the mean force amplitudes, F and the mean wave amplitudes, A, at the WGs for both the 2D and 3D model and include the mesh cell number and approximate execution times. To provide stable solver runs and to

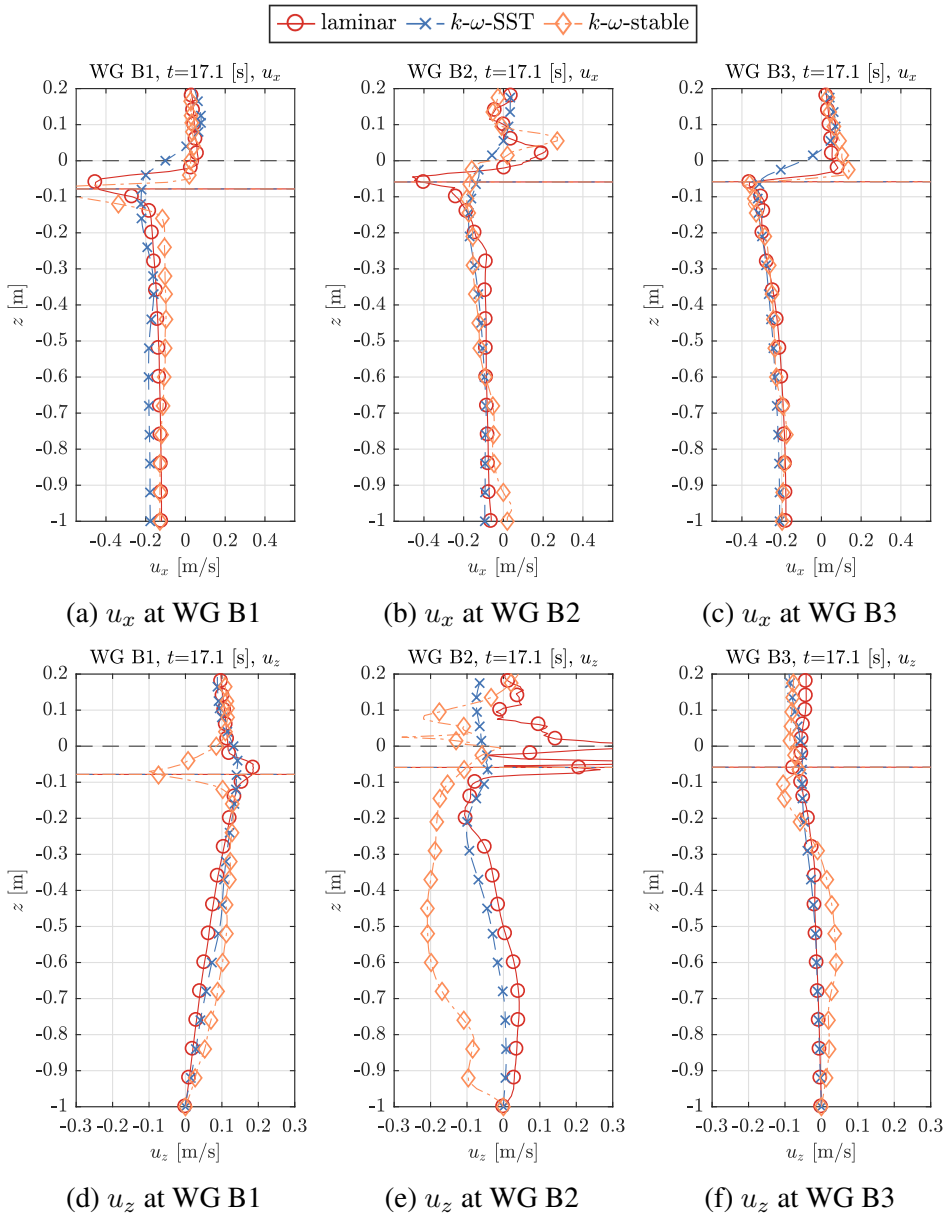

(a) u_x at WG B1 (b) u_x at WG B2 (c) u_x at WG B3

(d) u_z at WG B1 (e) u_z at WG B2 (f) u_z at WG B3

Figure 6.28: Velocity profiles in horizontal, u_x (a-c), and vertical, u_z (d-f), direction at the **cylinder** centre (WG B2 - b,e), 0.5 m before (WG B1 - a,e) and 0.5 m after (WG B3 - c,f) the axis for a wave **trough** at $t = 17.1$ s at the cylinder centre, using the **isotropic** implementation. Since local spurious velocities can be very high (»1 m/s) in the air just above the free-surface, it is not viable to include the whole profile in all figures. So for clarity, the x-scales have been kept the same and those very local data points are outside the axis bounds.

avoid divergence, the maximum CFL-numbers had to be reduced for the models with turbulence models in combination with both the isotropic and orthotropic porous media implementation. This has lead to significantly increased execution times. Interestingly, for the 2D models, the simulations with the k-ω-SST model had longer execution times compared to the simulations with the k-ω-stable model, whereas it was the opposite

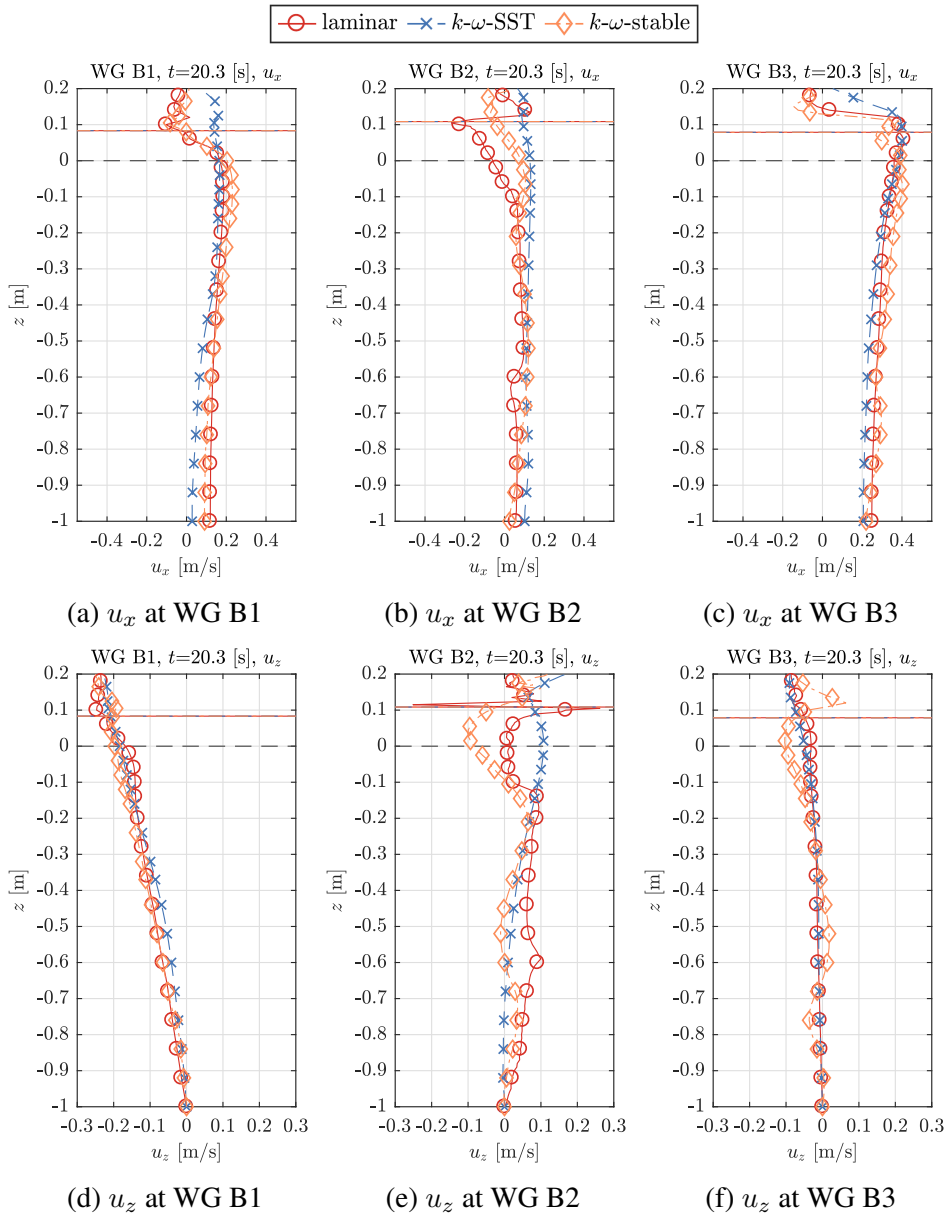

(a) u_x at WG B1 (b) u_x at WG B2 (c) u_x at WG B3

(d) u_z at WG B1 (e) u_z at WG B2 (f) u_z at WG B3

Figure 6.29: Velocity profiles in horizontal, u_x (a-c), and vertical, u_z (d-f), direction at the **cylinder** centre (WG B2 - b,e), 0.5 m before (WG B1 - a,e) and 0.5 m after (WG B3 - c,f) the axis for a wave **crest** at $t = 20.3$ s at the cylinder centre, using the **isotropic** implementation. Since local spurious velocities can be very high (»1 m/s) in the air just above the free-surface, it is not viable to include the whole profile in all figures. So for clarity, the x-scales have been kept the same and those very local data points are outside the axis bounds.

for the 3D cylinder model. It has to be noted though that these execution values are approximate values, since the maximum CFL-numbers have been slightly amended repeatedly due to solver crashes at certain time steps. This was usually the case at time steps when wave crests have passed the cylinder and spurious air velocities just above the water surface have caused a spike which lead the solver to diverge.

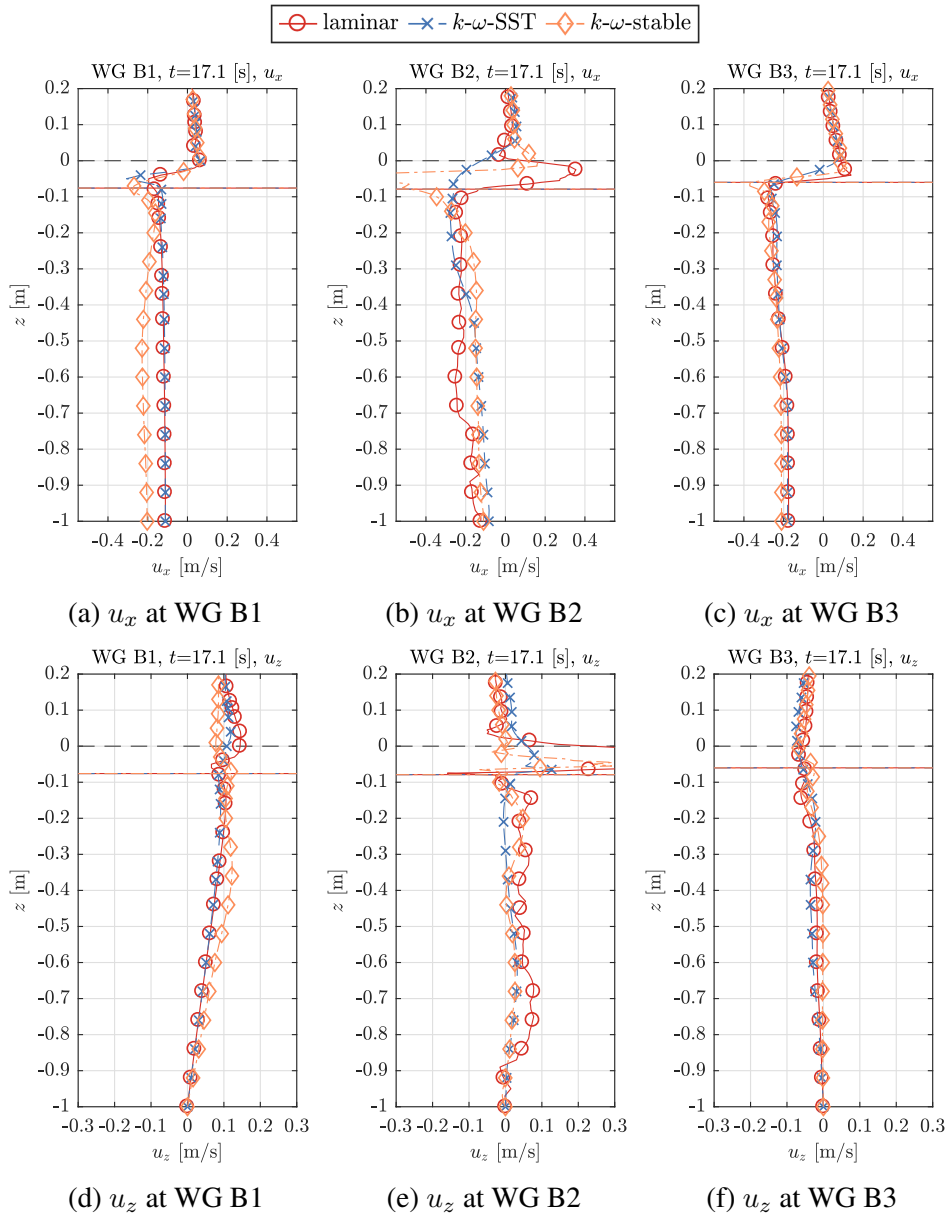

(a) u_x at WG B1 (b) u_x at WG B2 (c) u_x at WG B3

(d) u_z at WG B1 (e) u_z at WG B2 (f) u_z at WG B3

Figure 6.30: Velocity profiles in horizontal, u_x (a-c), and vertical, u_z (d-f), direction at the **cylinder** centre (WG B2 - b,e), 0.5 m before (WG B1 - a,e) and 0.5 m after (WG B3 - c,f) the axis for a wave **trough** at $t = 17.1$ s at the cylinder centre, using the **orthotropic** implementation. Since local spurious velocities can be very high (»1 m/s) in the air just above the free-surface, it is not viable to include the whole profile in all figures. So for clarity, the x-scales have been kept the same and those very local data points are outside the axis bounds.

The 2D models with the sheet were run on a single core and for a physical runtime of 50 s. For 3D models with the cylinder 28 CPUs were used and the physical runtime was reduced to 30 s.

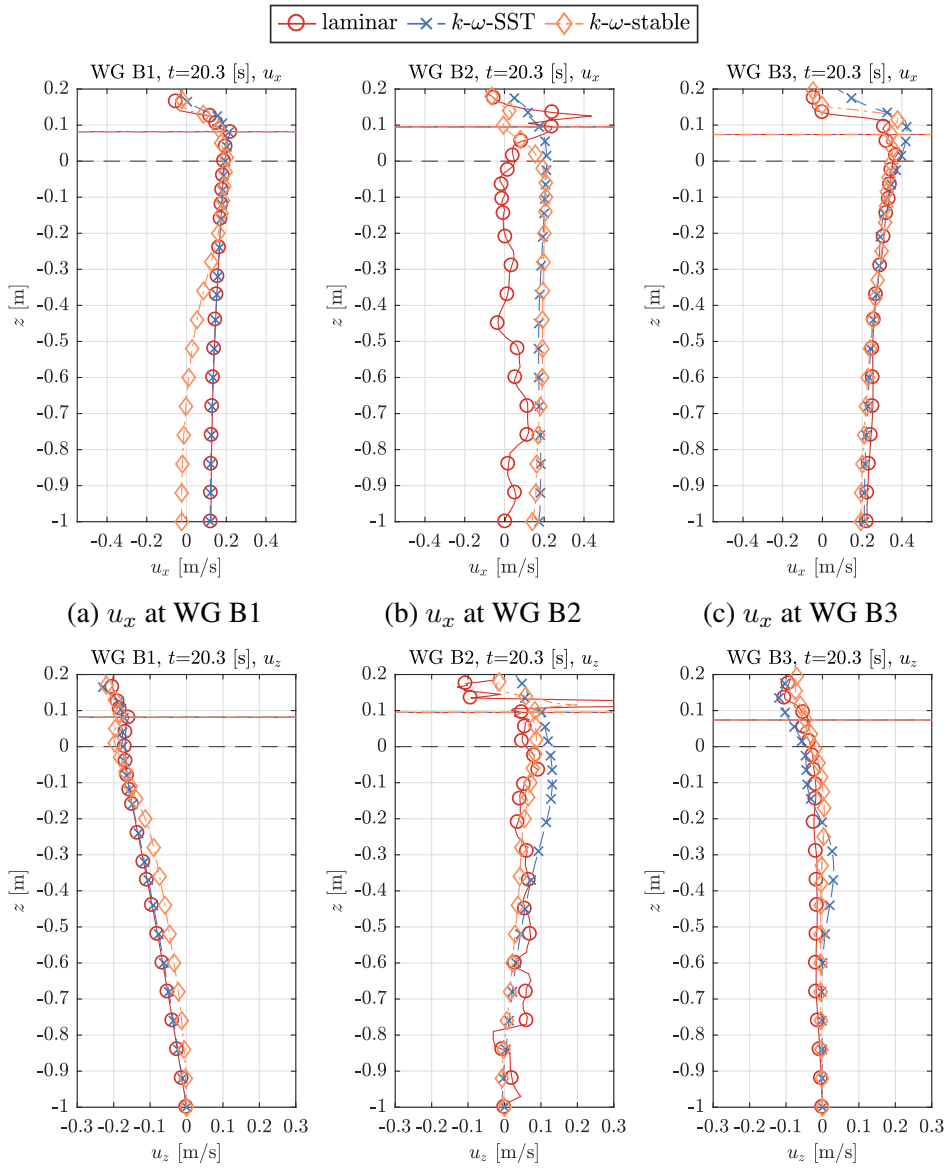

(a) u_x at WG B1 (b) u_x at WG B2 (c) u_x at WG B3

(d) u_z at WG B1 (e) u_z at WG B2 (f) u_z at WG B3

Figure 6.31: Velocity profiles in horizontal, u_x (a-c), and vertical, u_z (d-f), direction at the **cylinder** centre (WG B2 - b,e), 0.5 m before (WG B1 - a,e) and 0.5 m after (WG B3 - c,f) the axis for a wave **crest** at $t = 20.3$ s at the cylinder centre, using the **orthotropic** implementation. Since local spurious velocities can be very high (»1 m/s) in the air just above the free-surface, it is not viable to include the whole profile in all figures. So for clarity, the x-scales have been kept the same and those very local data points are outside the axis bounds.

Table 6.2: Summary of the results for the 2D sheet models with the investigated turbulence settings, showing the normalised mean force amplitudes, F/F_{exp}, and the normalised mean wave amplitudes, A/A_{input} at the WGs, including mesh cell number and execution times (for a physical runtime of 30 s).

Poros. impl.	**Isotropic**			**Orthotropic**			**Baffle**		
Turb. model	**none**	k-ω-**SST**	k-ω-**st.**	**none**	k-ω-**SST**	k-ω-**st.**	**none**	k-ω-**SST**	k-ω-**st.**
No. of Cells	68,890	68,890	68,890	68,890	68,890	68,890	68,060	68,060	68,060
Max. $\boldsymbol{CFL}$	0.3	0.22	0.22	0.3	0.22	0.22	0.05	0.05	0.05
Used CPUs	1	1	1	1	1	1	1	1	1
Exec. Time	4.0 h	7.8 h	5.7 h	4.7 h	9.2 h	6.8 h	20.3 h	12.1 h	22.7 h
$\boldsymbol{F/F_{exp}}$	1.086	1.069	1.029	1.066	1.064	1.076	1.024	1.029	1.022
$\boldsymbol{A/A_{input}}$									
WG A1	1.307	1.254	1.309	1.312	1.312	1.309	1.305	1.307	1.300
WG A2	1.207	1.141	1.211	1.203	1.203	1.206	1.207	1.209	1.207
WG A3	0.059	0.664	0.657	0.656	0.657	0.664	0.687	0.688	0.689
WG A4	0.640	0.613	0.641	0.641	0.642	0.643	0.660	0.660	0.657
WG A5	0.633	0.641	0.638	0.637	0.638	0.641	0.657	0.657	0.658
WG C1	1.348	1.286	1.349	1.352	1.352	1.351	1.340	1.343	1.345
WG C2	0.657	0.632	0.657	0.654	0.655	0.655	0.670	0.671	0.666

Table 6.3: Summary of the results for the cylinder models with the investigated turbulence settings, showing the normalised mean force amplitudes, F/F_{exp}, and the normalised mean wave amplitudes, A/A_{input} at the WGs, including mesh cell number and execution times (for a physical runtime of 30 s).

Poros. impl.	**Isotropic**			**Orthotropic**		
Turb. model	**none**	k-ω-**SST**	k-ω-**st.**	**none**	k-ω-**SST**	k-ω-**st.**
No. of Cells	9.84 MIO	9.84 MIO	9.84 MIO	9.84 MIO	9.84 MIO	9.84 MIO
Max. $\boldsymbol{CFL}$	0.3	0.17	0.08	0.3	0.3	0.22
Used CPUs	28	28	28	28	28	28
Exec. Time	5 d 4 h	24 d 6 h	31 d	7 d 21 h	30 d 21 h	49 d 17 h
$\boldsymbol{F/F_{exp}}$	1.039	0.995	0.982	0.957	0.814	0.821
$\boldsymbol{A/A_{input}}$						
WG A1	1.049	1.045	1.055	1.063	1.045	1.060
WG A2	1.020	1.004	1.007	1.018	0.997	1.018
WG A3	0.957	0.940	0.950	0.928	0.923	0.930
WG A4	0.978	0.938	0.959	0.941	0.936	0.958
WG A5	0.941	0.930	0.939	0.941	0.942	0.936
WG B1	1.120	1.119	1.134	1.113	1.123	1.105
WG B2	0.999	0.970	0.949	1.022	1.023	1.047
WG B3	1.088	0.941	0.977	1.110	0.915	0.938

6.6 Validation of the Pressure-Drop Model

To assess the validity of the theoretical pressure-drop model, (3.1), and the used formulation of the drag coefficient, C_f, (2.37), simulations of both the 2D and 3D model have been performed for a wide range of regular wave conditions and porosity values, n. For the 2D model with the sheet, all conditions in Table 4.1 have been applied. For the 3D cylinder models only a subset of those has been used. All simulations in this section have been performed with the isotropic porous media implementation and with the full NS equations without a turbulence model.

The horizontal force on the structures, defined as the main parameter of interest, has been analysed in two ways for both the sheet and the cylinder. Firstly, the force time series, $f(t)$, from the CFD results and the experimental results have been compared for both structures. As before, the experimental time series have been cropped to correspond with the CFD time series. Secondly, the variation of the mean force amplitude, F, with wave frequency (represented by $k_w h$), and steepness, $k_w A$, is examined for a range of

values of porosity, n. For the 3D model with the cylinder, the free-surface elevation, $\eta(t)$, around the cylinder has been compared for a number of WGs to verify the capability of the model to replicate the mean flow behaviour.

6.6.1 Force Results in the Time Domain - Sheet and Cylinder

The time series of the horizontal force on the structures, $f(t)$, are compared between the CFD models and experiments. The experimental results of the force on the physical sheet, which had a width of 1 m, have been scaled to match the sheet width of 0.01 m of the 2D CFD model.

Figure 6.32 shows a comparison between the CFD and experimental results of the time series of the horizontal force, $f(t)$, on the perforated sheet for the cases $n = 0.3$ with wave A02, $n = 0.2$ with wave A07, and $n = 0.1$ with wave A08. These cases are representative of all related results.

Differences between the CFD and experimental time series for the initial transient sections can be observed and are more significant for the longer waves, in particular for the case with $n = 0.1$ and wave A08. Also the differences in the reflection behaviour due to different tank lengths can be observed for all example cases. Reflections in the experimental results are present for the case with $n = 0.1$ with wave A08 and noticeable reflections in the CFD results are present for the case with $n = 0.3$ and wave A02, evident in the change in amplitude at around $t = 36$ s. As predicted, this corresponds to the time for the waves to propagate from the generation boundary to the absorption boundary and back to the sheet position. This highlights that the wave absorption method is a crucial component in the setup of NWTs. Since the level of reflections is not related to the porosity representation in the model, the agreement between the CFD and experimental results is considered as relatively good, in particular for the case with $n = 0.2$ and wave A07 after about $t = 30$ s. The shape of the measured force time series is well reproduced by the CFD model for all combinations of porosity, n, and wave condition, clearly showing the non-sinusoidal profile, due to the quadratic pressure-drop.

For the 3D model, Fig. 6.33 shows the time series of the horizontal force on the perforated cylinder. Results are presented for the cases with $n = 0.2$ and wave B03, $n = 0.3$ and wave B04, and $n = 0.3$ in combination with wave B06. These cases are representative of all other results.

The CFD and experimental force results agree very well with the CFD model being capable of reproducing the shape and amplitude of the horizontal force on the cylinder. The differences are related to the same factors affecting the 2D model, discussed above. The initial transient period differs significantly due to the differences in the wave ramp-up, previously discussed in Section 6.4. The reflections are more noticeable for the

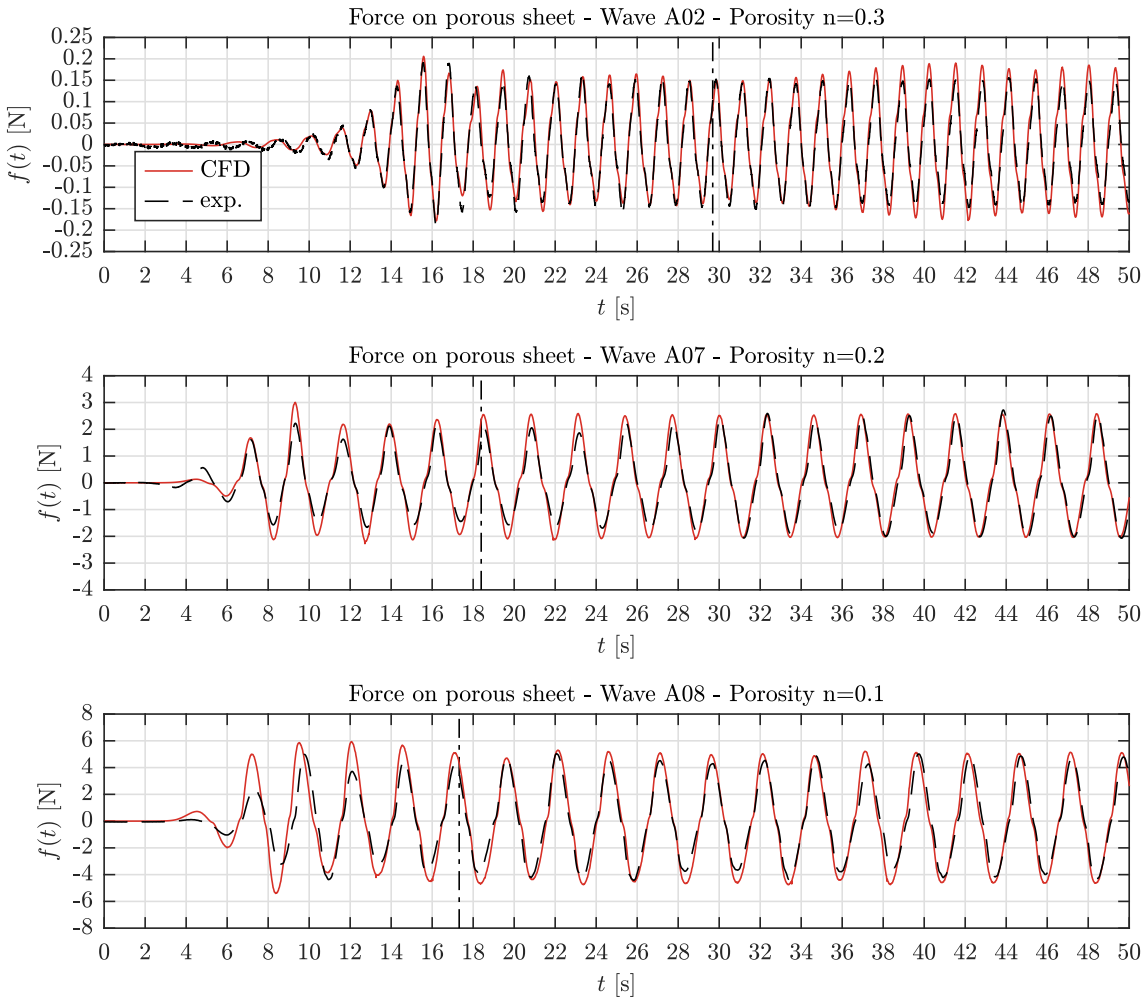

Figure 6.32: Experimental and CFD time series of the horizontal force, $f(t)$, on the porous **sheet** - examples for three wave conditions with steepness of $k_W A = 0.05$ and porosity values in the range of $n = 0.1$, 0.2 and 0.3. The vertical lines indicate the point in time for the numerical waves to propagate from the generation boundary to the absorption boundary and back to the sheet position.

experimental results, in particular for the second half of the time series between about $t = 25$ s and $t = 50$ s. In contrast, the CFD results exhibit a nearly periodically steady force response with negligible reflections from about $t = 15$ s onwards.

6.6.2 Force Results in the Frequency Domain - Sheet and Cylinder

This section investigates the ability of the CFD model to predict the variation of the force amplitude with wave frequency, $k_w h$, and steepness, $k_w A$. For reference, the CFD and experimental results are also compared to results from a potential-flow model by Mackay and Johanning [44], introduced in Section 4.5. The absolute mean uncertainty of the normalised experimental results was estimated to be $U_{f_x} = 2.1$ %, based on analysis of repeat tests where repeatability was proven. The overall uncertainty of the CFD results

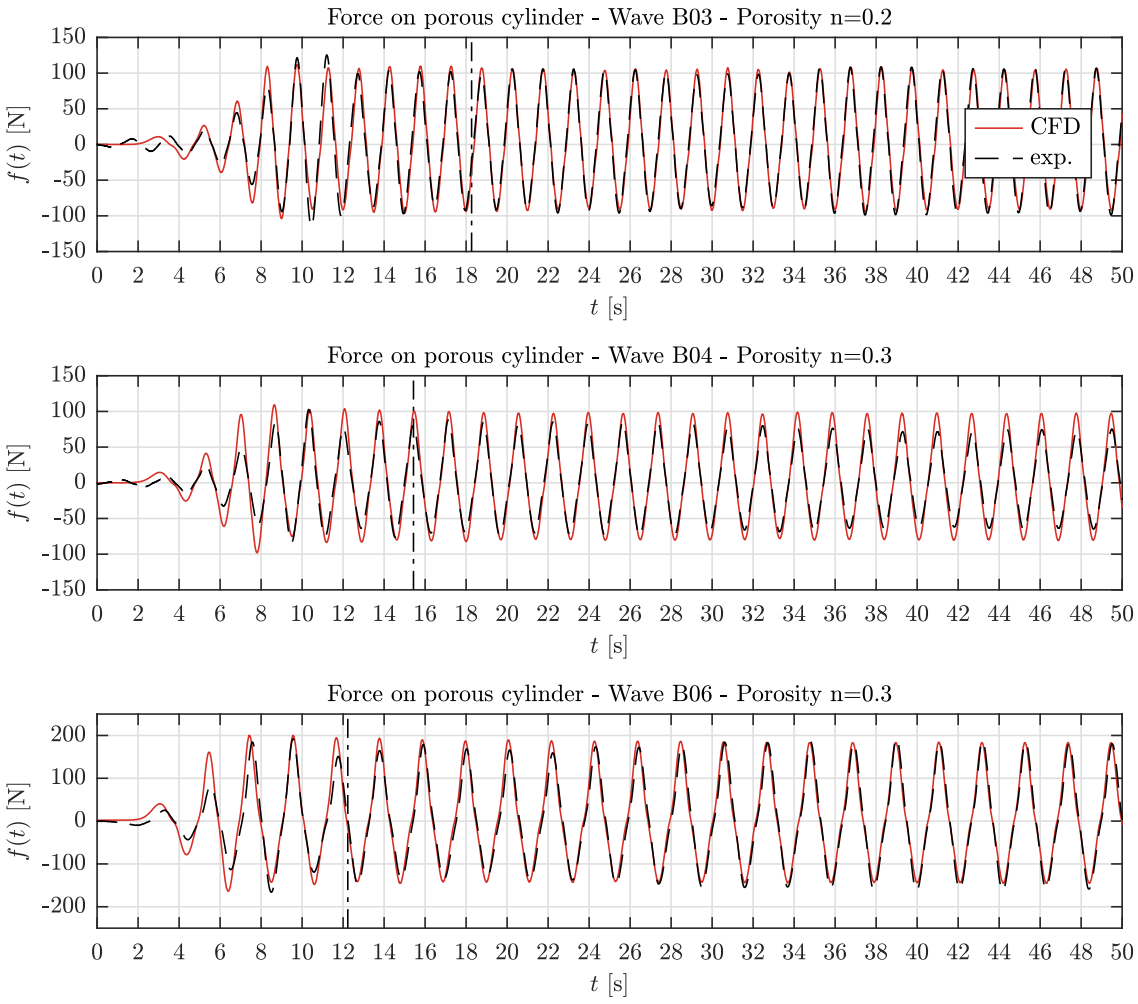

Figure 6.33: Experimental and CFD time series of the horizontal force, $f(t)$, on the porous **cylinder** for a selection of conditions.

of $U_{unc} = \pm 4.4\%$, estimated in Section 5.3, is indicated by means of error bars in all following figures. As stated in Section 4, a detailed error analysis is outside the scope of this work.

The results are presented in terms of a normalised force, f_x, defined as the ratio of the measured force, F_{porous}, to the force on the equivalent solid structure in the same wave conditions:

$$f_x = \frac{|F_{porous}|}{|F_{solid}|}. \tag{6.1}$$

The value of F_{solid} is based on linear wave theory. For the flat sheet it is [41, 44]:

$$\frac{F_{solid}}{\rho g A w h} = 2\frac{\tanh(k_w h)}{k_w h}, \tag{6.2}$$

and for the cylinder - based on MacCamy and Fuchs [300] - it is:

$$\frac{F_{solid}}{\rho g A r h} = \frac{4}{k_w r H_1^{(1)'}(k_w r)} \frac{\tanh(k_w h)}{k_w h}, \tag{6.3}$$

where w is the sheet width and r is the cylinder radius. $H_1^{(1)}$ is the Hankel function of the first kind of order 1 and the prime denotes differentiation with respect to the arguments.

Figure 6.34a shows the normalised force on the sheet for a constant target normalised wave steepness of $k_w A = 0.05$ and for porosity values of $n = 0.1$, 0.2 and 0.3. For $n = 0.1$ the whole range of wave conditions was simulated, for $n = 0.2$ and $n = 0.3$ a representative subset of conditions has been evaluated as a cross-check. Figure 6.34b shows the results for a constant porosity of $n = 0.3$ for wave steepnesses of $k_w A = 0.05$, 0.1 and 0.2. As discussed in Section 4.4, the experimental results are considered to be unreliable for the wave conditions A09, A10, A12 ($k_w h = 0.82$, 0.75, 0.65) for all porosities and A05 ($k_w h = 1.30$) for $n = 0.1$. Thus, these data points have been included in the graphs but omitted in the discussion of the results.

Overall, the averaged normalised force amplitudes, f_x, are in reasonably good agreement between the experimental, potential-flow and CFD results. Generally, the potential-flow and CFD results agree well for most frequencies. The experimental results exhibit more scatter. The results match particularly well for the larger porosity values ($n = 0.2$ and 0.3) with the theoretical pressure-drop model applied in the CFD models being capable of reproducing the variation with $k_w h$ to a satisfactory extent. The deviations increase for the smaller porosity value of $n = 0.1$. This may be related to the use of a reduced 2D model instead of replication of the full 3D and physical width of 1 m. It is suspected that the importance of 3D WSI effects increases for decreasing porosity values. Lower porosities imply a smaller number of perforations or a smaller perforation size which entail a less homogeneous fluid flow behaviour and increasingly anisotropic FSI. Thus, the significance of the wave parameters and geometrical parameters such as hole shape, perforation distance and perforation order may increase by means of its 3D effects. However, since the largest deviations for $n = 0.1$ are exhibited for frequencies where the experimental data is suspected of being unreliable (see Section 4.4) it is difficult to draw strong conclusions.

Overall, the CFD results lead to larger f_x-values compared to both the potential-flow and experimental results for nearly all cases. The difference ranges between -3.5 % and +21.9 % relative to the potential-flow results and between -10.5 % and +21.9 % relative to the experimental results (after removing the unreliable data). It is suspected that this effect is related to the use of the isotropic porous media implementation, where

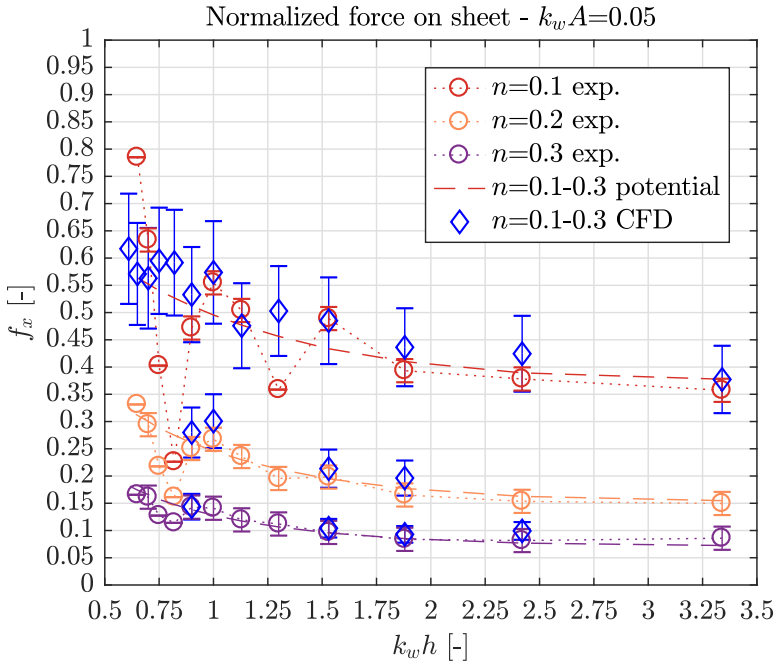

(a) constant wave steepness $k_wA = 0.05$ and variable porosities, n

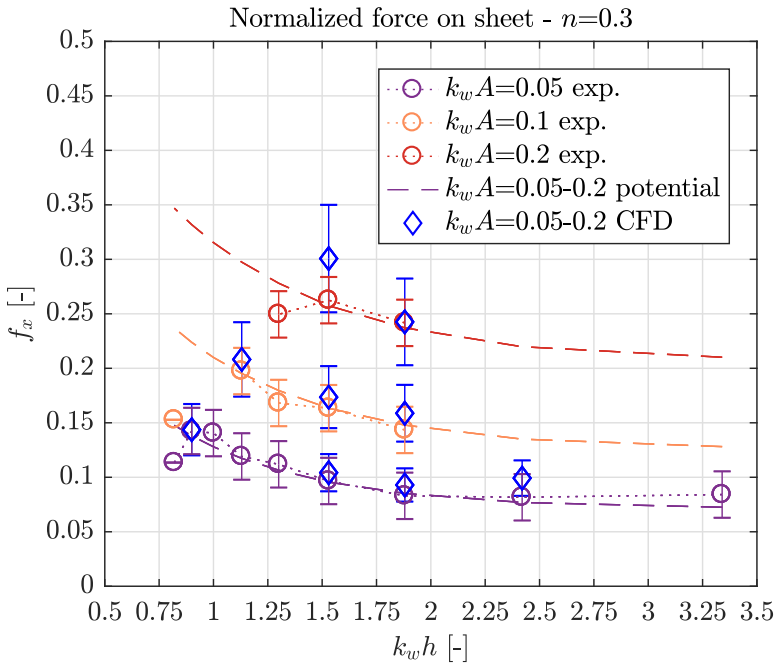

(b) constant porosity $n = 0.3$ and variable wave steepnesses, k_wA

Figure 6.34: Experimental (circles), potential-flow (dashed lines) and CFD (blue diamonds) results for the normalised force on the porous **sheet** against k_wh. Note the different y-axis scales.

the pressure drop is applied in all three (x, y, z) directions and not just in normal (x) direction across the sheet surface, discussed in Section 6.4. Since the uncertainty is defined as percentage, the error bars are larger for larger values, and smaller for smaller

values of the normalized force, f_x. This behaviour is exhibited in Fig. 6.34 for the results of the 2D models with the sheet, and in Fig. 6.35 for the results of the models with the cylinder.

Overall, the results indicate that the theoretical model with a constant discharge coefficient, $\delta = 0.5$ is capable of reproducing the change in the force with wave frequency and steepness as well as sheet porosity with sufficient accuracy.

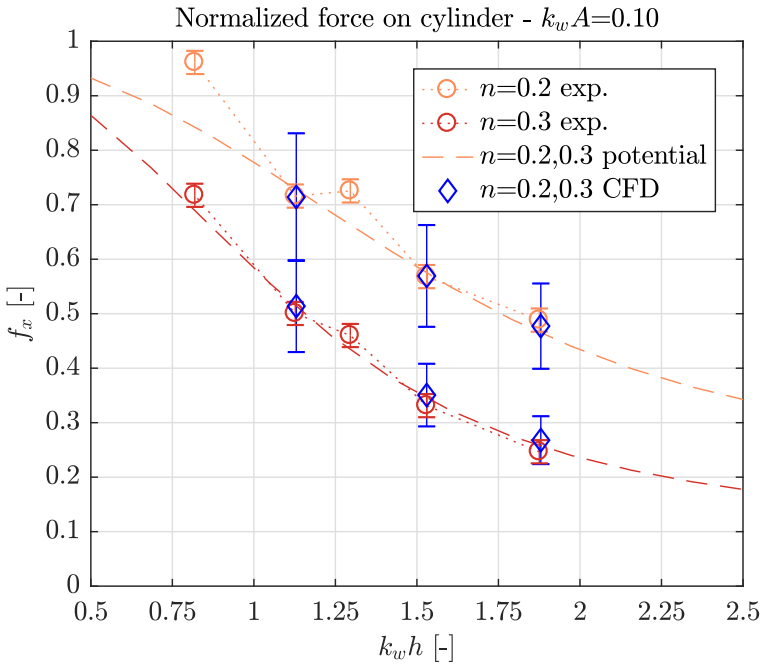

Figure 6.35: Experimental (circles), potential-flow (dashed lines) and CFD (blue diamonds) results for the normalised force on the porous **cylinder** against k_wh.

Figure 6.35 shows the normalised force on the perforated cylinders for a constant wave steepness of $k_wA = 0.10$ and porosities $n = 0.2$ and 0.3. The agreement between the numerical and experimental results is very good for the cylinder models, in particular between the potential-flow and CFD results with deviations ranging between -1.5 % and +2.9 % of the CFD results relative to the potential-flow results. The experimental results exhibit larger scatter and the differences between the CFD results and the experimental results range between +1.9 % and +12.4 % of the CFD relative to the experimental results.

The good agreement between the CFD, potential-flow and experimental results for the cylinder supports that the theoretical pressure-drop formulation with the use of a discharge coefficient, $\delta = 0.5$, and independent of any wave parameters, gives good results not only in 2D but also for 3D WSI.

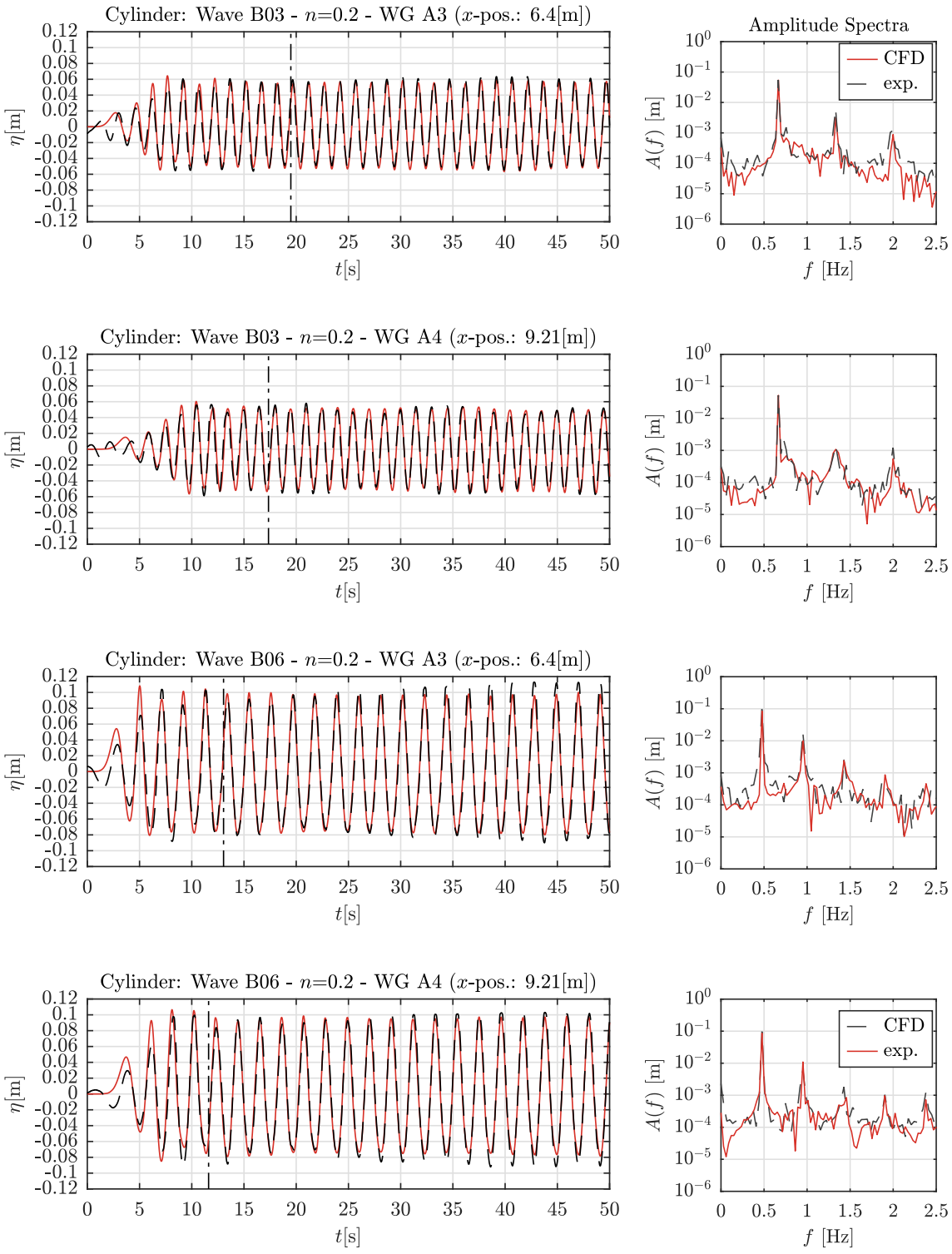

Figure 6.36: Time series and amplitude spectra of the surface elevation from the CFD models and experiments for various wave gauges around the **cylinder**.

6.6.3 Wave Gauges near the Cylinder

The time series of the wave elevation, $\eta(t)$, and mean amplitudes, A, are analysed for the set of WGs shown in Fig. 6.1a. Firstly, the time series are presented for the WGs closest to the structure which are WG A3 at $x = 6.4$ m (1.6 m before the cylinder centre) and WG A4 at $x = 9.21$ m (1.21 m after the cylinder centre). Figure 6.36 shows a selection of time series and amplitude spectra from the CFD model and experiments. The amplitude spectrum is defined as $A(f) = \sqrt{(}2S(f)\Delta f)$, where $S(f)$ is the variance density spectrum and Δf is the frequency resolution.

The agreement is very good for all cases shown. The surface elevation was also accurately reproduced at the WGs further away from the structure (not shown). The amplitude spectra indicate that the measured fundamental frequencies and higher harmonics are well captured by the CFD model. Small deviations are present with the computational results tending to under-predict the experiment. The deviations increase for cases where stronger reflections are present in the experiments.

Next, the normalised averaged wave amplitudes, A/A_{input}, are analysed for all WG positions. The comparison between experimental and CFD results is shown in Fig. 6.37 for the cases with $n = 0.2$ with waves B03 and B04, and $n = 0.3$ with wave B06. The spatial variation in the wave amplitude agrees reasonably well between the CFD model and experiments. The agreement is better for the shorter wave conditions B03 and B04. The longest wave B06 exhibits the largest deviations at WG A3, which is located furthest away from the cylinder and closest to the wavemaker. The experimental results do not contain wave reflections since averaged results were estimated from the portion of the record after the transient response and before the reflected waves had arrived back from the beach. The CFD results are estimated from the portion of the time series including reflected waves, but due to the low reflection coefficient in all the 3D CFD models ($R_{refl} < 0.5\,\%$ using the ER-AWA), the influence of reflections on the CFD results is minimal.

The good agreement between the numerical and experimental WG results indicates that the present porosity representation is able to capture the large-scale characteristics of the WSI over time. It is shown that the present approach is valid not only in 2D but also for 3D structures.

6.7 Summary

The overall results indicate that all types of investigated porosity implementation are capable of reproducing the horizontal force on the structures and the overall flow behaviour around the structures. The differences between the implementations are small

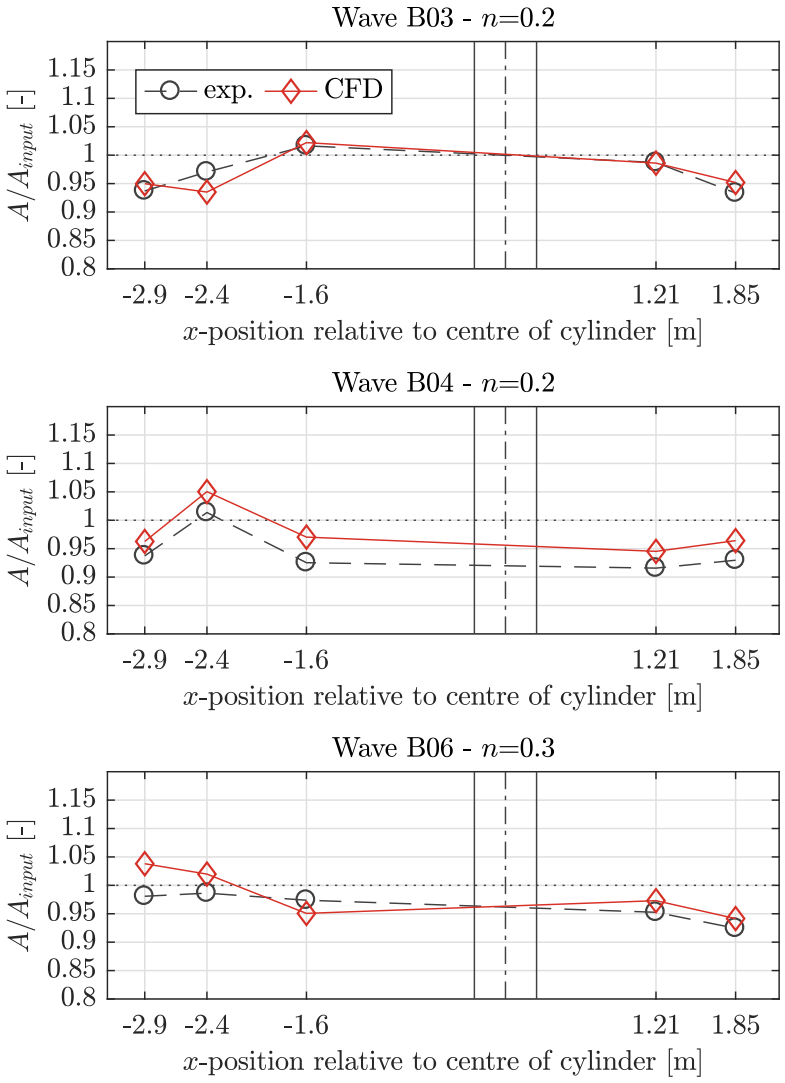

Figure 6.37: The normalized mean wave amplitudes, A/A_{input}, from the CFD models and experiments for all wave gauges before and after the **cylinder**. The position of the centre of the cylinder is indicated with dashed vertical lines and the cylinder front and back are indicated with solid vertical lines.

for both the force and fluid flow results. In particular for the 2D model with the vertical sheet, all results are almost identical for all types of porosity implementation.

For the present case of thin perforated structures, all types of implementations are suitable in principle. However, differences in numerical stability and execution times have been observed. While the solution process of all models with porous media-implementations maintained stability with a target maximum CFL-number of 0.3, the models with the baffle-implementation required very small time steps and a maximum CFL-number of 0.05 for a stable and un-supervised computation. Since the baffle implementation is usually reported to be more stable than the porous-media implementation in single-phase flow e.g. by Shim et al. [5], it is suspected that the

instabilities are caused by the spurious air velocities at the interface, as previously discussed in Section 2.3.3 in terms of their effect on the velocity profiles. Excessive velocity spikes at the sheet would directly lead to a spike in the pressure-drop source since it is a function of velocity, eq. (3.1), which can cause the solver to diverge and abort. Whilst the spurious velocities impact the baffle implementation significantly, they do not affect the porous-media implementations as much. It is suspected that the smeared pressure-drop application over a volumetric porous zone helps to avoid excessive pressure spikes. The baffle implementation is considered to be disadvantageous when an algebraic VOF method and a segregated pressure-velocity coupling algorithm is used for two-phase wave-structure interaction as in the present work. The small time steps increase the computation times significantly. However, this problem may be resolved with a different interface capturing method or a different solver algorithm (which could be investigated as part of future work). Furthermore, the execution time of the isotropic implementation is shorter than the orthotropic porous-media implementation, see Table 6.1. Despite both models being set up with the identical mesh and same scheme and solver settings, the orthotropic implementation requires smaller time steps to meet the maximum targeted CFL-number. It is suspected that this is caused by more chaotic flow patterns with higher local velocity values that result from the orthotropic implementation, see Fig. 6.13b.

The results demonstrate that the application of both the k-ω-SST and k-ω-stable turbulence models results in differences of the wave amplitude in the interior and the lee-wake of the thin porous cylinder, see Fig. 6.24. However, there is no significant effect on the force on neither the 2D sheet nor the cylinder. The use of turbulence models leads to significantly increased execution times due to two reasons. Firstly, two additional equations for the turbulence parameters (k, ω) need to be solved in each cell as part of the solution process. Secondly, the additional turbulence viscosity appears to amplify the instabilities of the used VOF interface capturing method. The latter requires the reduction of the time step size and thus, smaller maximum CFL-numbers (see Tables 6.2 and 6.3).

It has been concluded that the isotropic porous-media implementation without the use of a turbulence model is the best option for the specific conditions explored in this thesis. It is numerically stable and achieved the fastest execution times when it is used with automatic time-stepping. Its implementation is simple and does not require any considerations on directionality in comparison to the orthotropic porous-media implementation. It is capable of reproducing the mean force and fluid flow behaviour and is equally accurate as both the orthotropic porous-media and porous-baffle implementation. The use of the full NS equations without a turbulence model is considered as sufficiently accurate for the present investigations and possibly also for

other marine engineering problems where the turbulence levels are minimal. However, a turbulence model may be important for more general cases of WSI such as wave breaking, cases where significant BL effects exist or when large-scale turbulent vortex generation and shedding must be accounted for.

The results demonstrate that the applied theoretical pressure-drop model as volume-averaging closure term is capable of replicating the characteristic quadratic pressure-drop of the flow across thin perforated barriers for the range of regular wave frequencies, wave steepnesses and porosities considered.

Chapter 7

Simulations of a moving TLP with a thin perforated outer Cylinder

7.1 Introduction

In this chapter, the validation of the proposed macro-scale porosity representation for moving structures is presented. As explained previously in Chapter 3, further code development has been required to accurately simulate this problem. The modifications have been explained in Section 3.4.2 and the corresponding code sections of the custom solver are shown in Appendix C. The custom solver is used to simulate wave interaction with a moving TLP with a thin perforated outer cylinder represented by its macro-scale effects.

Following the results obtained from the work on static porous structures presented in the previous chapter, only the isotropic porous-media implementation is used from now on, and no turbulence model is applied, meaning that the full NS equations are to be solved. The complexity of the actual WSI problem as present in the experiments, has been simplified for the CFD studies. A reduced TLP geometry is investigated for a small range of wave and porosity conditions, The motion has been restricted to 1-DOF surge motion only and a simplified mooring line representation by means of a linear spring has been used in all following CFD models. To check the adequacy of this approach

in an isolated manner, the TLP is simulated without an outer porous cylinder utilizing the standard and widely validated `olaDyMFlow` solver. After successful verification of the simplified mooring representation, the simulation results of the models with the porous outer cylinder obtained by using the custom solver have been validated. The surge motion and the wave elevation at nearby WGs have been compared against the experimental results and against CFD results obtained with the standard solver. The comparison between the two CFD results using the standard solver and the developed custom solver demonstrates the requirement and advantages of the latter.

7.2 General Model Setup

All models with the TLP were generated with a focus on the main, large-scale features of the WSI problem seeking the smallest computational demand possible. Therefore, the geometry of the TLP is simplified, the domain of the NWT is kept small, the mesh is kept relatively coarse, the mooring line is represented simplistically, the motion is restricted and the physical runtime is kept short, all explained below.

The physical runtime has been set to 22 s (including run-up time), which allows for all wave conditions used (listed in Table 4.3), full 8-12 wave periods to pass the centre of the domain and thus the initial centre of the TLP. This equals the number of oscillation periods in surge.

7.2.1 TLP Geometry

Based on the geometry of the experimental TLP model as introduced in Section 4.4, further simplifications have been made for the CFD models. To simplify the mesh generation procedure and to reduce the number of mesh cells, both the top tower and the three legs at the bottom of the platform have been removed from the geometry. Hence, the CFD model consists of two impermeable cylinders only. The thin porous outer cylinder will be added to the top cylinder. These simplifications affect the geometry but not the body properties such as the total mass and the position of the COG. Those properties have been applied in accordance with the experiments.

It is expected that the reduced geometry leads to a slightly smaller overall drag, which is mainly attributed to form drag (and not viscous drag). The contribution of the top tower can be neglected since it is located in the air and no wind thrust has been applied in the experiments. Using Morison's equation [301], the drag contribution of the three platform legs is estimated to be small compared to the contribution of the main platform elements. Thus, omission of the three legs still allows for a sufficiently accurate method validation.

Two configurations of the TLP have been investigated in the following. Firstly, the TLP has been simulated without the porous cylinder in order to check the mooring line representation. Secondly, the outer porous cylinder has been added by means of an isotropic porous-media representation. The porous outer cylinder has not been resolved explicitly but is represented by its volume-averaged macro-scale effects.

7.2.2 Domain and Boundary Conditions

Based on the good performance of the ER-AWA in all previous simulations, and in order to keep the computational demand small, the NWT was set to a relatively short length of 6 m, a width of 1.5 m and a domain height of 1.7 m. The water depth has been set to $h = 1.2$ m, in accordance with the experiments. The simplified TLP geometry has been positioned at the tank centre at an x-position of 3 m and a y-position of 0.75 m. Following the experiments, a draft of 0.6 m was applied which equals $z = 0.6$ m measured from the tank bottom. The COG is at a vertical position of $z = 1.422$ m. This gives a relative vertical difference of 0.222 m between the COG and the still water level.

All external BCs, such as the wavemaker boundary, the end of the tank on the opposite side, the walls at the flume's bottom and the sides, and the top boundary, are specified as for all previous models, see the Sections 5.2 and 6.2. The boundary of the internal solid parts of the structure is set to a no-slip moving wall condition. This BC takes the movement of the structure into account and adjusts the normal velocity to equal the zero-velocity condition at the wall. It furthermore adjusts the mesh motion flux so that the total flux through the moving wall is zero. A sketch of the model configuration, including all BCs and WGs, is shown in Fig. 7.1a. WG A0 and A1 correspond to the WGs used in the experiments where WG A0 was used in the empty tank only. The WGs B1 and B2 have been added to the CFD model to provide wave amplitude measurement closer to the structure. Illustrations of a CFD simulation of wave interaction with the TLP model including the porous outer cylinder are shown in Figs. 7.1b and 7.1c.

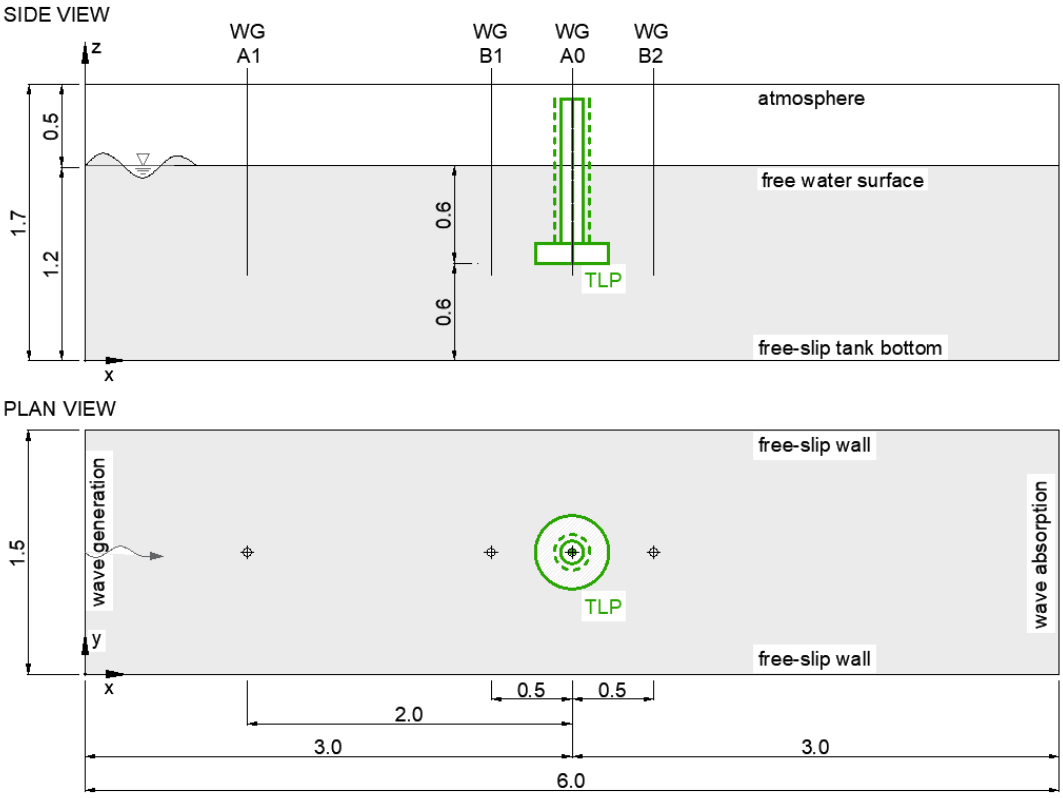

(a) Sketch of the TLP model configuration.

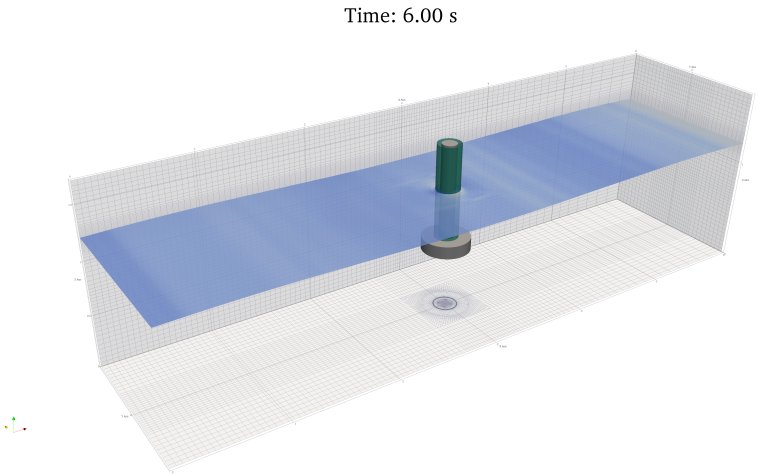

(b) Perspective view of the CFD model

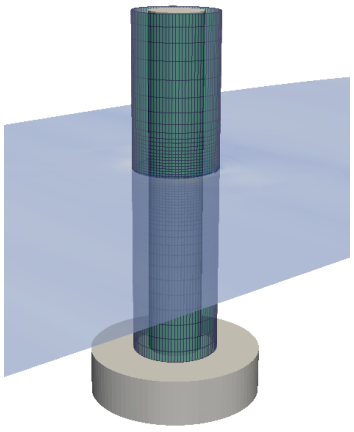

(c) Close-up of the simplified TLP geometry

Figure 7.1: CFD model setup and illustrations of the NWT including the simplified geometry of the TLP with the outer perforated cylinder represented by isotropic porous-media: (a) sketch of the model configuration with all dimensions in [m], (b) perspective view of the NWT, (c) close-up of the WSI. The solid part of the TLP is coloured in grey and the porous cylinder is coloured in green.

7.2.3 Governing Equations

Since the simulation results of the CFD models of the fixed structures have indicated that the application of a turbulence model has insignificant effect on the large-scale force results of the WSI, the full NS equations are used for all dynamic models. Omitting a turbulence model also reduces the computational demand significantly. As no turbulence model has been used and since viscous drag is assumed to have negligible effect, no attention has been given towards replication of any BL effects on the solid walls. To recall in that context, the porous media representing the perforated elements of the structure does not possess a boundary in the domain. Thus, it is not possible to account for any BL effects along the perforated elements in the CFD model.

7.2.4 Discretisation

The spatial discretisation of the NWT has been guided by two objectives: to keep the total number of mesh cells small and to provide a converged force on the porous sheet resulting from the pressure-drop across it. The number of mesh cells per sheet thickness that is required to achieve a converged pressure-drop for the isotropic porosity implementation, is 16 N_x/d (as derived in Section 6.3). This mesh resolution has been applied to the porous-media zone that represents the perforated outer cylinder. The rest of the domain has been discretised with a relatively coarse mesh, and with cell-stretching towards the end of the NWT. In the free shear region before and around the TLP, the cell size in vertical direction, x_z, ranged between 0.03-0.04 m, and the size in x-and y direction between $x_x = x_y = 0.025$-0.05 m. The cell dimension in the z-direction of the (initially vertical) impermeable boundaries of the TLP geometry is identical to the rest of the domain. The cell size in the radial direction is about $x_r = 0.005$ m along the top cylinder and tower, and $x_r = 0.015$ m along the bottom cylinder. Correspondingly and as stated above, the BL has not been resolved and the mesh cell size has not been decreased towards the solid wall boundaries, in contrast to common practice when BL effects are of interest. Also, the free surface region has not been resolved as finely as previously. Refinement was employed in z-direction, but not in x- and y direction. The cell size is in the range of 0.0065-0.02 m which corresponds to CPH and CPL ranging between $2 \leqslant \text{CPH} \leqslant 12$ and $76 \leqslant \text{CPL} \leqslant 378$ for the wave conditions investigated.

Figure 7.2 shows the mesh for a selection of time steps where the transient deformation of the mesh cells is exhibited.

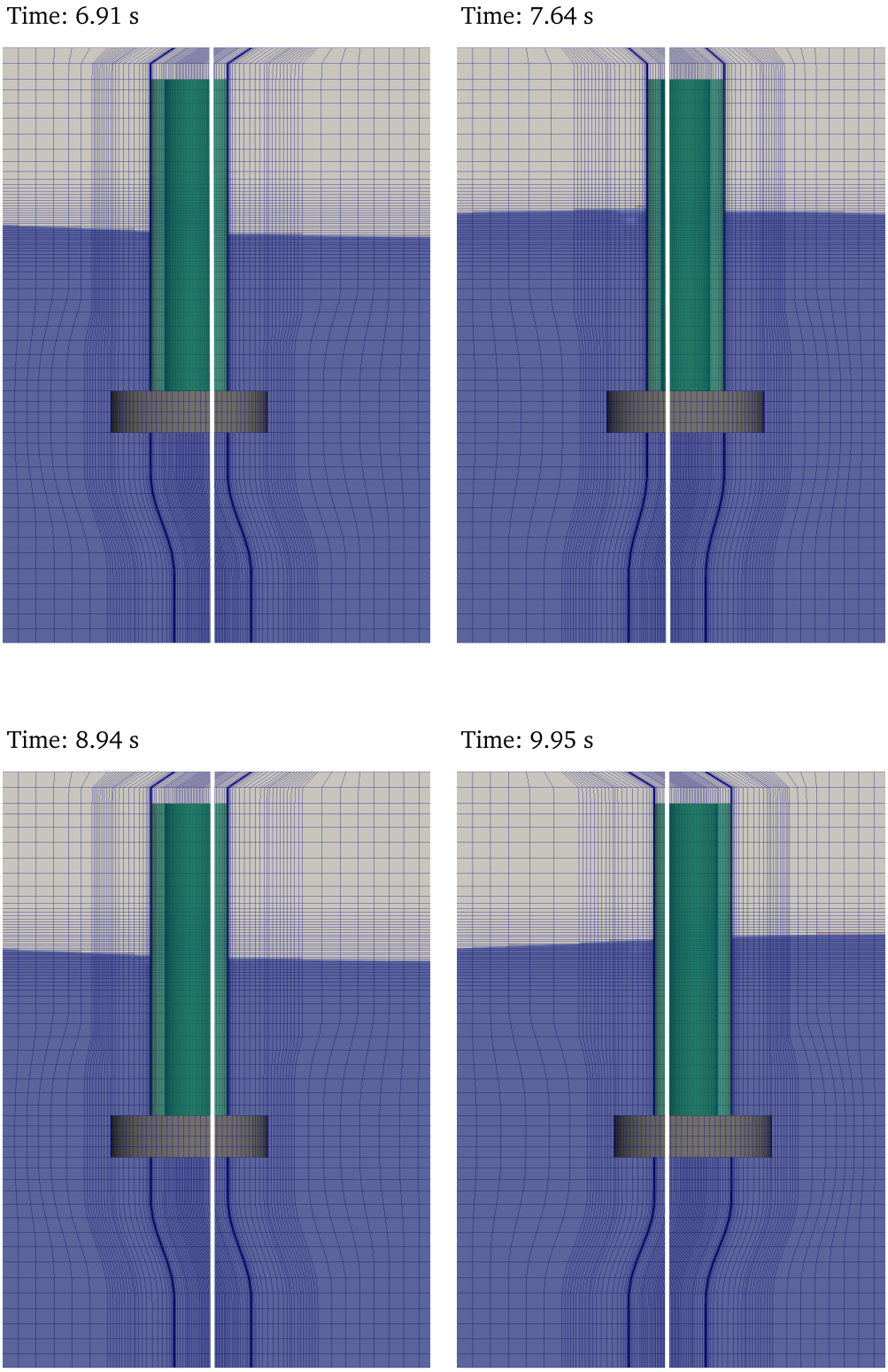

Figure 7.2: View of a vertical cut along the x - z-symmetry plane showing the surge motion displacement of the TLP model consisting of the main solid (grey) platform and the porous outer cylinder (green) as well as the mesh deformation. The vertical white line indicates the initial position of the vertical axis of the TLP.

As with all previous simulations, automatic time step control has been employed for all dynamic models with the TLP. For the models with no outer cylinder and where the default solver has been used, the maximum CFL-number has been set to 0.18-0.19 to achieve scheme and solver stability. The models with the porous cylinder using the amended solver required CFL-numbers between 0.10-0.19 for unsupervised solution processes without occurrence of divergence. These settings resulted in time steps of $4 \times 10^{-5}\,\text{s} \leqslant \Delta t \leqslant 3 \times 10^{-4}\,\text{s}$ for all TLP models (both with and without the porous outer cylinder).

7.2.5 Motion Constraints and Mooring Representation

As stated in Section 4.4, surge was the main mode of motion in all experiments with the physical TLP model. Therefore, and to reduce the complexity of the WSI, the motion of the CFD TLP model has been constrained to 1-DOF surge motion, which equals translational motion in x-direction. All other modes of motion have been restricted.

Following the considerations discussed in Section 3.2, a horizontal linear spring is deemed to provide a sufficiently accurate mooring line representation in this context. The CFD model requires the linear spring stiffness as input. Using (3.7) with the mean displaced water volume of $V_m = 29.6\,\text{l}$, and the mass of the structure, $M = 16.18\,\text{kg}$, the total pretension gives $T_{t0} = 131.4\,\text{N}$. With a tendon length of $L_t = 0.511\,\text{m}$, a total linear spring stiffness, T_{t0}/L_t, of 257.2 N/m has been obtained to represent the horizontal stiffness of all three vertical mooring tendons.

7.2.6 Motion Solver and Scheme Settings

The input for the mesh motion solver is an inner and outer distance, measured from the solid boundary of the TLP geometry, between which the mesh is being morphed. The values for all present models were specified to an inner distance of 0.12 m and an outer distance of 0.40 m. For the body motion solver, the implicit Newmark solver has been selected from the available solvers as stated in Section 2.5.3, and an acceleration relaxation of 0.7 has been applied. Strong coupling between the body motion solver and the fluid motion solver is achieved with `moveMeshOuterCorrectors = yes` and `nOuterCorrectors` = 2. With these settings, stable solver runs could be achieved when the time steps were kept small enough and in the maximum CFL range as stated above. All other applied solver and scheme settings are listed in Table C.1 in Appendix C.

7.3 Validation of the Mooring Representation for the TLP model with no porous Cylinder

As outlined in Section 3.3, the validity of the simplified mooring line representation by means of a horizontal spring is assessed in this section, before the modified solver is validated for modelling of the TLP with the porous outer cylinder in the subsequent section. For the mooring line validation, simulations have been performed with the impermeable main elements of the TLP geometry, and without an outer porous cylinder. For these checks, the default 6-DOF body motion solver within the `sixDoFRigidBodyMotion`-implementation of the `interDyMFoam` (and `olaDyMFlow`)- framework, as introduced in Section 2.5.3, has been used.

The surge motion response is considered to be the criteria for accurate mooring line representation. Hence, no other results have been assessed in this context.

7.3.1 Motion Response

The surge motion response has been compared between the experimental and the CFD results for a limited number of wave conditions. Figure 7.3 shows the time series results of the surge displacement, $x(t)$, for the waves D01, D02 and E01 as listed in Table 4.3. Since the signals have not reached a quasi-steady state within the first 22 s, only the time series have been compared and not the mean motion amplitude results.

All figures exhibit very good agreement between the experimental and CFD results. This demonstrates the validity of the simplified mooring line representation for the present specific conditions. Furthermore, this confirms that the assumption of a linear spring is a good approximation for surge amplitudes less than 100 m as observed by Mackay et al. [42], earlier stated in Section 3.2.4. The present level of accuracy is considered to be sufficient for the following studies with the TLP including the porous outer cylinder. Thus, the same linear spring stiffness is applied to all following simulations.

7.4 Assessment of the Porous-Media Method for a TLP with an outer porous Cylinder

In this section, the custom solver `sixDoFRigidBodyMotionPor` (see the explanation of the amendments in Section 3.4.2 and the corresponding code in Appendix C) has been applied to simulate wave interaction with the TLP including the porous outer cylinder. The surge motion response and the wave elevation at WGs around the structure

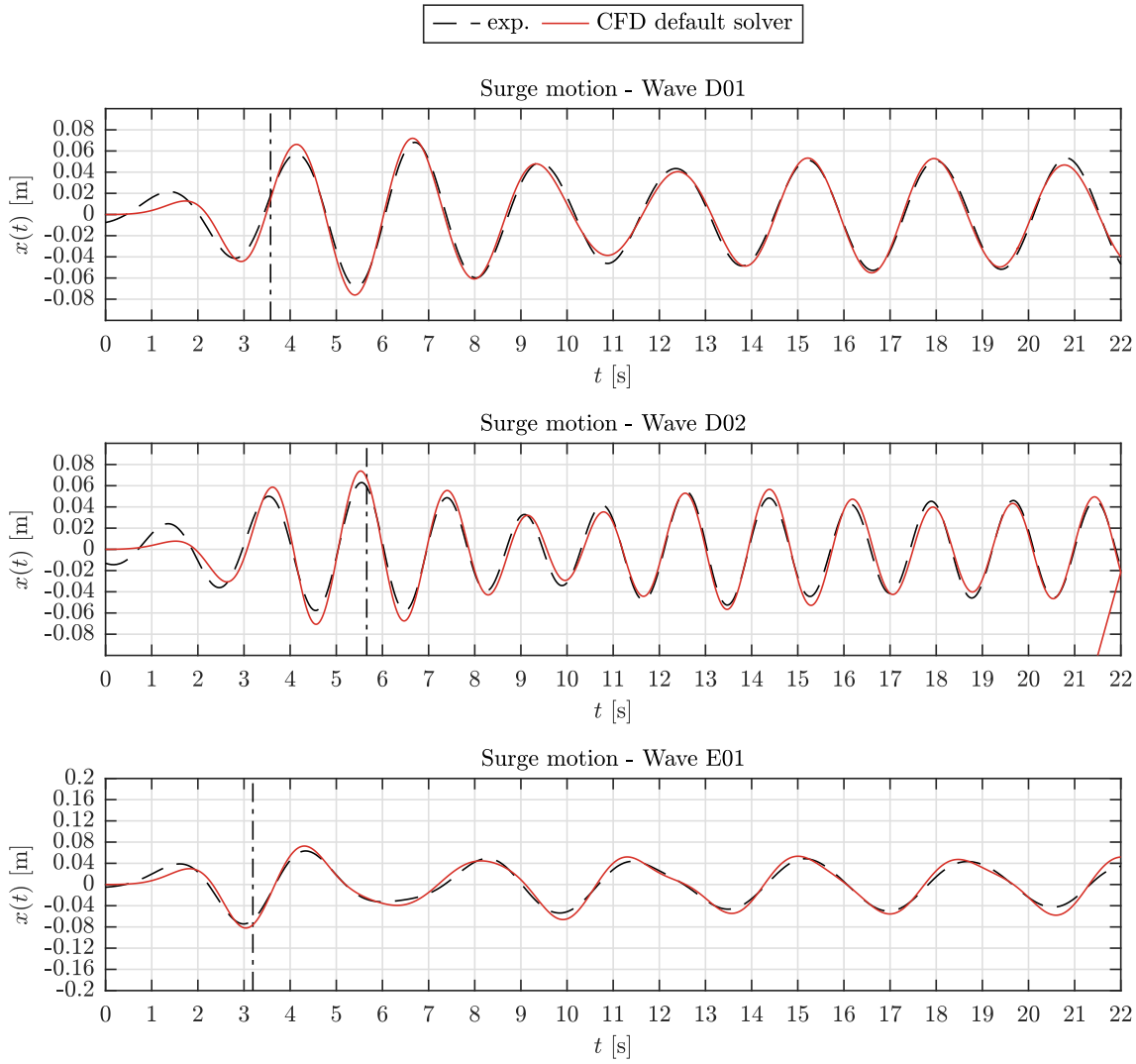

Figure 7.3: Experimental and CFD time series of the surge displacement, $x(t)$, of the TLP model with no outer cylinder. The vertical lines indicate the point in time for the CFD waves to propagate from the generation boundary to the absorption boundary and back to the tank centre. Note the different y-axis scale for wave E01.

have been analysed for the wave conditions D01, D02 and E02 and a porosity value of $n = 0.15$. The results obtained from the simulations with the custom motion solver have been compared against the results obtained from models with the default solver, as well as against the experimental data. The vertical lines in all following figures indicate the point in time for the numerical waves to propagate from the generation boundary to the absorption boundary and back to the sheet position.

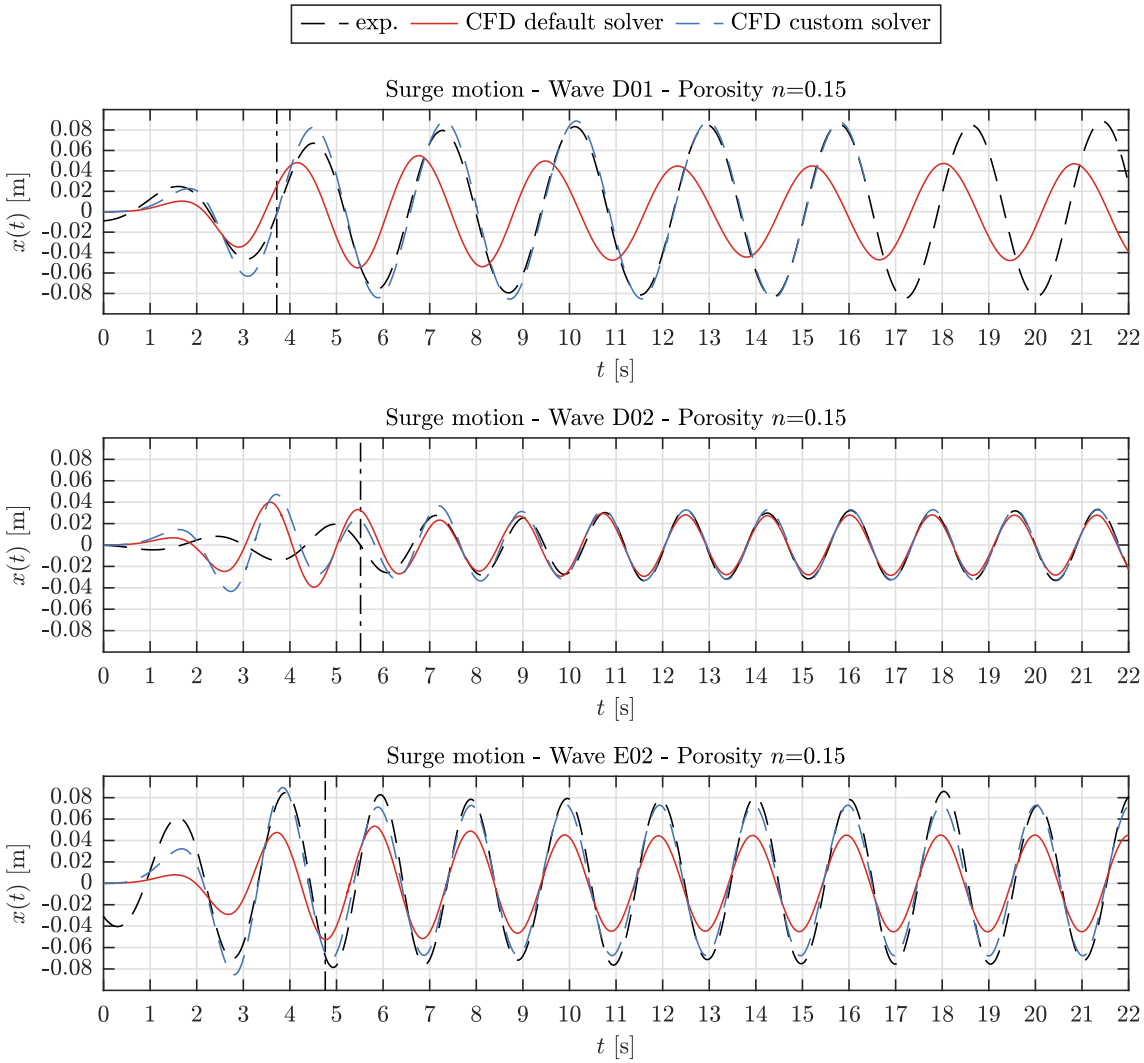

Figure 7.4: Experimental and CFD time series of the surge displacement, $x(t)$, of the TLP model with the outer porous cylinder for the selected wave conditions D01, D02 and E02. The vertical lines indicate the point in time for the CFD waves to propagate from the generation boundary to the absorption boundary and back to the tank centre.

7.4.1 Motion Response

Figure 7.4 shows the time series results of the surge displacement for the conditions investigated. As previously observed for the static structures and as initially discussed in Section 6.4, the initial transient periods of the time series differ between the experimental and CFD results due to the differences in the wave-ramp up process between the numerical and physical wave flume. Apart from this effect, all figures exhibit reasonably good agreement between the experimental results and the CFD results obtained with the custom solver. It is shown that the default solver is not capable of reproducing the real motion response. This mainly concerns the motion amplitude but also the oscillation phase shift. The discrepancies are most significant for the wave D01, where a clear

shift in motion amplitude is exhibited. The results obtained with the default solver are shifted by 0.6 s relative to the results obtained with the custom solver, which agree relatively well with the experiments. The mean motion amplitudes, X, give 0.043 m for the simulation with the default solver and 0.081 m for the one obtained with the custom solver. In relation to the experimental results, this corresponds to $X/X_{exp.} = 0.50$ and 0.95, respectively, where $X_{exp.} = 0.085$ m.

All other investigated wave conditions show good agreement in the motion period but differ in mean surge motion amplitude, X. For the wave condition D02, the differences between the results obtained by the default and custom solver are the smallest with $X/X_{exp.} = 0.073$ for the default and 0.95 for the custom solver. Here, $X_{exp.} = 0.033$ m. The surge amplitude results for wave E02 are $X/X_{exp.} = 0.53$ for the default and 0.77 for the custom solver, where $X_{exp.} = 0.078$ m. The default solver leads to smaller motion amplitudes for all cases, which is due to the lack of the force on the porous structure parts.

It is suspected that the different behaviours of the investigated conditions are rooted in the wave parameters, see Table 4.3, and their relative size to the structure's dimension, e.g. the tendon length, $L_t = 0.51$ m and the diameter of the porous outer cylinder, $D = 0.30$ m. The experimental results of the model tests done by Mackay et al. [42] indicate that the surge motion response amplitude operator (RAO) for the present porosity and geometrical parameters increases for frequencies smaller than about $k_w = 0.86$ 1/m (no clear value of surge natural frequency was obtained). Since the wave condition D01 has a wave frequency of $k_w = 0.72$ 1/m, which is in the region of an increased surge response, this may explain the significant deviations, particularly in terms of the phase shift. On the other hand, the waves D02 and E02 have frequencies of $k_w = 1.39$ 1/m and $k_w = 1.13$ 1/m, respectively, which are outside this indicated region of natural frequency in surge. Furthermore, the wave length of $\lambda = 7.27$ m of wave D01 is the largest in relation to relevant structure dimensions, which may corresponds to a larger impact in wave period.

The wave condition D02 exhibits the smallest deviations in surge amplitude, which is assumed to be related to its combination of a higher frequency, $k_w = 1.39$ 1/m, and a relatively small wave height, $H = 0.04$ m and in relation to the relatively large vertical mesh cell size which corresponds to about 3 CPH.

7.4.2 Wave Gauges

Next, the wave elevation, $\eta(t)$, at the WGs near the structure is assessed. Here, the whole time series for a physical runtime of 22 s and close-ups of sections of the time series are presented. Again, the vertical lines indicate the point in time when the wave

has travelled across the tank and back to the WG. The Figs. 7.5 and 7.6 present the wave elevation, $\eta(t)$, for the WGs shown in Fig. 7.1a for the conditions investigated. WG A1 is positioned 2 m in front of the initial TLP axis location at the tank centre. This is the closest one where experimental data is available. For the WGs B1 and B2, positioned 0.5 m in front and behind the tank centre, only the CFD results obtained with both the default and custom solver are compared between each other. Figure 7.5 shows the WG signals for the wave conditions D01 and D01 and Fig. 7.6 the results for the wave E02. Figure 7.5 exhibits good agreement between all WG signals for the wave conditions D01 and D02. The CFD results of the simulations performed with both the default and custom solver are close to being identical both before and after the TLP. For wave D01, the largest difference between the normalised wave amplitude results, A/A_{input}, appears at WG B02, where the result obtained with the custom solver ($A/A_{input} = 0.97$ where $A_{input} = 0.02$ m) is 3 % smaller than the one obtained with the default solver ($A/A_{input} = 1.0$). For wave D02, the differences between the CFD results due to the different solvers is less than 1% at all WGs. In comparison with the experimental data at WG A01, the amplitude results for the wave D01, A/A_{exp} (where $A_{exp} = 0.019$ m), are 1.07 for the default solver and 1.05 for the custom solver. For wave D02, A/A_{exp} (where $A_{exp} = 0.021$ m) is 0.95 for the default solver and 0.96 for the custom solver.

Figure 7.6 exhibits significant differences between the WG signals of the CFD results for the wave E02. At all WGs, the normalised wave amplitude results, A/A_{input}, obtained with the default solver are 50 % smaller than the ones where the custom solver was used. Here, $A_{input} = 0.04$ m. The models with the custom solver give good agreement with the experimental data at WG A1. Here, $A/A_{exp} = 1.05$ (where $A_{exp} = 0.038$ m) for the model with the custom solver and $A/A_{exp} = 0.53$ for the model with the default solver. Furthermore, a minimal phase shift of approximately 0.2 s is present between the numerical signals and the experimental time series for WG A1, although the initial section has been cut-off with the same amount of time as the motion amplitude signal.

Figure 7.5 covers the waves D01 and D02, which have a wave height of $H = 0.04$ m and wave steepnesses of $k_w A = 0.014$ and 0.028. Figure 7.6 shows the WG results for wave E02, which has a wave height of $H = 0.08$ m and a steepness of $k_w A = 0.045$. Comparison of both figures suggests that the differences between the wave elevation results due to the different solvers are more significant for steeper and higher waves. It is suspected that due to the small motion ranges of the TLP and the relatively large distance between the structure and the WGs, the different motion solvers do not affect the wave elevation as much when the waves are small. However, due to the relatively coarse mesh resolution, the numerical gauging process may not be capable of picking up sufficiently accurate wave elevations for small wave heights. A finer mesh resolution

along the free water level is expected to improve the accuracy of the wave elevation results, but to have a minor effect on the motion results.

Overall, the results for both the surge motion and WGs demonstrate that the default solver cannot replicate the experimental results. The custom solver has been required to account for the force on the porous structure parts of the TLP, and it leads to reasonably good agreement with the experimental data.

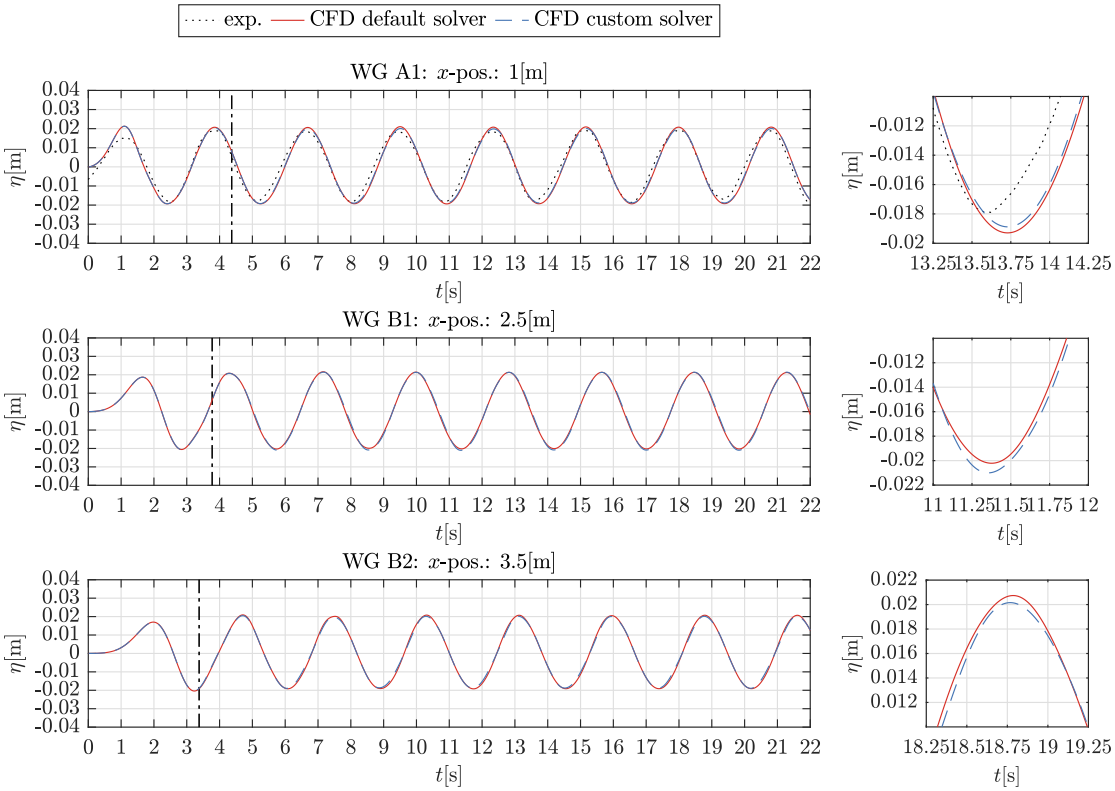

(a) Results for wave D01

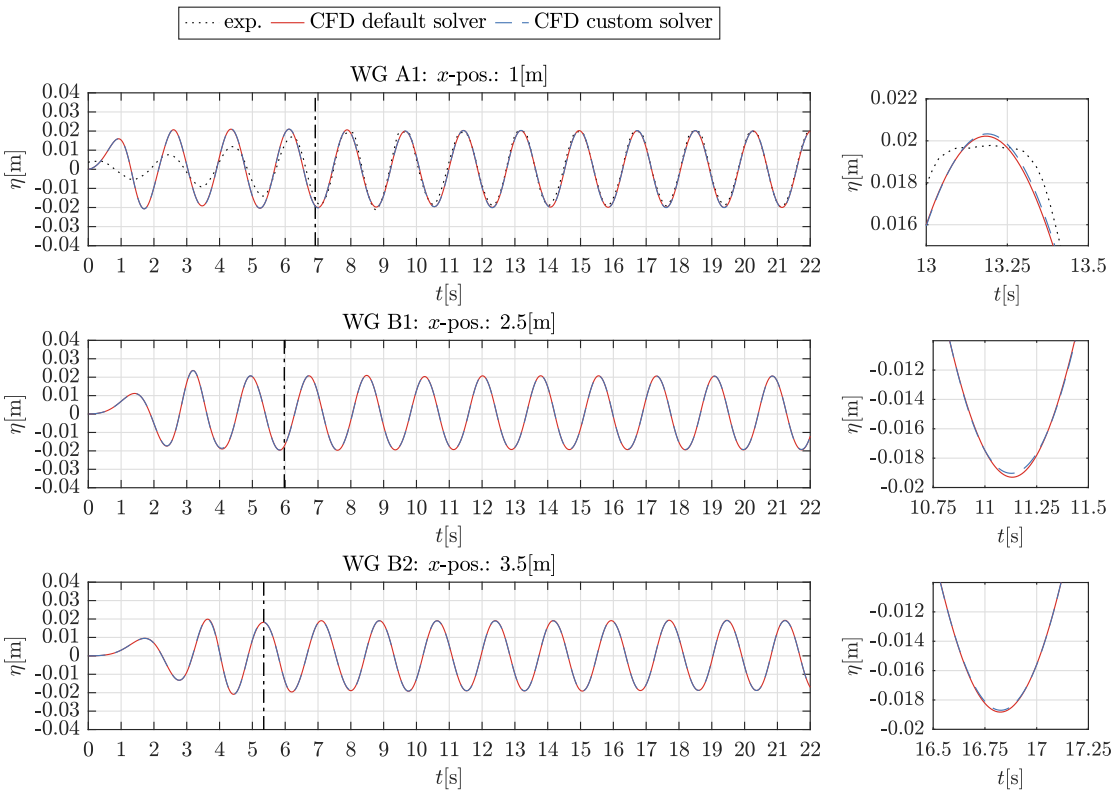

(b) Results for wave D02

Figure 7.5: Experimental and CFD results of the wave elevation, $\eta(t)$, at wave gauges around the TLP for the waves (a) D01 and (b) D02, including the whole time series and selected close-ups. Experimental data is available only for WG A1. The vertical lines indicate the point in time for the CFD waves to propagate from the generation boundary to the absorption boundary and back to the tank centre

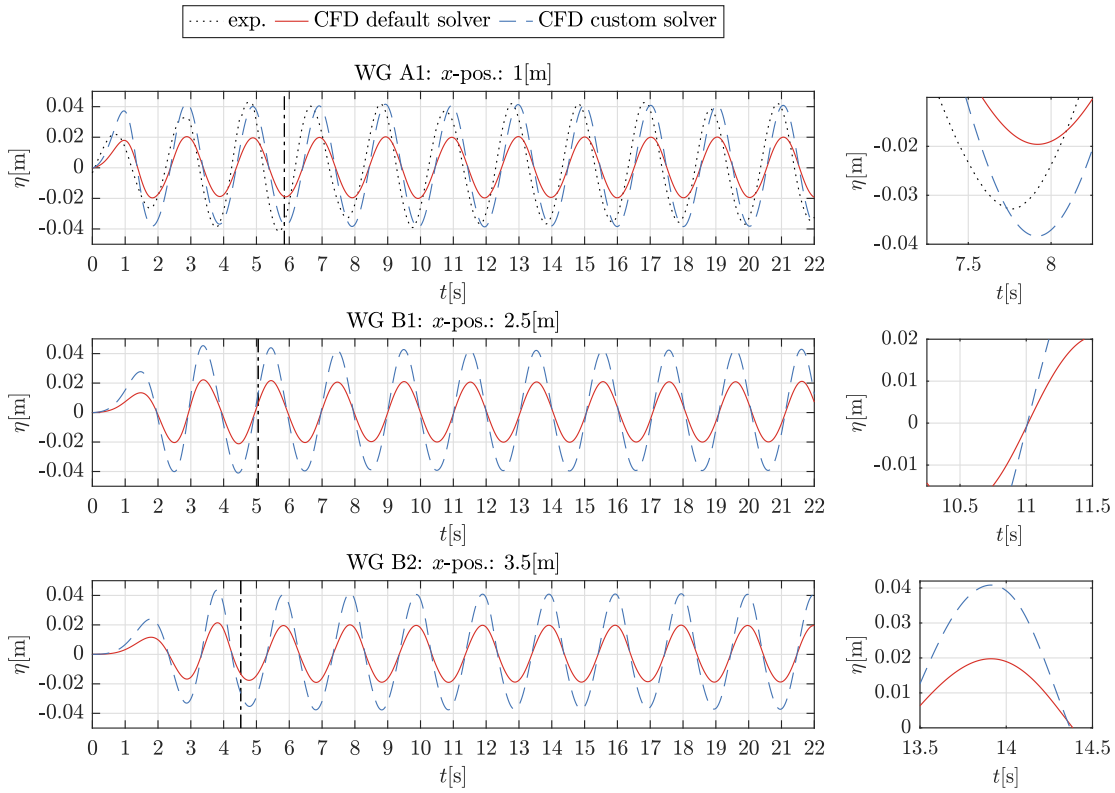

Figure 7.6: Experimental and CFD results of the wave elevation, $\eta(t)$, at wave gauges around the TLP for wave E02, including the whole time series and selected close-ups. Experimental data is available only for WG A1. Note the different y-scale compared to the subfigures in Fig. 7.5.

7.4.3 Tabular Summary

A summary of the results of the mean surge motion amplitudes, X and the mean wave amplitudes, A, at the WGs is given in Table 7.1. It includes the approximate execution times for each model for a physical runtime of 22 s. For the calculation of the mean amplitude values for both the CFD and experimental results, the time series have included reflected waves. Particularly, the time series window of the experimental data was taken from the end of the signal where the series have been closest to a quasi-steady state. The time series of the numerical results reach a quasi-steady state earlier, since the wave reflections are insignificantly small in the NWT.

Models were simulated using 12 CPUs on 14-core dual Intel(R) Xeon(R) Gold 5120 CPU @ 2.20GHz processors. For one simulation 4 CPUs were used. The computation times were between 31 and 79 days for the simulations with 12 CPUs, and 84 days for the simulation with 4 CPUs.

Table 7.1: Summary of the normalised mean surge amplitude, X/X_{exp}, and the normalised mean wave amplitude results, A/A_{input}, at the WGs, including execution times (for a physical runtime of 22 s) for all models.

Poros. n				**0.15**					
Wave		D01			D02			E02	
Solver		default	custom		default	custom		default	custom
Max. CFL		0.16	0.12		0.19	0.19		0.10	0.10
Used CPUs		12	12		12	12		12	4
Exec. Time		45 d	79 d		31 d	48 d		79 d	84 d
X/X_{exp}		0.50	0.85		0.73	0.83		0.53	0.77
A/A_{input}	**exp.**			**exp.**			**exp.**		
WG A1	0.93	1.00	0.98	1.06	1.01	1.01	0.94	0.50	1.00
WG B1	x	1.04	1.06	x	1.01	1.01	x	0.51	1.02
WG B2	x	1.00	0.97	x	0.96	0.96	x	0.48	0.98

7.5 Summary

This chapter has presented the validation of the proposed macro-scale method for porosity representation for wave interaction with a simplified TLP geometry with a thin porous outer cylinder. In the course of the assessment, the results obtained with the required modified rigid-body motion solver within the single-body mesh morphing library, `sixDoFRigidBodyMotionPor`, have been validated against the experimental measurements. For these studies, only the isotropic porous-media implementation has been used and no turbulence model has been applied. The complexity of the models has been reduced in terms of structure geometry, degrees of freedom and mooring line representation. Furthermore, a smaller number of conditions has been investigated compared to the more extensive assessment for the static structures in the previous chapter.

The validity of the mooring representation by means of a horizontal linear spring has been demonstrated for a TLP without the porous outer cylinder and by using the standard motion solver. Then, the results of the TLP models with the outer porous cylinder have been compared against experimental data and results of models with an identical setup, but by using the default solver. The surge motion results of the investigated conditions clearly show that the default solver is not capable of reproducing the correct surge motion response. This is due to the lack of the force on the porous cylinder. The mean surge motion amplitudes, X, obtained with the default solver are

noticeably smaller than the experimental results and the numerical results obtained with the custom solver. For one case, not only the size of the amplitudes differs, but also a clear oscillation phase shift is exhibited.

The CFD results obtained with the custom solver agree very well with the experimental results, for both the surge motion and wave elevation. The phases of the surge motion time series are almost identical and the differences in amplitude are minimal for all cases investigated.

The WG results for the wave condition E02, which is the largest and steepest wave, align well with the overall outcome in terms of a clear difference between the time series obtained with the default and custom solvers. Again, only the models with the custom solver are capable of replicating the experimental data. For the smaller and less steep wave conditions, the difference between the results obtained with the default and custom solvers are minimal and both are capable of replicating the experimental wave gauge signal. It is suspected that the mesh cell size along the air-water interface is too coarse in relation to the small wave height to allow a sufficiently accurate interface calculation. An additional factor may be that the differences in surge motion amplitudes are not large enough to lead to noticeable differences at the investigated WGs, which are at relatively large distances from the structure.

Since the CFD models with the custom solver give good results without the application of a turbulence model, the use of the full NS equations for the present specific WSI problem is considered to be sufficient. As for the simulations with the fixed structures, using a turbulence model for the dynamic models would lead to significantly increased execution times, which could make the present approach impractical. However, a turbulence model may be important for more general cases of WSI or when turbulence parameters are sought.

Overall, the results demonstrate that the macro-scale approach to representation of thin perforated structures with the use of a theoretical pressure-drop model by means of a drag force can be used for both fixed and moving structures. In this context, the custom motion solver within the mesh morphing framework, `sixDoFRigidBodyMotion-Por`, as an adaptation of `sixDoFRigidBodyMotion`, does work for the present specific WSI problem. However, the execution times of the dynamic models with the present solver and setup are considered to be prohibitive for an extensive validation with many wave and porosity conditions. These and other aspects are further discussed in the next Chapter.

Chapter 8

Discussion

This chapter discusses the key aspects of this work regarding the applicability and limitations of a macro-scale porosity representation for the present WSI problem, more general modelling aspects such as wave modelling and dynamic meshing and numerical implications.

A summary of the work conducted, its outcomes and further work is then provided in the final conclusions Chapter.

8.1 Applicability and Limitations of a Macro-scale Porosity Representation

A macro-scale porosity representation has been identified to be a suitable means to study the present problem of wave interaction with fixed and floating thin perforated structures, where large-scale hydrodynamic effects such as forces, motions, and the mean fluid flow behaviour were specified to be of the main interest, as outlined in Section 1.2. The described simplifications make the problem feasible, but also hold limitations. Therefore, the applicability of the used method for other engineering problems has to be discussed.

8.1.1 Navier-Stokes as Governing Equations

In a marine engineering context where large-scale WSI effects are of interest, a macro-scale porosity representation within a CFD framework that solves the (Reynolds-Averaged)-Navier-Stokes equations can be an efficient method that provides a valuable trade-off between computational cost, flexibility and accuracy.

Compared to simpler models based on potential-flow theory, it offers applicability in a wider range of wave conditions and allows for more complex WSI problems to be simulated, see Section 2.2. In that sense, using the NS equations provides greater flexibility in its application and in the present context, offers options for extension to more complex setups. It is straightforward to simulate steep and breaking waves, or to include current, wind and turbine rotor effects. Compared to micro-scale CFD approaches which resolve the flow through perforations explicitly, it demands less computational resource due to a reduced number of mesh cells and therefore, can make CFD simulations a viable method for this type of engineering applications. Conceptually, with regards to accuracy and computational demand, a macro-scale porosity approach within a CFD framework can be considered to be located between potential-flow modelling and micro-scale CFD modelling, and furthermore, located between approaches based on the Euler equations and the incompressible NS equations, as outlined in Fig. 2.1. However, in general, the choice of approach is largely problem-specific and dependent on the aim of an investigation. If many parameters need to be investigated, the computational efforts may still be prohibitive and simpler models would be advantageous. Particularly, for extensive design studies, time-domain simulations, whether CFD or potential-flow based, are generally rarely feasible. For cases where a higher level of accuracy is required, an approach providing higher fidelity may be needed and increased computational expense may be warrantable.

8.1.2 Replication of large-scale Effects

This thesis has shown that the macro-scale method, applying a momentum source term as a function of porosity, can reproduce the large-scale effects of wave interaction with thin porous structures. All investigated parameters exhibit relatively good agreement between all CFD and experimental results. Particularly, the accuracy of the force and motion results is considered to be very good. The good agreement refers to both the mean amplitudes of the force, motion and wave elevation time series, and the signal shapes. The most representative results, are the horizontal forces on the perforated cylinders. Here, the mean force amplitudes of the CFD results of all conditions investigated differ between 2 and 12 % from the experimental data. Regarding the time-dependent behaviour, the non-sinusoidal shape of the force time series is reproduced very accu-

rately, see Fig. 6.33. Comparison of the quality of replication of the force time series to results of similar work by Zhao et al. [176], where time series of forces on vertical and inclined plan net panels represented by porous media are presented, indicates that the present numerical approach provides significantly better agreement with experimental results.

The largest differences have been exhibited for the WG results, but the agreement is still reasonably good. In this context it is clear that a macro-scale approach is, due to its nature, not capable of reproducing the detailed flow field and exact air-water interface close to and across a perforated structure. A volume-averaged porous zone is a representation of the effect of a porous barrier on the flow, where only the bulk effects are replicated, parameterized by means of the pressure-drop model. Consequently, the flow across the barrier is smoothed and not a realistic replication of small-scale effects of the flow across and close to the openings of the barrier. Thus, water jets or vortex shedding are not replicated directly in the CFD model. The difference between the actual physical flow field and its numerical simulation can be compared when looking at Figs. 6.3a and 4.2a. The former shows a snapshot of the 2D NWT as well as a close-up of the wave interaction with the vertical sheet. The latter shows a photo of the real flow patterns of the wave interaction with the sheet in the experiments. Although the numerical illustration exhibits air entrapment at the RHS of the porous sheet, these flow patterns cannot be interpreted as accurate replication of the real flow field. These effects can merely be seen as an indicator for the presence of more complex physical effects.

If an accurate replication of the fluid flow is required, a micro-scale CFD approach would be necessary. Also, the mesh resolution may need to be increased to capture vortex generation with higher accuracy. Only then it is possible to study the exact fluid-structure interaction. In the context of wave interaction with the vertical sheet, this would for instance allow to replicate the jet-like flow through the perforation holes, its impact onto the main wave, potential interactions between the water and air, leading to air entrapment, bubble-like interactions etc. The higher modelling fidelity would, thus, significantly increase the flow accuracy. However, due to the good force and motion results obtained with the macro-scale method, it is hypothesised that higher modelling fidelity would not have a significant effect on the force and motion responses for the present conditions.

8.1.3 No porous Boundary

With a macro-scale porosity representation, no actual boundary exists around the porous or perforated parts of the structure in the CFD model. Consequently, no BL effects can be taken into account with the default BCs available in OF. This has two implications.

Firstly, flow separation and corresponding vortex generation, or shedding, cannot be replicated accurately. Secondly, the contribution of viscous drag on the overall force is not taken into account and thus, neglected.

As estimated with the diagram by Chakrabarti [142] (see Fig. 2.9) and stated in Section 2.3.3, form drag is dominant for all present physical conditions and friction drag makes a negligible contribution. The good overall agreement between the CFD and experimental results confirms this, and thus, shows that viscous and BL effects are not of importance for the specific present cases and the targeted large-scale forces and motions. However, for more general cases, viscous and BL effects may be of greater significance. If exact BL modelling is required, for instance for VIV modelling, a macro-scale approach may be unsuitable in general and a microscopic approach may have to be used instead. One possible solution as a trade-off between a microscopic approach and the macroscopic approach (without a boundary), would be a macro-scale approach including a BL model. Here, a custom BC could be developed where a BL condition is applied to the permeable outer surfaces of a porous-media zone, similar to the standard and existing wall-type condition.

8.1.4 The implemented Pressure-drop Formulation

The theoretical pressure-drop formulation by Molin and Fourest [34] that is used as momentum source term to represent the effects of the perforated barrier on the fluid is capable of reproducing the forces on the thin perforated structures. It has been demonstrated that its formulation by means of a porous drag force and with a drag coefficient as a function of porosity (and independent of any wave parameters) gives good results for all parameters for the range of regular wave conditions and porosity values investigated. The present CFD results confirm the good agreement between results from the potential-flow model by Mackay et al. [41], Mackay and Johanning [44] and the experiments. Furthermore, Qiao et al. [302] have used the same formulation for validation of their CFD model against the identical experimental results. As part of their studies, they have demonstrated that the application of a transient pressure-drop term has no effect on the results. Consequently, the formulation as a porous drag force is now considered to be well validated for thin circularly perforated barriers and no alternative formulation has been explored within the scope of this thesis.

It is expected that it can confidently be applied to a wider range of marine engineering problems when the following parameters are similar to the ones validated: regular wave conditions with moderate steepnesses, thin and circularly perforated barriers, and simple geometrical structures. The more those key parameters deviate, the more the confidence in the applicability of the present approach decreases. This means that the

present approach would require further validation for more general cases, particularly regarding two key aspects: the wave conditions, and the thickness and type of the porous barrier. Regarding the former, the limitations of the pressure-drop formulation would have to be assessed, particularly for very steep and breaking waves, since it is derived under the assumption of steady flow through the openings. Thus, with an increasing difference in water level on either side, its applicability is assumed to decrease. Regarding the characteristics of the porous barrier, the use of a drag force in representation of the structure is considered and evaluated as most suitable, but its applicability may decrease for more complex geometrical shapes such as net- or foam-like structures. Furthermore, it is assumed that with increasing barrier thickness, transient losses due to fluid flow acceleration (represented by the third term on the RHS of (2.35) will gain importance. However, a better way of investigating variations of the pressure-drop formulations is the use of a simpler (potential-flow) model with significantly faster execution times, as done by Mackay et al. [41] and Mackay and Johanning [44].

8.2 General Modelling Aspects

In terms of more general aspects such as wave and turbulence modelling and dynamic meshing, various decisions have been made based on the physical conditions that were present in the experiments. This section briefly evaluates the adequacy of each approach for the present context. For other or more general physical conditions, different approaches may have to be considered.

8.2.1 Wave Modelling

OlaFlow/IHFoam has been considered to be the most promising wave modelling toolbox for the present WSI problem. The performance and accuracy levels of its static boundary technique and active wave absorption (AWA) implementations have been assessed in terms of model setup and numerical settings. A reliable setup with good accuracy of wave replication, propagation and a low level of wave reflections has been derived in Chapter 5, which has served as an important basis for the main work of this thesis. Consequently, alternative wave modelling techniques have not been adopted.

8.2.2 Turbulence Modelling

The present physical conditions, i.e. geometrical and wave parameters, predict a relatively small level of turbulence away from the perforated structure's vicinity. For instance, no large-scale vortex shedding effects at the lee-side of the cylinder have been

expected. However, since turbulence modelling is the core of the RANS method, the effects of two common models have been assessed for the targeted large-scale results of the static models - the horizontal force and the mean flow behaviour. Since the actual turbulence levels in terms of turbulent kinetic energy and dissipation rate are not of interest in this work (see the outlined requirements in Section 1.2), no detailed analysis of those parameters has been performed.

Regarding the large-scale effects, it has been observed that the application of turbulence models has no significant effect on the force on the structure, which indicates that the turbulence inside and close to the perforations is sufficiently well accounted by the pressure-drop term by means of a porous drag force. Also the fluid flow, which was measured by means of WG signals nearby the structures, can be replicated with satisfactory agreement. Compared to the force results, the WG results are more sensitive to turbulence settings, which is mainly exhibited by unsteady ripples of the wave elevation trace in the centre and the lee-wake of the cylinder, see Fig. 6.24. Since the mean wave elevation signals agree relatively well (if the unsteady spikes would be filtered out), this effect is acknowledged and has been reported but was not further investigated.

8.2.3 Dynamic Mesh Morphing

The macro-scale porosity approach could be applied to any kind of marine structure or FOWT platform. However, due to the availability of experimental data for a TLP model, the CFD model setup is selected based on the specific characteristics of a TLP and in alignment with the experimental conditions. As is generally known and confirmed with the experimental results, the motion ranges of a TLP platform are relatively small. For small motion ranges, where also no overturning occurs, and where no narrow geometrical gaps are present in the domain, the mesh morphing method can be considered to be the most suitable dynamic meshing method, see Section 2.5. Mesh morphing allows for 6-DOF motion, is capable of dealing with the present rigid single-body motion and is less computationally demanding than, for instance, the overset meshing method.

Therefore, OF's specific mesh morphing solver for a single body and smaller motion ranges, `sixDoFRigidBodyMotion`, has been considered as the ideal basis for the present dynamic simulations. Thus, the required code development of adding the functionality to use a macro-scale approach for moving structures has been built on top of the existing solver. As a consequence, the custom solver, `sixDoFRigidBodyMotion-Por`, is only applicable for the same type of WSI problem. If the WSI problem diverges from that criteria, i.e. if geometrical narrow gaps are present in the domain, overtopping

occurs or multiple structures move, a different motion solver and dynamic meshing method has to be considered and further code development is required.

8.2.4 CFD Model Complexity

Since the CFD modelling is mainly validated against experimental data, the numerical setup is guided by the experimental conditions and the available data. Thus, this thesis deals with simple structures such as sheets and cylindrical shapes.

For the static structures, the CFD models have been setup in good accordance with the experiments. The models with the vertical sheet were reduced to 2D models. Overall, the CFD results achieved good agreement with both the experimental and potential-flow results. Since the deviations increase for smaller wave frequencies and smaller porosity values, see Fig. 6.34, it is assumed that 3D effects of the WSI gain importance for longer waves and less porous barriers where the fluid flow is less homogeneous due to the smaller number of perforations or smaller perforation size.

For the TLP structure, further simplifications have been made in the CFD setup. The impermeable part of the TLP geometry has been reduced to two connected cylinders, and the three platform legs and the top tower have been omitted. This has simplified the mesh generation process, reduced the number of mesh cells, and thus, the execution times. This has been valid for the present specific case since the drag on the legs has been estimated to have insignificant contribution (see Section 3.2.4), but may not be possible for other more general cases. Furthermore, the TLP motion has been constrained to 1-DOF surge motion and with a simplified mooring tendon representation, where the effect of the three tendons have been represented by means of a single horizontal linear spring, all explained in Section 3.2.4.

The simulation results of the TLP model without an outer porous cylinder have demonstrated that the simplifications are valid for the present conditions. If a more detailed investigation is required or different physical conditions are present, this has to be reviewed. Using the developed custom solver for the simplified model setup for the simulations of the TLP including the porous outer cylinder, has resulted in a successful validation of the macro-scale porosity approach for structures moving in surge motion.

To note, the noticeable differences in quality of the replication of the surge motion for the investigated wave conditions, see Fig. 7.4 mainly root in the wave frequency and their relative distance to a resonant response, and the mesh resolution in relation to the wave height, previously discussed in Section 7.4.

8.3 Numerical Implications

During the CFD modelling for this thesis, sensitivities to certain numerical settings have been observed. Most aspects have occurred rarely and without identifiable correlations or combinations of settings. Only the interface capturing method and the type of porosity implementation used exhibited major effects on the numerical stability of the solution processes.

8.3.1 The Interface Capturing Method

The VOF interface capturing method with MULES-limiting has been chosen for all present studies since it is a well validated method and a standard implementation in OF, as well as in the wave modelling toolboxes OlaFlow/IHFoam and waves2Foam. However, some challenging effects related to its deficits have been observed. Spurious velocities at the air-water interface, particularly relevant, when wave crests pass the structure, occurred when the specified time step size has been set as too large. This effect is directly linked to challenges with the macro-scale porosity representation. Since the pressure-drop is a drag term and thus, a function of velocity squared, a spike in velocity entails a spike in pressure. Although, it has been observed that the velocity spike occurs in the air phase [69, 109, 111], and not in the water, the pressure increase in the air should not significantly affect the porous zone. However, it is suspected that due to the smeared air-water interface, which may affect more mesh cells than expected, too much pressure can be generated locally in the affected mesh cells. This may lead to a local and sudden spike that may causes the solver become unstable or even to diverge.

In the present work, the time step size and maximum CFL-numbers have thus been reduced as a remedy to avoid velocity spikes, thus, pressure-drop spikes and the risk of solver divergence. With this measure it was possible to perform all simulations as required.

Interface capturing methods are a self-contained field of research (see the references in Section 2.2.4) and, thus, outside the scope of this thesis. Therefore, the deficit of longer execution times due to smaller time steps was accepted. However, exploration towards a more stable combination of macro-scale porosity implementation and interface capturing method is considered to be the most interesting topic for future work. Particularly, for the dynamic simulations with the moving TLP, the requirement of small time steps significantly reduces the initial advantages of a macro-scale porosity approach. This is considered to be prohibitive for a more extensive validation of the custom solver, despite the use of a simplified model setup including a relatively coarse mesh etc. Thus, the minimal viable validation has been completed within the scope of

this thesis. For extensive validation of the macro-scale porosity method, an alternative interface capturing method, which allows larger time step and increased numerical stability, is considered to be the crucial next step.

The effect of the VOF's deficits have furthermore appeared to be related to the type of macro-scale porosity implementation. This is discussed below.

8.3.2 Types of Porosity Implementation

The comparison between the CFD results due to different types of porosity implementations (isotropic and orthotropic porous media and porous baffle) shows that all three types of implementation are capable of reproducing large-scale effects of the wave interaction with the static structures, and that the differences between all obtained results are insignificantly small for all conditions investigated.

However, the baffle implementation required very small time steps since it was numerically sensitive to the local spurious velocities at the air-water interface. Also, the orthotropic porous-media representation required smaller time steps than the isotropic implementation. Since this is suspected to be furthermore a direct result of the VOF method used, this behaviour may be resolved with a different interface-capturing approach. However, as stated above, this was not investigated further, since the models with the isotropic porosity implementation achieved good agreement with the experimental results while being the most stable option.

Chapter 9

Conclusions

This chapter provides a summary of the work conducted, its outcome and further work.

9.1 Addressed Thesis Objectives

In order to identify and establish a numerical method to simulate wave interaction with fixed and floating structures that fully or partly consist of thin perforated elements, the following objectives have been addressed within the scope of this thesis.

- The general literature related to this area and all specific aspects such wave modelling and mooring line representation have been reviewed.
- The most suitable numerical framework has been identified in using the two-phase, incompressible (RA)NS equations.
- The most suitable wave modelling technique for the present specific conditions has been identified and assessed.
- Options of representation of thin perforated structures have been reviewed and assessed in detail to identify the most suitable option for application to FOWT platforms.

- The effect of the application of turbulence models has been assessed in combination with the investigated options of porosity representation.
- The validity of the macro-scale porosity representation has been assessed for both fixed and moving structures. For this, code extensions and development was required and have been implemented. Thus, not only the approach but also the developed functionalities have been validated and verified.

Since the present numerical investigations were strongly guided by the experimental conditions and setup in terms of specific wave conditions and geometry shapes and parameters, the thesis objectives and evaluation of the proposed macro-scale approach are bounded by these. Consequently, this work provides a reliable resource for numerical modelling of very similar marine engineering problems such as wave interaction with aquaculture containers or perforated vertical-wall breakwaters. For problems that deviate from the presently investigated range of wave and geometrical conditions, it provides a useful guide in terms of starting point for further evaluation.

9.2 Key Findings

A summary of the key outcome and findings is given in the following.

Wave Modelling

As basis for the main work of this thesis, a reliable wave modelling setup was sought. The wave modelling toolbox OlaFlow/IHFoam has been used with its static boundary and active wave absorption method. With the ER-AWA a very small level of wave reflections and an accurate wave replication could be achieved for all present regular wave conditions.

Pressure-Drop Model

The results of the models with static porous structures demonstrate that the applied theoretical pressure-drop model is capable of replicating the characteristic quadratic pressure-drop of the flow across thin perforated barriers for the range of regular wave frequencies, wave steepnesses as well as sheet porosities investigated. The macro-scale method by means of a drag momentum source term has been successfully validated for the investigated range of geometrical parameters and wave conditions.

Porosity Implementation

The overall results indicate that all types of investigated porosity implementation (isotropic and orthotropic porous media, baffle implementation) are capable of reproducing the horizontal force on the structures and the overall flow behaviour around the structures. Therefore, all types of implementations are suitable in principle but they differ in numerical stability and execution times, see Table 6.1. The solution processes of the models using porous-media implementations were stable and could be executed unsupervised. The execution times of the models with isotropic implementation have been shorter by a factor of approximately 0.85 for the 2D models and by approximately 0.65 for the 3D models, compared to the models with the orthotropic porous-media implementation. The baffle implementation required a very small time step size to run without solver divergence. Therefore, the baffle implementation is considered to be disadvantageous for the present application of two-phase WSI and the present specific numerical framework.

Overall, it is concluded that the isotropic implementation is the best option for the present specific problem and the use of the algebraic (MULES) VOF method and a segregated pressure-velocity coupling algorithm.

Turbulence Modelling

The results of the models with fixed structures demonstrate that the application of both the k-ω-SST and k-ω-stable turbulence models results in minor differences. The wave amplitude in the interior and the lee-wake of the thin porous cylinder differ, but do not affect the force on neither the 2D sheet nor the cylinder. Overall, the use of the full NS equations without a turbulence model is considered as sufficiently accurate for the present conditions. Furthermore, the use of turbulence models leads to significantly increased execution times, counteracting the advantages of the macro-scale porosity approach.

Fixed and Moving Structures

The relatively good agreement between all experimental and CFD results demonstrates that the macro-scale approach can be used for both fixed and moving porous structures. The standard mesh morphing and motion solver is not capable to replicate the motion of a body with thin porous structure parts that are represented by porous media. The modified custom solver has been applied to simulate the TLP model with a porous outer cylinder and has been successfully validated for 1-DOF surge motion. For this and similar cases, the developed solver can readily be used by the research community. For more complex problems, further validation is recommended as part of future work.

The Interface-Capturing Method

The main numerical challenges in terms of stability and convergence have been linked to spurious air velocities at the air-water interface, which are a direct consequence of the algebraic VOF interface capturing method used. Since the pressure-drop formulation and resistance source is a function of velocity, excessive velocity spikes directly cause pressure-drop spikes, which can cause the solver to diverge and crash. The results with the fixed sheet and cylinder indicate that the spurious velocities impact the baffle implementation significantly but less so the porous-media implementations. It is suspected that a volumetric porous zone and its rather smeared pressure-drop application supports the stability and avoids excessive pressure spikes.

Although the algebraic (MULES) VOF method has initially been identified as a suitable interface capturing method, as discussed above, it appeared to be an inconvenient choice in combination with a macro-scale porosity approach, particularly for the dynamic models. Finding a more suitable approach would be one of the key aspects to explore as part of future work. This would allow a more extensive validation of the dynamic simulations in the future. Possible alternative methods could be the geometric `isoAdvector` VOF method by Roenby et al. [107], or the use of the Ghost-Fluid-Method (GFM) as proposed by Vukčević et al. [94]. Once a feasible approach is found, the present assessment could be extended in terms of regular wave and porosity parameters. Then, simulations of decay tests could be performed confidently in order to study the motion-damping effect of the thin perforated outer cylinder.

9.3 Research Contributions

This thesis has made the following research contributions, where most have been published in Feichtner et al. [303] and Feichtner et al. [175], as listed in the preface of this thesis.

- The present pressure-drop formulation has been used in combination with the isotropic porous-media implementation to simulate wave interaction with bottom-fixed thin perforated sheets and cylinders for an extensive range of regular wave conditions and porosity values.
- Different types of porosity implementations (isotropic, orthotropic porous media, baffle implementation) have been compared for wave interaction with a 2D sheet and a cylinder for one regular wave condition and porosity value. The isotropic implementation has been identified as the best option in terms of result accuracy

and numerical stability, applicable to the present specific conditions and the numerical framework used.

- Minimum requirements in mesh resolution have been assessed for each type of porosity implementation. As shown in Fig. 6.4, a converged pressure-drop can be achieved with 8 cells per sheet thickness for the isotropic and 16 cells per sheet thickness for the orthotropic porous media implementation.
- The effect of various turbulence settings, i.e. the omission of a model using the full Navier-Stokes equations, the standard k-ω-SST model and the stabilized k-ω model, on the large-scale parameters of the WSI have been assessed.
- A modified solver based on OF's mesh morphing solver for a single rigid body has been developed and validated for simplified conditions. The modified code is presented in Appendix C and can be used by the research community
- The macro-scale porosity approach has been validated for regular wave interaction with fixed and floating thin perforated structures.

A working model with recommended setup to evaluate different porous shrouds as a load reduction method for FOWT has been developed. The model has been validated for 1-DOF against the available experimental measurements and has potential to be further applied and improved in the future.

9.4 Future Work

In the course of working on this thesis, the following aspects have been identified as relevant for further investigation.

Alternative Interface-Capturing Method

As a result of the algebraic (MULES) VOF method used, spurious local velocities at the air-water interface caused numerical problems in combination with the application of a pressure-drop formulation as a drag term (including velocity squared). The exploration of an alternative interface-capturing method as a remedy is considered to be a crucial next step of potential future work.

It is hypothesized that a different method may increase the numerical stability. This would allow for larger time steps and shorter computation times, respectively, for both the simulations with static and moving structures. Correspondingly, it may increase the numerical stability of the custom motion solver for porous structures. Particularly, the

recent adaptation of the `isoAdvector` geometric VOF interface-capturing method for inter-facial flow through porous media, which was released in June 2021 by Missios et al. [304], may be interesting to test for the present cases.

Wave Conditions

The pressure-drop formulation used in this thesis implies some limitations and this thesis covers validation only for non-breaking regular wave conditions with moderate steepness. The pressure-drop formulation is likely to achieve reasonably good results also for steep and breaking waves. It would however be interesting to assess the limitations of the pressure-drop formulation and its performance for very steep or breaking waves.

Thickness Limitations for the macro-scale Porosity Representation

Since the present study has focused on the validation against experimental data, only structures with corresponding sheet thicknesses have been investigated numerically. In the future it may be interesting to assess the limitations of the used pressure-drop formulation in terms of barrier thickness. Actual values of maximum thicknesses would be useful for both the porous-media and the porous baffle implementation, instead of defining the thickness to be "thin" in relation to its other dimensions. However, this would require an adequate experimental campaign for a reliable validation.

Improved Boundary Layer Representation

The setup in all present models does not accurately account for BL effects. Since the achieved CFD results agree very well with the experimental results, no further adaptations were conducted. However, it would be possible to develop a custom BC that allows flow to go across the porous barrier, whilst also applying a wall function.

Turbulence Modelling

Overall, the application of neither of the investigated turbulence models showed a significant effect on the results. However, their application resulted in unsteady spikes in the wave gauge results including differences between the k-ω-SST and k-ω-stable model. Thus, it may be interesting to investigate the cause for these differences.

Increased TLP Model-Fidelity

The investigations with the TLP have been performed with simplifications in terms of geometry, mooring line representation and numerical setup. To increase the accuracy

and to study the wave-structure interaction more extensively, the model fidelity could be increased as part of future work. Here, the exact TLP geometry could be used, more DOF or the full 6-DOF body motion could be investigated and the mooring lines could be represented by a quasi-static or dynamic model.

References

[1] M. J. Tait. Modelling and preliminary design of a structure-TLD system. *Engineering Structures*, 30(10):2644–2655, 2008.

[2] M. J. Tait, A. A. El Damatty, N. Isyumov, and M. R. Siddique. Numerical flow models to simulate tuned liquid dampers (TLD) with slat screens. *Journal of Fluids and Structures*, 20(8):1007–1023, 2005.

[3] J. A. Hamelin, J. S. Love, M. J. Tait, and J. C. Wilson. Tuned liquid dampers with a Keulegan-Carpenter number-dependent screen drag coefficient. *Journal of Fluids and Structures*, 43:271–286, 2013.

[4] H. Chen and E. D. Christensen. Investigations on the porous resistance coefficients for fishing net structures. *Journal of Fluids and Structures*, 65:76–107, 2016.

[5] K. Shim, P. Klebert, and A. Fredheim. Numerical investigation of the flow through and around a net cage. In *International Conference on Offshore Mechanics and Arctic Engineering, Honolulu, HI, USA, 31 May - 5 June*, volume 43444, pages 581–587, 2009.

[6] K.-H. Lee, J.-H. Bae, S.-G. Kim, and D.-S. Kim. Three-dimensional simulation of wave reflection and pressure acting on circular perforated caisson breakwater by OLAFOAM. *Journal of Korean Society of Coastal and Ocean Engineers*, 29 (6):286–304, 2017.

[7] A. Valizadeh, A. Rafiee, V. Francis, M. Rudman, and B. Ramakrishnan. An analysis of perforated plate breakwaters. In *Proceedings of the Twenty-eighth (2018) International Ocean and Polar Engineering Conference, 10-15 June 2018*, pages 1174–1180, Sapporo, Japan, 2018.

[8] P. Sclavounos, C. Tracy, and S. Lee. Floating offshore wind turbines: Responses in a seastate Pareto optimal designs and economic assessment. *Proceedings of the International Conference on Offshore Mechanics and Arctic Engineering - OMAE*, 6:31–41, 2008.

[9] IRENA. Floating foundations: A game changer for offshore wind power. pages 1–8, 2016.

[10] W. Musial and B. Ram. Large-scale offshore wind power in the United States: Assessment of opportunities and barriers (No. NREL/TP-500-40745). Technical report, National Renewable Energy Lab.(NREL), Golden, CO (United States), 2010.

[11] IRENA. Innovation Outlook: Offshore Wind, 2016.

[12] R. James and M. C. Ros. Floating offshore wind: Market and technology review. Technical Report June, The Carbon Trust, 2015.

[13] W. T. Hsu, K. P. Thiagarajan, M. Hall, M. MaCnicoll, and R. Akers. Snap loads on mooring lines of a floating offshore wind turbine structure. In *Proceedings of the International Conference on Offshore Mechanics and Arctic Engineering - OMAE*, volume 9A, pages 1–9, 2014.

[14] W.-T. Hsu, K. P. Thiagarajan, and M. Lance. Snap load citeria for mooring lines of a floating offshore wind turbine. In *Proceedings of the ASME 2018 1st International Offshore Wind Technical Conference, IOWTC2018, November 4-7*, pages 1–9, San Francisco, CA, 2018.

[15] B. L. Jones, W. H. Lio, and J. A. Rossiter. Overcoming fundamental limitations of wind turbine individual blade pitch control with inflow sensors. *Wind Energy*, 21(10):922–936, 2018.

[16] T. J. Larsen and T. D. Hanson. A method to avoid negative damped low frequent tower vibrations for a floating, pitch controlled wind turbine. *Journal of Physics: Conference Series*, 75(1), 2007.

[17] H. Namik and K. Stol. Individual blade pitch control of floating offshore wind turbines. *Wind Energy: An International Journal for Progress and Applications in Wind Power Conversion Technology*, 13(1):74–85, 2010.

[18] Y. Li. *Coupled computational fluid dynamics/multibody dynamics method with application to wind turbine simulations*. Phd thesis, University of Iowa, 2014.

[19] M. Ha and C. Cheong. Pitch motion mitigation of spar-type floating substructure for offshore wind turbine using multilayer tuned liquid damper. *Ocean Engineering*, 116:157–164, 2016.

[20] Y. Li, K. J. Paik, T. Xing, and P. Carrica. Dynamic overset CFD simulations of wind turbine aerodynamics. *Renewable Energy*, 37(1):285–298, 2012.

[21] P. J. Murtagh, A. Ghosh, B. Basu, and B. M. Broderick. Passive control of wind turbine vibrations including blade/tower interaction and rotationally sampled turbulence. *Wind Energy*, 11(4):305–317, 2008.

[22] Y. Si, H. R. Karimi, and H. Gao. Modelling and optimization of a passive structural control design for a spar-type floating wind turbine. *Engineering Structures*, 69:168–182, 2014.

[23] S. Colwell and B. Basu. Tuned liquid column dampers in offshore wind turbines for structural control. *Engineering Structures*, 31(2):358–368, 2009.

[24] B. Molin. Hydrodynamic modeling of perforated structures. *Applied Ocean Research*, 33(1):1–11, 2011.

[25] M. Fugazza and L. Natale. Hydraulic design of perforated breakwaters. *Journal of Waterway, Port, Coastal, and Ocean Engineering*, 118(1):1–14, 1992.

[26] A. Chakrabarti, Q. Chen, H. D. Smith, and D. Liu. Large eddy simulation of unidirectional and wave flows through vegetation. *Journal of Engineering Mechanics*, 142(8):04016048, 2016.

[27] L. Sun, J. Zang, L. Chen, R. Eatock Taylor, and P. H. Taylor. Regular waves onto a truncated circular column: a comparison of experiments and simulations. *Applied Ocean Research*, 59(0):650–662, 2016.

[28] B. Devolder, P. Rauwoens, and P. Troch. Application of a buoyancy-modified k-ω SST turbulence model to simulate wave run-up around a monopile subjected to regular waves using OpenFOAM. *Coastal Engineering*, 125(January):81–94, 2017.

[29] P. Schmitt and B. Elsaesser. On the use of OpenFOAM to model oscillating wave surge converters. *Ocean Engineering*, 108:98–104, 2015.

[30] J. Westphalen, D. M. Greaves, A. Raby, Z. Z. Hu, D. M. Causon, C. G. Mingham, P. Omidvar, P. K. Stansby, and B. D. Rogers. Investigation of wave-structure interaction using state of the art CFD techniques. *Open Journal of Fluid Dynamics*, 04(01):18–43, 2014.

[31] J. Palm, G. M. Paredes, C. Eskilsson, F. T. Pinto, and L. Bergdahl. Simulation of mooring cable dynamics using a discontinuous galerkin method. *Proceedings of the 5th International Conference on Computational Methods in Marine Engineering, MARINE 2013*, pages 455–466, 2013.

[32] C. C. Mei, P. L. F. Liu, and A. T. Ippen. Quadratic loss and scattering of long waves. *Journal of the Waterways, Harbors and Coastal Engineering Division*, 100:217–239, 1974.

[33] K. Hagiwara. Analysis of upright structure for wave dissipation using integral equation. In *Proceedings of the 19th International Conference on Coastal Engineering, 3–7 September*, pages 2810–2826, Houston, TX, USA, 1984.

[34] B. Molin and J.-M. Fourest. Numerical modeling of progressive wave absorbers. In *7th International Workshop water waves & floating bodies*, pages 199–203, 1992.

[35] P. J. Lynett, P. L.-F. Liu, I. J. Losada, and C. Vidal. Solitary wave interaction with porous breakwaters. *Journal of Waterway, Port, Coastal, and Ocean Engineering*, 126(6):314–322, 2000.

[36] P. Higuera, J. Lara, and I. Losada. Three-dimensional interaction of waves and porous coastal structures using OpenFOAM. Part I: Formulation and validation. *Coastal Engineering*, 83:243–258, 2014.

[37] B. Jensen, N. G. Jacobsen, and E. D. Christensen. Investigations on the porous media equations and resistance coefficients for coastal structures. *Coastal Engineering*, 84:56–72, 2014.

[38] M. Maza, J. L. Lara, and I. J. Losada. Tsunami wave interaction with mangrove forests: A 3-D numerical approach. *Coastal Engineering*, 98:33–54, 2015.

[39] M. del Jesus, J. L. Lara, and I. J. Losada. Three-dimensional interaction of waves and porous coastal structures Part I: Numerical model formulation. *Coastal Engineering*, 64:57–72, 2012.

[40] Y. P. Zhao, C. W. Bi, G. H. Dong, F. K. Gui, Y. Cui, C. T. Guan, and T. J. Xu. Numerical simulation of the flow around fishing plane nets using the porous media model. *Ocean Engineering*, 62:25–37, 2013.

[41] E. Mackay, L. Johanning, D. Qiao, and D. Ning. Numerical and experimental modelling of wave loads on thin porous sheets. In *Proceedings of the ASME*

2019 38th International Conference on Ocean, Offshore and Arctic Engineering, 9-14 June 2019, Glasgow, Scotland, 2019.

[42] E. Mackay, L. Johanning, W. Shi, and D. Ning. Model tests of a TLP floating offshore wind turbine with a porous outer column. In *30th International Ocean and Polar Engineering Conference*, pages 1–9, Shanghai, 2020.

[43] E. Mackay, W. Shi, D. Qiao, R. Gabl, T. Davey, D. Ning, and L. Johanning. Numerical and experimental modelling of wave interaction with fixed and floating porous cylinders. *Ocean Engineering*, 242(November):110118, 2021.

[44] E. Mackay and L. Johanning. Comparison of analytical and numerical solutions for wave interaction with a vertical porous barrier. *Ocean Engineering*, 199 (February):107032, 2020.

[45] C. Windt, J. Davidson, and J. V. Ringwood. High-fidelity numerical modelling of ocean wave energy systems: A review of computational fluid dynamics-based numerical wave tanks. *Renewable and Sustainable Energy Reviews*, 93(May): 610–630, 2018.

[46] R. Guanche. On the importance of calibration and validation procedures: hybrid modeling. In *Proceedings of the BCAM Workshop Hydrodynamics of Wave Energy Converters*, 2017.

[47] G. S. Bennett, P. McIver, and J. V. Smallman. A mathematical model of a slotted wavescreen breakwater. *Coastal Engineering*, 18(3-4):231–249, 1992.

[48] Y. Weng, X. Xu, and H. Huang. Interaction of cnoidal waves with an array of vertical concentric porous cylinders. *Applied Ocean Research*, 58:21–36, 2016.

[49] Z. Zhai, H. Huang, W. Ye, L. Yang, and S. Liu. Hydrodynamic interactions between cnoidal waves and a concentric cylindrical structure with arc-shaped outer cylinder. *Ocean Engineering*, 209(May):107448, 2020.

[50] Z. Zhong and K. H. Wang. Solitary wave interaction with a concentric porous cylinder system. *Ocean Engineering*, 33(7):927–949, 2006.

[51] A. Chakrabarti and T. Sahoo. Reflection of water waves by a nearly vertical porous wall. *ANZIAM Journal*, 37(3):417–429, 1996.

[52] R. B. Kaligatla and T. Sahoo. Wave trapping by dual porous barriers near a wall in the presence of bottom undulation. *Journal of Marine Science and Application*, 16(3):286–297, 2017.

[53] R. B. Kaligatla, S. Tabssum, and T. Sahoo. Effect of bottom topography on wave scattering by multiple porous barriers. *Meccanica*, 53(4-5):887–903, 2018.

[54] Y. Liu and H. J. Li. Iterative multi-domain BEM solution for water wave reflection by perforated caisson breakwaters. *Engineering Analysis with Boundary Elements*, 77(238):70–80, 2017.

[55] C. Yang, F. Noblesse, L. Rainald, and H. Dane. Practical CFD applications to design of a wave cancellation multihull ship. In *Twenty-Third Symposium on Naval Hydrodynamics*, pages 17–22, Val de Reuil, 2000.

[56] Z. Z. Hu, D. M. Causon, C. G. Mingham, and L. Qian. Numerical wave tank study of a wave energy converter in heave. *Proceedings of the International Offshore and Polar Engineering Conference*, 1:383–388, 2009.

[57] Z. Z. Hu, D. M. Causon, C. G. Mingham, and L. Qian. Numerical simulation of water impact on a wave energy converter in free fall motion. *Open Journal of Fluid Dynamics*, 03(02):109–115, 2013.

[58] C. Eskilsson, J. Palm, J. P. Kofoed, and E. Friis-Madsen. CFD study of the overtopping discharge of the Wave Dragon wave energy converter. *Renewable Energies Offshore - 1st International Conference on Renewable Energies Offshore, RENEW 2014*, pages 287–294, 2015.

[59] C. Yang, R. Lohner, and S. C. Yim. Development of a CFD simulation method for extreme wave and structure interactions. In *Proceedings of OMAE 2005 24th International Conference on Offshore Mechanics and Arctic Engineering June 12-17*, pages 1–13, Halkidiki, Greece, 2005.

[60] B. R. Seiffert, M. Hayatdavoodi, and R. C. Ertekin. Experiments and calculations of cnoidal wave loads on a coastal-bridge deck with girders. *European Journal of Mechanics B/Fluids*, 52:191–205, 2015.

[61] J. Palm, C. Eskilsson, L. Bergdahl, and R. E. Bensow. Assessment of scale effects, viscous forces and induced drag on a point-absorbing wave energy converter by CFD simulations. *Journal of Marine Science and Engineering*, 6(4):124–146, 2018.

[62] H. Versteeg and W. Malalasekera. *An introduction to Computational Fluid Dynamics - The Finite Volume Method*, volume 44. Pearson Education Limited, Harlow, 2 edition, 2005.

[63] F. Moukalled, L. Mangani, and M. Darwish. *The finite volume method in computational fluid dynamics*, volume 113. Springer, Berlin, Germany, 2016.

[64] R. A. Gingold and J. J. Monaghan. Smoothed particle hydrodynamics: theory and application to non-spherical stars. *Monthly Notices of the Royal Astronomical Society*, 181(3):375–389, dec 1977.

[65] V. Leble and G. N. Barakos. A coupled floating offshore wind turbine analysis with high-fidelity methods. *Energy Procedia*, 94:523–530, 2016.

[66] A. C. Crespo, J. M. Dominguez, A. Barreiro, M. Gomez-Gesteira, and B. D. Rogers. GPUs, a new tool of acceleration in CFD: efficiency and reliability on Smoothed Particle Hydrodynamics methods. *PLoS ONE*, 6(6), 2011.

[67] S. J. Lind, B. D. Rogers, and P. K. Stansby. Review of smoothed particle hydrodynamics: towards converged Lagrangian flow modelling. *Proceedings of the Royal Society A*, 476(2241), 2020.

[68] D. D. Meringolo, F. Aristodemo, and P. Veltri. SPH numerical modeling of wave-perforated breakwater interaction. *Coastal Engineering*, 101:48–68, 2015.

[69] P. D. Tomaselli. *A methodology for air entrainment in breaking waves and their interaction with a mono-pile*. Phd thesis, Technical University of Denmark, 2016.

[70] M. A. Hossain, S. Hossain, and M. I. H. Soiket. Numerical investigation of vortex shedding in a square cylinder using RANS and LES model. In *ASME 2014 International Mechanical Engineering Congress and Exposition, IMECE2014, November 14-20*, volume 7, Montreal, Canada, 2014.

[71] L. Chen, L. Sun, J. Zang, and A. Hillis. Numerical simulation of wave-induced roll of a 2-D rectangular barge using OpenFOAM. In *29th International Workshop on Water Waves and Floating Bodies*, pages 1–4, Osaka, Japan, 2014.

[72] L. Chen, L. Sun, J. Zang, A. J. Hillis, and A. R. Plummer. Numerical study of roll motion of a 2-D floating structure in viscous flow. *Journal of Hydrodynamics*, 28(4):544–563, 2016.

[73] E. J. Ransley, D. Greaves, A. Raby, D. Simmonds, and M. Hann. Survivability of wave energy converters using CFD. *Renewable Energy*, 109:235–247, 2017.

[74] M. Shives and C. Crawford. Adapted two-equation turbulence closures for actuator disk RANS simulations of wind & tidal turbine wakes. *Renewable Energy*, 92:273–292, 2016.

[75] T. T. Tran and D. H. Kim. A CFD study of coupled aerodynamic-hydrodynamic loads on a semisubmersible floating offshore wind turbine. *Wind Energy*, 21(1): 70–85, 2018.

[76] I. Rivera-Arreba. *Computation of Nonlinear Wave Loads on Floating Structures*. Master's thesis, Delft University of Technology, 2017.

[77] P. Higuera, J. Lara, and I. Losada. Three-dimensional interaction of waves and porous coastal structures using OpenFOAM®. Part II: Application. *Coastal Engineering*, 83:259–270, 2014.

[78] H. Oertel, M. Böhle, and U. Dohrmann. *Strömungsmechanik*. 2009.

[79] J. Peiró and S. Sherwin. Finite Difference, Finite Element and Finite Volume Methods for partial differential equations. In *Handbook of Materials Modeling*, volume 1, pages 2415–2446. Springer, Dordrecht, 2005.

[80] O. C. Zienkiewicz, R. L. Taylor, R. L. Taylor, and R. L. Taylor. *The finite element method: solid mechanics*, volume 2. Butterworth-heinemann, 2000.

[81] The_OpenFOAM_Foundation. OpenFOAM v5 User Guide.

[82] N. G. Jacobsen, D. R. Fuhrman, and J. Fredsoe. A wave generation toolbox for the open-source CFD library: OpenFoam. *International Journal for Numerical Methods in Fluids*, 70(November 2011):1073–1088, 2012.

[83] P. Higuera, I. J. Losada, and J. L. Lara. Three-dimensional numerical wave generation with moving boundaries. *Coastal Engineering*, 101:35–47, 2015.

[84] J. H. Ferziger and M. Peric. *Computational Methods for Fluid Dynamics*. Springer, Berlin, 3 edition, 2002.

[85] A. N. Kolmogorov. Energy dissipation in locally isotropic turbulence. In *Dokl. Akad. Nauk. SSSR*, volume 32, pages 19–21, 1941.

[86] L. Tay-Wo-Chong. *Numerical Simulation of the Dynamics of Turbulent Swirling Flames*. PhD thesis, 2012.

[87] O. Reynolds. On the dynamical theory of incompressible viscous fluids and the determination of the criterion. *Philosophical transactions of the royal society of London*, a(186):123–164, 1894.

[88] T. Holzmann. *Mathematics, Numerics, Derivations and OpenFOAM®*. Number 4. Holzmann CFD, Leoben, 4 edition, 2017.

[89] H. Rusche. *Computational Fluid Dynamics of dispersed two-phase flows at high phase fractions*. Phd thesis, Imperial College London, 2002.

[90] D. C. Wilcox. Reassessment of the scale-determining equation for advanced turbulence models. *AIAA journal*, 26(11):1299–1310, 1988.

[91] W. P. Jones and B. E. Launder. The prediction of laminarization with a two-equation model of turbulence. *International journal of heat and mass transfer*, 15(2):301–314, 1972.

[92] D. Wilcox. *Turbulence modelling for CFD*. Griffin Printing, Glendale, California, LA Canada, California, 1993.

[93] F. R. Menter. Two-equation eddy-viscosity turbulence models for engineering applications. *AIAA journal*, 32(8), 1994.

[94] V. Vukčević, H. Jasak, and I. Gatin. Implementation of the Ghost Fluid Method for free surface flows in polyhedral Finite Volume framework. *Computers and Fluids*, 153:1–19, 2017.

[95] C. W. Hirt and B. D. Nichols. Volume of fluid (VOF) method for the dynamics of free boundaries. *Journal of Computational Physics*, 39(1):201–225, jan 1981.

[96] S. Osher and R. P. Fedkiw. *Level set methods and dynamic implicit surfaces*, volume 153. Springer Science & Business Media, 2006.

[97] J. A. Sethian. *Level set methods and fast marching methods: evolving interfaces in computational geometry, fluid mechanics, computer vision, and materials science*, volume 3. Cambridge university press, 1999.

[98] Y. Sun and C. Beckermann. Sharp interface tracking using the phase-field equation. *Journal of Computational Physics*, 220(2):626–653, 2007.

[99] Y. Sun and C. Beckermann. A two-phase diffuse-interface model for Hele–Shaw flows with large property contrasts. *Physica D: Nonlinear Phenomena*, 237(23): 3089–3098, 2008.

[100] D. L. Sun and W. Q. Tao. A coupled volume-of-fluid and level set (VOSET) method for computing incompressible two-phase flows. *International Journal of Heat and Mass Transfer*, 53(4):645–655, 2010.

[101] P. Higuera, J. L. Lara, and I. J. Losada. Simulating coastal engineering processes with OpenFOAM®. *Coastal Engineering*, 71:119–134, 2012.

[102] I. J. Losada, J. L. Lara, and M. del Jesus. Modeling the interaction of water waves with porous coastal structures. *Journal of Waterway, Port, Coastal, and Ocean Engineering*, 142(6):03116003, 2016.

[103] B. T. Paulsen, H. Bredmose, H. B. Bingham, and N. G. Jacobsen. Forcing of a bottom-mounted circular cylinder by steep regular water waves at finite depth. *Journal of Fluid Mechanics*, 755:1–34, 2014.

[104] E. Berberovic, N. P. V. Hinsberg, S. Jakirlic, I. V. Roisman, and C. Tropea. Drop impact onto a liquid layer of finite thickness: dynamics of the cavity evolution. *Physical Review E*, 79(3):1–15, 2009.

[105] O. Ubbink and R. I. Issa. A method for capturing sharp fluid interfaces on arbitrary meshes. *Journal of computational physics*, 153(1):26–50, 1999.

[106] J. Roenby, H. Bredmose, and H. Jasak. A computational method for sharp interface advection. *Royal Society open science*, 3, 2016.

[107] J. Roenby, B. E. Larsen, H. Bredmose, and H. Jasak. A new volume-of-fluid method in OpenFOAM. In *VII International Conference on Computational Methods in Marine Engineering, MARINE 2017*, pages 266–278, 2017.

[108] S. S. Deshpande, L. Anumolu, and M. F. Trujillo. Evaluating the performance of the two-phase flow solver interFoam. *Computational Science and Discovery*, 5 (1), 2012.

[109] M. Amini Afshar. *Numerical Wave Generation In OpenFOAM®*. Master's thesis, Chalmers University of Technology, 2010.

[110] P. A. Wroniszewski, J. C. Verschaeve, and G. K. Pedersen. Benchmarking of Navier-Stokes codes for free surface simulations by means of a solitary wave. *Coastal Engineering*, 91:1–17, 2014.

[111] B. E. Larsen, D. R. Fuhrman, and J. Roenby. Performance of interFoam on the simulation of progressive waves. *Coastal Engineering Journal*, 2019.

[112] V. Vukčević. *Numerical modelling of coupled potential and viscous flow for marine applications*. Phd thesis, University of Zagreb, 2016.

[113] R. Courant, H. Friedrichs, and H. Lewy. Über die partiellen Differenzgleichungen der mathematischen Physik. *Mathematische Annalen*, 1(100):32–74, 1928.

[114] C. Greenshields. OpenFOAM Programmer's Guide, 2015.

[115] H. Shahmohamadi and M. Mehdi. Experimental investigation and a novel analytical solution of turbulent boundary layer flow over a flat plate in a wind tunnel. *International Journal of Mechanical Sciences*, 133(February):121–128, 2017.

[116] T. Von Kármán. Mechanische Ähnlichkeit und Turbulenz. *Nachrichten von der Gesellschaft der Wissenschaften zu Göttingen, Mathematisch-Physikalische Klasse*, 1930:58–76, 1930.

[117] S. V. Patankar and D. B. Spalding. A calculation procedure for heat, mass and momentum transfer in three-dimensional parabolic flows. *International Journal of Heat and Mass Transfer*, 15(10):1787–1806, 1972.

[118] R. I. Issa. Solution of the implicitly discretised fluid flow equations by operator-splitting. *Journal of computational physics*, 62(1):40–65, 1986.

[119] P. Higuera. OlaFOAM Reference Manual, 2016.

[120] B. Le Méhauté. *An introduction to hydrodynamics and water waves*. Springer, 1976.

[121] N. Karow, L. Kandler, M. Brede, and S. Grundmann. Turbulent transport of discharged ground water in oceanic bottom boundary layers in a water channel experiment. *Ocean Science Discussions*, (January):1–20, 2020.

[122] C. Windt, J. Davidson, P. Schmitt, and J. Ringwood. On the assessment of numerical wave makers in CFD simulations. *Journal of Marine Science and Engineering*, 7(2):47, 2019.

[123] P. Higuera. olaFlow: CFD for waves. 2017.

[124] P. Schmitt and B. Elsaesser. A review of wave makers for 3D numerical simulations. *VI International Conference on Computational Methods in Marine Engineering (MARINE 2015)*, pages 1–10, 2015.

[125] P. Lin and P. Liu. Internal wave-maker for Navier-Stokes equations models. *J. Waterway, Port, Coastal, Ocean Eng.*, 125(August):207–215, 1999.

[126] J. Choi and S. Yoon. Numerical simulations using momentum source wave-maker applied to RANS equation model. *Coastal Engineering*, 56(10):1043–1060, 2009.

[127] P. Schmitt, C. Windt, J. Davidson, J. V. Ringwood, and T. Whittaker. The efficient application of an impulse source wavemaker to CFD simulations. *Journal of Marine Science and Engineering*, 7(3):1–19, 2019.

[128] R. Peric and M. Abdel-Maksoud. Assessment of uncertainty due to wave reflections in experiments via numerical flow simulations. In *The Twenty-fifth International Ocean and Polar Engineering Conference*. International Society of Offshore and Polar Engineers, 2015.

[129] J. Larsen and H. Dancy. Open boundaries in short wave simulations - a new approach. *Coastal Engineering*, 7(3):285–297, 1983.

[130] P. Troch and J. de Rouck. An active wave generating-absorbing boundary condition for VOF type numerical model. *Coastal Engineering*, 38(4):223–247, 1999.

[131] J. Spinneken, M. Christou, and C. Swan. Force-controlled absorption in a fully-nonlinear numerical wave tank. *Journal of Computational Physics*, 272(272): 127–148, 2014.

[132] H. A. Schäffer and G. Klopmann. Review of multidirectional active wave absorption methods. *Journal of waterway, port, coastal, and ocean engineering*, 126(2):88–97, 2000.

[133] P. Higuera, J. L. Lara, and I. J. Losada. Realistic wave generation and active wave absorption for Navier-Stokes models. Application to OpenFOAM®. *Coastal Engineering*, 71:102–118, 2013.

[134] C. Windt, J. Davidson, P. Schmitt, and J. Ringwood. Assessment of numerical wave makers. In *Proceedings of the 12th European Wave and Tidal Energy Conference 27th Aug -1st Sept*, number 1, pages 1–10, Cork, Ireland, 2017. European Wave and Tidal Energy Conference 2017.

[135] A. M. Miquel, A. Kamath, M. A. Chella, R. Archetti, and H. Bihs. Analysis of different methods for wave generation and absorption in a CFD-based numerical wave tank. *Journal of Marine Science and Engineering*, 6(2):1–21, 2018.

[136] T. Vyzikas, D. Stagonas, E. Buldakov, and D. Greaves. The evolution of free and bound waves during dispersive focusing in a numerical and physical flume. *Coastal Engineering*, 132(February):95–109, 2018.

[137] P. Higuera. Enhancing active wave absorption in RANS models. *Applied Ocean Research*, 94(November 2019), 2019.

[138] A. Kamath, H. Bihs, and C. Pakozdi. Investigation of higher-harmonic wave forces and ringing using CFD Simulations. In *Proceedings of the International Conference on Offshore Mechanics and Arctic Engineering - OMAE*, volume 7B, pages 1–8, 2018.

[139] T. Sarpkaya. On the parameter β = Re/KC = D2/νT. *Journal of Fluids and Structures*, 21(4):435–440, 2005.

[140] J. Fredsoe and B. M. Sumer. *Hydrodynamics around cylindrical structures (revised edition)*, volume 26. World Scientific, Singapore, 2006.

[141] O. M. Faltinsen. *Sea Loads on Ships and Offshore Structures*. Cambridge University Press, Cambridge, 1 edition, 1990.

[142] S. K. Chakrabarti. *Hydrodynamics of offshore structures*. WIT press, 1987.

[143] DNV. Recommended practice DNV-RP-F205 - Global performance analysis of deepwater floating structures. Technical Report October, Det Norske Veritas (DNV), 2004.

[144] B. M. Sumer, N. Christiansen, and J. Fredsøe. The horseshoe vortex and vortex shedding around a vertical wall-mounted cylinder exposed to waves. *Journal of Fluid Mechanics*, 332:41–70, 1997.

[145] C. J. Baker. The laminar horseshoe vortex. *Journal of fluid mechanics*, 95(2): 347–367, 1979.

[146] T. Sarpkaya. A Critical Assessment of Morison's Equation. In *International Symposium on Hydrodynamics in Ocean Engineering*, volume 1, pages 447–468, 1981.

[147] T. Sarpkaya. Force on a circular cylinder in viscous oscillatory flow at low Keulegan - Carpenter numbers. *Journal of Fluid Mechanics*, 165:61–71, 1986.

[148] L. Sjökvist, J. Wu, E. Ransley, J. Engström, M. Eriksson, and M. Göteman. Numerical models for the motion and forces of point-absorbing wave energy converters in extreme waves. *Ocean Engineering*, 145(September):1–14, 2017.

[149] W. Wei. *Two-dimensional RANS simulation of flow induced motion of circular cylinder with passive turbulence control*. Phd thesis, The University of Michigan, 2011.

[150] A. Kang and B. Zhu. Wave-current interaction with a vertical square cylinder at different Reynolds numbers. *Journal of Modern Transportation*, 21(1):47–57, 2013.

[151] W. Li, J. Li, and S. Liu. Numerical simulation of vortex-induced vibration of a circular cylinder at low mass and damping with different turbulent models. *Oceans 2014 - Taipei*, 2014.

[152] Q. Li, Q. W. Ma, and S. Yan. Investigations on the feature of turbulent viscosity associated with vortex shedding. *Procedia Engineering*, 126:73–77, 2015.

[153] S. H. Yoon, D. H. Kim, H. Sadat-Hosseini, J. Yang, and F. Stern. High-fidelity CFD simulation of wave run-up for single/multiple surface-piercing cylinders in regular head waves. *Applied Ocean Research*, 59:687–708, 2016.

[154] N. B. Khan, Z. Ibrahim, L. T. T. Nguyen, M. F. Javed, and M. Jameel. Numerical investigation of the vortex-induced vibration of an elastically mounted circular cylinder at high Reynolds number (Re = 104) and low mass ratio using the RANS code. *PLoS ONE*, 12(10):1–17, 2017.

[155] A. Kamath, M. A. Chella, H. Bihs, and Ø. A. Arntsen. CFD investigations of wave interaction with a pair of large tandem cylinders. *Ocean Engineering*, 108: 738–748, 2015.

[156] Z. Z. Hu, D. Greaves, and A. Raby. Numerical wave tank study of extreme waves and wave-structure interaction using OpenFoam®. *Ocean Engineering*, 126(August):329–342, 2016.

[157] M. Anbarsooz, M. Passandideh-Fard, and M. Moghiman. Numerical simulation of a submerged cylindrical wave energy converter. *Renewable Energy*, 64: 132–143, 2014.

[158] G. Giorgi and J. V. Ringwood. Implementation of latching control in a numerical wave tank with regular waves. *Journal of Ocean Engineering and Marine Energy*, 2(2):211–226, 2016.

[159] B. Devolder, P. Rauwoens, and P. Troch. Numerical simulation of a single floating point absorber wave energy converter using OpenFOAM. *Progress in Renewable Energies Offshore - Proceedings of the 2nd International Conference on Renewable Energies Offshore, RENEW 2016*, (2014):197–206, 2016.

[160] B. T. Paulsen, H. Bredmose, and H. B. Bingham. An efficient domain decomposition strategy for wave loads on surface piercing circular cylinders. *Coastal Engineering*, 86:57–76, 2014.

[161] S. Mayer and P. A. Madsen. Simulation of breaking waves in the surf zone using a Navier-Stokes solver. In *Coastal Engineering 2000*, pages 928–941. 2001.

[162] D. Vanneste and P. Troch. 2D numerical simulation of large-scale physical model tests of wave interaction with a rubble-mound breakwater. *Coastal Engineering*, 103:22–41, 2015.

[163] A. Elhanafi, A. Fleming, Z. Leong, and G. Macfarlane. Effect of RANS-based turbulence models on nonlinear wave generation in a two-phase numerical wave tank. *Progress in Computational Fluid Dynamics, an International Journal*, 17 (3):141–158, 2017.

[164] P. A. Durbin. *Turbulence closure models for computational fluid dynamics*. Wiley Online Library, 2004.

[165] A. Kamath, G. Fleit, and H. Bihs. Investigation of free surface turbulence damping in RANS simulations for complex free surface flows. *Water (Switzerland)*, 11(3):1–26, 2019.

[166] B. E. Larsen and D. R. Fuhrman. On the over-production of turbulence beneath surface waves in Reynolds-averaged Navier–Stokes models. *Journal of Fluid Mechanics*, 853:419–460, 2018.

[167] Q. Zou and A. E. Hay. The vertical structure of the wave bottom boundary layer over a sloping bed : theory and field measurements. *Journal of Physical Oceanography*, 33(1991):1380–1400, 2003.

[168] J. A. B. Filho, M. A. Navarro, F. A. P. Magalhaes, and A. A. Campagnole dos Santos. Pressure drop of flow through perforated plate. In *Proceedings of COBEM 2007, 19th International Congress of Mechanical Engineering, 2007*, Brasilia, DF, 2007.

[169] B. Y. Guo, Q. F. Hou, A. B. Yu, L. F. Li, and J. Guo. Numerical modelling of the gas flow through perforated plates. *Chemical Engineering Research and Design*, 91(3):403–408, 2013.

[170] B. Chen, L. Wang, D. Ning, and L. Johanning. CFD analysis on wave load mitigation effect of a perforated wall on offshore structure. In *Proceedings of the*

Twenty-ninth (2019) International Ocean and Polar Engineering Conference , 16-21 June, pages 3653–3658, Honolulu, Hawaii, USA, 2019.

[171] A. George and I. H. Cho. Anti-sloshing effects of a vertical porous baffle in a rolling rectangular tank. *Ocean Engineering*, 214(March):107871, 2020.

[172] F. Mentzoni and T. Kristiansen. Numerical modeling of perforated plates in oscillating flow. *Applied Ocean Research*, 84(January):1–11, 2019.

[173] C. P. Tsai, C. H. Ko, and Y. C. Chen. Investigation on performance of a modified breakwater-integrated OWC wave energy converter. *Sustainability*, 10(3):1–20, 2018.

[174] S. K. Poguluri and I. H. Cho. Analytical and numerical study of wave interaction with a vertical slotted barrier. *Ships and Offshore Structures*, 0(0):1–13, 2020.

[175] A. Feichtner, E. Mackay, G. Tabor, P. R. Thies, and L. Johanning. Comparison of macro-scale porosity implementations for CFD modelling of wave interaction with thin porous structures. *Journal of Marine Science and Engineering*, 9(2): 150, 2021.

[176] Y.-P. Zhao, C.-W. Bi, Y.-X. Liu, G.-H. Dong, and F.-K. Gui. Numerical simulation of interaction between waves and net panel using porous media model. *Engineering Applications of Computational Fluid Mechanics*, 8(1):116–126 (2014), 2014.

[177] H. Darcy. Recherches Experimentales Relatives au Mouvement de l'Eau dans les Tuyax, 1858.

[178] P. Forchheimer. Wasserbewegung durch Boden. *Zeitschrift des Vereins deutscher Ingenieure, Düsseldorf*, 45:1781–1788, 1901.

[179] P. Polubarinova-Kochina. Theory of ground water movement, 1962.

[180] J. C. Ward. Turbulent flow in porous media. *Journal of the Hydraulics Division*, 90(5):1–12, 1964.

[181] C. K. Sollitt and R. H. Cross. Wave transmission through permeable breakwaters. *Coastal Engineering*, 1:1827–1846, 1972.

[182] O. S. Madsen. Wave transmission through porous structures. *Journal of the Waterways, Harbors and Coastal Engineering Division*, 100(3):169–188, 1974.

[183] A. T. Chwang and A. T. Chan. Interaction between porous media and wave motion. *Annual Review of Fluid Mechanics*, 30(1):53–84, 1998.

[184] G. Gan and S. B. Riffat. Pressure loss characteristics of orifice and perforated plates. *Experimental Thermal and Fluid Science*, 14(2):160–165, 1997.

[185] P. McIver. The blockage coefficient for a rectangular duct containing a barrier with a circular aperture. *Applied Ocean Research*, 20(3):173–178, 1998.

[186] Y. Li, Y. Liu, and B. Teng. Porous effect parameter of thin permeable plates. *Coastal Engineering Journal*, 48(4):309–336, 2006.

[187] F. Mentzoni, M. Abrahamsen-Prsic, and T. Kristiansen. Hydrodynamic coefficients of simplified subsea structures. In *Proceedings of the ASME 2018 37th International Conference on Ocean, Offshore and Arctic Engineering*, pages 1–11, 2018.

[188] Z. Huang, Y. Li, and Y. Liu. Hydraulic performance and wave loadings of perforated/slotted coastal structures: A review. *Ocean Engineering*, 38(10): 1031–1053, 2011.

[189] H. H. Li and Y. Y. Cheng. Effect of porous-jump model parameters on membrane flux prediction. In *Advanced Materials Research*, volume 734, pages 2210–2213, Stafa-Zurich, 2013. Trans. Tech. Publ.

[190] V. K. Arghode and Y. Joshi. Modeling strategies for air flow through perforated tiles in a data center. *IEEE Transactions on Components, Packaging and Manufacturing Technology*, 3(5):800–810, 2013.

[191] S. Chacko, B. Shome, V. Kumar, A. Agarwal, and D. Katkar. Numerical simulation for improving radiator efficiency by air flow optimization. In *Proceedings of the ANSA & ETA International Congress, Halkidiki, Greece, 2–3 June*, 2005.

[192] S. J. van der Spuy and T. W. von Backström. An evaluation of simplified CFD models applied to perimeter fans in air-cooled steam condensers. *Proceedings of the Institution of Mechanical Engineers, Part A: Journal of Power and Energy*, 229(8):948–967, 2015.

[193] Z. Sumara and M. Šochman. CFD study on the effects of boundary conditions on air flow through an air-cooled condenser. *EPJ Web of Conferences*, 180:1–5, 2018.

[194] M. A. Kizilaslan, E. Demirel, and M. M. Aral. Effect of porous baffles on the energy performance of contact tanks in water treatment. *Water (Switzerland)*, 10 (8):1–15, 2018.

[195] L. Wang, L. Zhang, and G. Lian. A CFD simulation of 3D air flow and temperature variation in refrigeration cabinet. *Procedia Engineering*, 102:1599–1611, 2015.

[196] X. Shen, T. Wang, and W. Zhong. Numerical simulation and wake modeling of wind turbine rotor as an actuator disk. *International Journal of Modern Physics: Conference Series*, 19:320–330, 2012.

[197] W. Hunter. *Actuator disk methods for tidal turbine arrays*. Phd thesis, University of Oxford, 2015.

[198] A. Bakica, I. Gatin, V. Vukčević, H. Jasak, and N. Vladimir. Accurate assessment of ship-propulsion characteristics using CFD. *Ocean Engineering*, 175:149–162, 2019.

[199] G. N. Barakos, T. Fitzgibbon, A. N. Kusyumov, S. A. Kusyumov, and S. A. Mikhailov. CFD simulation of helicopter rotor flow based on unsteady actuator disk model. *Chinese Journal of Aeronautics*, 33(9):2313–2328, 2020.

[200] A. Filippone and R. Mikkelsen. Advances in CFD & actuator disk models for helicopter aerodynamics. In *35th European Rotorcraft Forum 2009, ERF 2009, Hamburg, Germany, 22-25 September*, volume 2, pages 661–669, 2009.

[201] J. L. Lara, M. del Jesus, and I. J. Losada. Three-dimensional interaction of waves and porous coastal structures Part II: Experimental validation. *Coastal Engineering*, 64:26–46, 2012.

[202] M. Brito, J. Fernandes, and J. B. Leal. Porous media approach for RANS simulation of compound open-channel flows with submerged vegetated floodplains. *Environmental Fluid Mechanics*, 6(16):1247–1266, 2016.

[203] S. Hadadpour, M. Paul, and H. Oumeraci. Numerical investigation of wave attenuation by rigid vegetation based on a porous media approach. *Journal of Coastal Research*, 92(1):92–100, 2019.

[204] A. Kyte. Practical use of computational fluid dynamics (CFD) in improving the efficiency of domestic ventilation waste heat recovery systems. *International Journal of Energy and Environmental Engineering*, 5(2-3):1–7, 2014.

[205] H. E. Hafsteinsson. Porous media in OpenFOAM. Technical report, Chalmers, 2009.

[206] S. Whitaker. Diffusion and dispersion in porous media. *A.l.Ch.E. Journal*, 1967.

[207] J. C. Slattery. Flow of viscoelastic fluids through porous media. *AIChE Journal*, 13(6):1066–1071, 1967.

[208] P. L.-F. Liu, P. Lin, K.-A. Chang, and T. Sakakiyama. Numerical modeling of wave interaction with porous structures. *Journal of waterway, port, coastal, and ocean engineering*, 125(6):322–330, 1999.

[209] W. G. Gray. A derivation of the equations for multi-phase transport. *Chemical Engineering Science*, 30(2):229–233, 1975.

[210] V. K. Srineash, A. Kamath, K. Murali, and H. Bihs. Numerical simulation of wave interaction with submerged porous structures and application for coastal resilience. *Journal of Coastal Research*, 36(4):752–770, 2020.

[211] A. Nakayama and F. Kuwahara. A macroscopic turbulence model for flow in a porous medium. 1999.

[212] T. J. Hsu, T. Sakakiyama, and P. L. Liu. A numerical model for wave motions and turbulence flows in front of a composite breakwater. *Coastal Engineering*, 46(1):25–50, 2002.

[213] B. D. Wood, X. He, and S. V. Apte. Modeling Turbulent Flows in Porous Media. *Annual Review of Fluid Mechanics*, 52(1):171–203, 2020.

[214] N. G. Jacobsen, M. R. van Gent, and G. Wolters. Numerical analysis of the interaction of irregular waves with two dimensional permeable coastal structures. *Coastal Engineering*, 102:13–29, 2015.

[215] W. Zhao and D. Wan. Numerical study of interactions between phase II of OC4 wind turbine and its semi-submersible floating support system. *Journal of Ocean and Wind Energy*, 2(1):45–53, 2015.

[216] G. Morgan. *Application of the interfoam VoF Code to coastal wave/structure interaction*. Phd thesis, University of Bath, 2013.

[217] B. Devolder. *Hydrodynamic modelling of wave energy converter arrays*. Phd thesis, Unversiteit Gent, KU Leuven, 2018.

[218] M. M. Horoub. Dynamic analysis of a tension leg platforms (TLPs) inspired by parallel robotic manipulators. *IEEE Access*, 8:35222–35230, 2020.

[219] J. Donea, A. Huerta, J.-P. Ponthot, and A. Rodriguez-Ferran. Arbitrary Lagrangian–Eulerian methods. *The Encyclopedia of Computational Mechanics*, 1: 413–437, 2004.

[220] C. W. Hirt, A. A. Amsden, and J. L. Cook. An arbitray Lagrangian-Eulerian computing method for all flow speeds. *Journal of Computational Physics*, 14(3): 227–253, 1974.

[221] G. Starius. Composite mesh difference methods for elliptic boundary value problems. *Numerische Mathematik*, 28(2):243–258, 1977.

[222] G. Starius. On composite mesh difference methods for hyperbolic differential equations. *Numerische Mathematik*, 35(3):241–255, 1980.

[223] J. Steger, F. C. Dougherty, and J. A. Benek. A chimera grid scheme. In *Ghia KN and Chia U (eds) Advances in grid generation, ASME-FED5*, pages 59–69, 1983.

[224] J. Benek, P. Buning, and J. Steger. A 3-D chimera grid embedding technique. In *7th Computational Physics Conference*, 1985.

[225] C. Windt, J. Davidson, D. D. Chandar, N. Faedo, and J. V. Ringwood. Evaluation of the overset grid method for control studies of wave energy converters in OpenFOAM numerical wave tanks. *Journal of Ocean Engineering and Marine Energy*, 6(1):55–70, 2020.

[226] R. G. Coe, B. J. Rosenberg, E. W. Quon, C. C. Chartrand, Y. H. Yu, J. van Rij, and T. R. Mundon. CFD design-load analysis of a two-body wave energy converter. *Journal of Ocean Engineering and Marine Energy*, 5(2):99–117, 2019.

[227] H. Chen, Z. Lin, L. Qian, Z. Ma, and W. Bai. CFD simulation of wave energy converters in focused wave groups using overset mesh. *International Journal of Offshore and Polar Engineering*, 30(1):70–77, 2020.

[228] X. Zhang, Z. Lin, S. Mancini, P. Li, D. Liu, F. Liu, and Z. Pang. Numerical investigation into the effect of damage openings on ship hydrodynamics by the overset mesh technique. *Journal of Marine Science and Engineering*, 8(1), 2020.

[229] J. Jiao and S. Huang. CFD simulation of ship seakeeping performance and slamming loads in bi-directional cross wave. *Journal of Marine Science and Engineering*, 8(5):1–24, 2020.

[230] T. C. Yao, Y. S. Zhao, Y. P. He, Y. L. Shao, Z. L. Han, L. Duan, and Chao-Huang. CFD-based analysis of a 6MW spar-type floating wind turbine with focus on nonlinear wave loads. *Proceedings of the International Offshore and Polar Engineering Conference*, 2020-Octob:432–439, 2020.

[231] P. Cheng and D. Wan. Fully coupled aero-hydrodynamic simulation of floating offshore wind turbines with overset grid technology. In *Proceedings of the Fourth International Conference in Ocean Engineering (ICOE2018), Lecture Notes in Civil Engineering*, volume 22, pages 647–661, 2019.

[232] M. Močilan, Š. Husár, J. Labaj, and M. Žmindák. Non-stationary CFD simulation of a gear pump. *Procedia Engineering*, 177:532–539, 2017.

[233] W. M. Dziedzic, B. T. Vu, and M. G. Shah. Three-dimensional, multi-phase modeling of a water nozzle injection system using adaptive re-meshing. *2018 Fluid Dynamics Conference*, pages 1–14, 2018.

[234] E. E. Panagiotopoulos and S. D. Kyparissis. CFD transonic store separation trajectory predictions with comparison to wind tunnel investigations. *International Journal of Engineering*, 3(6):538–555, 2010.

[235] M. M. Selim and R. P. Koomullil. Mesh deformation approaches – s survey. *Journal of Physical Mathematics*, 7(2), 2016.

[236] A. A. Johnson and T. E. Tezduyar. Mesh update strategies in parallel finite element computations of flow problems with moving boundaries and interfaces. *Computer methods in applied mechanics and engineering*, 119(1-2):73–94, 1994.

[237] T. E. Tezduyar. Finite element methods for flow problems with moving boundaries and interfaces. *Archives of computational methods in engineering: state of the art reviews*, 8(2):83–130, 2001.

[238] H. Jasak and Ž. Tuković. Automatic mesh motion for the unstructured Finite Volume Method. *Transactions of Famena*, 30(2):1–20, 2006.

[239] J. T. Batina. Unsteady Euler airfoil solutions using unstructured dynamic meshes. *AIAA journal*, 28(8):1381–1388, 1990.

[240] J. Thompson, Z. U. A. Warsi, and C. Mastin. Numerical grid generation: Foundations and applications. *Computer Science*, 1985.

[241] Y. Zhao and A. Forhad. A general method for simulation of fluid flows with moving and compliant boundaries on unstructured grids. *Computer Methods in Applied Mechanics and Engineering*, 192(39-40):4439–4466, 2003.

[242] A. de Boer, M. S. van der Schoot, and H. Bijl. Mesh deformation based on radial basis function interpolation. *Computers and Structures*, 85(11-14):784–795, 2007.

[243] K. Shoemake. Animating rotation with quaternion curves. In *Proceedings of the 12th annual conference on Computer graphics and interactive techniques*, pages 245–254, 1985.

[244] J. McNaughton, I. Afgan, D. D. Apsley, S. Rolfo, T. Stallard, and P. K. Stansby. A simple sliding-mesh interface procedure and its application to the CFD simulation of a tidal-stream turbine. *International journal for numerical methods in Fluids*, 74(4):250–269, 2013.

[245] Z. Jaworski, M. L. Wyszynski, I. P. Moore, and A. W. Nienow. Sliding mesh computational fluid dynamics - a predictive tool in stirred tank design. *Proceedings of the Institution of Mechanical Engineers, Part E*, 211(3):149–156, 1997.

[246] J. Bridgeman, B. Jefferson, and S. A. Parsons. The development and application of CFD models for water treatment flocculators. *Advances in Engineering Software*, 41(1):99–109, 2010.

[247] N. Durrani, H. Hameed, H. Rahman, and S. Chaudhry. A detailed aerodynamic design and analysis of a 2D vertical axis wind turbine using sliding mesh in CFD. In *49th AIAA aerospace sciences meeting including the new horizons forum and aerospace exposition*, page 541, Orlando, Florida, 2011.

[248] R. Lanzafame, S. Mauro, and M. Messina. 2D CFD modeling of H-Darrieus wind turbines using a transition turbulence model. *Energy Procedia*, 45:131–140, 2014.

[249] Y. Liu, Q. Xiao, A. Incecik, C. Peyrard, and D. Wan. Establishing a fully coupled CFD analysis tool for floating offshore wind turbines. *Renewable Energy*, 112: 280–301, 2017.

[250] N. Ren, Y. Li, and J. Ou. Coupled wind-wave time domain analysis of floating offshore wind turbine based on Computational Fluid Dynamics method. *Journal of Renewable and Sustainable Energy*, 6(2):023106–1 – 023106–13, 2014.

[251] N. M. Newmark. A method of computation for structural dynamics. *ASCE Journal of the engineering mechanics division*, 85(3):67–94, 1959.

[252] J. Crank and P. Nicolson. A practical method for numerical evaluation of solutions of partial differential equations of the heat-conduction type. In *Mathematical*

Proceedings of the Cambridge Philosophical Society, volume 43, pages 50–67. Cambridge University Press, 1947.

[253] F. M. Bos, D. Matijašević, Z. Terze, B. W. van Oudheusden, and H. Bijl. OpenFOAM mesh motion using Radial Basis Function interpolation. In *8th. World Congress on Computational Mechanics (WCCM8) 5th European Congress on Computational Methods in Applied Sciences and Engineering (ECCOMAS 2008), June 30 - July*, pages 5–6, Venice, Italy, 2008.

[254] S. Seo, S. Park, and B. Y. Koo. Effect of wave periods on added resistance and motions of a ship in head sea simulations. *Ocean Engineering*, 137(April): 309–327, 2017.

[255] B. Devolder, P. Schmitt, P. Rauwoens, B. Elsaesser, and P. Troch. A review of the implicit motion solver algorithm in OpenFOAM to simulate a heaving buoy. In *18th Numerical Towing Tank Symposium (NuTTS'15)*, Cortona, Italy, 2015.

[256] E. J. Ransley, D. M. Greaves, A. Raby, D. Simmonds, M. M. Jakobsen, and M. Kramer. RANS-VOF modelling of the Wavestar point absorber. *Renewable Energy*, 109:49–65, 2017.

[257] S. A. Brown, E. J. Ransley, and D. M. Greaves. Assessing focused wave impacts on floating WECs using OpenFOAM. *Proceedings of the Institution of Civil Engineers: Engineering and Computational Mechanics*, pages 1–28, 2021.

[258] N. Bruinsma, B. T. Paulsen, and N. G. Jacobsen. Validation and application of a fully nonlinear numerical wave tank for simulating floating offshore wind turbines. *Ocean Engineering*, 147(October 2017):647–658, 2018.

[259] J. H. Chow and E. Y. Ng. Strongly coupled partitioned six degree-of-freedom rigid body motion solver with Aitken's dynamic under-relaxation. *International Journal of Naval Architecture and Ocean Engineering*, 8(4):320–329, 2016.

[260] C. Förster, W. A. Wall, and E. Ramm. Artificial added mass instabilities in sequential staggered coupling of nonlinear structures and incompressible viscous flows. *Computer Methods in Applied Mechanics and Engineering*, 196(7):1278–1293, 2007.

[261] H. G. Matthies and J. Steindorf. Partitioned but strongly coupled iteration schemes for nonlinear fluid – structure interaction. *Computers and Structures*, 80:1991–1999, 2002.

[262] P. Causin, J. F. Gerbeau, and F. Nobile. Added-mass effect in the design of partitioned algorithms for fluid-structure problems. *Computer Methods in Applied Mechanics and Engineering*, 194(42-44):4506–4527, 2005.

[263] I. Gatin, V. Vukčević, H. Jasak, and H. Rusche. Enhanced coupling of solid body motion and fluid flow in finite volume framework. *Ocean Engineering*, 143 (June):295–304, 2017.

[264] A. J. Dunbar, B. A. Craven, and E. G. Paterson. Development and validation of a tightly coupled CFD/6-DOF solver for simulating floating offshore wind turbine platforms. *Ocean Engineering*, 110:98–105, 2015.

[265] B. Devolder, P. Troch, and P. Rauwoens. Accelerated numerical simulations of a heaving floating body by coupling a motion solver with a two-phase fluid solver. *Computers and Mathematics with Applications*, 77(6):1605–1625, 2019.

[266] R. L. Campbell. Fluid-structure interaction and inverse design simulations for highly flexible turbomachinery. *The Journal of the Acoustical Society of America*, 129(4):2385, 2011.

[267] E. G. Paterson, R. V. Wilson, and F. Stern. General-purpose parallel unsteady RANS ship hydrodynamics code : CFDSHIP-IOWA. Technical report, 2003.

[268] J. Davidson and J. V. Ringwood. Mathematical modelling of mooring systems for wave energy converters - A review. *Energies*, 10(5), 2017.

[269] G. M. Paredes, C. Eskilsson, J. Palm, J. P. Kofoed, and L. Bergdahl. Coupled BEM/hp-FEM modelling of moored floaters. *Lecture Notes in Civil Engineering*, 18:504–510, 2019.

[270] M. Hall and A. Goupee. Validation of a lumped-mass mooring line model with DeepCwind semisubmersible model test data. *Ocean Engineering*, 104:590–603, 2015.

[271] J. Palm, C. Eskilsson, G. M. Paredes, and L. Bergdahl. Coupled mooring analysis for floating wave energy converters using CFD: Formulation and validation. *International Journal of Marine Energy*, 16:83–99, 2016.

[272] J. Palm, L. Bergdahl, and C. Eskilsson. Parametric excitation of moored wave energy converters using viscous and non-viscous CFD simulations. In *Advances in Renewable Energies Offshore – Guedes Soares (Ed.)*, number October, 2018.

[273] C. Hoeg and Z. Zhang. The influence of different mooring line models on the stochastic dynamic responses of floating wind turbines. *Journal of Physics: Conference Series*, 1037(6), 2018.

[274] S. Aliabadi, J. Abedi, and B. Zellars. Parallel finite element simulation of mooring forces on floating objects. *International Journal for Numerical Methods in Fluids*, 41:809–822, 2003.

[275] S. H. Jeon, Y. U. Cho, M. W. Seo, J. R. Cho, and W. B. Jeong. Dynamic response of floating substructure of spar-type offshore wind turbine with catenary mooring cables. *Ocean Engineering*, 72:356–364, 2013.

[276] S. Burmester, G. Vaz, and S. Gueydon. Investigation of a semi-submersible floating wind turbine in surge decay using CFD. *Ship Technology Research*, 2018.

[277] E. Huse. Influence of mooring line damping upon rig motions. In *Offshore Technology Conference*. OnePetro, 1986.

[278] Y. Liu and L. Bergdahl. Improvements of Huse's model for estimating mooring cable induced damping. In *ASME, 17 th International Conference on Offshore Mechanics and Arctic Engineering, USA*, page 7, 1998.

[279] C. Bauduin and M. Naciri. A conribution on quasi-static mooring line damping. In *18th International Conference on Offshore mechanics and Arctic Engineering, July 11-16*, St. Johns, Newfoundland, Canada, 1999.

[280] S. Quallen, T. Xing, P. Carrica, Y. Li, and J. Xu. CFD simulation of a floating offshore wind turbine system using a quasi-static crowfoot mooring-line model. *Journal of Ocean and Wind Energy*, 1(3):143–152, 2014.

[281] T. T. Tran and D. H. Kim. The coupled dynamic response computation for a semi-submersible platform of floating offshore wind turbine. *Journal of Wind Engineering and Industrial Aerodynamics*, 147:104–119, 2015.

[282] T. T. Tran and D. H. Kim. Fully coupled aero-hydrodynamic analysis of a semi-submersible FOWT using a dynamic fluid body interaction approach. *Renewable Energy*, 92:244–261, 2016.

[283] S. Burmester and G. Vaz. Towards credible CFD simulations for floating offshore wind turbines. *Ocean Engineering*, 209(June):107237, 2020.

[284] L. Li, S. Fu, and Y. Xu. Nonlinear hydroelastic analysis of an aquaculture fish cage in irregular waves. *Marine Structures*, 34:56–73, 2013.

[285] E. E. Bachynski. *Design and dynamic analysis of tension leg platform wind turbines*. Phd thesis, NTNU, 2014.

[286] S. Butterfield, W. Musial, J. Jonkman, and P. Sclavounos. Engineering challenges for floating offshore wind turbines. In *2005 Copenhagen Offshore Wind Conference, October 26-28*, Copenhagen, Denmark, 2007.

[287] E. B. L. Mackay, A. Feichtner, R. Smith, P. R. Thies, and L. Johanning. Verification of a Boundary Element model for wave forces on structures with porous elements. In *Proceedings of the 3rd International Conference on Renewable Energies Offshore (RENEW 2018)*, Lisbon, Portugal, 2018.

[288] P. J. Roache. Quantification of uncertainty in Computational Fluid Dynamics. *Annual Review of Fluid Mechanics*, 29(1):123–160, 1997.

[289] F. Stern, R. V. Wilson, H. W. Coleman, and E. G. Paterson. Comprehensive approach to verification and validation of CFD simulations - part 1: methodology and procedures. *Journal of Fluids Engineering*, 123(4):793, 2001.

[290] L. Eça and M. Hoekstra. A procedure for the estimation of the numerical uncertainty of CFD calculations based on grid refinement studies. *Journal of Computational Physics*, 262:104–130, 2014.

[291] L. Eça and M. Hoekstra. Evaluation of numerical error estimation based on grid refinement studies with the method of the manufactured solutions. *Computers and Fluids*, 38(8):1580–1591, 2009.

[292] B. J. Koo, A. J. Goupee, R. W. Kimball, and K. F. Lambrakos. Model tests for a floating wind turbine on three different floaters. *Journal of Offshore Mechanics and Arctic Engineering*, 136(2):1–11, 2014.

[293] A. J. Goupee, B. Koo, R. W. Kimball, K. F. Lambrakos, and H. J. Dagher. Experimental comparison of three floating wind turbine concepts. *Proceedings of the International Conference on Offshore Mechanics and Arctic Engineering - OMAE*, 7:467–476, 2012.

[294] J. M. Jonkman. Dynamics of offshore floating wind turbines - model development and verification. *Wind Energy*, 12(5):459–492, 2009.

[295] L. Chen, J. Zang, A. Hillis, G. Morgan, and A. Plummer. Numerical investigation of wave–structure interaction using OpenFOAM. *Ocean Engineering*, 88:91–109, 2014.

[296] B. Devolder, P. Troch, and P. Rauwoens. Performance of a buoyancy-modified k-ω and k-ω SST turbulence model for simulating wave breaking under regular waves using OpenFOAM®. *Coastal Engineering*, 138(March):49–65, 2018.

[297] S. Brown, V. Magar, D. Greaves, and D. Conley. An evaluation of RANS turbulence models for spilling breakers. *Coastal Engineering Proceedings*, 34: 5–5, 2014.

[298] Y. Goda and Y. Suzuki. Estimation of incident and reflected waves in random wave experiments. *Coastal Engineering*, pages 828–845, 1976.

[299] E. Mansard and E. Funke. The measurement of incident and reflected spectra using a least squares method. In *Proceedings of the 17th International Conference on Coastal Engineering, 23–28 March 1980*, pages 154–172, Sydney, Australia, 1980.

[300] R. C. MacCamy and R. A. Fuchs. Wave forces on piles: a diffraction theory, 1954.

[301] J. R. Morison, J. W. Johnson, and S. A. Schaaf. The force exerted by surface waves on piles. *Journal of Petroleum Technology*, 2(05):149–154, 1950.

[302] D. Qiao, C. Feng, J. Yan, H. Liang, D. Ning, and B. Li. Numerical simulation and experimental analysis of wave interaction with a porous plate. *Ocean Engineering*, 218, 2020.

[303] A. Feichtner, E. Mackay, G. Tabor, P. R. Thies, L. Johanning, and D. Ning. Using a porous-media approach for CFD modelling of wave interaction with thin perforated structures. *Journal of Ocean Engineering and Marine Energy*, 2020.

[304] K. Missios, N. G. Jacobsen, and J. Roenby. Using the isoAdvector geometric VOF method for interfacial flows through porous media. In *9th Conference on Computational Methods in Marine Engineering (Marine 2021)*, number June, 2021.

Appendices

Appendix A

Pure Wave Propagation

A.1 Scheme and Solver Settings

The solver and scheme settings applied for the simulations of pure wave propagation are listed in Table A.1.

Table A.1: Solver and scheme settings for pure wave propagation

Parameters	**Settings/Schemes/Method**
controlDict	
adjustTimeStep	yes
maxCo	0.5
maxAlphaCo	0.5
fvSolution	
momentumPredictor	yes
nOuterCorrectors	1
nCorrectors	3
nNonOrthogonalCorrectors	1
nAlphaCorr	1
nAlphaSubCycles	2
cAlpha	1
alpha.water: solver,tol,relTol	smoothSolver/symGaussSeidel, 1e-06, 0
pcorr: solver,tol,relTol	PCG/DIC, 1e-05, 0
p_rgh: solver,tol,relTol	PCG/DIC, 1e-07, 0.05
p_rghFinal: solver,tol,relTol	PCG/DIC, 1e-07, 0
U: solver,tol,relTol	smoothSolver/symGaussSeidel, 1e-06, 0
fvSchemes	
ddt $\left(\frac{\partial}{\partial t}\right)$	Euler
grad $(\nabla \boldsymbol{u}, \nabla \alpha)$	Gauss linear
laplacian $\left(\nabla^2\right)$	Gauss linear corrected
div(rhoPhi,U) $(\nabla \cdot (\rho\phi \boldsymbol{u}))$	Gauss limitedLinearV 1
div(phi,alpha) $(\nabla \cdot (\phi\alpha))$	Gauss vanLeer
div(phirb,alpha) $(\nabla \cdot (\rho\phi_{rb} \boldsymbol{u}))$	Gauss interfaceCompression
interpolation	linear
snGrad	corrected
interphase capturing method	MULES
RASmodel	laminar

Appendix B

Fixed Thin Perforated Structures

B.1 Scheme and Solver Settings

The solver and scheme settings applied for the simulations of pure wave propagation (as listed in Table A.1 in Appendix A) have also been used for the simulations with the static structures. Only the maximum CFL-numbers needed to be reduced from 0.5 to 0.3. All porosity related scheme settings such as `div(rhoPhiPor, UPor)` use the same schemes as for the non-porous values and are not listed separately.

B.2 Coordinate Transformation for the Orthotropic Implementation

In this work, the anisotropic porosity implementation of waves2Foam has been modified for application to a porous cylinder and combined with OlaFlow/IHFoam's wave modelling capabilities. In the orthotropic case, the direction of the porosity coefficient tensor, C_f, needs to be aligned with the local coordinate system of the structure in each mesh cell and the pressure-drop only needs to be applied in normal direction across the sheet.

The following code listings contain the relevant files and sections of the code as part

of the `poroWavesFoam` -solver:

- `cylPorousZone.C` (Code Section B.1) which applies the coefficient vectors in 3D cylindrical shape (no changes are required in the declarations in `cylPorousZone.H`), and
- the `porosityZones` file which serves as simulation input.

Modifications are coloured, where red font indicates commented and unused previous code and blue font indicates extended and modified code as well as key comments.

Since the porosity model and library is based on waves2Foam's porosity solver, also `poroWavesFoam` uses D and F as notation for the linear (Darcy) and quadratic (Forchheimer) porosity coefficients, respectively.

Code Section B.1: poroWavesFoam: cylPorousZone.C file

```
50 ...

52 Foam::cylPorousZone::cylPorousZone
   (
54     const word& name,
       const fvMesh& mesh,
56     const dictionary& dict
   )
58 :
       name_(name),
60     mesh_(mesh),
       dict_(dict),
62     cellZoneID_(mesh_.cellZones().findZoneID(name)),

64     coordSys_(mesh, dict), //A: Cartesian system, not
           cylindrical

66     porosity_(readScalar(dict_.lookup("porosity"))),
       addedMassCoeff_(readScalar( dict_.lookup("gammaAddedMass"))
           ),
68     D_("D", dimensionSet(0, -2, 0, 0, 0), tensor::zero),
       F_("F", dimensionSet(0, -1, 0, 0, 0), tensor::zero)
70     {
       Info<< "Creating porous zone: " << name_ << endl;
72

       autoPtr<Foam::porosityCoefficient> pcPtr(Foam::
           porosityCoefficient::New(dict));
```

```
74
   bool foundZone = (cellZoneID_ != -1);
76 reduce(foundZone, orOp<bool>());

78 if (!foundZone && Pstream::master())
   {
80    FatalErrorIn
      (
82       "Foam::cylPorousZone::cylPorousZone"
         "(const fvMesh&, const word&, const dictionary&)"
84    )   << "cannot find porous cellZone " << name_
         << exit(FatalError);
86 }

88 // porosity
   if (porosity_ <= 0.0 || porosity_ > 1.0)
90 {
      FatalIOErrorIn
92    (
         "Foam::cylPorousZone::cylPorousZone"
94       "(const fvMesh&, const word&, const dictionary&)",
         dict_
96    )
      << "out-of-range porosity value " << porosity_
98    << exit(FatalIOError);
   }
100

   // local-to-global transformation tensor
102 //A:  only rotational R() transformations around 2 axes here
   //A:    const tensor E = coordSys_.R().R();
104

   dimensionedVector d(pcPtr->linearCoefficient());
106

   if (D_.dimensions() != d.dimensions())
108 {
      FatalIOErrorIn
110   (
         "Foam::cylPorousZone::cylPorousZone"
112      "(const fvMesh&, const word&, const dictionary&)",
         dict_
```

```
114         )    << "incorrect dimensions for d: " << d.dimensions()
                 << " should be " << D_.dimensions()
116              << exit(FatalIOError);
        }
118
        checkNegativeResistance(d);
120
    //A: transformation from dimensionedVector d to
        dimensionedTensor D_; via assigning the diagonal elements (
        non-diagonals are initialized with 0.0); and coordinate
        system transformation
122     D_.value().xx() = d.value().x();
        D_.value().yy() = d.value().y();
124     D_.value().zz() = d.value().z();
    //A:    D_.value() = (E & D_ & E.T()).value();
126 //A: only rotation R() here; no cylindrical <-> cartesian

128     dimensionedVector f(pcPtr->quadraticCoefficient());

130     if (F_.dimensions() != f.dimensions())
        {
132         FatalIOErrorIn
            (
134             "Foam::cylPorousZone::cylPorousZone"
                "(const fvMesh&, const word&, const dictionary&)",
136             dict_
            )    << "incorrect dimensions for f: " << f.dimensions()
138              << " should be " << F_.dimensions()
                 << exit(FatalIOError);
140     }

142     checkNegativeResistance(f);

144     //A:  0.5 is applied by means of a typical Forcheimer-term
        F_.value().xx() = 0.5*f.value().x();
146     F_.value().yy() = 0.5*f.value().y();
        F_.value().zz() = 0.5*f.value().z();
148 //A:     F_.value() = (E & F_ & E.T()).value();
    //A: only rotation R() here; no cylindrical <-> cartesian
150
```

```
    // it is an error not to define anything
152 if
    (
154     magSqr(D_.value()) <= VSMALL
        && magSqr(F_.value()) <= VSMALL
156 )
    {
158     FatalIOErrorIn
        (
160         "Foam::cylPorousZone::cylPorousZone"
            "(const fvMesh&, const word&, const dictionary&)",
162         dict_
        )   << "neither powerLaw (C0/C1) "
164         "nor Darcy-Forchheimer law (d/f) specified"
            << exit(FatalIOError);
166 }
}
168

170 // * * * * * * * * * * * * * * * * Member Functions  * * * * * *
     * * * * * * * //

172 void Foam::cylPorousZone::porosity
(
174 volScalarField & poro
) const
176 {
    if ( cellZoneID_ == -1 )
178 {
        return;
180 }

182 const labelList& cells = mesh_.cellZones()[cellZoneID_];

184 forAll( cells, celli )
    {
186     poro[cells[celli]] = porosity_;
    }
188 }
```

```
190 void Foam::cylPorousZone::D //A: Dfield - linear porosity term
    (
192     volTensorField & Dfie
    ) const
194 {
    if ( cellZoneID_ == -1 )
196 {
        return;
198 }

200 const labelList& cells = mesh_.cellZones()[cellZoneID_];

202 /*A: same tensor D in each cell
    forAll( cells, celli )
204 {
        Dfie[cells[celli]] = D_.value();
206 }

208 const vectorField& ccLokal = coordSys_.localVector(ccGlobal
        );
    :A*/
210
    const vectorField& cc = mesh_.C(); //:A get a field of cell
         centres
212
    forAll( cells, celli )
214 {

216     const vector c = cc[cells[celli]];
        const scalar x = c[0];
218     const scalar y = c[1];

220     //A: get theta angle
        const scalar theta = atan2(y,x);///
222
        //A: construct the transformation tensor TR (local <->
            global) on cartesian basis
224     const tensor TR
        (
226         cos(theta) , -sin(theta) , 0 ,
```

```
            sin(theta) , cos(theta)   , 0 ,
            0      , 0        , 1
        );

        //A: transform the coefficent tensors from cylindrical
            to cartesian
        tensor DD = (TR & D_ & TR.T()).value();

        //A: transform from cartesian to global cartesian (
            rotations around axes)
        const tensor E = coordSys_.R().R();
        const tensor& D = E & DD & E.T();

        //A: D_ is given for the local cylindricalCS in the
            dictionary
        Dfie[cells[celli]] = D;
    }
}

void Foam::cylPorousZone::F //A: Ffield - drag porosity term
(
    volTensorField & Ffie
) const
{
    if ( cellZoneID_ == -1 )
    {
        return;
    }

    const labelList& cells = mesh_.cellZones()[cellZoneID_];

/*A: same tensor F in each cell
    forAll( cells, celli )
    {
        Ffie[cells[celli]] = F_.value();
    }

    const vectorField& ccLokal = coordSys_.localVector(ccGlobal
        );
:A*/
```

```
264     const vectorField& cc = mesh_.C(); //A: get a field of cell
            centres

266     forAll( cells, celli )
        {
268
            const vector c = cc[cells[celli]];
270         const scalar x = c[0];
            const scalar y = c[1];
272
            //A: get theta angle
274         const scalar theta = atan2(y,x);

276         //A: construct the transformation tensor TR (local <->
                global) on cartesian basis
            const tensor TR
278         (
                cos(theta) , -sin(theta) , 0 ,
280             sin(theta) , cos(theta)  , 0 ,
                0      , 0        , 1
282         );

284         //A: transform the coefficent tensors from cylindrical
                to cartesian
            tensor FF = (TR & F_ & TR.T()).value();
286
            //A: transform from cartesian to global cartesian (
                rotations around exes)
288         const tensor E = coordSys_.R().R();
            const tensor& F = E & FF & E.T();
290
            //A: F_ is given for the local cylindricalCS in the
                dictionary
292         Ffie[cells[celli]] = F;
        }
294 }

296 ...
```

Code Section B.2: poroWavesFoam: porosityZones file

```
...

1
(
  porosity
  {
   type cartesian;
   origin (8.005 0 0); //A:centre of cylinder
   coordinateRotation
   {
      type   axesRotation;
      e1   (1 0 0);
      e2   (0 1 0);
   }

   resistanceFormulation nativeOF; //A: using D and F

   porosity 0.2;
   gammaAddedMass 0.0; //A: transient porosity term

   d d [0 -2 0 0 0 0 0] (0 0 0);
         //A: coefficient for linear porosity term
   f f [0 -1 0 0 0 0 0] (4e3 4e12 4e12);
         //A: coefficient for drag porosity term
  }
)

...
```

The rest and most code of `poroWavesFoam` equals both `olaFlow` and `waveFoam` (of waves2Foam) since both base on `interFoam`. Only minor notation needed to be matched and are not presented here in detail.

Appendix C

Moving Thin Perforated Structures

C.1 Scheme and Solver Settings

The solver and scheme settings applied for the simulations for the models with the moving TLP are listed in Table C.1.

C.2 Code Extensions for correct Motion including Porosity

The following code listings only contain the relevant files and sections of the code that have been modified in the original files. This concerns all altered files of the duplicated `libsixDoFRigidBodyMotionPor.so` library,

- `sixDoFRigidBodyMotionSolver.H` and
- `sixDoFRigidBodyMotionSolver.C`,

and the corresponding extended

- `dynamicMeshDict`

file that is needed as simulation input. As before, red font indicates commented and unused previously existing code. Blue font indicates extended and modified code as well as key comments.

The original code consists of a single set of `patches` on which the forces are calculated and from which the mesh morphing is guided. The amended code splits the patch specification for the mesh morphing and the force calculation. The mesh motion boundaries are still specified and calculated with `patches` as initially. For the force calculation, solid and porous structures are considered separately. The force on the solid parts of the structure is specified and calculated with `patchesSolid`. The force on the porous part of the structure are specified and calculated with `patchesPorous`. For a simulation, theses patches are specified in the `dynamicMeshDict`, shown in Code Section C.3. In the code, these amendments are declared in `sixDoFRigidBodyMotionSolver.H` (Code Section C.1) and their functions are introduced in `sixDoFRigidBodyMotionSolver.C` (Code Section C.2). In the latter, the separate solid and porous force calculation are `fSolid.calcForcesMoment()` in line 263 and `fPorous.calcForcesMoment()` in line 276. Then, both the porous and solid force are included in the 6-DOF body motion solver to update the motion in `motion_.update`, ranging from line 279 to 290.

Code Section C.1: sixDoFRigidBodyMotionPor: sixDoFRigidBodyMotionSolver.H file

```
...
52
class sixDoFRigidBodyMotionSolver
54 :
public displacementMotionSolver
56 {
    // Private data
58
    //- Six dof motion object
60  sixDoFRigidBodyMotion motion_;

62  wordReList patches_;

64  wordReList patchesSolid_; //:A declaration of solid patches
    wordReList patchesPorous_; //:A declaration of porous
       patches
66
    //- Patches to integrate forces
68  const labelHashSet patchSet_;

70  //- Inner morphing distance (limit of solid-body region)
    const scalar di_;
72
    //- Outer morphing distance (limit of linear interpolation
```

```
      region)
74    const scalar do_;

76    ...
```

Code Section C.2: sixDoFRigidBodyMotionPor: sixDoFRigidBodyMotionSolver.C file

```
...
172
void Foam::sixDoFRigidBodyMotionSolver::solve()
174 {
    const Time& t = mesh().time();
176
    if (mesh().nPoints() != points0().size())
178 {
       FatalErrorInFunction
180    << "The number of points in the mesh seems to have
          changed." << endl
       << "In constant/polyMesh there are " << points0().size()
182    << " points; in the current mesh there are " << mesh().
          nPoints()
       << " points." << exit(FatalError);
184 }

186 // Store the motion state at the beginning of the time-
       stepbool
    bool firstIter = false;
188 if (curTimeIndex_ != this->db().time().timeIndex())
    {
190    motion_.newTime();
       curTimeIndex_ = this->db().time().timeIndex();
192    firstIter = true;
    }
194
    dimensionedVector g("g", dimAcceleration, Zero);
196
    if (db().foundObject<uniformDimensionedVectorField>("g"))
198 {
       g = db().lookupObject<uniformDimensionedVectorField>("g
          ");
200 }
```

```
    else if (coeffDict().found("g"))
202 {
        coeffDict().lookup("g") >> g;
204 }

206 // scalar ramp = min(max((this->db().time().value() - 5)
        /10, 0), 1);
    scalar ramp = 1.0;
208
    if (test_)
210 {
        motion_.update
212     (
            firstIter,
214         ramp*(motion_.mass()*g.value()),
            ramp*(motion_.mass()*(motion_.momentArm() ^ g.value()
                )),
216         t.deltaTValue(),
            t.deltaT0Value()
218     );
    }
220 else
    {
222
    /*A:
224
        dictionary forcesDict;
226
        forcesDict.add("type", functionObjects::forces::typeName
            );
228     forcesDict.add("patches", patchesSolid_);  //:A in the
            temporary forcesDict it needs to stay "patches"
        forcesDict.add("rhoInf", rhoInf_);
230     forcesDict.add("rho", rhoName_);
        forcesDict.add("CofR", motion_.centreOfRotation());
232
        functionObjects::forces f("forces", db(), forcesDict);
234
        f.calcForcesMoment();  //A: forces are calculated on
            solid patches here only
```

```
236
//A: motion update with forces on solid patches only
238       motion_.update
          (
240           firstIter,
              ramp*(f.forceEff() + motion_.mass()*g.value()),
242           ramp
              *(
244           f.momentEff()
              + motion_.mass()*(motion_.momentArm() ^ g.value())
246           ),
              t.deltaTValue(),
248           t.deltaT0Value()
          );
250    :A*/

252 //A: force calculation for solid patches separately
          dictionary forcesDictSolid;
254
          forcesDictSolid.add("type", functionObjects::forces::
              typeName);
256       forcesDictSolid.add("patches", patchesSolid_);
          forcesDictSolid.add("rhoInf", rhoInf_);
258       forcesDictSolid.add("rho", rhoName_);
          forcesDictSolid.add("CofR", motion_.centreOfRotation());
260
          functionObjects::forces fSolid("forces", db(),
              forcesDictSolid);
262
          fSolid.calcForcesMoment(); //:A
264
//A: force calculation for porous (outer+inner) patches
    separately
266       dictionary forcesDictPorous;

268       forcesDictPorous.add("type", functionObjects::forces::
              typeName);
          forcesDictPorous.add("patches", patchesPorous_);
270       forcesDictPorous.add("rhoInf", rhoInf_);
          forcesDictPorous.add("rho", rhoName_);
```

```
272         forcesDictPorous.add("CofR", motion_.centreOfRotation())
               ;

274         functionObjects::forces fPorous("forces", db(),
               forcesDictPorous);

276         fPorous.calcForcesMoment(); //:A

278 //A: motion update including forces on porous structure
         motion_.update
280         (
               firstIter,
282            ramp*(fSolid.forceEff() + fPorous.forceEff() +
                  motion_.mass()*g.value()),
               ramp
284            *(
               fSolid.momentEff() + fPorous.momentEff()
286            + motion_.mass()*(motion_.momentArm() ^ g.value())
               ),
288            t.deltaTValue(),
               t.deltaT0Value()
290         );
   //:A
292      }

294      // Update the displacements
      pointDisplacement_.primitiveFieldRef() =
296   motion_.transform(points0(), scale_) - points0();

298      // Displacement has changed. Update boundary conditions
      pointConstraints::New
300      (
         pointDisplacement_.mesh()
302   ).constrainDisplacement(pointDisplacement_);
   }
```

Code Section C.3: example of a dynamicMeshDict file

```
   ...
16
   dynamicFvMesh       dynamicMotionSolverFvMesh;
```

```
18
   motionSolverLibs    ("libsixDoFRigidBodyMotionPor.so");
20    //A: "libsixDoFRigidBodyMotion.so"

22 motionSolver        sixDoFRigidBodyMotion;

24 sixDoFRigidBodyMotionCoeffs
   {
26    patches     (floatingObject); //A: for mesh morphing
         displacement

28    patchesSolid   (floatingObject);    //A: solid patches
      patchesPorous  (                    //A: porous patches
30                 cylOutPatch_half0
                   cylInPatch_half1
32                 );

34    innerDistance  0.12;
      outerDistance   0.40;
36
      centreOfMass    (3.0 0.0 1.422);
38
      mass            16.18;
40
      momentOfInertia ( 4.3747e7 4.3747e7 5.3035e5  );
42       //A: TLP model with legs, whole tower and porous
            cylinder

44    report          on;

46    accelerationRelaxation 0.7;
      accelerationDamping 0.95;
48
      solver   {  type Newmark;  }
50
      //A: only surge/translational motion in x direction
52    constraints
      {
54       fixedLineX //A: horizontal translation allowed here
         {
```

```
56          sixDoFRigidBodyMotionConstraint line;
            direction (1 0 0);
58      }
        fixedRotation //A: no rotation
60      {
            sixDoFRigidBodyMotionConstraint orientation;
62      }
    }
64
    restraints
66  {
        mooring //A: one horizontal spring as a sum of the three
             tendons
68      {
            sixDoFRigidBodyMotionRestraint   linearSpring;
70          anchor                          (2.333 0 0.553);
            refAttachmentPt                 (2.433 0 0.553);
72          stiffness                       257.2;
            damping                         0;
74          restLength                      0.1;
        }
76  }
}
```

Table C.1: Solver and scheme settings for the models with the moving TLP

Parameters	**Settings/Schemes/Methods**
controlDict	
adjustTimeStep	yes
maxCo	0.10–0.19
maxAlphaCo	0.10–0.19
maxDeltaT	0.0001–0.0.0006
fvSolution	
momentumPredictor	no
moveMeshOuterCorrectors	yes
nOuterCorrectors	2
nCorrectors	2
nNonOrthogonalCorrectors	1
nAlphaCorr	1
nAlphaSubCycles	2
cAlpha	1
alpha.water: solver,tol,relTol	smoothSolver/symGaussSeidel, 1e-08, 0
pcorr: solver,tol,relTol	PCG/DIC, 1e-05, 0
p_rgh: solver,tol,relTol	GAMG/DIC, 1e-08, 0.01
p_rghFinal: solver,tol,relTol	PCG/DICGaussSeidel (precond.), 1e-08, 0
U: solver,tol,relTol	smoothSolver/GaussSeidel, 1e-06, 0.1
UFinal: solver,tol,relTol	smoothSolver/GaussSeidel, 1e-06, 0
cellDisplacement/Final: solver,tol,relTol	GAMG/GaussSeidel, 1e-05, 0
fvSchemes	
ddt $\left(\frac{\partial}{\partial t}\right)$	Euler
grad $(\nabla \boldsymbol{u}, \nabla \alpha)$	Gauss linear
laplacian $\left(\nabla^2\right)$	Gauss linear corrected
div(rhoPhi,U) $(\nabla \cdot (\rho\phi \boldsymbol{u}))$	Gauss vanLeerV
div(phi,alpha) $(\nabla \cdot (\phi\alpha))$	Gauss vanLeer
div(phirb,alpha) $(\nabla \cdot (\rho\phi_{rb} \boldsymbol{u}))$	Gauss linear
interpolation	linear
snGrad	corrected
interphase capturing method	MULES
RASmodel	laminar
dynamicMeshDict	
motionSolver	sixDoFRigidBodyMotion(Por)
accelerationRelaxation	0.7
accelerationDamping	0.95
solver	Newmark

And now, Rex, let's go and find a place to thrive...